DOCTORAL THESIS

A micromechanical study of the Standard Penetration Test

Author: Ningning Zhang

Division of Geotechnical Engineering and Geosciences, Department of Civil and Environmental Engineering, Polytechnic University of Catalonia - Barcelona Tech

Supervisors:

Antonio Gens Solé

Marcos Arroyo Álvarez de Toledo

Matteo Oryem Ciantia

Barcelona

November 2019

To *My family*

Abstract

This thesis explores the potential of models based on the discrete element method (DEM) to study dynamic probing of granular materials, considering realistic particle-scale properties.

The virtual calibration chamber technique, based on the discrete element method, is applied to study the standard penetration test (SPT). A macro-element approach is used to represent a rod driven with an impact like those applied to perform SPT. The rod is driven into a chamber filled with a scaled discrete analogue of a quartz sand. The contact properties of the discrete analogue are calibrated simulating two low-pressure triaxial tests. The rod is driven changing input energy and controlling initial density and confinement stress. Energy-based blowcount normalization is shown to be effective. Results obtained are in good quantitative agreement with well-accepted experimentally-based relations between blowcount, density and overburden.

A comprehensive energetic balance of the virtual calibration chamber is conducted. Energy balance is applied separately to the driven rod and the chamber system, giving a detailed account of all the different energy terms. The characterization of the evolution and distribution of each energy component is investigated. It appears that the SPT test input energy is mainly dissipated in friction. The energy-based interpretation of SPT dynamic response proposed by Schnaid et al. (2017) is then validated in comparisons between static and dynamic penetration results. Moreover, microscale investigation provides important information on energy dissipation mechanisms.

A well-established DEM crushing contact model and a rough Hertzian contact model are combined to incorporate both effects in a single contact model. The efficient user defined contact model (UDCM) technique is used for the contact model implementation. Parametric studies explore the effect of particle roughness on single particle crushing event. The model is then used to recalibrate the contact properties of the quartz sand, being able to use realistic contact properties and then correctly capture both load-unload behaviour and particle size distribution evolution.

The calibration chamber results are exploited to investigate the relation between static and dynamic penetration test. This is done first for unbreakable materials and later for crushable and rough-crushable ones. It is shown that the tip resistance measured under impact dynamic penetration conditions is very

close to that under constant velocity conditions, hence supporting recent proposals to relate CPT and SPT results. It is also shown that penetration resistance reduces if particles are allowed to break, particularly when roughness is also considered.

Keywords: granular materials, discrete element method, dynamic probing, standard penetration test, energy-based interpretation, particle surface roughness, particle crushing, rough crushable contact model, static penetration test

Resumen

Esta tesis explora el potencial de los modelos basados en el método de elementos discretos (DEM) para estudiar el sondeo dinámico de materiales granulares, considerando propiedades realistas a escala de partículas.

La técnica de cámara de calibración virtual, basada en el método de elemento discreto, se aplica para estudiar la prueba de penetración estándar (SPT). Se utiliza un enfoque de macroelemento para representar una barra impulsada con un impacto como los aplicados para realizar SPT. La varilla se introduce en una cámara llena de un análogo discreto escalado de arena de cuarzo. Las propiedades de contacto del análogo discreto se calibran simulando dos pruebas triaxiales de baja presión. La varilla se acciona cambiando la energía de entrada y controlando la densidad inicial y el estrés de confinamiento. La normalización del recuento de golpes basado en energía se muestra efectiva. Los resultados obtenidos están en buen acuerdo cuantitativo con relaciones basadas en experimentos bien aceptadas entre recuento de golpes, densidad y sobrecarga.

Se realiza un balance energético integral de la cámara de calibración virtual. El balance de energía se aplica por separado a la varilla impulsada y al sistema de cámara, dando una descripción detallada de todos los diferentes términos de energía. Se investiga la caracterización de la evolución y distribución de cada componente energético. Parece que la energía de entrada de prueba SPT se disipa principalmente en fricción. La interpretación basada en la energía de la respuesta dinámica SPT propuesta por Schnaid et al. (2017) luego se valida en comparaciones entre los resultados de penetración estática y dinámica. Además, la investigación en microescala proporciona información importante sobre los mecanismos de disipación de energía.

Un modelo de contacto de trituración DEM bien establecido y un modelo de contacto hertziano aproximado se combinan para incorporar ambos efectos en un modelo de contacto único. La técnica eficiente de modelo de contacto definido por el usuario (UDCM) se utiliza para la implementación del modelo de contacto. Los estudios paramétricos exploran el efecto de la rugosidad de las partículas en el evento de trituración de partículas individuales. El modelo se usa para recalibrar las propiedades de contacto de la arena de cuarzo, pudiendo usar propiedades de contacto realistas y luego capturar correctamente el comportamiento de carga y descarga y la evolución de la distribución del tamaño de partícula.

Los resultados de la cámara de calibración se explotan para investigar la relación entre la prueba de penetración estática y dinámica. Esto se hace primero para materiales irrompibles y luego para materiales triturables y desmenuzables. Se muestra que la resistencia de la punta medida en condiciones de penetración dinámica de impacto es muy cercana a la de condiciones de velocidad constante, por lo tanto, respalda propuestas recientes para relacionar los resultados de CPT y SPT. También se muestra que la resistencia a la penetración se reduce si se permite que las partículas se rompan, particularmente cuando también se considera la aspereza.

Palabras clave: materiales granulares, método de elementos discretos, sondeo dinámico, prueba de penetración estándar, interpretación basada en energía, rugosidad de la superficie de las partículas, trituración de partículas, modelo de contacto triturable en bruto, prueba de penetración estática

Acknowledgements

The author would like to acknowledge the countless support, assistance and care received from all the following organizations, people and enterprises for making this doctoral thesis possible.

First of all, the financial support of the China Scholarship Council and UPC is greatly acknowledged. The support from the Ministry of Science and Innovation of Spain through the research grant BIA2017-84752-R and the EU funded GEO-RAMP RISE project (H2020-645665-GEO-RAMP) is also acknowledged.

I would express many of my thankfulness and appreciation to my supervisors, Professor Antonio Gens, Marcos Arroyo and Matteo Ciantia, for their generous support and guidance all over the years. Thank you Antonio for bringing me here at your excellent team, since then the way of my research and life experience has been getting broader and broader. Thank you Marcos for convincingly leading me to be professional always with full of your patience. I do truly appreciate your efforts in placing me in wonderful research environment by bringing me to numerous high-level conferences, symposiums, meetings and discussions. Thank you Matteo for your persistent help in my study. Without your help, the target of the thesis work would not have been achieved. Your enthusiastic and confidential attitude towards research has inspired me deeply.

I would like to thank all the people that were hosting me during my exchange and training stay abroad. Thank you Professor Mingjing Jiang for having warmly hosted me in Tongji University. Thanks to the ITASCA company in Lyon, particularly to their employee Sacha Emam, for giving a fantastic training course on PFC software and thereafter providing continuous technical support. Thanks to Quoc Anh Tran, Bastien Chevalier and Pierre Breul for broadening my vision on the thesis topic in Clermont Université. Thanks to the Sol Solution company in Clermont Ferrand, particularly to Miguel Benz, for the detailed introduction of the super advanced soil investigation apparatus. Thank you Matteo Ciantia for your DEM support and for hosting me at Imperial College.

Very special thanks are given to all the friends and colleagues I met at UPC campus and in daily life. I cannot list all the names here as everyone has been engraved in my heart and I will never forget. Thanks to all my CSC colleagues for accompanying me at the initial periods of studying abroad. Thanks to all

my amazing and interesting colleagues at UPC in making my daily work possible and colorful. A great thanks to all my friends distributed in Barcelona city, for helping me become mature and stable.

Finally, thanks to my wife Min and my son Qianmu. Without whose daily support and encouragement, this thesis could not have been accomplished. The arrival of Qianmu has brought me endless joy, love and peace.

I truly thank everyone from the bottom of my heart.

Contents

Publications

This is a list of all the work published, accepted, to be submitted, related to this PhD.

Peer reviewed journals

Zhang, N., Ciantia, M. O., Arroyo, M., & Gens, A., (2019b). A contact model for rough crushable particlesual calibration chamber. (to be submitted)

Zhang, N., Ciantia, M. O., Arroyo, M., & Gens, A., (2019c). Energy balance analysis during the Standard Penetration Test. (to be submitted)

Zhang, N., Arroyo, M., Ciantia, M. O., Gens, A., & Butlanska, J. (2019a). Standard penetration testing in a virtual calibration chamber. *Computers and Geotechnics*, *111*(3), 277–289. https://doi.org/10.1016/j.compgeo.2019.03.021

Conference proceedings

Zhang, N., Arroyo, M., Ciantia, M., & Gens, A., (2019), Incorporating surface roughness into DEM models of crushable soils, *5th International Itasca Symposium*, Vienna, Austria. (accepted)

Zhang, N., Arroyo, M., Gens, A., & Ciantia, M., (2018), DEM modelling of dynamic penetration in granular material, 2018, *NUMGE conference*, Porto, Portugal.

Zhang, N., Arroyo, M., Ciantia, M., & Gens, A., (2018), DEM investigation of particle crushing effects on static and dynamic penetration tests, *China Europe Conference on Geotechnical Engineering*, Vienna, Austria.

Ciantia, M., Arroyo, M., **Zhang, N**., & Emam, S., (2017). Periodic cells for large-scale problem initialization, *8th International Conference on Micromechanics of Granular Media*, Montpellier, France.

Ciantia, M., **Zhang, N**., & Arroyo, M., (2017). Enhancing efficiency of DEM modeling of particle breakage, *Proceedings of the 25th UKACM conference on Computational Mechanics,* 12 –13 April, Birmingham, United Kingdom.

List of figures

List of tables

Chapter 1 Introduction

*Everything should be made **as simple as possible, but no simpler.***

-- Einstein (1950)

1.1 Motivations

Dynamic probing soil investigation technique involves driving a device into the soil by striking it with repeated blows of a hammer. This technique is employed in a variety of ground investigation tests such as the Standard Penetration Test (SPT), Becker Penetration Test (BPT), Dynamic Cone Penetration Test (DCPT) or light, medium and heavy dynamic penetrometers. Of these, the Standard Penetration Test (SPT) remains as one of the most popular in-situ testing procedures (Schnaid et al., 2009). The results of dynamic testing have been widely used to estimate soil properties, foundation design parameters and evaluate liquefaction potential.

There are many advantages of tests based on dynamic probing technique, for instance, they allow (a) recording continuous profiles with depth, (b) testing in any ground condition, particularly on granular deposits and (c) fast, economical and robust soil characterization. Dynamic probing tests also have important limitations because (a) they are hard to control precisely in many aspects such as hammer types and technical procedures, leading to difficulties in repeating test results, (b) they usually produce a single measurement per test (i.e. N, repeated blows to drive a sampler 300 mm into the ground), which inherently limits the interpretation of dynamic penetration mechanisms, (c) the mechanics of their interaction with the ground are very poorly understood and (d) they are often correlated with other alternatives strongly relying on empirical database.

Many efforts have concentrated in overcoming the limitations by means of energy-related approaches. With the development of energy measurement techniques which were firstly applied in SPT (Kovacs & Salomone, 1982; Schmertmann & Palacios, 1979), the blow number N was normalized as N_{60} by measured energy input from hammer blows. This energy normalization approach was conceived as a major step in improving test control and repeatability (Robertson et al., 1983; Seed et al., 1985; Skempton, 1986). Energy-related proposals for test output interpretation have also recently appeared, in them dynamic penetration resistance is computed based on net energy input from hammer blows and

penetration per blow $\Delta\rho$ (Schnaid et al., 2009; Schnaid et al., 2017). Although the results appear promising the uptake has been limited, in part due to the necessary introduction of experimentally-based correcting factors that obscure the underlying logic.

Simulating in-situ tests in the laboratory is essential to understand the factors affecting the dynamic interaction between probes and soils. *Calibration chambers* have therefore been developed, in which ground conditions are well controlled. However, tests in such equipment is not cost-effective in terms of time and resources. In addition, dynamic probing in calibration chamber involves numerous complexities, so that comparatively little work has been reported.

Alternatively, numerical simulations can also be used to carry out controlled dynamic probing experiments. For granular soils, models based on the *discrete element method* (DEM) (Cundall & Strack, 1979) appears to be attractive because (a) they are appropriate in addressing large displacement problems in a dynamic probing, (b) they allow easy incorporation of grain scale characteristics, such as *crushability*, surface *roughness*, etc. and (c) they facilitate acquisition of very precise information about *energy* input (macroscale) and dissipation (microscale) mechanisms in granular materials.

The numerical creation of three dimensional DEM virtual calibration chambers has been successfully demonstrated for quasi-static tests like the cone penetration test (CPT), in which particles were represented by smooth spheres and were not allowed to break (Arroyo et al., 2011). An extension to their work would be to demonstrate the capabilities of the DEM VCC technique to study dynamic probing tests in granular materials and it is the starting objective of this doctoral work. When dynamic probing tests are performed in DEM VCC, it is necessary to take particle crushability into account since it is known to strongly affect the test results (Ahmed et al., 2014). Furthermore, surface roughness has been recognized to directly affect mechanical behaviors of granular materials, i.e. causing a significant reduction in stiffness (Otsubo et al., 2015), which might in turn affect particle crushing behavior. Therefore, a novel contact model for rough crushable sands is proposed, to give more complete representation of soil behavior.

1.2 Aim & Objectives

This doctoral work aims to make contributions to the following aspects:

- Present an overview of in-situ site investigation tools in which dynamic probing technique is involved;
- Explore the capabilities of the DEM virtual calibration chamber in studying dynamic probing tests (i.e. standard penetration testing, SPT) in granular materials;

- Analyze the energy balance during SPT simulations and verify energy-based interpretation method of SPT test results;
- Develop a DEM contact model for breakable sands taking particle surface roughness into account;
- Calibrate and validate of the newly developed contact model, with successful reproduction of physical experiments;
- Examine the validity of energy-based interpretation approaches for dynamic probing in rough breakable sands.

1.3 Outline of the thesis

This thesis is organized in 8 chapters, of which the first and last one are dedicated to the *Introduction* and *Conclusions*, respectively. Chapter 2 presents a general overview of dynamic testing of soils, while the introduction of the adopted methodology and its state-of-art in applications related to the work in the thesis is given by Chapter 3. From Chapter 4 to 7, the main body of the research is presented.

Chapter 4 was compiled on the basis of the manuscript of a published journal paper, of which the authors reserve the copyright for non-commercial purposes. No attempt is made to infringe publisher's copyright polices.

In particular, this work is organized as follows:

Chapter 2 overviews the diversity of testing apparatus which employs dynamic probing technique in geotechnical engineering and prominently introduces general procedure, interpretation and numerical analysis of the SPT.

Chapter 3 presents details on DEM fundamentals and a brief overview of DEM applications in geomechanics, with emphasis on subjects close to the ones of this thesis, i.e. particle surface roughness, particle breakage and site investigation.

Chapter 4 explores the capabilities of the DEM VCC approach to model dynamic probing tests in granular materials.

Chapter 5 aims to analyze energy balance regarding input from boundaries and dissipation within granular materials during the numerical setting of dynamic probing. Microscale observations of energy dissipation are presented.

Chapter 6 describes the establishment of a contact model for rough breakable sand. The novel model is calibrated and validated against experimental evidence.

Chapter 7 explores the newly proposed contact model for large scale simulations, i.e. static and dynamic penetration tests in the DEM VCC.

Finally, ***Chapter 8*** summarizes the main outcomes of this thesis and presents some recommendations for future work.

Additional information has been organized in the Appendices in order not to disturb the natural flow of the report. This thesis also contains several appendices:

Appendix I presents the validation of the user-defined contact model efficiency in modelling particle crushing.

Appendix II presents MATLAB scripts dealing with the analytical expression for ball-ball contact force.

Appendix III presents C++ scripts dealing with the implementation of user-defined rough crushable contact model.

Chapter 2 Dynamic testing of soils

2.1 Introduction

Dynamic probing technique involves driving a device into the soil by striking it with a hammer. In this technique, the penetrometer installed at the end of a steel rod is driven into the soil, while blow count is recorded. The steel rod generally has a diameter smaller than the penetrometer to minimize the effect of skin friction. Testing is sometimes carried out from the ground level to the final penetration location so that continuous profiles are available and sometimes from the bottom of a previously excavated borehole. This technique is employed in several site investigation tests such as the Standard Penetration Test (SPT), Becker Penetration Test (BPT), Dynamic Cone Penetration Test (DCPT) or light dynamic penetrometers (e.g. Panda). Of these, the Standard Penetration Test (SPT) remains as one of the most popular in-situ testing procedures (Schnaid et al., 2009). The results of dynamic testing have been widely used to estimate soil properties, evaluate liquefaction potential, etc.

In this chapter, the diversity of dynamic testing is reviewed by giving a brief introduction of some widely used penetrometers. Then special emphasis is placed on the SPT. Finally, available numerical analyses of dynamic testing including analytical solutions and DEM simulation are briefly recalled.

2.2 Diversity of dynamic testing

There is a wide range of the tests based on dynamic probing including PANDA, dynamic cone penetration test (DCPT), dynamic probing light (DPL), dynamic probing medium (DPM), dynamic probing heavy (DPH), dynamic probing super heavy -A (DPSH-A), dynamic probing super heavy -B (DPSH-B), standard penetration test (SPT), GRIZZLY, Becker penetration test (BPT), Chinese dynamic penetration test (CDPT), etc. The PANDA and GRIZZLY are developed by the Sol Solution company in France for carrying out dynamic probing more conveniently and simply. Those penetrometers differ in many aspects, such as hammer weight, hammer falling height, tip shape, operation, energy measurement, soil type concerns, countries/regions most in use, outputs, etc. A summary description of those aspects for each penetrometer mentioned can be found in Table 2-1. In subsequent sections several prominent examples of these technologies are discussed in more detail.

Table 2-1 Overview of basic data for dynamic probing tests

Testing	Document	Impact hammer type	Hammer weight: kg	Drop height: mm	Hammer work per blow: J	Tip shape	Operation	Energy measurement method	Soil type conerns	Contries /regions	Outputs
PANDA	Benz Navarrete, (2009)	Handled hammer	<1	-	5 - 130	Cone, with base area of 2 cm^2, 4 cm^2 or 10 cm^2	Manual	Strain and acceleration measurement	Fine sands	France	Penetrogram in dynamic resistance q_d
DCPT	ASTM D6951, (2003)	Drop hammer	8	575	45	60º Cone, with 20 mm base diameter, vertical side length of 3 mm	Manual	Not measured	Sandy soils	United states	DPI, the slope of the relationship
DPL	EN ISO 22476-2, (2002)	Drop hammer	10	500	49	90° Cone, with 35.7 mm diameter, mantle length of 35.7 mm	Automatic	Strain and acceleration measurement	poorly graded sands	German y, UK	N_{10}, blow number per 10 cm
DPM	EN ISO 22476-2, (2002)	Drop hammer	30	500	147	90° Cone, with 43.7 mm diameter, mantle length of 43.7 mm	Automatic	Strain and acceleration measurement	poorly graded sands	German y, UK	N_{10}, blow number per 10 cm
DPH	EN ISO 22476-2, (2002)	Drop hammer	50	500	245	90° Cone, with 43.7 mm diameter, mantle length of 43.7 mm	Automatic	Strain and acceleration measurement	well graded gravel-sand mixtures	German y, UK	N_{10}, blow number per 10 cm
DPSH-A	EN ISO 22476-2, (2002)	Drop hammer	63.5	500	311	90° Cone, with 45.0 mm diameter, mantle length of 90.0 mm	Automatic	Strain and acceleration measurement	Gravels	German y, UK	N_{20}, blow number per 20 cm
DPSH-B	EN ISO 22476-2, (2002)	Drop hammer	63.5	750	467	90° Cone, with 51 mm diameter, mantle length of 51 mm	Automatic	Strain and acceleration measurement	Gravels	German y, UK	N_{20}, blow number per 20 cm
SPT	UNE-EN ISO 22476-3, (2005)	Drop hammer	63.5	760	473	Split-barrel sampler, with 51 mm diameter	Manual, automatic	Strain and acceleration measurement	Granular soils	Japan, China, Brasil	N_{60}, blow counts normalized by
GRIZZLY	Escobar et al., (2016b)	Drop hammer	63.5	190, 380, 570 or 760	118, 236, 354 or 473	Cone, with 32 mm diameter, point area 20 cm	Automatic	Strain and acceleration measurement	Sandy soils	France	Penetrogram in dynamic resistance q_d,
iBPT	Dejong et al., (2017)	Diesel hammer	-	-	-	Closed-ended steel drill string, with diameter of 168 mm	Automatic	Strain and acceleration measurement	Gravels	Canada, United States	N_{B30}, 30% energy normalization
CDPT	Cao et al., (2013)	Drop hammer	120	1000	1176	60° Cone, with base diameter of 74 mm	Manual	Strain and acceleration measurement	Gravels	China	Blow counts required to drive the cone

2.2.1 PANDA 3 – a light dynamic penetrometer

PANDA 3 is the latest version of PANDA portable and lightweight dynamic penetrometers designed and developed by Sol Solution company in France (Benz, 2009). The operation method of the PANDA penetrometers features as striking a drill rod by a light handheld hammer, which facilities variable strike energy input adapted to relative ground resistance (Table 2-1). In PANDA 3, the force and acceleration at the measuring point (Figure 2-1) are recorded from each strike. Then an instantaneous load-penetration curve relating tip resistance and penetration distance can be obtained. From this curve, more soil mechanical parameters can be derived, e.g., wave velocity, damping coefficient, elastic modulus.

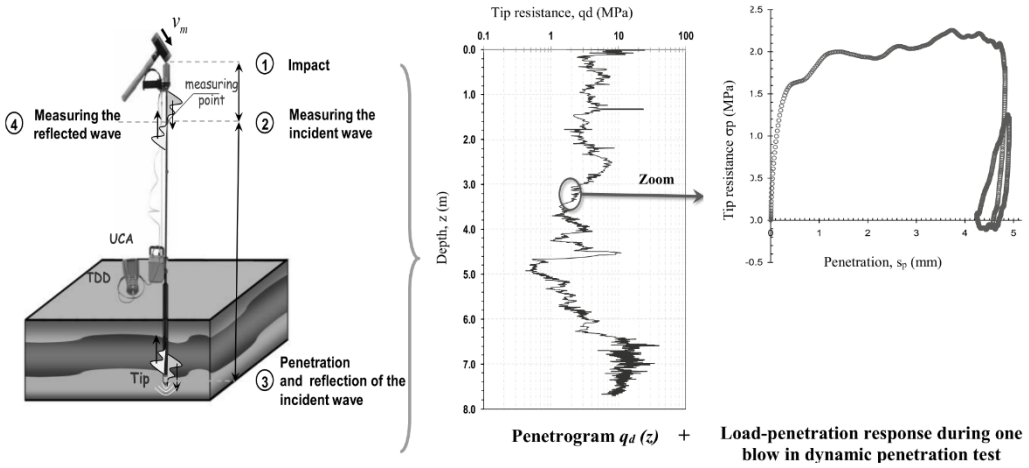

Figure 2-1 Principle of Panda 3 (Escobar et al., 2016a)

2.2.2 Dynamic cone penetration test (DCPT)

The dynamic cone penetration test (DCPT) was originally developed by Scala (1956). It drives a lightweight dynamic penetrometer, which is particularly suitable for low-depth sandy soil exploration. Compared with some other penetrometers, the DCPT is characterized as a fast, cheap and convenient tool. Since its first development, it has been used of worldwide scope for assessment of subgrade stability (Edil & Benson, 2005), determination of engineering parameters of sandy soils (Mohammadi et al., 2008), etc.

The typical DCPT consists of an 8 kg hammer falling over a height of 57.5 cm, which drives a 60º 20 mm base diameter cone tip vertically into the ground (Figure 2-2). The steel rod to which the cone is attached has a smaller diameter than the cone (16 mm) to minimize the effect of skin friction. Therefore the test yields a theoretical hammer potential driving energy of 45 J. The blow number is counted with penetration depth. The DCP penetration index (DPI) is given by the slope of the curve describing the

relationship between blow counts and depth of penetration (in millimeters per blow) at a given linear depth segment.

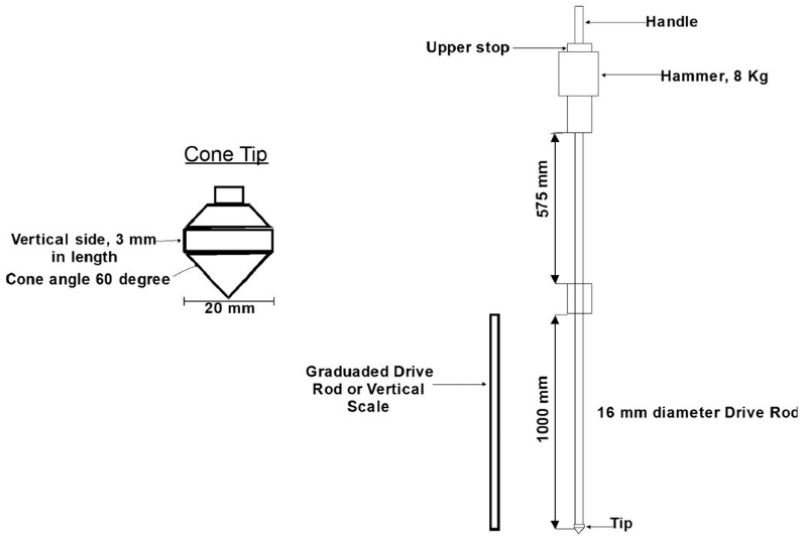

Figure 2-2 Dynamic cone penetration device (Edil & Benson, 2005)

2.2.3 Becker penetration test (BPT)

Becker penetration test (BPT) was developed in Canada in the late 1950s for oil exploration at gravel site (Sy & Campanella, 1993) and has become a primary field tests used to measure the penetration resistance of gravels for liquefaction resistance assessments (Dejong et al., 2017).

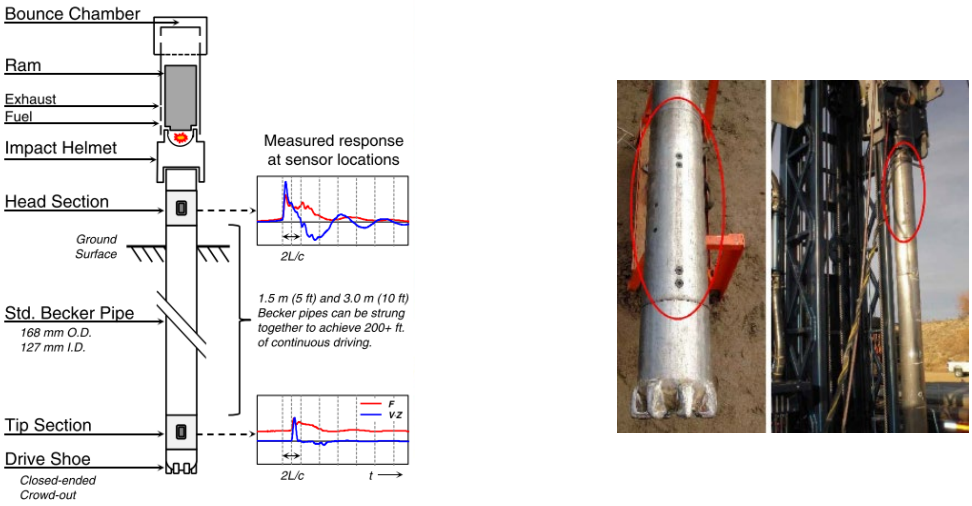

(a) (b)

Figure 2-3 Instrumented BPT system: (a) schematic system and Becker hammer and (b) tip and head sections (Dejong et al., 2017)

The BPT consists of driving a hollow steel drill string into the ground using a diesel pile-driving hammer. The BPT can be performed open-ended or closed-ended using one of three different drill string diameters [140 mm, 168 mm, and 230 mm]. The BPT is particularly applicable for coarse materials (e.g., gravel) due to its large diameter. It can provide more repeatable results and fewer refusals compared to smaller-scale split-spoon penetrometers (e.g., SPT). But the BPT has generally been limited to high-cost investigation activities (e.g., earth dams) (Cao et al., 2013).

2.2.4 Chinese Dynamic Penetration Test (CDPT)

The Chinese dynamic penetration test (CDPT) was developed in China during the early 1950s, as an in situ test specifically designed for measuring penetration resistance in gravelly soils (Cao et al., 2013).. It is a super heavy penetrometer which consists of a 120 kg hammer with a nominal free-fall of 100 cm dropped onto an anvil attached to 60 mm diameter drill rods. Moreover, the rods are in turn attached to a solid cone tip with a diameter of 74 mm and a cone angle of 60°. Two different results are usually recorded from the CDPT. One is the measured blow count which is defined by the number of hammer drops required to drive the cone tip 10 cm into the ground. The other penetration resistance result is N_{120}, which is the blow number required to advance the tip 30 cm. Actually, N_{120} is simply calculated by multiplying the measured blow count by a factor of 3, thus preserving the 10-cm detail in the penetration profile.

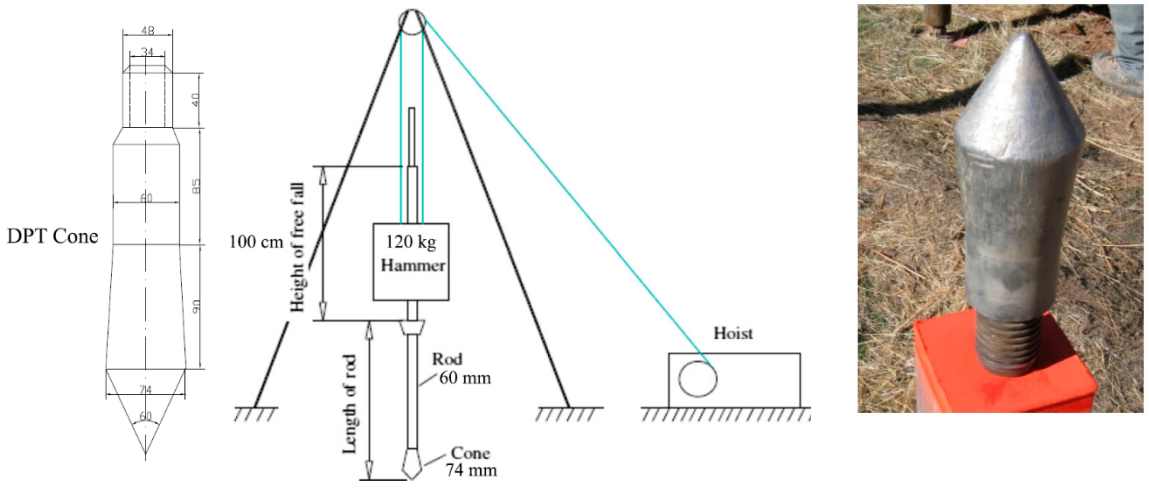

(a) (b)

Figure 2-4 Chinese dynamic penetration test (DPT) apparatus: (a) sketch and (b) cone tip

2.2.5 Standard penetration test (SPT)

The standard penetration test (SPT) remains as one of the most popular in-situ testing procedures (Schnaid et al., 2009). Since decades ago, the SPT *N*-values have been correlated with a wide range of engineering properties of soils, including relative density, internal friction angle, stress level, liquefaction potential, etc. The SPT can be used in any ground condition, primarily recommended for granular soils and other ground conditions in which it is difficult to retrieve sampling or to perform other in situ tests. Its capacity of being a simple, cheap and robust in situ testing technique explains partially its wide acceptance.

The SPT drives a split-barrel sampler into the ground at the bottom of a borehole by blows from a slide 63.5 kg hammer falling through a distance of 760 mm. Each hammer blow yields a theoretical driving energy of 475 J. The sampler is driven 150 mm into the ground and then the number of blows required to penetrate the sampler each 150 mm up to a depth of 450 mm is recorded. The first 150 mm is regarded as a possible zone of disturbance from drilling operations. The sum of the number of blows required for the second and third 150 mm of penetration is termed as the 'standard penetration resistance' or the '*N*-value'. Figure 2-5 shows the schematic illustration of equipment used for the SPT. Strain transducer and accelerometer may be installed below the anvil to measure energy transmitted from the hammer to the rod. Due to its widespread presence and large historical track record, SPT test performance and interpretation has been the object of considerable research work. That work is described in larger detail in the following section.

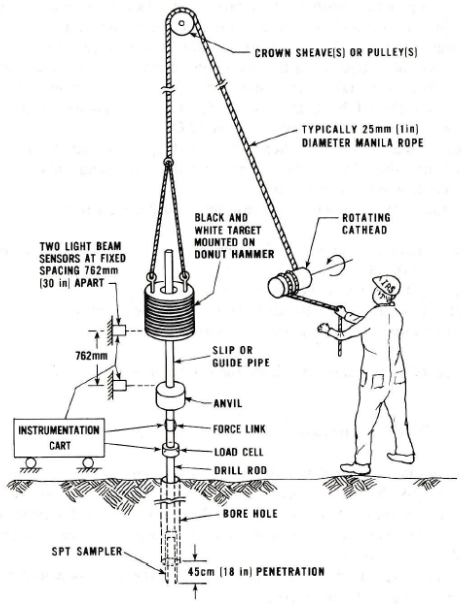

Figure 2-5 Schematic of instrumentation used in a SPT test (Kovacs & Salomone, 1982)

2.3 Standard Penetration Test: procedure and interpretation

2.3.1 SPT equipment

The sampler configuration for the SPT given in UNE-EN ISO 22476-3 (2005) is illustrated in Figure 2-6. The open-ended hollow sampler has an outside diameter of 51 mm. The inside diameter of the split-barrel can be either 35 mm or 38.1 mm. The driving shoe also have specified dimensions and configuration. A ball value chamber must be attached at the top of the sampler (between the sampler and the drill rods) so that fluids can exit from the top of the tube during driving.

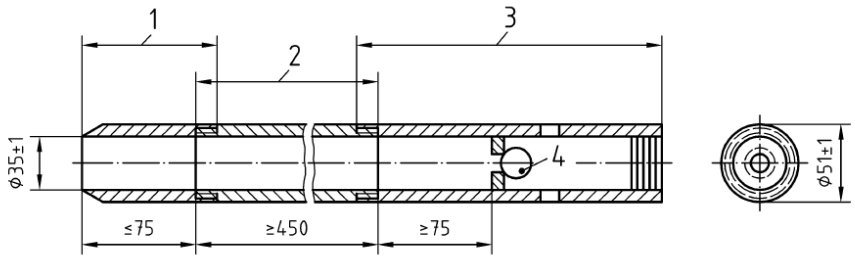

Key

1 Drive shoe
2 Split barrel
3 Coupling
4 Non return valve

Figure 2-6 Split-spoon Sampler configuration for the SPT (UNE-EN ISO 22476-3, 2005)

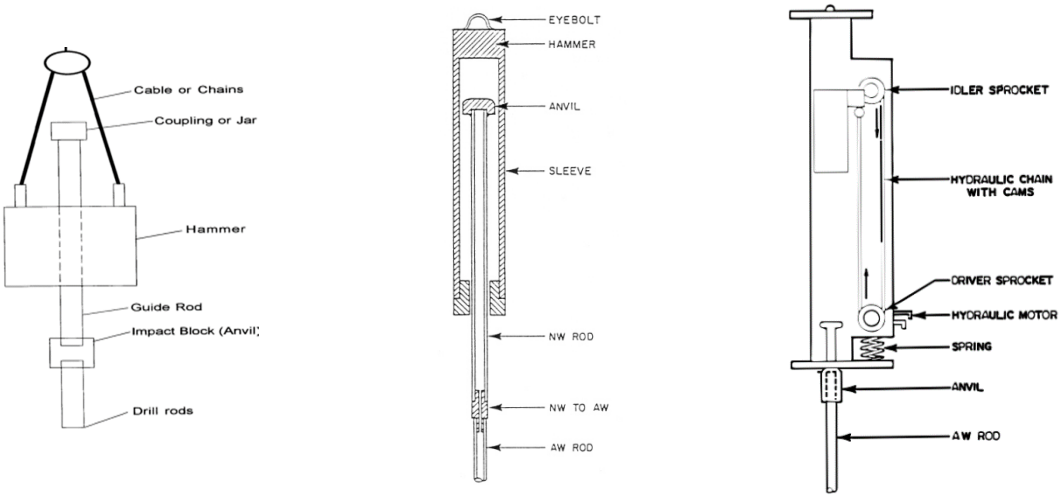

(a) (b) (c)

Figure 2-7 Schematic illustration of various SPT hammer configurations: (a) donut hammer, (b) safety hammer and (c) automatic hammer (Howie et al., 2003)

The fact is that the SPT hammer is not fully specified in the standards (ASTM D1586 -11, 2011; UNE-EN ISO 22476-3, 2005), which instead state only that the hammer must have a mass of 63.5 kg and must drop vertically as freely as possible from a height of 0.76 m. As a result, different hammer types have been designed and they vary considerably. As indicated by Howie et al. (2003), the donut, safety and automatic hammers are very widely used (Figure 2-7).

The donut hammer system was one of the earliest SPT hammers and is described as a donut-shaped cylindrical 63.5 kg mass falling through a guide rod (Figure 2-7a). The hammer mass is manually lifted by pulling on a rope which connects the hammer mass and a rotating cathead. The operator drops the hammer, by releasing the rope. The safety hammer was later designed to protect operators from injury occasionally occurred at the impact point between the falling mass and the anvil rod (Figure 2-7b). The hammer is typically a long steel tube closed at the top. The safety hammer uses the same lift and release methods as used for the donut hammer. The automatic trip hammer automates the process of lifting and dropping the hammer mass typically through a hydraulic motor (Figure 2-7c).

2.3.2 Energy measurements

Stress wave that propagates down the drill rods after one impact can be used to calculate the energy delivered to the sampler, which gives the *FV* method for energy calculation (Sy & Campanella, 1991) as described by ASTM D4633 -10 (2010)

$$EFV = \max \int F(t)v(t)dt \qquad \text{Eq. 2-1}$$

Where, *F(t)* and *v(t)* are the force and velocity of the rod recorded at the measurement point below the anvil, respectively. *F(t)* can be calculated by

$$F(t) = E_r A_r \varepsilon(t) \qquad \text{Eq. 2-2}$$

Where E_r and A_r are Young's modulus and the cross-sectional area of the rod, respectively, *ε(t)* is the strain date measured the strain transducer. The velocity *v(t)* is integrated from the acceleration signal recorded by the accelerometer installed below the anvil. The *FV* approach allows separate measurements of force and acceleration.

Recently, some researchers (Odebrecht et al., 2005; Lukiantchuki et al., 2017) have attempted to measure the transferred energy also at an extra measurement point which lies just above the sampler. With this development, the amount of energy loss along the rod can be estimated.

This energy calculation formula had an earlier version, *EF2* method, in which load cells or strain gages were used exclusively because accelerometers capable of measuring high acceleration were not reliable (Schmertmann & Palacios, 1979). *EF2* method applies the theoretical proportionality of force and velocity derived from wave propagation theories. Assumed there are no reflections from rod tip and changed cross-sectional area, *EF2* energy can be computed by integrating the square of the force:

$$EF2 = \frac{c}{a\,E}\int F\left(t\right)^2\,dt \qquad \text{Eq. 2-3}$$

Where, c is the rod wave speed, E is the Young's modulus of the rod and a is the cross section of the rod. F is the axial normal force measured in the rod.

2.3.3 Correction factors to blow count

The blow count is affected by inherent variabilities, such as equipment from different manufactures, hammer configurations, rod length, effect of overburden pressure, etc. Many efforts have concentrated in improving test reliability and repeatability, i.e., its ability to reproduce blow counts using different drill systems under the same soil conditions. Consequentially, it is necessary to correct the SPT data by a number of site specific correction factors, i.e. the energy ratio *ER*, the short rod correction factor λ and the overburden stress correction factor C_N. Therefore the standardized penetration resistance $(N_1)_{60}$ is given by

$$\left(N_1\right)_{60} = C_N \lambda \frac{ER}{60} N \qquad \text{Eq. 2-4}$$

Noting that some or all of the correction factors should be applied, depending on the purposes and different investigators.

2.3.3.1 Energy ratio *ER*

The theoretical potential energy (*PE*) of the SPT hammer is 475 *J*, while the energy delivered to the sampler from the falling hammer is less than the *PE* due to losses caused by factors interfering with the hammer and by energy dissipation during the hammer-anvil impact. The delivered energy is denominated as E_{blow}. The energy ratio *ER* for the test is defined as

$$ER = \frac{E_{blow}}{PE} \qquad \text{Eq. 2-5}$$

The energy transferred from the falling hammer to the sampler (it was called *ENTHRU* to emphasize the difference) is an important factor controlling the SPT *N*-value. The energy ratio *ER* in practical field testing can vary in a wide range from 30% to 90% (Schmertmann, 1979; Skempton, 1986). Schmertmann and his co-workers found that it was this *ENTHRU*, not the energy in the hammer at impact, penetrate the sampler to a distance so that the SPT *N*-value could be determined. It has been shown that the measured blow counts is inversely proportional to the energy delivered to the sampler (Schmertmann & Palacios, 1979). Robertson et al., (1983) used the ratio of 55% to normalize the blow counts from different hammer blows. After correction, considerably less scatter in the SPT results was observed (Figure 2-8). Nowadays, an *ER* of 60% has been accepted in practice as a reference value to obtain a standardized blow number N_{60}.

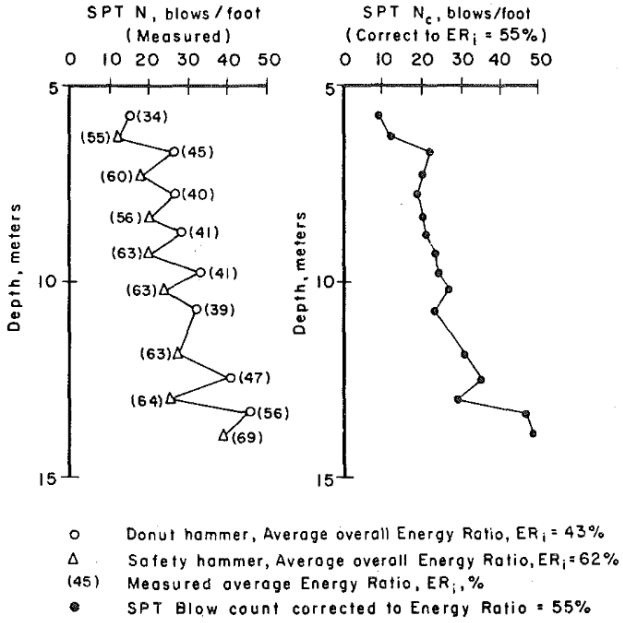

Figure 2-8 Normalization effect of energy ratio on SPT blow count values (Robertson et al., 1983)

2.3.3.2 Short rod correction factor λ

Short rod corrections are reduction factors in the transformation from raw blowcount number to energy-normalized blowcount (see Eq. 2-4). Table 2-2 summaries the short rod correction factors from the literature. Short rod corrections to SPT blow counts were introduced in engineering practice in the late 1970's and the early 1980's (Deger, 2014). Nowadays this correction has been compiled into some standards, i.e. UNE-EN ISO 22476-3 (2005).

A short rod correction factor is equivalent to a reduced blow energy ratio. Short rod corrections were based on field observations (e.g. Schmertmann & Palacios, 1979) of Enthru energy that showed rod-

length dependent reduction (Figure 2-9). At that time, due to the low reliability of accelerometers in measuring high acceleration, energy transferred to the rod could not be precisely measured. It was assumed that energy transferred after hammer-anvil separation at time *2l/c* would not contribute to sampler penetration, so that the transferred energy is calculated to be a reduced amount.

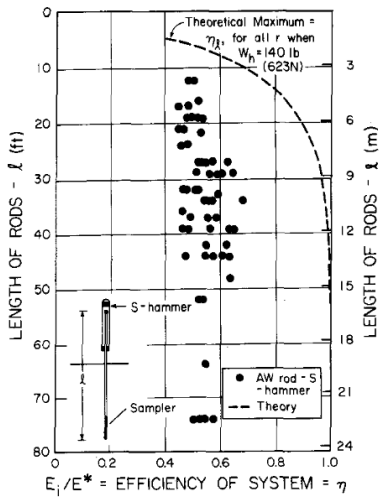

Figure 2-9 rod length effect on energy transfer ratio for safety hammer (Schmertmann & Palacios, 1979)

Table 2-2 SPT short rod corrections in literature (from Daniel et al. 2005)

Rod length / m	Short rod length correction factor λ			
	Seed et al. (1985)	Skempton (1986)	Youd et al. (2001)	Morgano & Liang (1992)
>10	1.0	1.0	1.0	1.0
6-10	1.0	0.95	0.95	0.96-0.99
4-6	1.0	0.85	0.85	0.90-0.96
3-4	1.0	0.75	0.80	0.86-0.90
<3	0.75	0.75	0.75	0.86

Currently with considerable improvement of energy measurement precision, some researchers have shown that early short rod corrections lead to overestimate somewhat the importance of short rod effects. Aoki & Cintra (2000) questioned the rationale for a reduction in energy losses as the transmission rods became longer, arguing an opposite rod length effect as they observed a decrease of energy efficiency with the increase of rod length. Those controversies are likely to be related with potential energy increase of the rod itself after hammer impacts. By taking that factor into account, Odebrecht et al., (2005) presented a more comprehensive study, identifying a twofold effect of rod length on energy

efficiency. On the one hand blow energy is transmitted as a wave and losses increase with increasing rod length, but, on the other hand, in a long rod composition the gain in potential energy from rod weight is significant and may partially compensate measured blow energy transmission losses.

2.3.3.3 Overburden stress correction factor C_N

An important factor is the overburden stress correction factor C_N which is defined to be the ratio of the SPT resistance measured at a given effective vertical stress level σ_v to the resistance measured at a standard stress level σ_{v_ref}, usually 1 kg/cm^2. In practice, the measured SPT resistance N is then normaliz-

$$N_1 = C_N \cdot N \qquad \text{Eq. 2-6}$$

Table 2-3 Summary of published C_N relationships (modified from Liao and Whitman 1986)

Reference	Correction factor C_N	Unit of σ_v
Teng (1962)	$C_N = 50/(10+\sigma_v)$	lbf/in^2
Bazaraa (1967)	$C_N = 4/(1+2\sigma_v)$ for σ_v<=1.5 $C_N = 4/(3.25+0.5\sigma_v)$ for σ_v>1.5	kips/ft^2
Seed (1976)	$C_N = 1-1.25\log_{10}\sigma_v$	tons/ ft^2
Tokimatsu & Yoshimi (1983)	$C_N = 1.7/(0.7+\sigma_v)$	kg/cm^2
Liao and Whitman (1986)	$C_N = \sqrt{1/\sigma_v}$	tons/ ft^2 or kg/cm^2
Skempton (1986)	$C_N = 2/(1+\sigma_v)$ for fine sand $C_N = 3/(2+\sigma_v)$ for coarse sand	kg/cm^2
Boulanger (2003)	$C_N = \left(\frac{1}{\sigma_v}\right)^m$ $m = 0.784 - 0.0768\sqrt{N_{1,60}}$	tons/ ft^2
Deger (2014)	$C_N = \left(\frac{1}{\sigma_v}\right)^m$ $m = 0.31 + 0.57e^{(-0.078N_{1,60})}$ for clean sands $m = 0.27 + 0.23e^{(-0.040N_{1,60})}$ for silty soils	tons/ ft^2

ed to N_1 using Eq 2-6. The need of using overburden stress correction factor to normalize or correct the SPT results in sands was first clearly demonstrated by Meyerhof (1957) based on the data published by Gibbs and Holtz (1957). Many efforts have been concentrated in developing overburden correction relationships. The commonly used overburden stress correction factors derived from already published papers are summarized in Table 2-3.

2.3.4 Influences of soil properties

There are a great number of soil-related factors known to influence the test results of dynamic probing in granular materials. These factors include void ratio, current stress levels, particle crushability, particle surface roughness, average particle size, coefficient of uniformity, particle angularity, cementation, aging, etc.

2.3.4.1 Influence of macroscale properties of soil

For granular soils, it was clearly noticed that a main focus has been always placed on relating relative density with SPT blow count. Although the effect of relative density on SPT was very strong, it could not be considered separately from that of stress level. A number of researchers have proposed various formulations expressing the relation between N, relative density (D_r) and overburden pressure (P_0) using calibration chamber testing (Gibbs & Holtz, 1957; Meyerhof, 1957; Marcuson & Bieganousky, 1977; Ishikawa et al., 2013). Generally, N has not been normalized by any correction factor. That of Meyerhof (1957) is a classical study, in which the following relation was proposed by summarizing the results of Gibbs & Holtz (1957)

$$N = 1.7 \times \left(\frac{D_r}{100} \right)^2 (0.145 P_0 + 10) \qquad \text{Eq. 2-7}$$

Where the overburden pressure P_0 is expressed in kP. Eq 2-7 revealed two basic relations:

- The blow count N increases linearly with overburden pressure P_0 at a constant relative density D_r
- At a constant overburden pressure, N increases as D_r^2

The later calibration chamber studies of SPT in sands have proposed slightly different formulations. This type of formulation using raw blow count N is likely to cause discrepancy with experimental data as energy delivered to the SPT sampler is affected by many factors during penetration. To avoid this

kind of difficulty, Skempton (1986) made a systematic effort to compare field and laboratory tests using only normalized blowcount, giving

$$\frac{N_{60}}{D_r^2} = a + b\frac{P_0}{100} \qquad \text{Eq. 2-8}$$

Where *a* and *b* are material dependent parameters. Skempton (1986) presented results indicating that, for normally consolidated sands, parameter *a* ranged between 17 and 46 and parameter *b* between 17-28. In this formulation, the shape of the Meyerhof (1957) expression was also valid when the normalized blowcount was employed.

2.3.4.2 Influence of micromechanics features of granular soils

Grain strength or crushability is one of the most important micromechanics factors influencing responses of penetration tests in granular soils. Weak sand material such as volcanic pumice sand (Pender et al., 2006) show significant crushing at pressures below 1 MPa. Wesley (2007) concluded from his CPT tests in calibration chambers that the fragility of pumice sand made cone tip resistance completely insensitive to the initial relative density. Strong sand does also crush, but at larger stresses, typically of above 5 MPa for quartz sands (Ciantia et al., 2019c). Ahmed et al. (2014) demonstrated that particle crushability affected strongly the results of in situ probing tests by illustrating how many common SPT-CPT correlations did not apply for crushable carbonate sands. The time dependent settlement of pile foundations in sand was found to be due to the progressive breakage of sand particles below pile tips (Leung et al., 1996).

Several material characteristics could also affect mechanical behaviors of granular soils, hence consequentially impact the interaction between probes and soils. These characteristics include particle shape (Falagush et al, 2015), surface roughness (Otsubo et al, 2015), etc. However no systematic study of the effect of those aspects on SPT results has been undertaken.

2.3.5 Energy balance approach for SPT test interpretation

In recent years, energy-based approaches have been proposed for SPT test interpretations by researchers. Two representatives are Hettiarachchi & Brown, (2009) and Schnaid et al., (2009), who have initially promoted to use the energy balance of test equipment as starting point to relate test results and soil properties. Both approaches are relatively simple by addressing SPT interpretations based on penetration per blow, $\Delta\rho$.

The energy conservation equation for test equipment (hammer, rods, sampler) during one single impact, from the at-rest position before hammer release to the at-rest position after penetration ends, is given as

$$E_{blow} = F_d \Delta\rho \qquad \text{Eq. 2-9}$$

Where, F_d is the dynamic soil reaction force at the sampler.

A main difference between Hettiarachchi & Brown, (2009) and Schnaid et al., (2009) lies in the computation of E_{blow}. The first one is obtained based on energy measurement in field

$$E_{blow} = ER \cdot m_h g h \qquad \text{Eq. 2-10}$$

Where, m_h is the hammer weight, h is the hammer falling height and g is the gravitational acceleration.

Unlike the first one only considering the hammer weight and falling height, the second one also counts the extra hammer displacement with penetration and the rod mass, m_r,

$$E_{blow} = \eta_3 \left[\eta_1 \left(h + \Delta\rho \right) m_h g + \eta_2 \Delta\rho \, m_r g \right] \qquad \text{Eq. 2-11}$$

Where, η_1, η_2 and η_3 are the hammer, rod and system coefficients, respectively, used to account for energy losses (Odebrecht et al., 2005).

2.4 Numerical analyses of dynamic testing

The dynamic testing is a boundary value problem which involves large deformations, non-linear material behavior, fast impact, etc. All these factors have made numerical models difficult to perform. In principle, numerical analyses of dynamic probing need to be performed under well controlled conditions, e.g. in a calibration chamber. Additionally, it is essential to represent the time-dependent driving force of hammer impact.

2.4.1 Force-time signal input

The force-time signal generated by a hammer impact is required as an input in the analysis of dynamic probing in soils. The signal may be measured directly by strain sensors attached below the anvil or estimated by numerical models.

Fairhurst (1961) proposed a simple model to describe the time history of an ideal impact force between a hammer and a rod. His model reflects ideally what happens when a hammer impact rods. At the beginning of hammer impact, a compression wave travels with the same velocity both down the rods and up the hammer. The compression wave reaches the upper surface of the hammer relatively quickly because the hammer length is relatively short. On reaching the free, upper end of the hammer this wave rebounds and reflects as a tension wave of the same magnitude and form. This rebound wave then travels down to the hammer/rod interface and emit a new pulse into the rods at a reduced stress and energy level. This process continues with each cycle of wave transmission and reflection in the hammer. These cycles produce successive compression pulses with progressively reduced stress and energy levels, travelling down the rods (Figure 2-10).

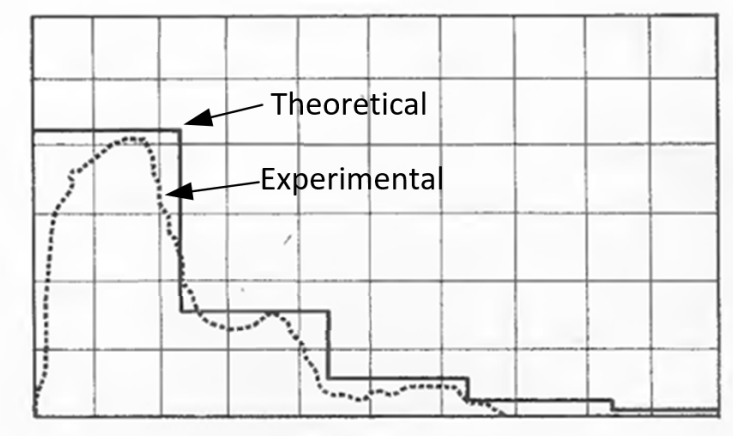

Figure 2-10 Theoretical wave form against field data (Fairhurst, 1961)

Later, more analytical models using one dimensional wave mechanics were proposed to predict input force characteristics which was then employed to calculate energy input (Abou Matar & Goble, 1997; Schmertmann & Palacios, 1979). These models were built based on the Fairhurst (1961)'s description on what ideally happens when hammer impacts rod. By comparisons with laboratory measurement of force and acceleration on SPT systems, the models were proved to be valid. According to basic concepts of those analytical solutions, a proportional relationship between the measured force and velocity was used to evaluate measurement quality. As an extension work for evaluating data quality, Daniel et al. (2003) developed a spreadsheet for modeling the propagation of stress waves of SPT. Recent experimental work (Daniel & Howie, 2005; Lee et al., 2010) indicates that a single SPT blow may result in relatively complex time-force signals in the rod, with several impacts due to hammer rebound and/or hammer delay and subsequent catch-up. The characteristics of the input force are thus strongly dependent on the particularities of the driving mechanism and the soil nature.

2.4.2 DEM simulations

In geotechnical practice, the discrete element method (DEM) is gaining wide acceptance as a powerful modelling tool due to the inherent advantages of being able to examine relevant mechanisms from micromechanical viewpoint. DEM has been used to simulate large deformations in geotechnical engineering, e.g. driven pile installation, cone penetration test and light dynamic penetrometers. Zhang & Wang (2015) performed a three-dimensional simulation of a centrifuge model of jacked pile test using the discrete element method. The soil responses in terms of strain and stress distributions, stress paths, the movement of particles and contact force mobilization during monotonic jacking are properly examined; Guo & Yu (2015) studied the soil plugging mechanism inside the large diameter pipe piles by means of DEM simulations. The interaction between soil particles and pipe pile was well examined. A sensitivity study was performed on the effects of factors such as soil column length, pile internal diameter, particle size, friction coefficient of interface between soil and pile, etc. These offers insight on the formation mechanisms of soil plugs inside the large diameter pipe piles.

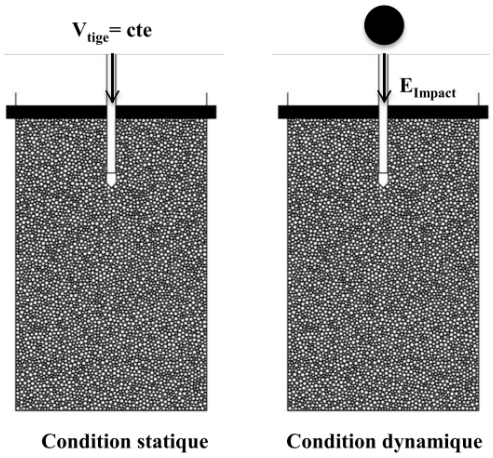

Figure 2-11 Numerical penetration models under static (left) and dynamic (right) conditions (Tran, 2015)

Researchers in Clermont Ferrand have been focusing on DEM modelling of the light dynamic penetrometers PANDA in recent years and have gained abundant and fruitful experience in dynamic probing simulations. Benz Navarrete (2009) has presented a study over the influence on penetration resistance of several parameters such as driving velocity and friction between cone and grains. He has showed microscale observations including contact force network evolution during one single impact. Quezada et al., (2014) have done penetration test in samples filled with particles with irregular shapes. They employ contact dynamics to consider physical particle shape. Tran et al. (2016) have carried out light penetrometer driving tests under constant driving velocity and impact conditions in 2D (Figure 2-11). It has been found that the tip force obtained from impact penetration is smaller than that obtained

in constant velocity condition. Later, the simulations of dynamic penetration were extended to 3D (Tran et al., 2017).

2.5 Summary

In this chapter, an overview of the diversity of dynamic testing apparatus is presented, followed by specific emphasis on the SPT. The following remarks can be drawn:

- A great number of site investigation tests employ dynamic penetration technique. The tests differ in quantitative aspects (impact weigh, impact energy, etc.) and qualitative aspects (operation, test outputs, etc.);
- Energy measurement is essential in SPT test;
- Correction factors on SPT blow counts are needed to improve test reliability and repeatability; the most common correction factor is the energy efficiency *ER*;
- A number of soil properties affect test results of dynamic probing. The related soil properties can be described separately as macroscale features including relative density and stress level and grain-scale features such as crushability and surface roughness.
- Analytical solutions and DEM simulations have been used to study mechanical responses of SPT.

Chapter 3 Discrete element method

3.1 Introduction

Understanding the complex response characteristics of soil is favored by inspection of soil behavior at the particle scale (O'Sullivan, 2011). The Discrete Element Method (DEM) proposed by Cundall & Strack (1979) has been accepted as an effective method to study fundamental aspects of soil response. Over recent decades, the use of DEM have increased exponentially across a wide range of disciplines consisting of mathematics, chemical engineering, geology, etc. (Zhu et al., 2007). DEM simulation is capable of generating information about internal force networks which cannot be easily obtained from existing experimental tests. DEM is a mesh-free method, well adapted to simulate large displacement problems such as pile driving. However, DEM simulations consume many computational resources, which limits either the model dimension or the number of particles.

In this study, a three-dimensional DEM code PFC3D (Particle Flow Code 3D) developed by Itasca Consulting Group, Inc. is used (Itasca Consulting Group, 2016). This code is a simplified version of the classical DEM due to its restriction to rigid spherical particles. After a new version 5.0 released, PFC3D became faster, multi-threaded, more powerful and flexible than its previous versions. The most common types of DEMs are soft particle approach and hard particle approach. In hard particle approach, the interaction forces between particles are assumed to be impulsive and hence the particles only exchange momentum by means of collisions (Zhu et al., 2007). Hard particle approach is suitable for rapid granular flow analysis where the granular material is completely or partially fluidized. This approach is not commonly used in current geotechnical engineering research and practice. PFC3D adopts a soft particle approach where particles are rigid but may overlap in the vicinity of the contact point.

In this chapter, an overview on the fundamentals of the discrete element method is presented. Some basic concepts in DEM modelling such as energy partitions, sample boundary conditions and commonly used sample generation methods are later described. Finally, a brief overview of DEM applications in geomechanics is presented, emphasizing those close to the subject matter of this thesis, i.e. those addressing particle surface roughness, particle breakage and site investigation testing.

3.2 DEM fundamentals employed in PFC3D

The Distinct element method (DEM) is based on the use of an explicit numerical scheme in which the interaction of the particles is monitored contact by contact and the motion of the particles is modeled particle by particle (Cundall & Strack, 1979). The law of motion and law of force-displacement are incrementally applied during the execution of numerous timesteps. The law of motion (Newton's second law) is used to determine the motion of each particle arising from the contact and body forces acting upon it, while the force–displacement law is used to update the contact forces arising from the relative motion (overlap) at each contact. At each timestep the position of each particle is identified and updated.

3.2.1 Calculation cycle

As the simulation in PFC3D progresses, the model state is advanced in time via a series of calculation cycles. During a single calculation cycle, a sequence of operations are executed (Figure 3-1). These operations include:

1. Timestep Determination – A valid, finite timestep is fundamental in the DEM method to ensure the numerical stability of the model and that contacts are created prior to the development of forces/moments.
2. Law of Motion – Newton's laws of motion are used to update the position and velocity of each body/piece using the current timestep and the forces/moments calculated in the previous cycle.
3. Advance Time – The model time is simply advanced by adding the current timestep to the previous model time.
4. Contact Detection – Creation and deletion of contacts are executed based on the updated piece positions.
5. Force-Displacement Law – The forces/moments developing at each contact are calculated and updated by the appropriate contact model using the current state of the pieces.

The calculation process is illustrated in Figure 3-1. In the following part, the law of motion and the force-displacement law will be described.

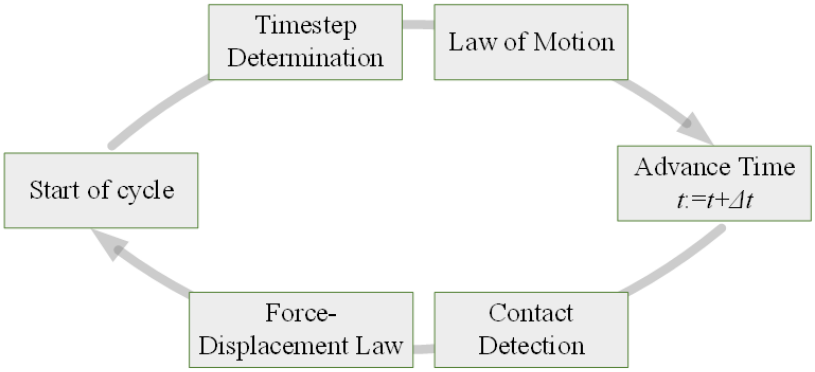

Figure 3-1 Calculation cycle in PFC3D

3.2.1.1 Law of motion

The motion of a single, rigid particle is determined by the resultant force and moment vectors acting upon it. The motion can be described in terms of the translational motion of a point in the particle and the rotational motion of the particle. The equations for translational motion and rotation motion can be written in Eq. and Eq. The translational motion of the center of mass is described in terms of its position x_i, velocity $\dot{x}_i$, and acceleration $\ddot{x}_i$, while the rotational motion is described in terms of its angular velocity ω_i and angular acceleration $\dot{\omega}_i$.

$$F_i = m(\ddot{x}_i - g_i) \qquad \text{Eq. 3-1}$$

$$M_i = I\dot{\omega}_i \qquad \text{Eq. 3-2}$$

Where F_i is the resultant force, or the sum of all externally applied forces acting on the particle; m is the total mass of the particle; and g is the body force acceleration vector (e.g., gravitational loading), M_i is the resultant moment acting upon the particle and I is the inertia tensor.

Suppose that the previous cycle solved $F_i = m(\ddot{x}_i - g_i)$ Eq. 3-1 and $M_i = I\dot{\omega}_i$ Eq. 3-2 at time t and that the timestep revolved for the current cycle is Δt. The 1/2 step velocity, $\dot{x}_i^{(t+\Delta t/2)}$, and angular velocity $\omega_i^{(t+\Delta t/2)}$, are calculated as

$$\dot{x}_i^{(t+\Delta t/2)} = \dot{x}_i^{(t)} + \frac{1}{2}\left(\frac{F_i^{(t)}}{m} + g_i\right)\Delta t \qquad \text{Eq. 3-3}$$

$$\omega_i^{(t+\Delta t/2)} = \omega_i^{(t)} + \frac{1}{2}\left(\frac{M_i^{(t)}}{I}\right)\Delta t \qquad \text{Eq. 3-4}$$

The position at time $t+\Delta t$ is updated using the 1/2 step velocity

$$x_i^{(t+\Delta t)} = x_i^{(t)} + \dot{x}_i^{(t+\Delta t/2)}\Delta t \qquad \text{Eq. 3-5}$$

During the force displacement cycle point, the forces and moments are updated for the current cycle, leading the updated accelerations $\ddot{x}_i^{(t+\Delta t)}$ and $\dot{\omega}_i^{(t+\Delta t)}$. The translational and angular velocities are subsequently calculated as

$$\dot{x}_i^{(t+\Delta t)} = \dot{x}_i^{(t+\Delta t/2)} + \frac{1}{2}\left(\frac{F_i^{(t+\Delta t)}}{m} + g_i\right)\Delta t \qquad \text{Eq. 3-6}$$

$$\omega_i^{(t+\Delta t)} = \omega_i^{(t+\Delta t/2)} + \frac{1}{2}\left(\frac{M_i^{(t+\Delta t)}}{I}\right)\Delta t \qquad \text{Eq. 3-7}$$

3.2.1.2 Force-displacement law

The force-displacement law relates the relative displacement between two entities at a contact (either ball-ball (Figure 3-2 (a)) or ball-wall (Figure 3-2 (b))) to the contact force acting on the entities. The relative contact displacement in the normal contact direction is defined to be the overlap U^n at the contact. The contact plane is defined by the unit normal n^i. The contact force vector F_i can be decomposed into normal component vector F_i^n and shear component vector F_i^s with respect to the contact plane as:

$$F_i = F_i^n + F_i^s \qquad \text{Eq. 3-8}$$

The contact forces are related to their corresponding displacements via normal and shear stiffness. The normal and shear contact force vectors are calculated as:

$$F_i^n = k^n U^n n_i \qquad \text{Eq. 3-9}$$

$$F_i^s = F_{i,old}^s + \Delta F_i^s \qquad \text{Eq. 3-10}$$

Where, k^n is the normal stiffness at the contact, $F^s_{i,old}$ is the old shear force vector at the start of the timestep (after it has been rotated to account for the motion of the contact plane), ΔF_i^s is the increment of shear force calculated as:

$$\Delta F_i^s = -k^s \Delta U_i^s \qquad \text{Eq. 3-11}$$

Where k^s is the shear stiffness at the contact , ΔU_i^s is the increment of shear displacement. Both the normal and shear stiffnesses are determined by the employed contact-stiffness model such as linear or Hertz contact model. The contact stiffness depends on the contact model in use, which may also apply other restrictions to the contact forces (e.g. a sliding limit). Contact models are described in the next section.

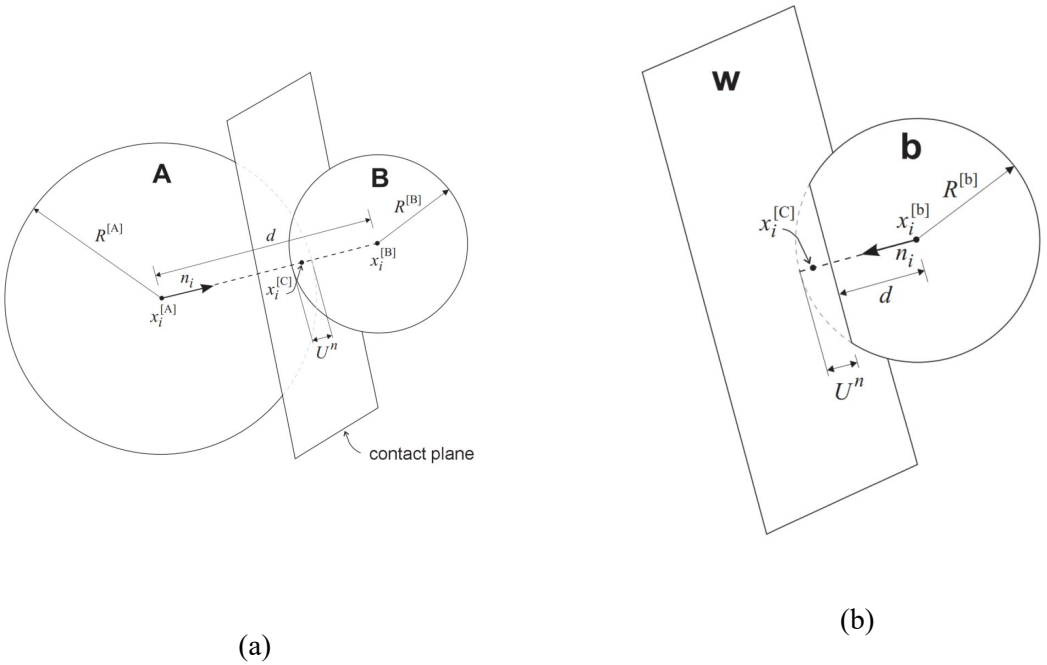

(a) (b)

Figure 3-2 (a) ball-ball contact; (b) ball-wall contact

To the end, after satisfying the contact constitutive relations, the resultant force and moment on the two contacting entities can be updated by adding the contribution of the final contact force and then can be applied in the Law of Motion.

3.2.1.3 Timestep determination

At the start of one cycle, a timestep is determined for the numerical integration of Newton's laws. The timestep must be suitable in order to reliably update the model state. Relatively large timestep may result in instability manifested by bodies flying off to infinity. On the other hand, relatively small timestep may cause excessively long simulation time. The DEM algorithm applies a central-difference time integration scheme, which is an explicit time integration solution. In order or remain the stability of the solution, the timestep must not exceed a critical value. A critical timestep for each particle is estimated by applying the following equation separately to each degree of freedom.

$$t_{crit} = \min \begin{cases} \sqrt{m / k^{tran}} \\ \sqrt{I / k^{rot}} \end{cases} \qquad \text{Eq. 3-12}$$

Where k^{tran} and k^{rot} are the translational and rotational stiffnesses, respectively; I is the moment of interia of the particle. The stiffnesses are estimated by summing the contribution from all contacts. The final timestep is taken to be the minimum of all critical timesteps computed for all degrees of freedom of all particles.

3.2.2 Contact models

Each contact is associated with a contact model. The contact model provides a particle-interaction law to update the interparticle force and moment between two contacting entities (ball-ball or ball-wall). PFC offers a number of built-in contact models including the most commonly used contact models: the linear contact model and the hertz contact model. The user may also build their own contact model using C++ Plug-in capability.

3.2.2.1 Linear contact model

The Linear contact model was originally proposed by (Cundall & Strack, 1979). The load-displacement relationship between two entities is represented by linear springs. The normal and shear stiffness for each contact is constant. The contact stiffnesses are defined by the normal and shear stiffnesses, k_n and k_s, of the two entities in contact (ball-ball or ball-wall). The normal contact stiffness k^n is given by

$$k^n = \frac{k_n^{(A)} k_n^{(B)}}{k_n^{(A)} + k_n^{(B)}} \qquad \text{Eq. 3-13}$$

And the shear contact stiffness k^s is given by

$$k^s = \frac{k_s^{(A)} k_s^{(B)}}{k_s^{(A)} + k_s^{(B)}} \qquad \text{Eq. 3-14}$$

Where the superscripts (A) and (B) denote the two entities in contact.

3.2.2.2 Hertz-Mindlin contact model

The Hertz contact model considers the variation of stiffness as a function of the elastic constants of the two contacting entities, overlap and normal force. The model is defined by two parameters: shear modulus G and Poisson's ratio v of the two contacting entities. The normal tangent stiffness k^n is given by

$$k^n = \frac{G\sqrt{2R'}}{(1-v)}\sqrt{U^n} \qquad \text{Eq. 3-15}$$

Where U^n is the sphere overlap and R' is the effective contact radius. The effective radius of the contact is given by the radii of the two contacting piece via

$$\frac{1}{R'} = \frac{1}{2}\left(\frac{1}{R^{(A)}} + \frac{1}{R^{(B)}}\right) \qquad \text{Eq. 3-16}$$

The shear tangent contact stiffness is calculated as a function of the normal contact force via

$$k^s = \frac{2G\sqrt{2R'}}{(2-v)}\left|F^n\right|^{1/3} \qquad \text{Eq. 3-17}$$

3.2.2.3 User-defined contact model

Users are allowed to create custom contact models to introduce new physics into PFC models. The ability to implement user-defined contact models (UDCM) is realized using C++ plug-in options. With the C++ plug-in capability, contact models in C++ can be loaded at runtime and used in exactly the same fashion as built-in contact models. Plug-ins are compiled in DLL (dynamic link library) files and provide several distinct advantages over FISH codes:

1) Generally C++ functions execute 10 to 100 times faster than the equivalent FISH functions.
2) Users familiar with concurrent programming can produce plug-ins that execute even faster on multiprocessor hardware.
3) Users have direct access to internal data structures and methods that are not available through predefined FISH intrinsics or contact models.
4) A C++ plug-in can link to, and make use of, any other C++ library or DLL it requires.

In this study, a rough sphere contact model developed from a standard Hertzian contact model for breakable particles is implemented in PFC5 (Itasca Consulting Group, 2016) by means of a C++ coded user defined contact model. The original model based on standard smooth contacts (Ciantia et al., 2015) was implemented via FISH functions, where a time-consuming loop through all the contacts was required. In the current version, such a loop is not required. The computational efficiency of the UDCM in detecting breakage in particles with smooth contacts has been validated by (Ciantia et al., 2017).

3.2.3 Energy partitions

The total energy of a particulate system (spherical particles and clumps) is formed by six following terms: body work, bond energy, boundary work, frictional work, kinetic energy and strain energy. These partitions may be calculated and traced in PFC.

- Body work – total accumulated work done by all body forces on the assembly;
- Bond energy – total strain energy of the assembly stored in all parallel bonds;
- Boundary work – total accumulated work done by all walls on the assembly;
- Frictional work – total energy dissipated by frictional sliding at all contacts;
- Kinetic energy – total kinetic energy of all bodies (spheres and clumps), accounting for both translational and rotational motion;
- Strain energy – total strain energy stored at all contacts, assuming the linear contact-stiffness model.

3.2.4 Damping

In PFC, energy can be dissipated by three different mechanisms: friction between particles, dissipation at contacts (e.g., viscous damping, inelastic contact laws, etc.) or dissipation introduced in the equations of motion of balls and/or clumps. The latter, termed as local damping, adds a damping force F^d to the equation of motion

$$F^d = -\delta |F| sign(v) \qquad \text{Eq. 3-18}$$

$$\text{sign}(y) = \begin{cases} +1, & \text{if } y > 0; \\ -1, & \text{if } y < 0; \\ 0, & \text{if } y = 0; \end{cases}$$

Where, δ is the damping constant which controls the damping force, F is the generalized force and v is the particle velocity. PFC 4.0 assumed a large value (0.7) of local damping by default. However, local damping is set to 0.0 in PFC 5.0 and later version by default. Local damping is available to remove additional kinetic energy and in consequence to accelerate convergence toward a steady configuration for quasi-static simulations. For dynamic analyses, this value should be set as zero or a very small one.

3.2.5 Boundary conditions

In DEM simulations, particles are constrained within a range established by boundaries. Displacement and force boundary conditions are commonly used in the manner of fixing or specifying the coordinates of selected particles, applying displacements to selected particles or applying a specified force to selected particles. Other types of boundary conditions can be applied in DEM, as periodic space or membrane boundaries. The most widely employed boundary type is rigid wall.

3.2.5.1 Using wall as boundaries

The rigid plane wall is the most frequently used boundary type, also in this thesis. For complex wall geometry, e.g. cylinder, multiple faces can be specified for the wall and these faces must be planar. When walls move displacements and forces are applied to the assembly of particles through wall-particle contacts. The kinematics of wall motion is user specified. In some cases, they are completely lacking motion and act, for example, as a fixed container. Walls moving with a certain specified velocity are also frequently employed (e.g. an indenter or penetrometer). More sophisticated approaches are also available, for instance:

1) Assign mass to the wall and let it move according to dynamically and meanwhile monitor their reaction forces (e.g., as history variables). Equations of velocity of the following form are then used:

$$\dot{u}_{wall} \leftarrow \dot{u}_{wall} + \left\{ \sum F - \alpha \left| \sum F \right| \text{sgn}\left(\dot{u}_{wall}\right) \right\} \frac{\Delta t}{m} \qquad \text{Eq. 3-19}$$

Where $\dot{u}_{wall}$ is the wall velocity, $\sum F$ is the total force acting on the wall, m is the assigned mass of wall, Δt is the timestep, and α is the damping coefficient. The new velocities are then conveyed to the wall at each timestep.

2) Control wall velocity using numerical servo-control algorithms to maintain a prescribed reaction stress on the wall. FISH function should be developed to implement the motion. The equation of wall velocity $\dot{u}_{wall}$ is:

$$\dot{u}_{wall} = G \bullet \left(\sigma^{measured} - \sigma^{required} \right) \qquad \text{Eq. 3-20}$$

Where G is the 'gain' parameter, σ^{measured} and $\sigma^{required}$ are respectively the measured force and required force on the wall.

3.2.5.2 Using particles as boundaries

It is possible to generate a regular 'sheet' of particles, and use one or more of these sheets as boundaries (Figure 3-3). Another way of setting up particle boundaries is to identify the particles that are in touch with the bounding walls after the compaction phase. Then one or more of the walls can be removed before the particles are already under control. However, this boundary condition becomes difficult to use when thousands of particles are included in a system. The particle boundaries can be controlled by either fixing their velocity or applying an external force to them.

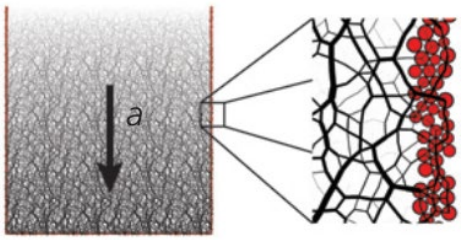

Figure 3-3 Fixed particles as boundaries (Ciantia et al., 2018)

3.2.5.3 Periodic boundaries

Periodic boundaries have the advantage of reducing dramatically the number of particles in DEM models and eliminating boundary-effects thus offering direct access to material responses. Within the periodic space, a particle may be viewed as an interior particle, a controller particle or a slave particle, as shown in Figure 3-4. Any particle situated far enough from the boundaries is an interior particle, and

behaves normally (not as in periodical situation). When a particle is approaching close to the boundary, it is treated as a controller, and is replicated as many times as required to fill up the system. Every replicate of a controller particle is a slave. Each controller exchanges mechanical and physical information (force, position and velocity) with its slaves during cycles of calculation, so that they behave as one particle.

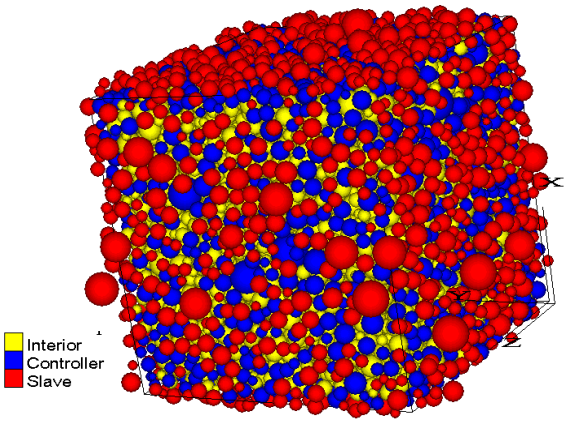

Figure 3-4 Particle assembly within periodic space

3.2.6 Sample generation methods

A number of different methods of specimen generation in DEM have been proposed (Jiang et al., 2003). The mostly used methods are:

3.2.6.1 Expansion Method

A population of particles with reduced radii and reduced friction are randomly placed within a specific volume, which is very close to desired specimen size, and no overlap/contact force is generated between any two particles. The particles are then expanded gradually until the desired radii is achieved, during which the consolidation pressure is maintained constant on boundaries. The overlap/contact force evolved between any two particles during the expansion process allows particles to displace and rotate, resulting in a dense specimen. The boundary positions are allowed to change accordingly, for the purpose of equilibrating the specimen into target stress state. Once the desired radii are achieved, interparticle friction coefficient are reset to normal value. The expansion method allows to produce dense specimen.

3.2.6.2 Fixed Point Method

Particles and contact data are obtained from two methods:

(a) Visual observations and laboratory testing (photos, density, normal stiffness). This method is suitable for proposing comparisons between DEM results and experimental outcomes;
(b) Theoretically achieved data for ideally packed cases, such as simple cubic systems. This method is often applied for verifying the accuracies of novel theories and/or DEM codes (2D or 3D case).

3.2.6.3 Isotropic Compression Method

The Isotropic Compression Method is conducted following these steps:

(a) All particles are located randomly within a large volume, so that overlap / contact force between any pair of particles do not appear.
(b) Initially, interparticle friction coefficient is set to relatively small values in order to allow particles to slide casually. Boundaries are then moved inward by imposing a specified velocity, or applying a prescribed pressure on the boundaries. The movement continues until a target void ratio or stress state is achieved at equilibrium.
(c) Then, the interparticle friction coefficient is reset to representative values before the loading tests are carried out.

3.2.6.4 Multi-layer Under Compaction Method

Under-compaction method is in principle an analogue to the actual multi-layer method described by Ladd (1978). In DEM, the specimen is gradually generated in the form of layer-by-layer. The particles are randomly generated within the first layer. Then compression is carried out by moving the top wall downward to the specific height while the rest of walls are fixed. This process is repeated until all layers are filled with particles and compacted. As expected, the average void ratio of the n layers below the (n+1)th layer is initially compacted to a void ratio $\bar{e}_n$ slightly larger than the final $\bar{e}$ of the specimen. This principle is executed during the generation of each layer until the average void ratio of all layers required to fill up the specimen is equal to the desired void ratio $\bar{e}$. In a word, the requirement of Under-compaction method is $\bar{e}_1 > \bar{e}_2 > \cdots > \bar{e}_n > \cdots > \bar{e}_t = \bar{e}$, where $\bar{e}_n$ is the average of void ratios of all n layers, $\bar{e}_t$ is the void ratio of whole specimen after compacting the last layer.

3.2.6.5 Periodic Cell Repetition Method

A brick compacted from an assembly of particles within periodic space may be replicated as many times as needed to construct a large model. Copies of this assembly can then be fitted together perfectly, because the geometrical arrangement of particles on one side of a brick is the negative image of that on the opposite side (Figure 3-5). A large model can then be constructed very quickly because the bricks are already compacted and in equilibrium.

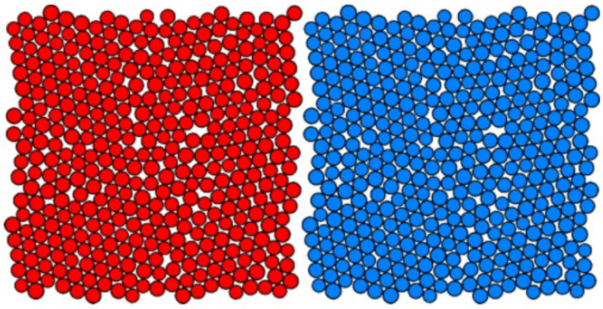

Figure 3-5 Copies of compacted brick

This is the essence of the Periodic Cell Repetition Method (PCRM),originally presented by Ciantia et al., (2018) for a fast initialization of DEM models. The approach builds upon the outstanding capability of using periodic boundaries in building homogeneous models in DEM. Firstly, periodic cells are generated with a sufficient number of particles matching a desired particle size distribution (PSD). The cells are then equilibrated at low-level isotropic stress at target porosity. Once the cell reaches an equilibrium state, it is replicated in space in order to fill the model domain. After the domain is thus filled only a few mechanical cycles are needed to re-equilibrate the large domain. A large, homogeneous sample, equilibrated under prescribed stress at the desired porosity. This method has proved to be very computationally efficient in generating large scale models. By means of contact force scaling, the method can then be extended for cases when the stress state varies in magnitude but not in orientation (i.e. the principal stress directions are uniform within the domain).

3.3 Applications in geomechanics

Profiting from the obvious advantages in addressing particle-scale interactions, DEM is being used more frequently within geomechinics research community. Obstructed by high cost when computing engineering-scale models where a large number of particles are included, its use in industry is less popular. However this situation is likely to change with the increase of computing power (O'Sullivan, 2011). In this section, three themes of DEM applications in geomechanicas addressing the topics closely

related to the subject matter of this thesis are reviewed. They are particle surface roughness, particle breakage and site investigation testing.

3.3.1 Surface roughness

Conventional understating of the contact mechanics between interacting particles has been established mostly based on the assumption that particle surfaces are smooth. This assumption apparently ignores the real surface characteristic that asperities exist on particle surfaces. These asperities give a finite surface roughness which can be precisely measured and quantified. Recent studies have shown that surface roughness has an influence on the force-displacement relationships (i.e. Hertz-Mindlin model) between contacting particles (Feng et al., 2017; Nardelli & Coop, 2018; O'Donovan et al., 2015; Otsubo et al., 2015).

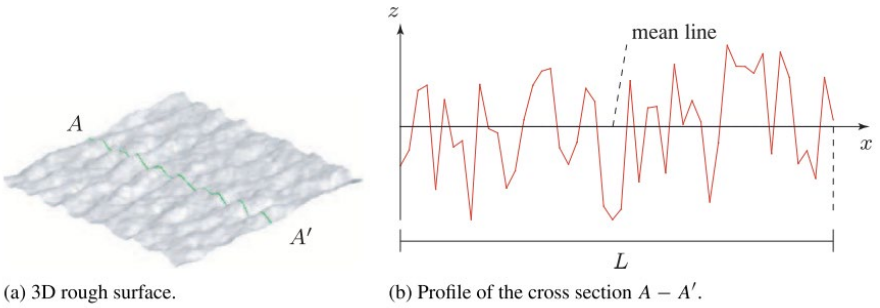

(a) 3D rough surface. (b) Profile of the cross section $A - A'$.

Figure 3-6 Topography of a rough surface (Feng et al., 2017)

In DEM simulations, a rough surface can be represented using spherical asperities as shown in Figure 3-7 (Wilson et al., 2017; Nadimi et al., 2019b). Another conventional approach to consider roughness is to propose mechanical modifications to contact models such as Hertzian model. Yimsiri & Soga, (2000) investigated the effect of surface roughness on small strain stiffness. They assumed the tangential contact behavior is not influenced by roughness. Otsubo et al., (2017a) proposed a three-stage load-displacement relationship for rough contact based on the Hertzian contact model (Figure 3-8). At small strains, the load-displacement relationship is dominated by asperities. However at large strains, Hertzian contact theory is recovered. In addition, a transition stage is defined between the stages of asperity-dominated and Hertzian.

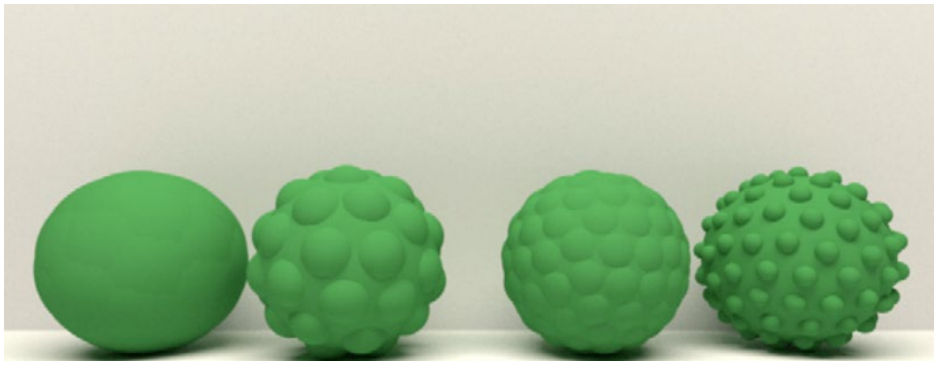

Figure 3-7 DEM modelling of rough particles (Wilson et al., 2017)

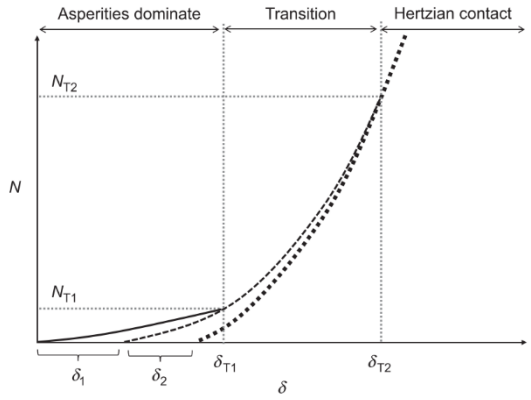

Figure 3-8 A proposed three-stage contact model for considering roughness (Otsubo et al., 2017a)

3.3.2 Grain crushing

The mechanical effects of grain crushing are important for several geotechnical problems, such as side friction on driven piles (Yang et al., 2010), railway ballast durability (Sun et al., 2014) and slaking induced irreversible deformations (Kikumoto et al., 2016). These, and other applications, have motivated efforts to experimentally investigate the mechanical consequences of particle breakage (Coop et al., 2004) to incorporate grain crushing into constitutive models for soils (Muir Wood, 2007) and to model soil crushing using DEM (Cheng et al., 2004). To model particle fragmentation using DEM, two alternative approaches can be applied:

- Multigenerational approach: Single particles crush and are replaced by newly generated smaller grains. In this approach several controlling aspects have to be defined including contact model,

crushing criterion, fragment replacement mode, etc. This approach is practical and has been adopted intensively for large scale 2D problems (Lobo-Guerrero & Vallejo, 2005) and in a 3D case (Ciantia et al., 2015; McDowell & De Bono, 2013).

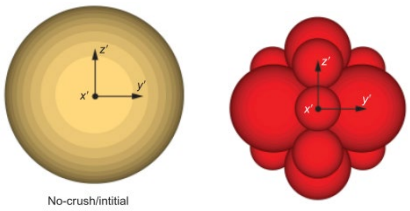

Figure 3-9 Configuration of one multigenerational approach (Ciantia et al., 2015)

- Multigrain agglomerates: grain clusters break into smaller fragments, no new particles introduced (Cheng et al., 2003; Cil & Alshibli, 2012; Cil & Alshibli, 2014; Sun et al., 2018). This approach, despite allowing handling various types of grain shape and being very helpful for the understanding of the micromechanics occurring to a single grain, usually becomes an unpractical tool if larger scale problems are intended to be modelled due to the high computational cost.

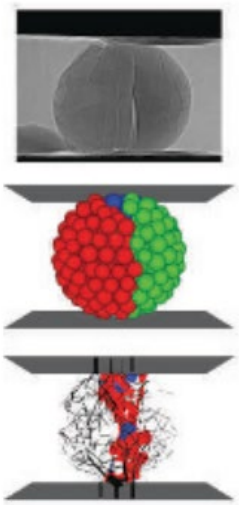

Figure 3-10 Particle fragmentation modelled with multigrain agglomerates (Cil & Alshibli, 2012)

Besides the two breakage approaches, different concepts or other combined methods are also able to provide evidence for the versatility of DEM breakage modelling. Tapias et al., (2015) proposed a breakage model for rockfill behavior from the concept of fracture mechanics. They have defined that a particle breakage starts if certain conditions associated with the propagation of internal cracks (i.e. toughness) are met. The breakage condition of a single particle may also be expressed in terms of energy

(Shen et al., 2018). In addition to pure DEM, a variety of hybrid modeling approaches have been proposed to simulate granular material breakage. For instance, the finite-discrete element method (FDEM) (Ma et al., 2019) and the micro finite-element (μFM) (Nadimi & Fonseca, 2018; Nadimi et al., 2019b) have demonstrated their good capacity in modelling breakable grains. Besides these combined approaches, Zhu & Zhao (2019) proposed another one integrating the peridynamic and contact dynamics to simulate continuous grain crushing.

3.3.3 Site investigation testing

Currently, the greatest interest in the use of DEM to simulate industrial scale problems are to simulate large deformation problems such as pile installation (Guo & Yu, 2015; Z. Zhang & Wang, 2015) and site investigation testing procedures. A variety of pile installation techniques have been simulated with DEM-based models, such as monotonic jacked pile (Zhang & Wang, 2015) and screw piles (Sharif et al., 2019). Soil plugging phenomenon formed during pile installation has also been investigated (Thongmunee et al., 2011; Guo & Yu, 2015).

Site investigation testing techniques are widely applied in geotechnical engineering, including cone penetration test (CPT), standard penetration test (SPT), dynamic cone penetration test (DCPT), Becker penetration test (BPT), etc. By referring to different penetration principles, penetrometers can broadly be divided into two categories: static and dynamic. Researchers have contributed many efforts to realize DEM simulations of static and dynamic penetration techniques. In terms of static cone penetration test (CPT) simulation, some notable early contributions are the wok of Huang & Ma (1994), Calvetti & Nova (2015) and Jiang et al. (2006) where DEM-based two-dimensional models of cone penetration tests were presented. Although qualitative insight was successfully gained, quantitative comparisons with physical tests were still lacking due to the intrinsic limitations of disc-based models. Arroyo et al. (2011) considered three-dimensional CPT simulations in a virtual calibration chamber (VCC) (Figure 3-11). Particle sizes were scaled and rotation of spherical particles was prevented. Good quantitative agreement with physical results were obtained. Butlanska et al. (2014) then conducted multi-scale analysis consisting of macroscale, mesoscale and microscale responses of the CPT simulations. Thus a complete view of penetration resistance values, stress and strain fields and particle displacements and contact force distributions, etc., was provided. The VCC concept has been also applied to the simulation of other quasi-static tests like the Marchetti dilatometer (Butlanska et al., 2018).

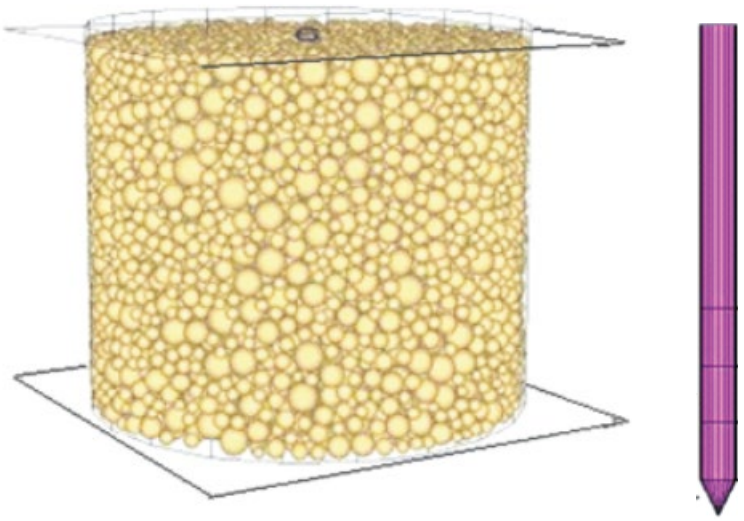

Figure 3-11 View of the DEM model created for CPT simulation (Arroyo et al., 2011)

Different approaches have been used to mimic dynamic driven rods in DEM simulations. Escobar et al., (2013), building a two-dimensional model to simulate a light dynamic penetrometer Panda, used particles bonded by a combination of contact and parallel bond to represent a solid steel rod. This allows to model elastic wave propagation through the rod. On the other hand, and because of the large contact rigidity necessary to model steel, the time step required by the explicit time integration method becomes very small, and large computational costs are incurred.

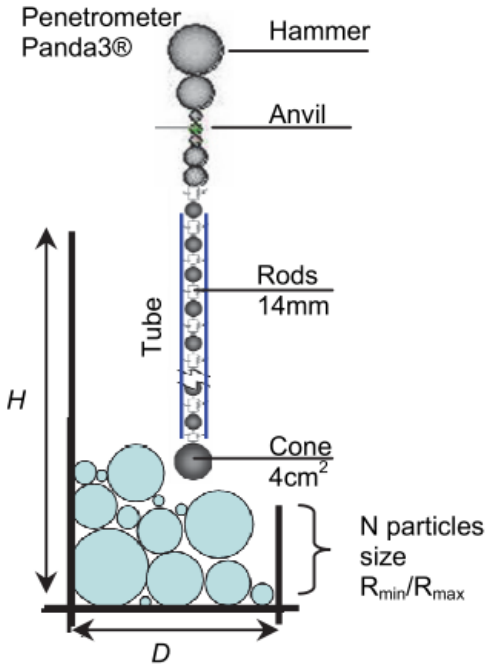

Figure 3-12 Principle of the simulation of penetrometric driving Panda (E. Escobar et al., 2013)

Due to its computational efficiency characteristic, the multigenerational approach of particle breakage has been used in field-scale applications. Lobo-Guerrero & Vallejo (2005) considered pile installation (in two dimensions) into breakable grains. The shape effect of the driven pile or penetrometer on penetration resistance and particle crushing was later studied by Lobo-Guerrero & Vallejo (2007) (Figure 3-13). Ciantia et al., (2016) built a three-dimensional DEM-based model to investigate the effect of grain crushing on the tip resistance of CPT. The granular material used in their study is pumice sand, a double-porosity crushable volcanic material. One of their main achievements is that good agreement with physical tests was gained.

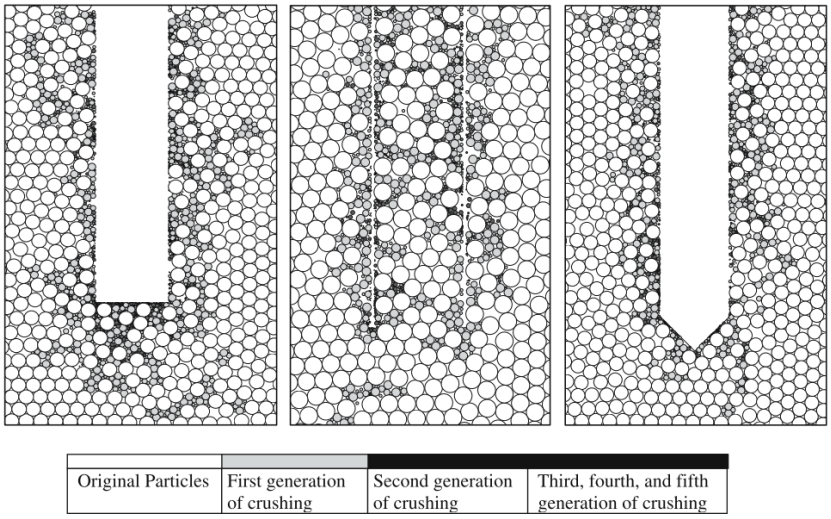

Figure 3-13 DEM study of influence of particle shape on the crushable behavior of granular materials around driven piles (Lobo-Guerrero & Vallejo, 2007)

3.4 Summary

In this chapter, after a synthetic overview on the fundamentals of the DEM methodology and typical features of the DEM employed in PFC3D such as boundary conditions and sample generation approaches, the DEM applications in geomechanics particularly on penetration tests is reviewed. The main concepts can be summarized as follows:

- Surface roughness effect on the mechanics of contact behavior between particles in contact can be investigated by either proposing modified contact model or using spherical asperities on the particle surface;
- Multigenerational method of mimicking particle breakage is economical in terms of computational cost;
- Many other hybrid modelling approaches for breakable grains have been proposed;

- DEM is widely used in simulating large deformation problems such as pile installation and penetration test techniques;
- Various approaches can address dynamic probing test problems in DEM;
- Multigenerational crushed particle algorithm is appropriate for modelling large-scale engineering applications in breakable grains.

Chapter 4 Standard Penetration Testing in a virtual calibration chamber

Based on the published manuscript of the following article:

Zhang, N., Arroyo, M., Ciantia, M. O., Gens, A., & Butlanska, J. (2019). Standard penetration testing in a virtual calibration chamber. *Computers and Geotechnics*, 111(3), 277–289. https://doi.org/10.1016/j.compgeo.2019.03.021

4.1 Introduction

Dynamic probing involves driving a device into the soil by striking it with a hammer. This technique is employed in several site investigation tests such as the Standard Penetration Test (SPT), Becker Penetration Test (BPT), Dynamic Cone Penetration Test (DCPT) or light dynamic penetrometers (e.g. Panda; Gourves & Barjot, 1995). Of these, the Standard Penetration Test (SPT) remains as one of the most popular in-situ testing procedures (Schnaid et al. 2009), frequently used to estimate soil properties (Hatanaka & Feng, 2006; Hettiarachchi & Brown, 2009), foundation design parameters and evaluate liquefaction potential (Idriss & Boulanger, 2008).

Tests based on dynamic probing have several advantages: they are widely available, economical and robust. They can be used in any ground condition, particularly on coarse materials such as gravels, ballast or weathered rock, where most alternatives fail. Dynamic probing tests also have important limitations. First: they are difficult to control precisely, which is detrimental for test repeatability. Second: they usually produce a single measurement per test (for instance *N*, number of blows to drive a sampler 300 mm in the ground) and such a restricted output inherently limits interpretation. Third: the mechanics of their interaction with the ground are poorly understood, which forces interpretation by strictly empirical approaches. All these shortcomings have been addressed in previous research, but to a different extent.

Many efforts have concentrated in improving test control and repeatability. A major step in this direction was made when energy input measurements were developed for the SPT (Schmertmann & Palacios, 1979; Kovacs & Salomone, 1982). Recording the energy input from hammer blows on the

rod-sampler system allowed to introduce an energy normalized blow number, N_{60}, which was shown to improve significantly test output repeatability(Seed et al., 1985; Skempton, 1986). The energy-normalized value N_{60} is now a required basis for quantitative SPT interpretation (UNE-EN ISO 22476-3, 2005; ASTM D1586 -11, 2011). Further research (Sy & Campanella, 1991; Abou Matar & Goble, 1997; Odebrecht et al., 2005) has progressively refined the methodology applied to measure and extract the amount of energy actually delivered to the driven sampler. Energy input measurement techniques have been also developed for other dynamic probes, like the Panda or the BPT (Dejong et al., 2017).

Several proposals are also available to increase the number of results obtained from each test. Some, like the torsional SPT or SPT-T (Décourt & Quaresma Filho, 1994), require extra specific procedural steps. Perhaps more interesting are those that obtain extra results from the same procedure, for instance through interpretations of SPT based on penetration per blow, $\Delta\rho$, (Schnaid et al., 2009) or enhanced dynamic data acquisition for light dynamic penetrometers (Escobar et al., 2016a).

Testing under well controlled conditions is essential to understand the factors underlying the dynamic interaction between probes and soils. In the laboratory in situ tests are typically studied using calibration chambers. Because of the complexities involved, comparatively little calibration chamber work on dynamic driven probes has been reported (Gibbs & Holtz, 1957; Marcuson & Bieganousky, 1977; Ishikawa et al., 2013). Experimental data supporting dynamic test interpretation is then mostly gathered from field studies (Skempton, 1986; Hatanaka & Feng, 2006). Unfortunately, field studies are costly, slow and subject to numerous uncertainties.

In principle, numerical simulation may be also used to perform controlled dynamic probing experiments. This, however, is difficult to put into practice, since dynamic probing involves large displacements, large strains, moving boundaries and high loading frequencies. It is not clear which numerical technology will be more appropriate for this kind of study. For granular soils, models based on the Discrete Element Method (DEM) (Cundall and Strack (1979)) appear attractive because 1) they are able to deal with large displacement contact problems in a dynamic setting, 2) they have relatively few free material parameters to calibrate, and 3) they can easily incorporate grain scale properties such as crushability, which are known to strongly affect the results of dynamic probing tests (Ahmed et al., 2014).

The use of 3D DEM models to create virtual calibration chambers (VCC) is well established for quasi-static tests like the cone penetration test (CPT) (Arroyo et al., 2011; Zhang & Wang, 2015; Ciantia et al., 2016b; Holmen et al., 2017) or the Marchetti dilatometer (Butlanska et al., 2018). VCC for light dynamic penetrometers have been used by Breul and co-workers, mostly using 2D models (Escobar et

al., 2013; Tran et al., 2016) but sometimes also in 3D (Quezada et al., 2014). A similar approach has been also recently used to study the impact of torpedo anchors (Zhang & Evans, 2019).

The objective of this work is to demonstrate the potential of the DEM virtual calibration chamber technique to study standard penetration testing in granular soils. In previous VCC studies (Arroyo et al., 2011; Ciantia et al., 2016b; Butlanska et al., 2018) a specific physical test series has been selected for comparison. For the case of SPT such approach was not possible because the old key studies (Gibbs & Holtz, 1957; Marcuson & Bieganousky, 1977) lacked energy measurements while more contemporary research (Ishikawa et al., 2013) was too succinctly described. Furthermore, directly mimicking these studies would have required simulation of a borehole excavation phase, which introduces distracting complications. It was then decided to validate the VCC method in this case by examining if the results obtained for a more generic case would fit into well-established general empirical trends.

In the following sections we describe in what follows how a 3D VCC model was built, filled with a calibrated discrete analogue of a representative quartz sand and then subject to a series of dynamic probes at varying confinement and density. The results obtained are then quantitatively compared with the existing physical database. The methodology employed to build the model is described in detail, paying particular attention to those aspects involved in the specification of the dynamic driving force. For reasons of space, the work presented here will focus on macro-scale results, leaving aside for the moment the possibilities of DEM models to explore the microscale (Butlanska et al., 2014).

4.2 Model description

4.2.1 A discrete analogue of Fontainebleau sand

Fontainebleau sand is a standard test silica sand that has been extensively used in geotechnical research (Plumelle & Schlosser, 1991; Seif El Dineet al, 2010; Jardine et al., 2013). Some of its physical properties are presented in Table 4-1.

Table 4-1 Physical properties of Fontainebleau sand

Database	D_{50}: mm	e_{min}	e_{max}	ρ_s	$\rho_{d,min}$: kN/m^3	$\rho_{d,max}$: kN/m^3
Exp: Luong and Touati (1983)	0.17	0.54	0.94	2.69	13.6	17.1
Exp: Seif El Dine et al. (2010)	0.21	0.54	0.94	2.65	13.4	16.9
NE34 FS: Ciantia et al. (2019)	0.21	0.51	0.9	2.65	13.7	17.2

A discrete analogue of Fontainebleau sand is obtained using the DEM code PFC3D (Itasca Consulting Group, 2008), which is employed in all the simulations described in this work. Particle crushing effects (e.g. Ciantia et al, 2015) are not included here, and the discrete elements employed are always unbreakable spheres. To roughly mimic the effect of non-spherical particle shapes, particle rotation was inhibited, directly fixing the rotational degrees of freedom of the particles. This approach, can be traced back to Ting et al. (1989) and was successfully applied in previous work with granular materials (Arroyo et al., 2011; Calvetti et al., 2015; Ciantia et al., 2018; Zhang et al., 2018a; Zhang et al., 2018b). More refined consideration of particle shape effects may be obtained using rolling-resistance contact models (e.g. Rorato et al., 2019a). However, such refinements complicate calibration and were thus left aside in this first exploratory study.

The constitutive contact law describing force-displacement interaction between particles is elasto-plastic. A friction coefficient μ defines the slip behavior at contacts. Contact rigidity is given by the ratio of contact forces and incremental displacements in the normal and tangential directions. In this study, the simplified Hertz-Mindlin theory is used to define the normal and tangential rigidity at each contact:

$$k_n = \left(\frac{2\langle G \rangle \sqrt{2\frac{d_1 d_2}{d_1 + d_2}}}{3\left(1 - \langle v \rangle\right)} \right) \sqrt{U} \qquad \text{Eq. 4-1}$$

$$k_s = \left(\frac{2\left(\langle G \rangle^2 3\left(1 - \langle v \rangle\right) \frac{d_1 d_2}{d_1 + d_2} \right)^{1/3}}{2 - \langle v \rangle} \right) \left| F_n \right|^{1/3} \qquad \text{Eq. 4-2}$$

Where, U is the sphere overlap, $\left|F_n\right|$ is the magnitude of the normal contact force and the $\langle\ \rangle$ brackets indicate the mean value of the quantity considered of the contacting elements; G is the shear modulus, v is the Poisson's ratio and d_1, d_2 are the diameters of the contacting elements.

Table 4-2 DEM contact model parameters

Material	G: GPa	μ	v
F-Sand	9	0.28	0.2
Rod	77	0.3	0.52

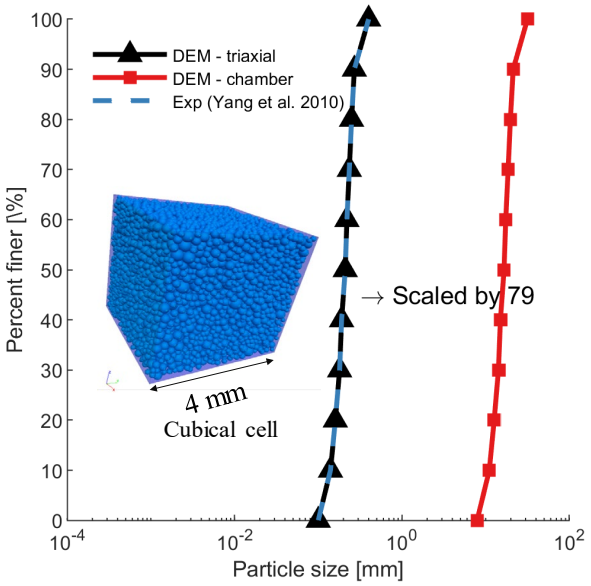

Figure 4-1 Particle size distribution of Fontainebleau sand and DEM models

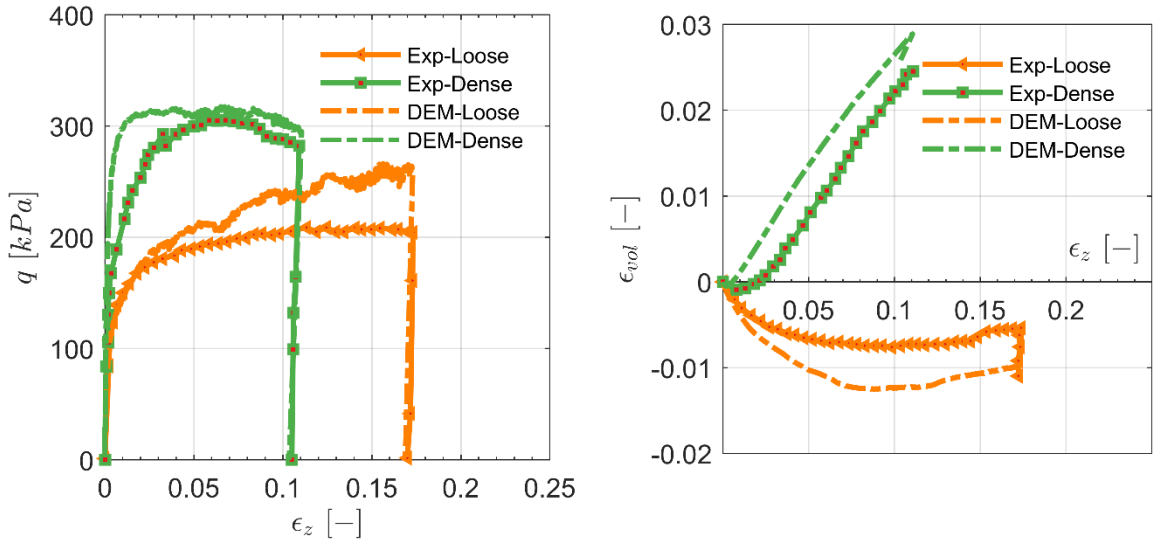

(a) (b)

Figure 4-2 Contact model calibration (G, μ, ν) with triaxial tests on Fontainebleau sand from Seif El Dine et al. (2010): a) q vs ε_z, b) ε_{vol} vs ε_z. Loose means at 30% relative density; dense at 70%

The contact model properties (G, μ, ν) (Table 4-2) were taken from a previous calibration made by Ciantia et al., (2019). Since a new version of the PFC software was employed here, the calibration set of triaxial compression tests was simulated again. The numerical model response was thus compared anew with the macroscopic responses of Fontainebleau sand in two low-pressure (100 kPa) triaxial

compression tests reported by Seif El Dine et al. (2010). The numerical tests were performed using a cubical cell of 4 mm in size containing 11,000 elements. Element sizes for this cubical cell were selected to closely match the PSD of Fontainebleau NE34 sand (Figure 4-1). The matching obtained (Figure 4-2) is considered adequate, given the simplicity of the model.

4.2.2 Chamber construction

The construction of 3-dimensional VCC models followed a procedure described previously (Arroyo et al., 2011; Ciantia et al., 2016b). A calibration chamber with 0.5 m height and 0.76 m diameter was built using wall elements. Discrete elements filling up the chamber have the same contact properties and shape as those used for calibration. However, to obtain a model with a manageable number of particles, their size was uniformly upscaled applying a uniform scaling factor of 79, leading to a rod/particle ratio, n_p = 3.06, similar to that employed in previous studies (Arroyo et al., 2011; Ciantia et al., 2015). The resulting size distribution is a shifted version of that from the original sand (Figure 4-1). All the chamber boundaries were set to be frictionless.

Geometrical model details can be seen in Figure 4-3 and Table 4-3. The choice of chamber dimensions was inspired by previous experimental work on the topic (see Table 4-4). In most of those studies, SPT was performed at various locations within the chamber plan, apparently without major impact on the test results. Here only testing at the axis of the chamber has been attempted. The resulting chamber/rod diameter ratio is 15, a ratio that results in some chamber size effects for fully penetrating CPT (e.g. Butlanska et al., 2014). It is not clear that such effects are equally relevant for the short dynamic probes performed here.

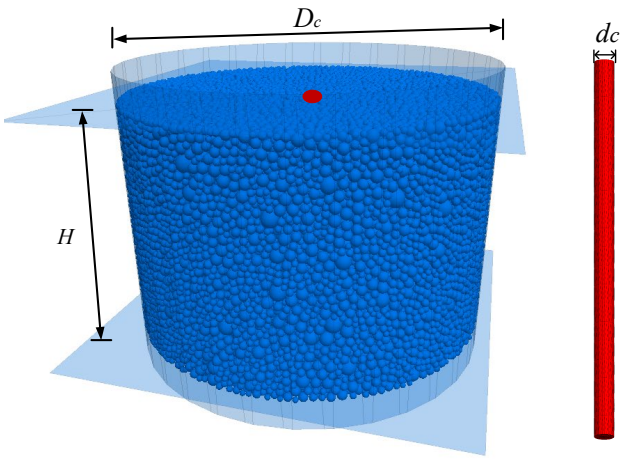

Figure 4-3 View of DEM model of calibration chamber and rod (flat-ended rod)

Table 4-3 Geometrical characteristics of the virtual calibration chamber

Variable (unit)	Symbol	DEM
Chamber diameter (mm)	D_c	760
Rod outside diameter (mm)	d_c	50.8
Chamber height (mm)	H	500
Scaling factor	-	79
mean element size (mm)	D_{50}	16.6
Chamber/rod diameter ratio	D_c / d_c=R_d	15
Rod/particle ratio	d_c / D_{50}=n_p	3.06

Table 4-4 Some characteristics of previous calibration chamber studies of SPT

Researchers	Range of D_r /%	Range of P_0 / kPa	Range of N	Container size	Radial BC	D_{50}/ mm	Proposed equation
Gibbs and Holtz /, Meyerhof (1957)	15-105	0-276	2-73	ϕ=90 cm H=120 cm	Steel wall	1.58	$N=1.7\times\left(\frac{D_r}{100}\right)^2(0.145P_0+10)$
Marcuson and Bieganousky (1977)	35-75	69-552	6-26	ϕ=122 cm H=183 cm	Steel/rubber wall	0.23	$N=-5.5+0.2(0.145P_0)+0.0046(D_r)^2$
Yamada et al. (1992)	24-89	49-294	10-37	ϕ=50 cm H=70 cm	Triaxial cell	0.2	$N=3.0\times\exp(0.023D_r)\times\left(\frac{P_0}{98.1}\right)^{(1-0.0035D_r)}$
Ishikawa et al. (2013)	68-96	150-600	10-21	ϕ=58.4 cm H=70 cm	Steel wall	0.54	$N=\exp(2.21\ln D_r+0.646\ln P_0-10.437)$

Tests were performed with the material in the chamber at pre-established values of density and isotropic confinement. The radius expansion method (REM) was used to fill the chamber. To attain the target porosity, inter-particle friction was reduced while all chamber walls were servo controlled to maintain an isotropic compression of 5 kPa. After equilibration, inter-particle friction was reset to the calibrated value and isotropic stress was ramped up to the target level. In all the simulations a local damping of 0.05 (Cundall, 1987) was employed and no viscous damping was considered. Detailed energy balances

of the VCC during driving in Chapter 5 show that such a small amount of damping results in negligible dissipation compared with that due to contact friction.

A flat-ended rod of outside diameter 50.8 mm was created by using frictional rigid walls. Rod diameter has been selected to coincide with the normalized dimension of the SPT sampling tube. A closed ended rod is a feature of some dynamic probing tests, like the BPT, and may be also interpreted as representing a plugged SPT sampler. Sampler plugging in sand has been assumed in previous SPT interpretation methods (Schnaid et al., 2009). Realistic modelling of the plugging phenomenon is beyond the scope of this work as would likely require applying a significantly smaller particle scaling factors. The contact model between rod and particles is also a simplified Hertz-Mindlin with limiting friction. The parameters for the rod are given in Table 4-2. The entire rod surface is assumed frictional.

During rod penetration, the VCC radial boundary was maintained at constant radial stress using a servo-mechanism. The same stress level was also maintained at the top horizontal boundary. On the other hand, the bottom horizontal boundary was fixed and no displacement was allowed.

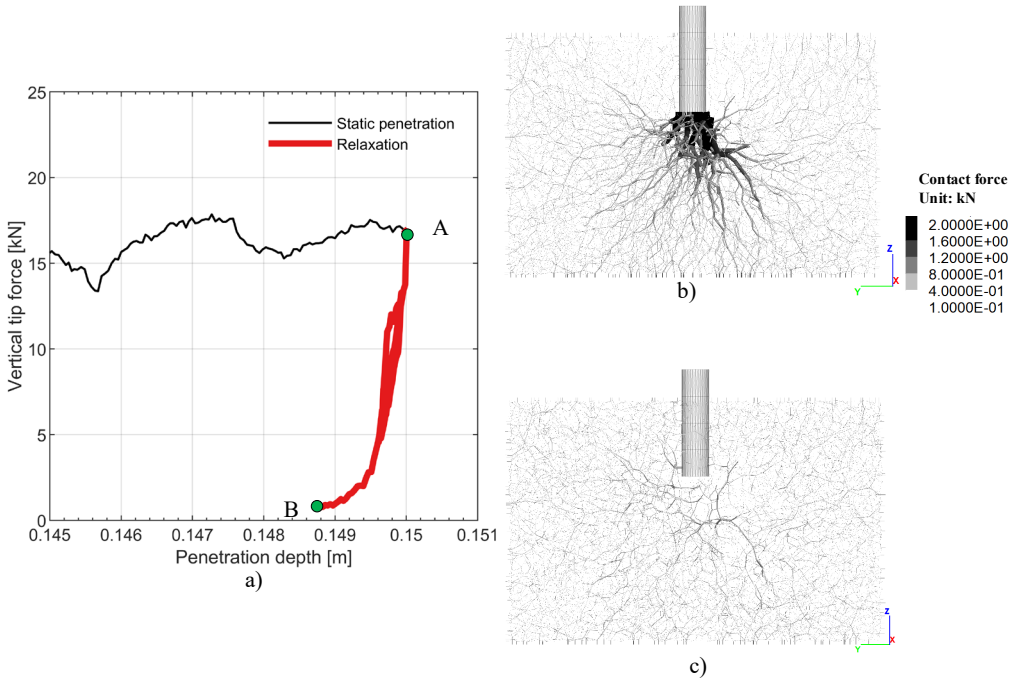

Figure 4-4 Residual force relaxation procedure (example: Loose_400): a) reduction of rod-particle contact force; b) contact force network at point A; c) contact force network at point B

When performing a SPT the first 15 cm of penetration are described as a seating drive, and not considered when evaluating the test result. A similar procedure was employed here and the rod was firstly pushed into the sample at a constant rate of 40 cm/s until the tip reached a depth of 15 cm. This also had the advantage of minimizing any major influence of the top boundary during driving (Butlanska

et al., 2014). On the other hand, simply stopping static penetration will result in locked-in residual forces against the rod. Therefore, after the 15 cm static penetration phase, a servo control was applied to slightly pull back the rod from the sample, restoring the vertical total force on the rod to zero (see example in Figure 4-4). At this point, the model was deemed to be in an appropriate state for launching dynamic penetration.

4.2.3 Dynamic driving

4.2.3.1 Representation of driven rods

Different approaches have been used to mimic driven rods in DEM simulations. Escobar et al. (2013), using 2D DEM, represented a solid steel rod using bonded particles. This allows to model elastic wave propagation through the rod. On the other hand, and because of the large contact rigidity necessary to model steel, the time step required by the explicit time integration method becomes very small, and large computational costs are incurred.

A computationally less costly alternative (Quezada et al., 2014) is to represent the rod using a macro-element. This was done here by bundling walls together and imposing on them a uniform rigid-body motion that approximates that of the rod. The wall-bundle is forced to move vertically and, to ensure a dynamically correct motion, the following equation is used:

$$\dot{z}^{t+\Delta t} = \dot{z}^{t} + \frac{F_{tot}^{t}}{m_r}\Delta t \qquad \text{Eq. 4-3}$$

Where, $\dot{z}^{t+\Delta t}$ and $\dot{z}^{t}$ are the vertical velocities of rod at time (t+Δt) and t, respectively, Δt is the time step and m_r is an assigned rod mass (see below). F_{tot}^{t} is the total force acting on the rod, i.e.

$$F_{tot}^{t} = \sum_i F_{s\_i}^{t} + \sum_j F_{p\_j}^{t} + F_{drv}^{t} + m_r g \qquad \text{Eq. 4-4}$$

Where, $F_{s\_i}^{t}$ is the vertical reaction force from particle i along the shaft, $F_{p\_j}^{t}$ is the vertical reaction from particle j at the rod tip, F_{drv}^{t} is an imposed driving force and g is the gravitational acceleration.

The virtual rod mass, m_r is determined from values of rod length l and rod material density ρ_r that are assigned in the specification of the imposed driving force.

4.2.3.2 Specification of driving force

In Eq. 4-4, a time-dependent force input is specified to represent the driving force. The force input employed in this work was intended to approximate the characteristics of an SPT blow.

Recent experimental work (Daniel & Howie, 2005; Lee et al., 2010) indicates that a single SPT blow may result in relatively complex time-force signals in the rod, with several impacts due to hammer rebound and/or hammer delay and subsequent catch-up. The characteristics of the input force are thus strongly dependent on the particularities of the driving mechanism and the soil nature. Structural dynamic 1D models may be used to predict input force characteristics for a particular configuration of the impact mechanism (Abou Matar & Goble, 1997; Schmertmann & Palacios, 1979) Such approaches seemed unnecessarily complex for the exploratory work presented here. Instead, a relatively simple but realistic input force was derived from a simplified hammer-rod interaction analysis. Fairhurst (1961) proposed an elastodynamic model to describe the time history of an ideal impact force between a hammer and a rod. It assumes cylindrical pieces, no separation between hammer and rod and takes into account the transmission, at the hammer/rod interface, of rebound waves from the upper hammer end as successive compression pulses of progressively reduced stress levels.

According to this model the peak compressive wave stress during the first impact, σ_{max}, is given by

$$\sigma_{\max} = \rho c \left(\frac{V_h}{1+r} \right) \qquad \text{Eq. 4-5}$$

Where, ρ is the mass density of the rod material, c is the wave propagation velocity in the rod. V_h is the hammer impact velocity, and r is the hammer-rod impedance ratio, equal to the ratio of cross-sectional area of the rod, a, to the area of the hammer A_h, if both are of the same material. The wave propagation velocity is calculated as

$$c = \sqrt{E / \rho} \qquad \text{Eq. 4-6}$$

Where, E is the elastic modulus of the rod material. The hammer impact velocity is here calculated through

$$V_h = \eta_d \sqrt{2gh} \qquad \text{Eq. 4-7}$$

Where, g is the gravitational acceleration, h is the falling height of hammer and η_d represents a dynamic efficiency ratio. Unless otherwise stated, in all the simulations below, the value of this parameter is always set as 1. From the relations above it follows that the maximum impact force can be expressed as

$$F_{\max} = \frac{\eta_d a \sqrt{2ghE\rho}}{1+\left(\frac{a}{A_h}\right)} \qquad \text{Eq. 4-8}$$

The corresponding impact force F_n for the nth (n >1) compression pulse, is

$$F_n = F_{\max}\left(\frac{1-r}{1+r}\right)^{n-1} \quad \text{for } \frac{2(n-1)L}{c} < t < \frac{2nL}{c} \qquad \text{Eq. 4-9}$$

Where, L is the hammer length and t defines the time duration of each compression wave.

The simulated impact is terminated at time $t_{max} = 2l/c$ after the start of impact, where l is the length of rod. This would be the time when an elastic wave reflected from the rod tip as a tension wave returns to the rod head and pulls it away from the hammer. The maximum number of completed stress steps n before loss of hammer contact is then given by the integer part of l/L. In experimental records of SPT blows, (Schmertmann & Palacios, 1979; Lee et al., 2010), this round-trip time t_{max} coincides, approximately, with the duration of the first hammer impact which is that delivering the largest amount of energy to the sample.

Table 4-5 Parameters describing the simulated driving system

ρ (kg/m^3)	E (GPa)	c (m/s)	m_h (kg)	h (m)	g (m/s^2)	a (m^2)	A_h (m^2)	r (-)	L (m)	l (m)	$t_{\max}$(ms)	$Fmax$ (kN)
8,050	200	4,984	63.5	0.76	9.8	0.002	0.008	0.25	0.97	10	4	251

The parameters describing the simulated driving system are collected in Table 4-5. The hammer and the rod are assumed to be of the same steel material. The rod is assumed to be 10 m long. The hammer diameter is assumed to be twice that of the rod and its length (approximately 1/10 of that if the rod) was computed from its assumed mass and steel density. Using these inputs, a 63.5 kg hammer falling from a height of 0.76 m will generate a 4 ms impact force with F_{max}= 251 kN (Figure 4-5).

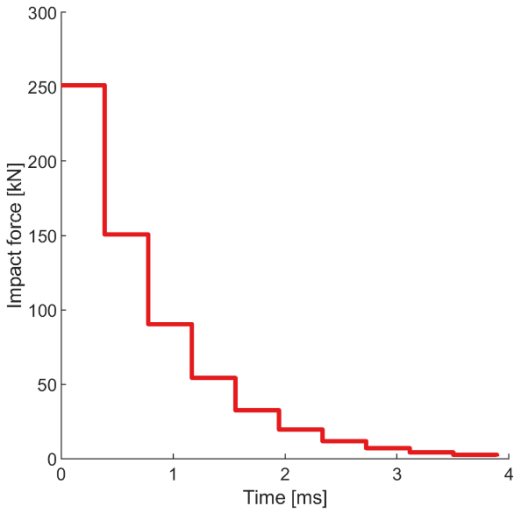

Figure 4-5 Base case for input driving force F_{drv}

4.2.3.3 Blowcount, blow energy and energy ratio

The value of equivalent blow counts N is determined by the ratio of the reference 30 cm distance by the penetration depth per blow $\Delta\rho$. Following a similar reasoning to that presented by Odebrecht et al., (2005) the energy delivered by the driven rod to the VCC in a given blow, E_{blow}, is computed as the sum of hammer input work W_H and work done by the rod self-weight, U_R. These energy terms can be calculated by integrating the work done by the impact force and gravitational forces on the driven rod,

$$E_{blow} = W_H + U_R = \int_0^{t\_eq} F_{drv}(t) v_r(t) dt + m_r g \int_0^{t\_eq} v_r(t) dt \qquad \text{Eq. 4-10}$$

Where, $v_r(t)$ represents the driven rod velocity history, which is an output of the test and the upper limit of the integral, $t_{\_eq}$ is the time for equilibration.

Following standard practice, an energy ratio is then computed normalizing the energy delivered by the theoretical driving energy of an SPT (given by a hammer mass, m_h = 63.5 kg; fall height h = 0.76 m)

$$ER = \frac{E_{blow}}{m_h g h} \qquad \text{Eq. 4-11}$$

Depending on various hammer types and testing details, the energy ratio in practical field testing can vary in a wide range from 30% to 90% (Schmertmann, 1979; Seed et al., 1985; Skempton, 1986; Odebrecht et al., 2005). It has become common practice to normalize the blow count, taking into

account the energy ratio delivered to obtain a standardized blow number N_{60} (corresponding to blows of 60% energy efficiency) as:

$$N_{60} = \frac{ER}{60} N \qquad \text{Eq. 4-12}$$

4.2.3.4 Simulation program

The main soil state variables affecting dynamic penetration results are density and stress level. These are represented here by relative density D_r and mean confining pressure P_0. The specimens were generated by combining four density levels, namely very dense (D_r=82%), dense (D_r=72%), medium (D_r=60.5%) and loose (D_r=38.6%) and three confining stress levels (P_0=100 kPa, 200 kPa and 400 kPa). A series of impact tests were conducted in all the 12 specimens by prescribing the same force-time signal proposed previously. The main characteristics of these DEM-based tests are collected in Table 4-6.

Table 4-6 Basic programme of DEM-based dynamic probing tests

Test ID	D_r: %	P_0: kPa	N. of particles
Very Dense_100	82.6	100	69,166
Very Dense_200	83.0	200	69,166
Very Dense_400	83.7	400	69,166
Dense_100	74.0	100	66,059
Dense_200	74.7	200	66,059
Dense_400	75.7	400	66,059
Medium_100	62.1	100	60,031
Medium_200	62.9	200	60,031
Medium_400	63.9	400	60,031
Loose_100	40.7	100	50,335
Loose_200	41.7	200	50,335
Loose_400	43.2	400	50,335

4.3 Results

Even restricting ourselves to the macroscopic level, a wealth of results are available, since tip resistance, hammer input energy, rod motion features are continuously tracked in time. Before examining the effects of the main controlling variables on test results it is interesting to consider in detail the dynamics of a single blow.

4.3.1 Impact dynamics

The evolution in time of rod velocity, rod acceleration, rod tip position (i.e. penetration depth) and tip resistance is illustrated in Figure 4-6 for a representative example (test Loose_200 in Table 4-6). The record was interrupted after 0.15 s, as most variables had by then reached a stationary value.

A dynamic penetration curve can be deduced from the previous results by representing tip resistance vs dynamic penetration (i.e. rod penetration minus the 0.15 m achieved statically). The dynamic penetration curves obtained appear very similar to those registered using instrumented dynamic penetrometers (Escobar et al., 2013; Escobar et al., 2016a). Several characteristic points are identified in the penetration curve, corresponding to times t_1, t_2, t_3 and t_4. Using these characteristic times 5 phases (I, II, III, IV and V) are distinguished in the dynamic process (Figure 4-6).

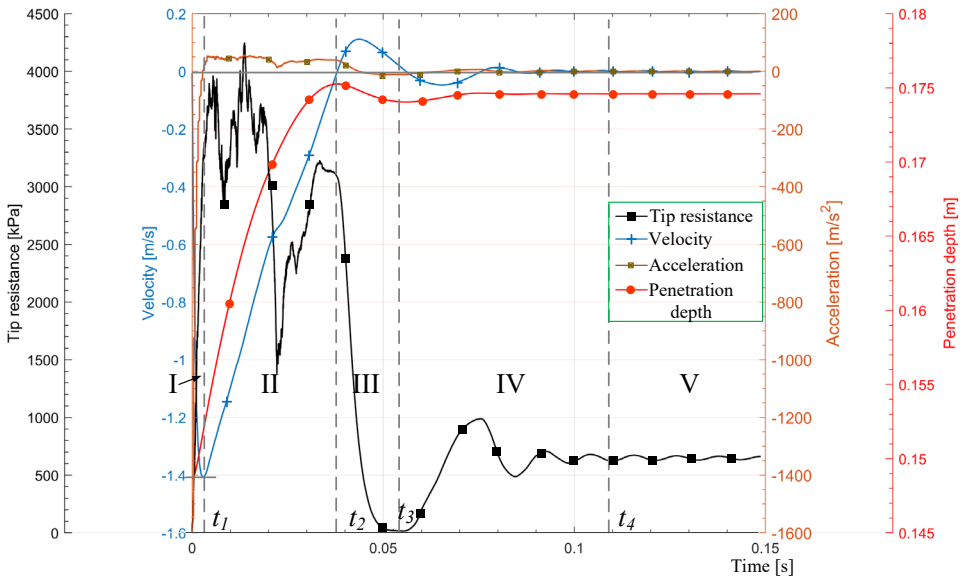

(a)

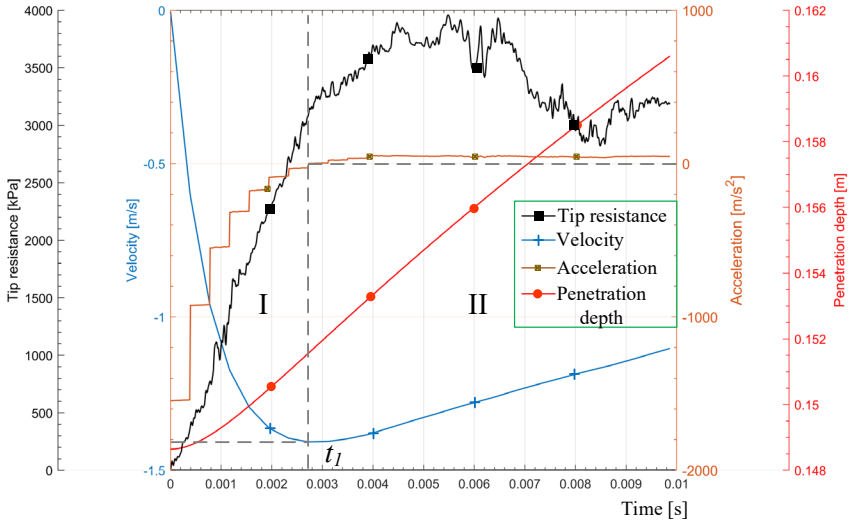

(b)

Figure 4-6 Evolution of tip resistance, rod velocity, rod acceleration and penetration depth during one impact with time in Test Loose_200: (a) full analysis; (b) zoom-in view till 0.01s

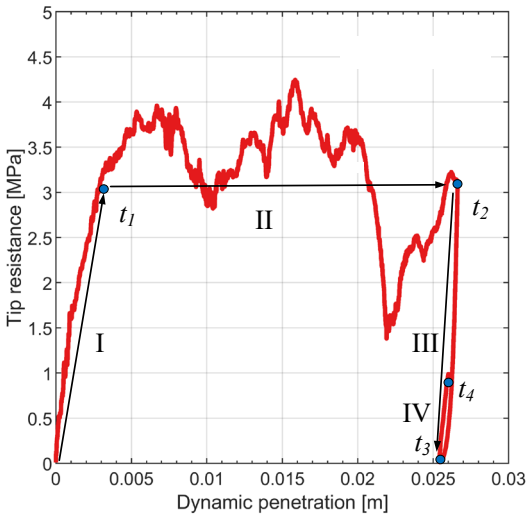

Figure 4-7 Example penetration curve during a blow (Loose_200, Table 4-6)

The first phase (*I;* which might be called *"acceleration"*) corresponds to the period in which rod acceleration is negative (i.e. downwards), with t_1 selected as the time in which acceleration first changes sign (Figure 4-6b). Until this moment the imposed driving force is overcoming the soil resistance acting on the rod. Rod velocity attains then its maximum at 1.4 m/s, a value close to the anvil velocities under SPT registered by Lee et al. (2010). Phase *I* is also characterized by a quasi-linear rise in tip resistance. Shortly after t_1 the tip resistance begins to oscillate while penetration advances.

The second phase (*II; "deceleration"*) finishes when the velocity of the rod crosses zero at t_2. Of course, at this point penetration advance stops. In this phase soil resistance decelerates the rod with a relatively constant magnitude, hence reducing rod velocity at an almost constant rate. Penetration continues accompanied of large tip resistance oscillations -the largest of which is coincident with the only significant step in acceleration magnitude during this phase.

The third phase (*III; "unloading"*) corresponds to a period in which the rod rebounds and the tip is progressively unloaded until it becomes practically 0 at t_3. There is still some inertia in the system that is revealed in rod oscillations during phase *IV*, which lasts until the rod attains is final penetration depth at t_4. The rod was driven to a permanent penetration of 0.026 m, corresponding to a blow number N = 12. Beyond that time, in phase *V*, only small oscillations in the residual tip resistance are visible, perhaps best seen as an indication of a somewhat insufficiently damped system.

4.3.2 Penetration and driving energy

As recorded in Table 4-7 the energy ratios delivered to the chamber lie mostly within the 40% - 50% range. Those values are within the range of observed field energy ratios 30%-90% (Idriss & Boulanger, 2008) although clustered towards the lower end. Note that, in the field, the energy delivered by a hammer blow frequently requires more time than the strict two-way rod wave trip time assumed here to establish t_{max}. (Idriss & Boulanger, 2008)(Idriss & Boulanger, 2008)(Idriss & Boulanger, 2008)(Idriss & Boulanger, 2008)Figure 4-8 plots the energy ratio levels and the penetration per blow observed for all the different tested conditions of density and confining stress. A proportionality between these two magnitudes is evident from the figure, much like that observed by Schnaid et al (2009b) in field testing.

The energy normalization of blowcount in Eq.4-12 implies that the normalized value is independent of the driving system characteristics or, equivalently, that N_{60} is only affected by soil properties (parameters and state). As noted before that was verified empirically by field testing, driving SPT at the same site with different, independently measured, energies (Schmertmann & Palacios, 1979; Skempton, 1986). It seemed reasonable to check if this energy normalization is also verified in the VCC. To this end, a separate series of simulations was run, modifying the driving force history by the simple expedient of using different values of the dynamic efficiency ratio, η_d (0.7, 0.9, 1.0 and 1.2). All the other settings were maintained constant and therefore the driving time was kept constant at 4 ms. The different resulting force-time curves are illustrated in Figure 4-9.

Table 4-7 Results of DEM-based dynamic probing tests

Test ID	v_{peak}: m/s	q_d: MPa	$\Delta\rho$: cm	N	E_{blow}: J	ER: %	N_{60}	N/D_r^2	N_{60}/D_r^2
Very Dense_100	1.37	9.45	0.67	44	196	41.5	31	66	45
Very Dense_200	1.26	15.76	0.36	83	199	42.1	58	123	84
Very Dense_400	1.31	21.64	0.24	123	200	43.0	87	184	124
Dense_100	1.42	5.39	1.45	21	203	42.9	15	36	24
Dense_200	1.35	10.19	0.7	42	197	41.7	30	82	53
Dense_400	1.30	14.62	0.31	97	179	38.1	61	186	107
Medium_100	1.42	4.56	2.27	13	213	45.1	10	36	25
Medium_200	1.35	9.71	1.01	30	190	40.4	20	82	50
Medium_400	1.38	10.33	0.5	60	189	40.0	40	166	98
Loose_100	1.47	1.56	5.63	5	270	57.1	5	35	30
Loose_200	1.40	3.09	2.54	12	221	46.7	9	77	53
Loose_400	1.35	7.72	0.93	32	196	41.5	22	212	119

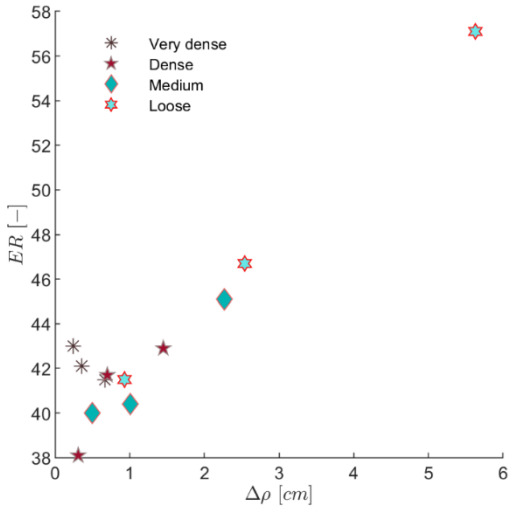

Figure 4-8 Energy input variations with blow depth

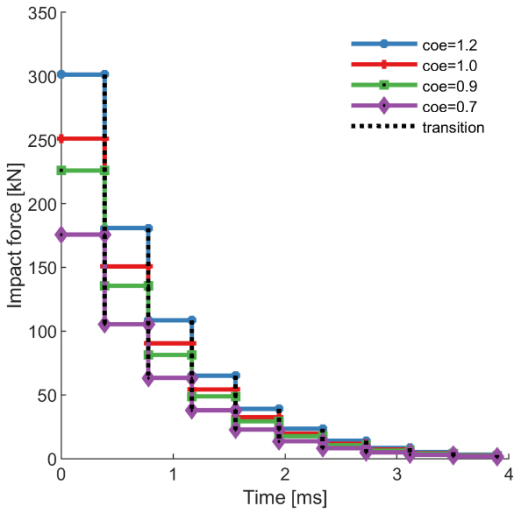

Figure 4-9 Various force-time input configurations

The blows at different energy were simulated on specimen Dense_100. The results are summarized in Table 4-8 and both measured blowcounts, N, and normalized blowcounts N_{60} are presented in Figure 4-10. It is evident that the energy normalization works well, with all the normalized N_{60} values very close to one another.

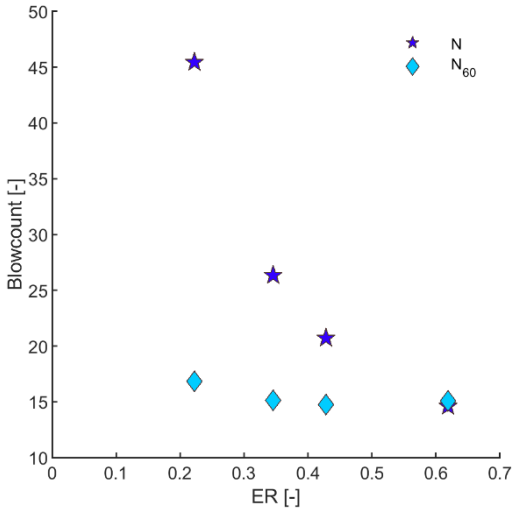

Figure 4-10 Raw and normalized blow counts versus energy ratio observed in one single blow

Table 4-8 Results from tests performed in similar conditions at different input energy

Test ID	η_d	F_{max} : kN	t_{max} : ms	$\Delta\rho$: cm	N	E_{blow}: J	ER: %	N_{60}	ER*N
Dense_100_0.7	0.7	175.7	4	0.66	45	105	22.0	17	9.9
Dense_100_0.9	0.9	225.9	4	1.14	26	163	34.5	15	9.1
Dense_100	1.0	251	4	1.45	21	203	42.9	15	9.03
Dense_100_1.2	1.2	301.2	4	2.05	15	292	61.9	15	9.3

4.3.3 Influence of ground conditions on penetration resistance

There are a great number of soil-related factors known to influence the resistance to dynamic penetration, including void ratio, current stress levels, average particle size, coefficient of uniformity, particle angularity, cementation, aging, etc. For granular soils, however, a main focus has been always on establishing the relation between SPT blow count and relative density.

It was early noticed that, although the influence of relative density on SPT was very strong, it could not be considered separately from that of stress level. In a classical study, Gibbs & Holtz (1957) used calibration chamber testing to explore the relation between N, relative density (D_r) and overburden pressure (P_0). Their results for dry sands were summarized by Meyerhof (1957) in the following relation

$$N = 1.7 \times \left(\frac{D_r}{100} \right)^2 (0.145 P_0 + 10) \qquad \text{Eq. 4-13}$$

where the overburden pressure P_0 is expressed in kPa.

Later calibration chamber studies (Table 4-4) of SPT in sands have proposed slightly different formulations, generally indicating a feebler effect of relative density than that observed by Gibbs & Holtz (1957). Differences are attributed (Marcuson & Bieganousky, 1977; Ishikawa et al., 2013) to the effects of saturation, to details of the dynamic testing procedure or to fabric effects derived from specimen formation procedures (e.g. dynamic compaction vs pluviation). It is also clear that creating homogeneous tank-sized specimens of sand is a very difficult task, as shown by the large variability in results reported by Marcuson & Bieganousky (1977).

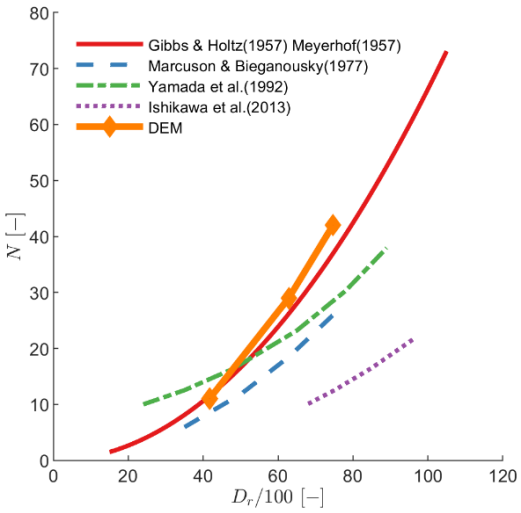

Figure 4-11 Relationship between D_r and penetration resistance at P_0= 200 kPa

Figure 4-11compares the prediction of the summary equations proposed by different authors with the results obtained from the DEM simulations for the case in which P_0 equals 200 kPa. The DEM results appear to match very well the Meyerhof (1957) expression. A more complete comparison with this classical experimental result is presented in Figure 4-12. It appears that the comparison deteriorates as the blow number increases, with the DEM simulation resulting in smaller blow-counts than those predicted by Meyerhof (1957). Because the blow energy applied by Gibbs & Holtz (1957) was not measured it is difficult to pin down possible causes for this discrepancy, although it is likely that the numerical experiments delivered too little energy for the stronger specimens.

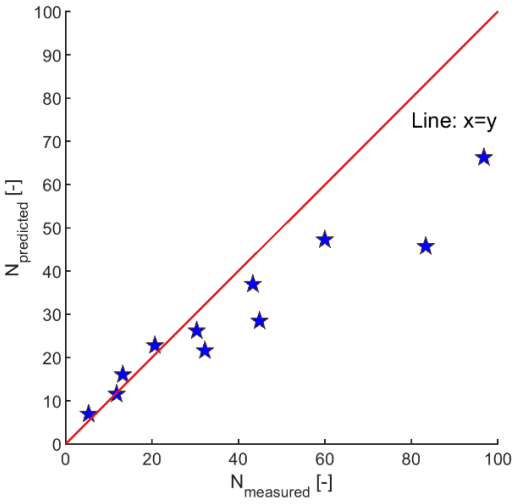

Figure 4-12 Measured blow numbers in SPT DEM simulation compared with those predicted by the Meyerhof expression (1957)

To avoid this kind of difficulty, Skempton (1986) made a systematic effort to compare field and laboratory tests using only normalized blowcount. He found that the shape of the Meyerhof (1957) expression was also valid when the normalized blowcount was employed, thus giving

$$\frac{N_{60}}{D_r^{\,2}} = a + b\frac{P_0}{100} \qquad \text{Eq. 4-14}$$

Where *a* and *b* are material dependent parameters. Skempton (1986) presented results indicating that, for normally consolidated sands, parameter *a* ranged between 17 and 46 and parameter *b* between 17and 28.

Figure 4-13 presents the influence of overburden and relative density on the N_{60} values obtained from the simulations. The lineal influence of overburden and the quadratic influence of relative density are apparent in these results. When all the data is summarized in a single regression (Figure 4-14) it is observed that while the slope (b ~ 27) is very much in line with Skempton (1986) values, the intercept value (a = 5) appears comparatively small. It should be noticed, however, that the field values quoted by Skempton (1986) did carry significant uncertainty, as they were frequently obtained using reasonable guesses about the intervening variables (energy applied, efficiency, relative density or stress level). Figure 4-14 also includes the results obtained using downhole frozen samples by Hatanaka & Uchida (1996). It is noticeable how these experimental results also cluster in the low intercept range.

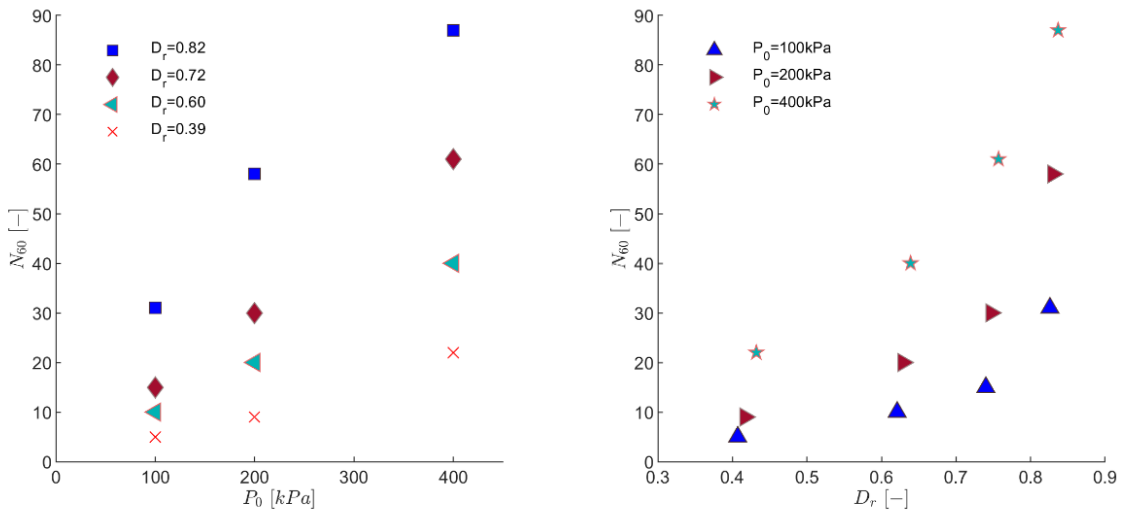

(a) (b)

Figure 4-13 Influence of (a) overburden (b) relative density on the normalized blowcount estimated from the simulations

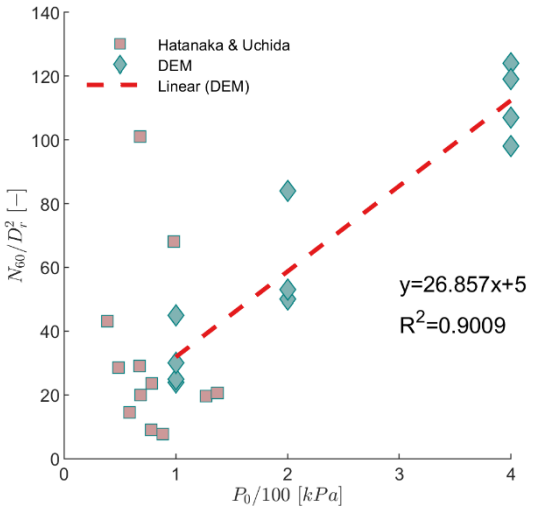

Figure 4-14 Comparison between normalized DEM results and test on frozen samples

4.4 Dynamic vs static resistance

It is interesting to compare the tip resistance obtained from the dynamic probes with the values that are obtained if the static penetration is continued to the same depths (Figure 4-15). Because of the large oscillations visible in the traces the comparison is best based on some representative statistics. The dynamic tip resistance q_d is thus obtained averaging the tip resistance measured during the "*deceleration*" phase (phase *II* in Figure 4-7). The reference static tip resistance q_e is obtained averaging the static tip resistance within the same depths. As illustrated in Figure 4-16a the mean values of dynamic and static tip resistances are very close to one another when they are below 10 MPa. Above this value the dynamic tip resistance is smaller than the static one. The 10 MPa limit also corresponds to a significant increase in the magnitude of dynamic oscillations of tip resistance, as indicated by the standard deviations plotted in Figure 4-16b.

When cone penetration is performed at constant velocity there is a marked increase in tip resistance when the push velocity increases above 1 m/s (Quezada et al., 2014; Tran et al., 2016). This increase is due to inertial effects kicking in above that limit. The peak velocity in the dynamic probes performed here is always above that limit, but reduces as penetration resistance increases (Figure 4-17). Note also that the time fraction spent above this inertial velocity limit is relatively small, due to the fast deceleration occurring in phase II (Figure 4-6). It is therefore unclear how inertial effects, by themselves, may explain the observed discrepancy between static and dynamic penetration values.

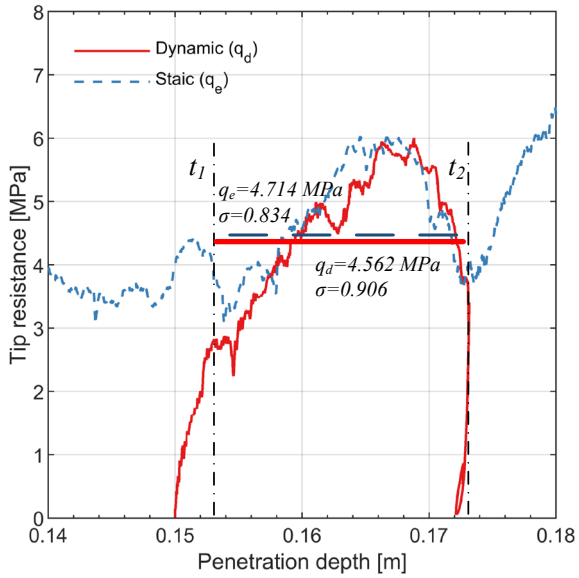

Figure 4-15 Example comparison of static and dynamic penetration (Medium_100)

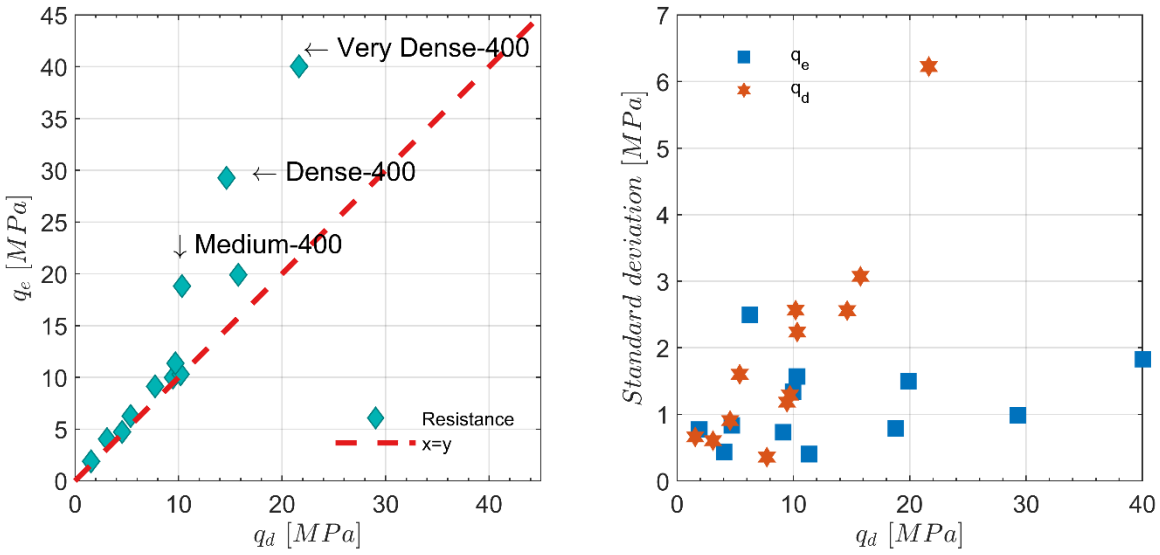

(a) (b)

Figure 4-16 q_e vs q_d and standard deviation of each case

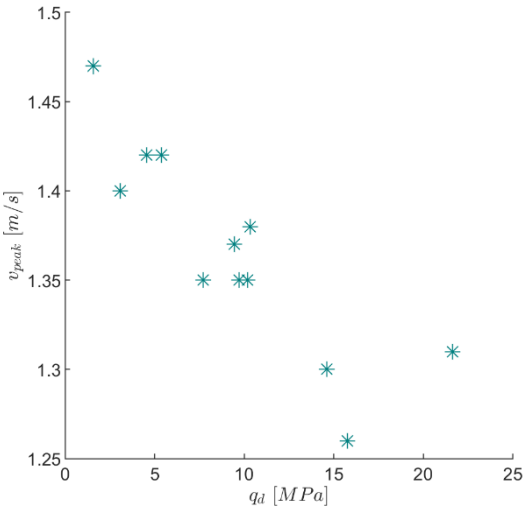

Figure 4-17 Peak velocity during dynamic probing vs average dynamic tip resistance

Other factors that seem relevant for this issue are energy limits, blowrate and contact model effects. Figure 4-18 illustrates the effect of density on the dynamic penetration curves at the highest confinement. It is evident that the plastic penetration at constant tip resistance that is characteristic of *phase II* is much reduced as density increases. It may be then inferred that in the denser more confined specimens the energy of the blow delivered was not enough to fully mobilized the available penetration resistance. Interestingly some of the tests in which the ratio q_d/q_e is smaller have blowcounts above or very close to the normalized limit for field test acceptance ($N = 100$).

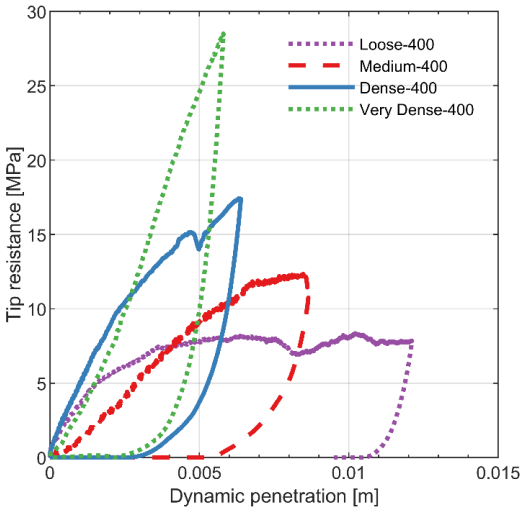

Figure 4-18 Influence of initial density on dynamic penetration curves for the series at $P_0 = 400$ kPa

Blow-rate may be also involved. Schnaid et al, (2017) showed that, after properly accounting for the energy input in the dynamic test, the tip resistance in static and standard penetration tests had very similar values, a result independent of the resistance value. Schnaid et al, (2017) performed SPT according to the standard procedure, delivering blow after blow until 30 cm of penetration was achieved. On the other hand, the simulations presented here included a single blow. For fast blow-rates there may be an overlap in the mechanical effects of separate blows. Unfortunately blow-rate is neither prescribed in standard procedures nor typically recorded.

Finally, it should be noted that the contact model employed here has some limitations to represent load-unload cycles. A somewhat excessive elastic compliance is included to alleviate a simplified description of contact mechanics in which, for instance, roughness-induced effects (Cavarretta et al, 2010) are not considered. The increased contact density of denser specimens would make this limitation more relevant, as can be seen in the continuation of rebound after unloading in the curves of Figure 4-18. Ongoing work is exploring how to alleviate this problem using more refined contact models, in which the effect of contact roughness is included (Otsubo et al, 2017a).

4.5 Summary

This work set out to explore the capabilities of the DEM VCC approach to model SPT. In this respect, and despite the limitations noted for the higher density specimens, the main results obtained appear very positive. These are

- The macro-element approach may be applied to model a driving rod with a realistic driving force input.
- Input energy normalization has been shown to be as effective an approach as in field testing.
- The effects of density and overburden pressure are in good agreement with well-established empirically –based expressions.
- In blows that result on fully developed plastic penetration, a close correspondence between dynamic and static tip resistance is observed.

Even if continuum based simulation models are advancing fast (Monforte et al., 2018; Moug et al, 2019) it is our impression that DEM VCC models do offer some advantages for the case of dynamic probing. The macro-element approach allows for easy generalization to represent more realistic impact dynamics, for instance by coupling it with driving tool models such as those presented by Daniel & Howie (2005). Consideration of drainage effects is also possible with resource to complementary modelling techniques, (e.g. CFD-DEM coupling, Climent et al., 2014). But perhaps the most interesting applications will be

those focusing on particle-scale influences on test result, such as grain crushing, gran size distribution effects or grain shape effects (either modelled directly or through a contact rolling resistance model). It is hoped that the work presented here will encourage those developments.

Chapter 5 Energy balance analysis during the Standard Penetration Test

Based on a manuscript to be submitted.

5.1 Introduction

Despite the Standard Penetration Test (SPT) being a very frequently used in-situ test in geotechnical engineering its results are not very highly rated by engineers, as they are seen as unlikely to guarantee the consistency of the soil properties and parameters derived from them. This limitation results from two important reasons:

(1) It is difficult to control the test precisely as the test procedures are not fully standardized;

(2) Empirical methods are used to interpret test results, which in turn will cause uncertainties.

Researchers have dedicated many efforts in addressing these shortcomings. The development of energy based approaches has been recognized as a big step in improving the SPT test execution repeatability and more recently in bringing out more rigorous interpretation procedures. The effect on test execution repeatability was ensured using energy-based normalizations of the reported SPT N-value. Recording the energy input from hammer blows on the rod-sampler system allowed to introduce an energy normalized blow number, N_{60}, which was identified as the best means to compare SPT results obtained using different systems (Seed et al., 1985; Skempton, 1986). This effectiveness of this approach was verified empirically by field testing and it has also been verified numerically in this Thesis (see chapter 4).

Going beyond input normalization, energetic considerations have also been used more recently to open new ways of interpreting test results. From the concept of energy balance of test equipment, both Hettiarachchi & Brown, (2009) and Schnaid et al., (2009) proposed simple interpretation formulations of test results for the determination of soil properties including internal friction angle and undrained shear strength. More detailed description of the proposed energy balance approaches can be found in chapter 2, section 2.3.5.

The discrete element method (DEM) is advantageous in giving very precise information about energy input (macroscale) and dissipation (microscale) mechanisms in granular materials. Such information can be used to gain insight on soil behaviors. For instance, Hanley et al., (2017) tracked all decomposed energy components in the simulation of triaxial compression of large-scale, polydisperse numerical samples which were sheared to critical state. They concluded that frictional dissipation was almost equal to work input at the boundary independently of initial sample density. Based on this, they proposed a thermodynamically consistent formulation of incremental plastic continuum dissipation, alternative to the modified Cam Clay work equation. DEM energy analysis has been applied also to a wide range of geotechnical applications. In the simulation of a medium-velocity (e.g. 5 m/s) impactor penetration in sand, Holmen et al., (2017) identified the distribution of frictional sliding energy (particle-particle and particle-intruder) and energy terms of the impactor. They concluded, again, that most of the energy in the system was dissipated by friction, to which particle fracture may contribute. Zhang & Evans (2019) simulated a higher-velocity impact (25-40 m/s) – free falling torpedo anchor installation. In their study a relatively larger ratio of collisional energy to frictional energy dissipation was obtained, due to the fast impact.

In our previous chapter, we demonstrated the capabilities of 3D DEM calibration chamber technique in modelling SPT in granular soils, reproducing various representative test features. As it happens in the field, energy input based normalization was shown to be as an effective method to eliminate result variability derived from differently specified inputs. In this chapter we go beyond the consideration of variable energy inputs, and we proceed to carry out a comprehensive study of energetic balances in the virtual calibration chamber dynamic experiments.

In this study, energy analyses is applied to the same test series used in the previous study. The specimens combine four density levels and three confining stress levels. Energy input contribution by rod and boundaries and energy dissipation within granular soils are systematically tracked for each simulation in all specimens.. The results obtained are then used to present energy balances and study the effect of test conditions on different energy components. A validation of proposed energy-based interpretation methods for the test is also presented. Microscale observations on energy dissipation is also be presented.

Particle crushing is not addressed in this chapter: similar analyses featuring this property will be presented in chapter 7.

5.2 Energy terms during rod probing in a calibration chamber

Dynamic rod penetration in a calibration chamber is a dissipative process in which granular assemblies transit from one equilibrium state to another (from the at-rest position before hammer release to the at-

rest position after penetration ends). During this process energy exchanges and dissipation take place in the system. To investigate the evolution of energy input/dissipation behavior between these two states, all involved energy terms in each simulation were traced. All symbols for the variables encountered in energy calculations, such as force, velocity etc., were determined according to the coordinate system illustrated in Figure 5-1. Note that the origin of the coordinate system was located at the center of the chamber bottom wall.

For subsequent analysis it is useful to consider separately two subsystems: the driven rod and the calibration chamber.

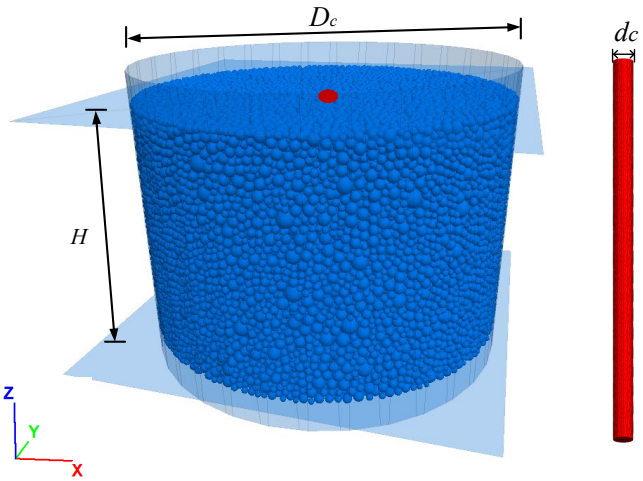

Figure 5-1 View of DEM model of calibration chamber, rod and coordinate (originated at the center of bottom wall

5.2.1 Work and energy components for the rod subsystem

The rod is assumed rigid and, therefore, energy delivered by the hammer impact on the rod top, W_H can be theoretically computed by integrating the impact force F_{drv} multiplied by the rod velocity history v_r

$$W_H = \int_0^{t\_eq} F_{drv}(t) v_r(t) dt \qquad \text{Eq. 5-1}$$

Where t_eq is the time for equilibration.

Following a similar reasoning to that presented by Odebrecht et al., (2005), the work done by the rod self-weight during rod displacement, or change in potential energy, U_R is also considered. It can be computed by integrating the rod gravitational forces $m_r g$ multiplied by the rod velocity,

$$U_R = m_r g \int_0^{t\_eq} v_r(t)dt \qquad \text{Eq. 5-2}$$

As rod driving proceeds, the soil in the chamber presents resistance to the rod. The work done by the soil resisting rod driving R_R can be calculated by integrating the recorded reaction force F_{rea} multiplied by the rod velocity,

$$R_R = \int_0^{t\_eq} F_{rea}(t) v_r(t)dt \qquad \text{Eq. 5-3}$$

Finally, the kinetic energy of the rod is evaluated from the assigned value of rod mass m_r and computed rod velocity,

$$K_R = 0.5 * m_r v_r^2(t) \qquad \text{Eq. 5-4}$$

5.2.2 Work and energy components for the VCC subsystem

Considering now the virtual calibration chamber, the following energy components can be traced within the system during a blow: work done at chamber boundaries, energy delivered by the driven rod to the VCC W_R, energy dissipated by frictional sliding D_F, energy dissipated by damping D_D, elastic strain energy increment ΔE_S and kinetic energy E_K.

5.2.2.1 Work done at chamber outer boundaries

During the process of rod advancing, the top and radial boundaries of the calibration chamber are servo controlled to maintain a constant stress level, whereas –in the chamber here employed- the bottom boundary remains fixed. At the moving boundaries there is a work flux that may have a significant effect on the energy balance. The work done by these boundaries is here denoted as W_{rad} and W_{top} respectively. Work done by each boundary is calculated by integrating the force of each boundary which acts vertically on the specimen multiplied by the velocity of the boundary.

$$W_{rad} = \int_0^{t\_eq} F_{rad}(t) v_{rad}(t)dt \qquad \text{Eq. 5-5}$$

$$W_{top} = \int_0^{t\_eq} F_{top}(t) v_{top}(t) dt \qquad \text{Eq. 5-6}$$

Where, F_{rad} and F_{top} are the forces of radial and top boundary, respectively; v_{rad} and v_{top} are the velocities of radial and top boundary, respectively.

Another chamber boundary is given by the rod itself. The work done by the rod W_R into the chamber can be calculated by adding up the contact forces at the rod to obtain F_{act} and multiplying this resultant by rod velocity v_r,

$$W_R = \int_0^{t\_eq} F_{act}(t) v_r(t) dt \qquad \text{Eq. 5-7}$$

Clearly, the forces F_{act} and F_{rea} have the same magnitude but are in opposite direction, that is $F_{act} = -F_{rea}$ and therefore the work done by the rod into the chamber is equal and opposite to the resisting work done by the soil on the rod $W_R = -R_R$.

5.2.2.2 Energy components within the chamber

The net energy flow into the chamber is partly dissipated and partly stored into reversible mechanisms (kinetic particle energy and strain energy). All the relevant terms may be computed form a particle-scale perspective.

The kinetic energy of all particles E_K accounts for both translational and rotational velocities of particle j.

$$E_{Kt} = \frac{1}{2} \sum_{j=1}^{n_p} m_j v_j^2 \qquad \text{Eq. 5-8}$$

$$E_{Kr} = \frac{1}{2} \sum_{j=1}^{n_p} I_j \omega_j^2 \qquad \text{Eq. 5-9}$$

Where, n_p is the total number of particles, m_j, v_j, I_j and ω_j are, the mass, translational speed, moment of inertia and rotational speed of a spherical particle j, respectively. Note that in simulations in which rotational motion is impeded the second term is zero.

The strain energy stored at all contacts upon particle deformation is formed by normal and shear components, termed as E_{Sn} and E_{St}, respectively,

$$E_S = E_{Sn} + E_{St} \qquad \text{Eq. 5-10}$$

Assuming a Hertz-Mindlin contact model, the normal component of strain energy E_{Sn} stored at all contacts is (Itasca Consulting Group, 2016):

$$E_{Sn} = \sum_{i=1}^{n_c} \left(\frac{2}{5} \left| \mathbf{F_{n\_i}} \right| \alpha_{n\_i} \right) \qquad \text{Eq. 5-11}$$

Where, n_c is the total number of contacts, $\mathbf{F_{n\_k}}$ is the normal force at contact i and α_{n_i} is the interparticle overlap at contact i.

The tangential component of strain energy is calculated as

$$E_{St} = \int_0^t \sum_{i=1}^{n_c} \mathbf{F_{t\_i}}(t) \frac{\Delta \dot{\mathbf{F}}_{\mathbf{t\_i}}(t)}{k_{t\_i}} dt \qquad \text{Eq. 5-12}$$

Where, $\mathbf{F_{t\_i}}$ is the tangential force, $\mathbf{\Delta F_{t\_i}}$ is the increment rate of tangential force and k_{t_i} is the tangential stiffness.

Before launching a dynamic test, strain energy has been accumulated to a certain extent. The increment of strain energy between final and initial equilibrated states is expressed as

$$\Delta E_S = E_S^{t\_eq} - E_S^0 \qquad \text{Eq. 5-13}$$

Where, $E_S^{t\_eq}$ is the strain energy at final state and E_S^0 is the strain energy right before launching dynamic test.

Frictional dissipation is the main mechanism for energy dissipation. A slip criterion is imposed to determine the limit of the tangential force $\mathbf{F_t}$, as described in Eq. 5-14

$$\mathbf{F_t} > \mu \mathbf{F_n} \qquad \text{Eq. 5-14}$$

Where, μ is the friction coefficient.

When friction slip occurs between contacts, the energy dissipated by frictional sliding D_F over all contacts can be also calculated

$$D_F = \int_0^{t\_eq} \sum_{i=1}^{n_c} \mathbf{F_{t\_i}}(t)\,\Delta\dot{\mathbf{U}}_\mathbf{i}(t)\,dt \qquad \text{Eq. 5-15}$$

Where, $\Delta\dot{\mathbf{U}}_\mathbf{i}$ is the increment rate of slip displacement.

Besides frictional sliding, energy can also be dissipated by numerical damping, which is denoted here as D_D and calculated as

$$D_D = \int_0^{t\_eq} \sum_{i=1}^{n_c} \mathbf{F^d}(t)\left(\dot{\mathbf{x}}(t)\right)dt \qquad \text{Eq. 5-16}$$

Where, $\mathbf{F^D}$ is the damping force and $\dot{\mathbf{x}}$ is the relative translational velocity.

Generally speaking, damping is introduced in mechanical models to represent indirectly small energy sinks that are too onerous to be directly modelled (Crandall, 1970). DEM based simulations are no exception and those using a linear contact model require damping to represent, for instance, heat radiation. As a result of damping elastic fixed-fabric oscillations are avoided and equilibrium is achieved in reasonable time. The damping ratio is set here as a relatively small value 0.05. It is shown below that the energy dissipation due to this term is pretty small and has a small influence on the energy balance. Noting that W_R, W_{rad}, W_{top}, E_K and ΔE_S, might have either positive or negative values, while D_F and D_D must be positive for any loading or unloading step.

5.3 Energy balance analyses of SPT blows

5.3.1 Energy balance on driven rod

The work input from the hammer to the VCC should go through the driven rod as a transmission media. By considering all the identified energy sources on rod, the energy balance equation on rod can be written

$$W_H + R_R = K_R - U_R \qquad \text{Eq. 5-17}$$

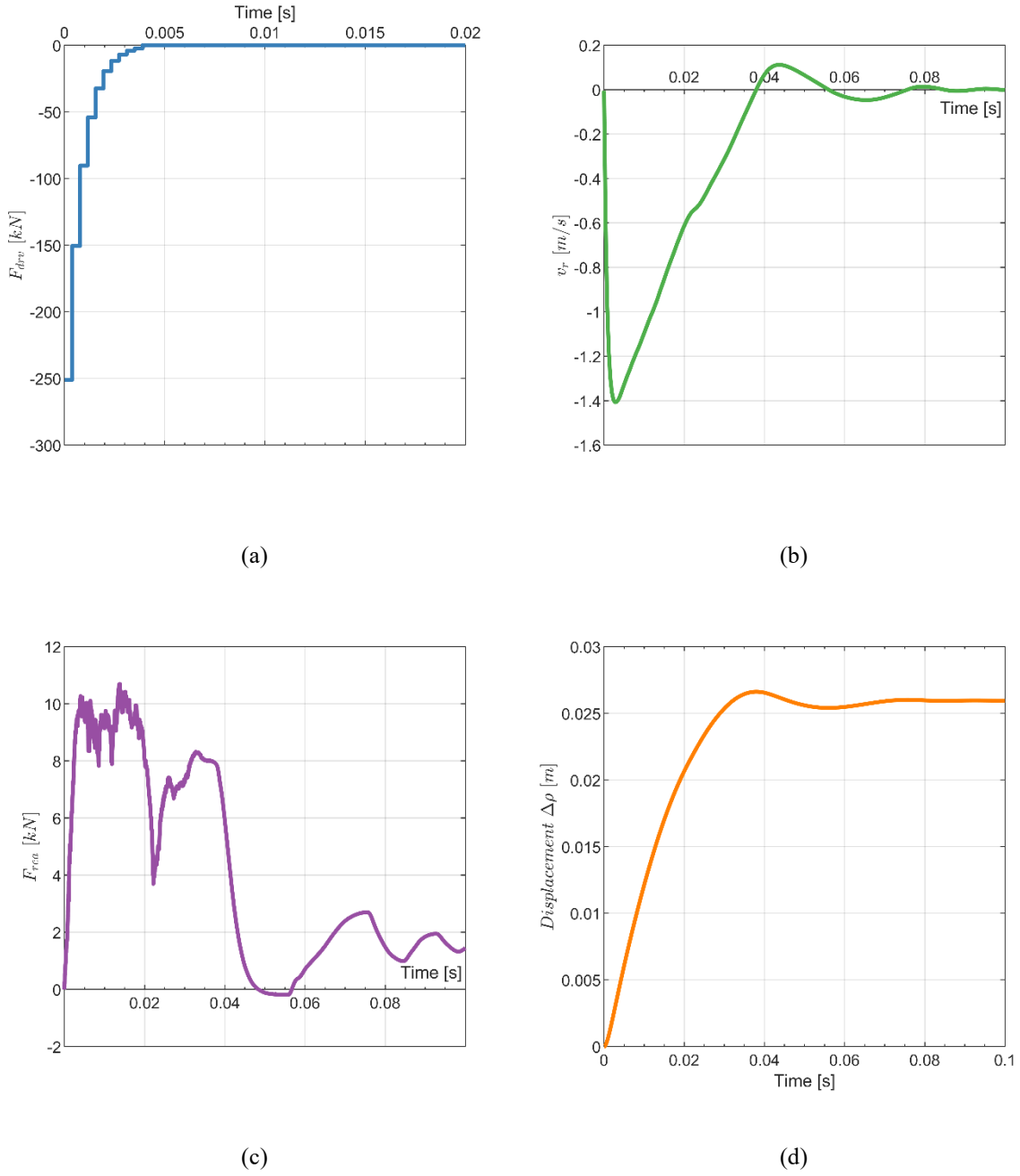

Figure 5-2 Example of measured variables on rod with time in an SPT (Loose_200): (a) driving force F_{drv}; (b) penetration velocity v_r; (c) reaction force on rod F_{rea} and (d) displacement $\Delta\rho$

One representative test of those discussed in Chapter 4 (Loose_200) is selected as an example for energy analyses in this section. The evolution of the variables used for energy calculation on rod such as driving force F_{drv}, penetration velocity v_r, reaction force on rod F_{rea} and rod displacement $\Delta\rho$ with time is illustrated in Figure 5-2. The records are displayed until the variables reach an stationary value (0.1 s for all the variables expect for the driving force which is represented in a shorter scale as it is zero after 0.02 s). As discussed in Chapter 4, the driving force presents a shape of successive compression pulses of progressively reduced stress and terminates at time 0.004s (Figure 5-2a). The rod attains a maximum

value of velocity 1.4m/s (Figure 5-2b). The reaction force on rod is composed by forces acting on the tip and the shaft. Its trend appears very similar to the tip resistance curve (Figure 5-2c). In this blow the rod was driven to a permanent penetration of 0.026 m (Figure 5-2d).

Based on the recorded signals shown in Figure 5-2, the evolution of each energy term on the rod can be computed (Figure 5-3). The hammer work input reaches a final constant value (179.9 J) when the impact terminates, corresponding to the separation point between the hammer and the rod. The rod kinetic energy is deduced to a sharp increase till attaining its peak value and then performs a sharp decrease before the rod becomes stagnant. The contribution of rod potential energy (41.4 J) to the energy balance is significant, approximately 25% of the hammer energy in this case. The sum of the hammer energy and the rod potential energy change is 46.7 % of the hammer free fall potential energy. The hammer energy input is rapid, while resistant energy takes longer time to terminate till the end of penetration. K_R and R_R are travelling almost in parallel against time, indicating an instant transform between the rod kinetic energy and the resistant work.

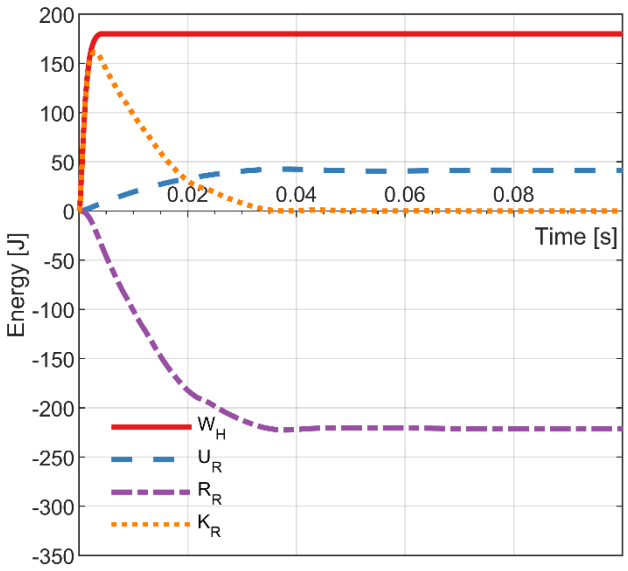

Figure 5-3 Example energy evolution on rod (example: Loose_200)

To confirm that all the sources of energy on rod were correctly identified, and the calculations of each term are correct, the energy error ΔW was calculated as

$$\Delta W = W_H + U_R + R_R - K_R \qquad \text{Eq. 5-18}$$

Figure 5-4 shows the error in energy balance as a percentage of work done by rod resistance. The ratio error is completely negligible, confirming that the expressions for each energy calculation on rod are appropriately identified and the energy balance among all sources of energy on rod is consistent.

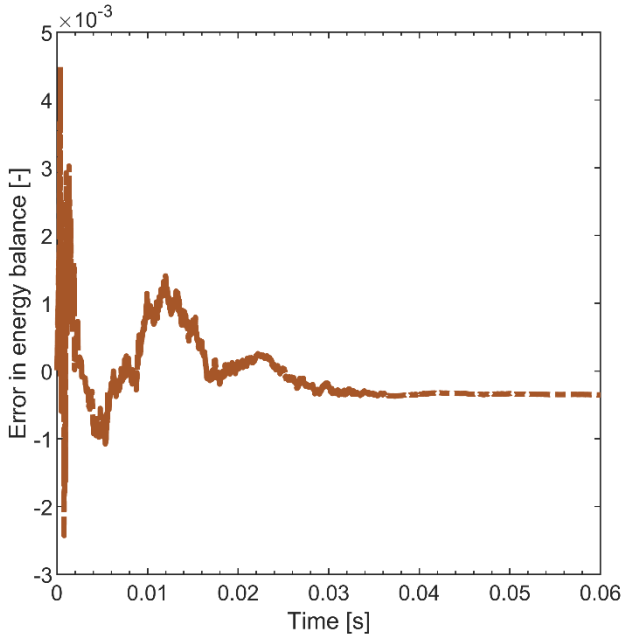

Figure 5-4 Error in energy balance expressed as a percentage of work done by resistance to rod (example: Loose_200)

5.3.2 Energy balance within a VCC SPT system

Based on the concept of conservation of energy in a system, the following relation between the macro-scale quantities and the micro-scale quantities is proposed:

$$W_R + W_{rad} + W_{top} = D_F + D_D + E_K + \Delta E_S \qquad \text{Eq. 5-19}$$

Energy balance computations in the VCC are also explored using the Loose_200 test. Figure 5-5 shows the evolution in time of the variables used for boundary work calculation such as rod action force F_{act}, penetration velocity v_r, radial boundary force F_{rad}, radial boundary velocity v_{rad}, top boundary force F_{top} and top boundary velocity v_{top}. The displacements of radial and top wall are also recorded. These records on boundaries are interrupted at the time of 0.1 s when the system has reached an equilibrated state. Note that the magnitude of action force is equal to that of rod reaction force (Figure 5-2c), but with opposite sign. Both the radial and top boundary forces present large oscillations resulted from the servo-control mechanism of constant stress (Figure 5-5c and e). Similar oscillations can be observed in their

velocity evolution as well (Figure 5-5d and f). The radial wall first displaces rapidly outwards till a relatively steady position and then after a certain time, a rapid movement towards the chamber center is observed. The radial wall final position results in an inward motion of 6 mm (Figure 5-5e). Motion at the top wall is much smaller throughout (Figure 5-5h).

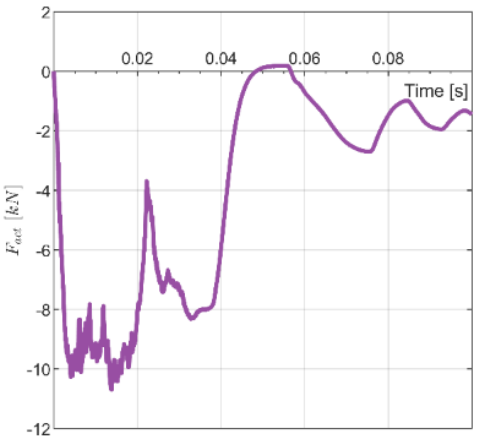

(a)

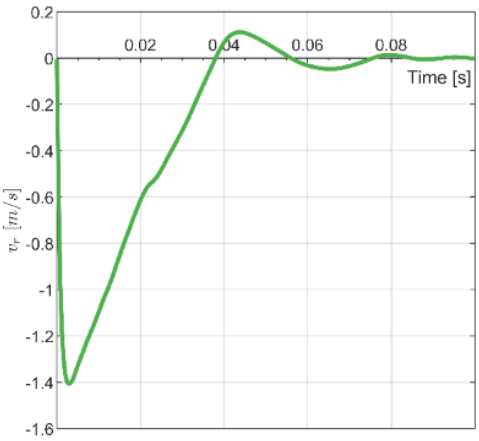

(b)

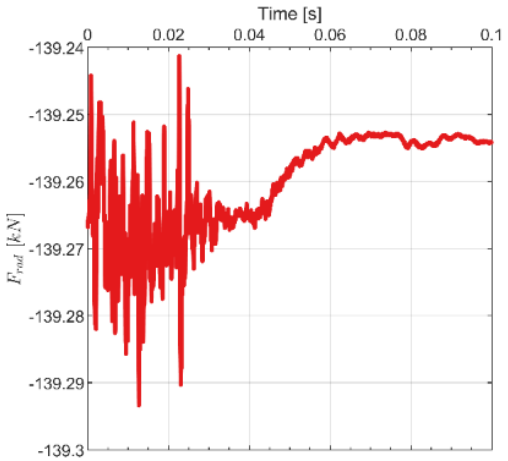

(c)

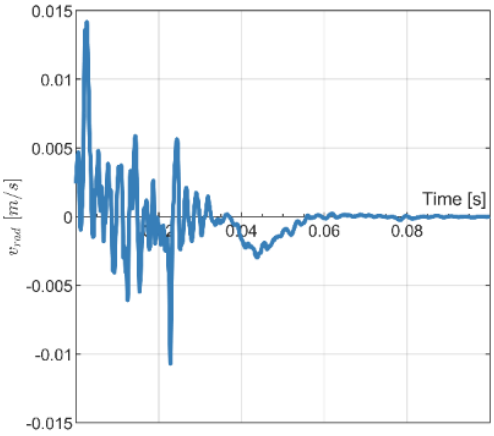

(d)

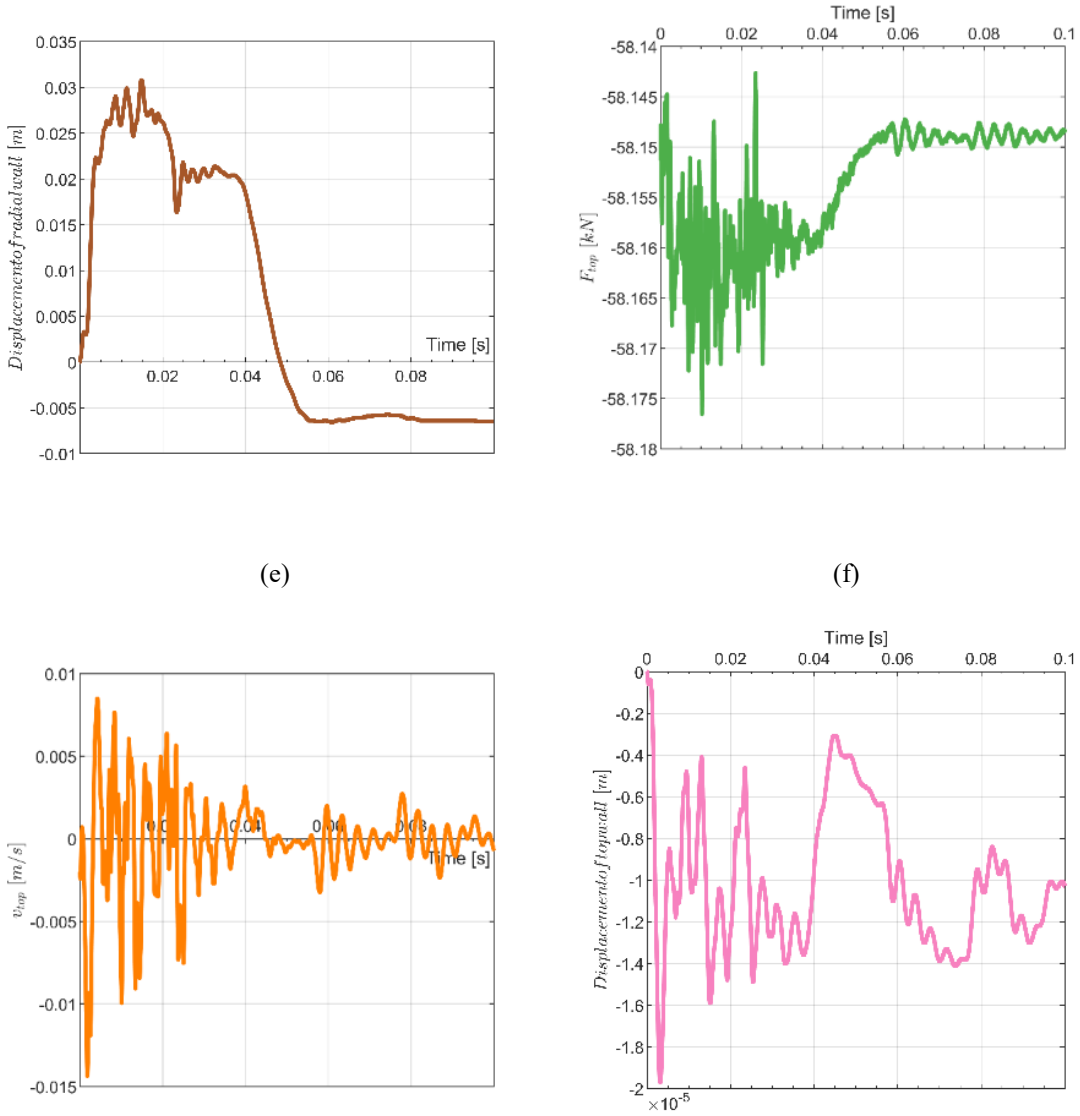

(e) (f)

(g) (h)

Figure 5-5 Example of chamber boundaries variables evolution during an SPT blow (Loose_200): (a) rod action force F_{act}; (b) penetration velocity v_r; (c) radial boundary force F_{rad}; (d) radial boundary velocity v_{rad}; (e) displacement of radial wall; (f) top boundary force F_{top}; (g) top boundary velocity v_{top} and (h) displacement of top wall

Using the data plotted in Figure 5-5, the boundary work input terms can be calculated (Figure 5-6). The particle-scale energy terms are obtained by tracking the corresponding energy history in the DEM simulations. In this case, the rotational kinetic energy (Eq. 5-9) maintains as 0 because of the prohibition of particle rotation and the damping energy and translational kinetic energy (Eq. 5-8) are much smaller than the others so that they are not represented to avoid clutter. The rod work input reaches a final magnitude of 221.4 J, corresponding to 46.7% of the hammer potential energy. It is obvious that the work input is mostly dissipated by frictional sliding between contacts. The increment of strain energy rises somewhat just after the impact and then reduces to almost 0, indicating that no much strain energy

is newly stored after one single impact. During the initial stages of the SPT blow, the radial wall does absorb some work while the top wall does positive work. However, their final net contribution is almost 0.

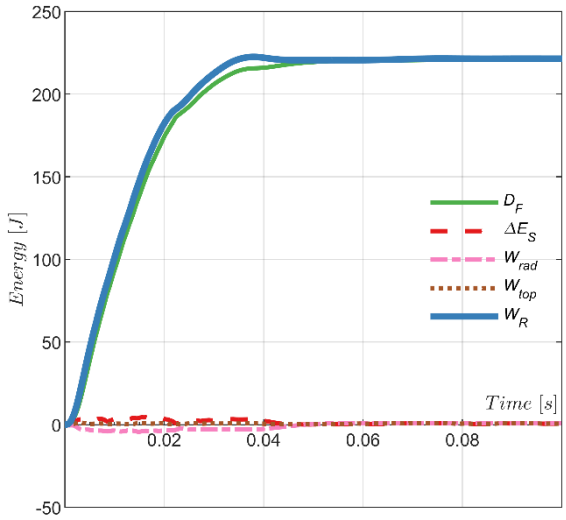

Figure 5-6 Example energy terms evolution within VCC SPT system (example: Loose_200)

Similar to Eq. 5-18, Eq. 5-19 can be written in a form of energy error

$$\Delta E = W_R + W_{rad} + W_{top} - D_F - D_D - E_K - \Delta E_S \qquad \text{Eq. 5-20}$$

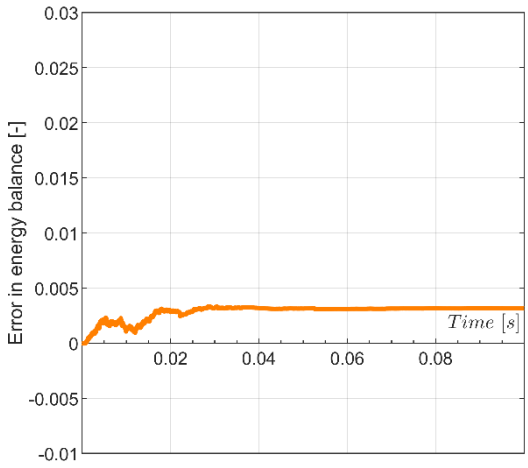

Figure 5-7 Error in the energy balance expressed as a ratio of rod input work (example: Loose_200)

For the reason that the rod is represented by bundled rigid walls in the DEM simulations, the three energy input terms can be combined as total energy input. The four terms on the right side of Eq. 5-19 describes energy dissipation and storage and can be classified into two groups: non-recoverable energy (D_F and D_D) and recoverable energy (E_K and E_S). So we have

$$W = D + E \qquad \text{Eq. 5-21}$$

Figure 5-7 shows the error in energy balance as a percentage of rod work input. The ratio error is negligible, confirming the accuracy of the computations performed.

5.3.3 Evolution of selected energy components with penetration depth

Several observations follow from the previous analyses. Figure 5-8 illustrates the evolution of friction dissipation and rod work input vs dynamic penetration depth. It can be seen that they follow almost parallel trajectories, increasing proportionally with depth during most of the process. A tiny lag between the rod work input and the friction term is present: that is mostly due to strain energy and chamber boundary terms.

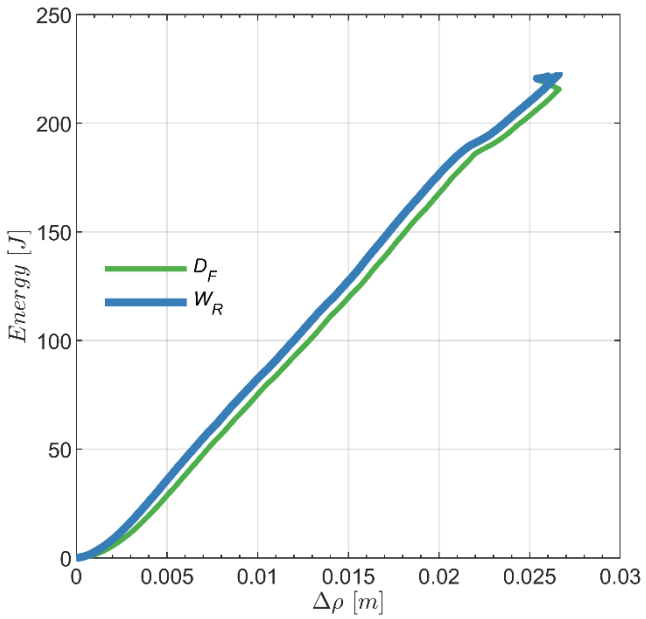

Figure 5-8 Friction energy and rod work input vs penetration

Even contributing relatively small amount of energy to the total energy input to the sample, work done by chamber walls W_{rad} and W_{top} and strain energy change ΔEs reveal interesting trends when plotted

against dynamic penetration depth (Figure 5-9b). The positive and negative energy value of chamber boundary walls corresponds to inward and outward movement, respectively. Clearly, the evolution of all the three energy items is very similar to that of tip resistance while rod penetration advances downwards (Figure 5-9a). A sharp change of each term is triggered by the imposed driving force until time t_1. Shortly after t_1, the energy terms begin to oscillate while penetration advances, marking the start of phase *II*. In phase *II*, the energy terms remain at almost constant magnitudes. Sharp reduction is observed at the moment of entering phase *III* until the rod reaches the final penetration depth.

The fact that strain energy follows closely the history of tip resistance, suggests that the increment of strain energy is concentrated close to the rod tip surface. This will be more directly explored in section 5.5. The final value of strain energy increment is related to the final position of driving rod.

During the initial phases of the blow the radial wall moves outwards to maintain a constant stress level. This involves some energy flow outwards, somehow dampening the fast energy input of the dropping hammer. However, during the rod unloading phase this flow is reversed, as the radial wall begins to move inwards, finally resulting in a positive net value of work input. The top wall contributes positive work to the chamber during the whole impact event. It can then be inferred that the dynamic penetration of driving rod causes particles right below the top wall moving away from the wall itself. More detailed insights are expected to be discovered by investigating particle displacements in the VCC SPT system.

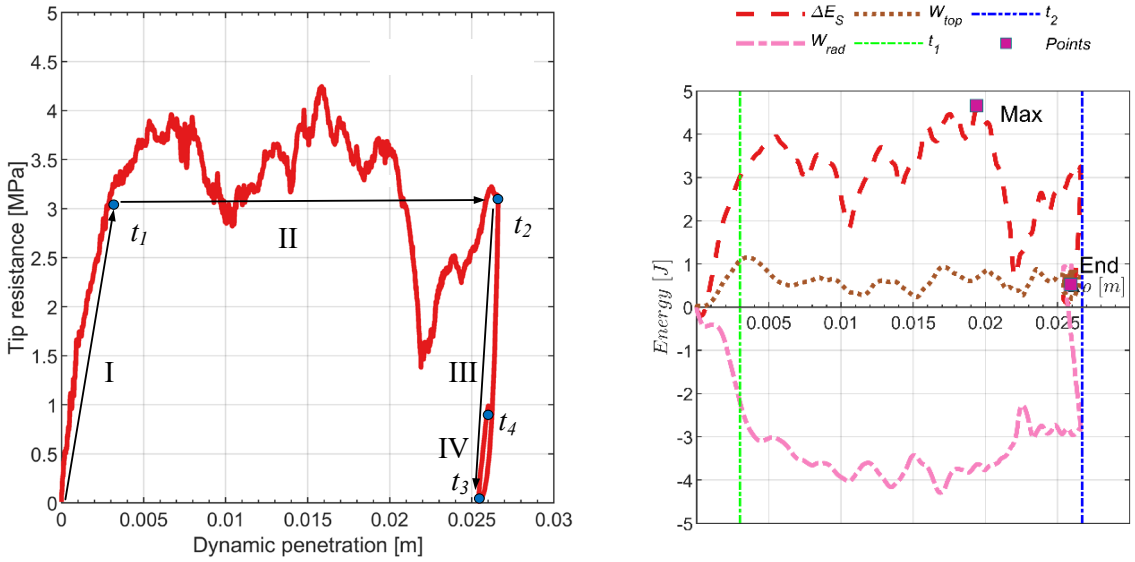

(a) (b)

Figure 5-9 Evolution of SPT results with dynamic penetration (example: Loose_200): (a) tip resistance; (b) strain energy, top and radial work input

5.4 Macroscale observations

5.4.1 Average dynamic tip resistance and energy components

By averaging the tip resistance measured during the 'deceleration' phase (phase *II*) of dynamic penetration curve, dynamic resistance q_d was obtained as an interpretation of the dynamic test results in Chapter 4. The purpose of this method was to facilitate the comparisons with static penetration tests.

As shown in Figure 5-10, it is evident that the hammer input energy is mostly dissipated by frictional sliding, where the ratios of D_F/W are reaching very close to 1. This is in agreement with Bolton et al. (2008). For denser more confined specimens, a part of strain energy stored before launching dynamic penetration is released during the rebound of driven rod after unloading and is consequentially dissipated by frictional sliding. Hence the ratios of D_F/W of these specimens have values slightly above 1.

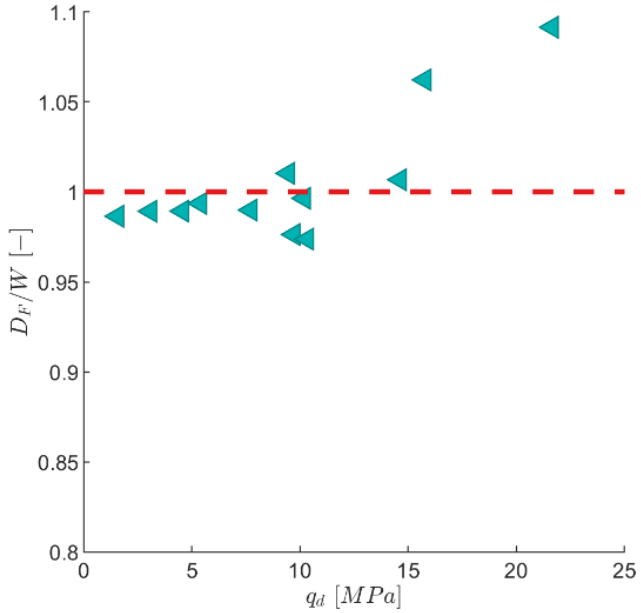

Figure 5-10 Energy dissipated by frictional sliding

During dynamic probing, strain energy is stored in the system while rod penetration advances downwards (phase *I* and *II*) and then released –i.e. given back to the rod- during the unloading phase (phase *III*). The overall result need not be neutral, since there are other terms in the energy balance. Overall strain energy of the specimen may increase or decrease compared with that at the initial state. So it is interesting to place emphasis on the strain energy value at the final point, named as '*End*', and

the maximum value during the process, named as '*Max*' (Figure 5-9b). These two values are plotted against the penetration resistance q_d (Figure 5-11). The maximum change in stored strain energy increases almost linearly with penetration resistance. At the final moment of penetration, the strain energy incremental values return to negligible magnitudes except for those tests in more confined specimens where negative values are observed.

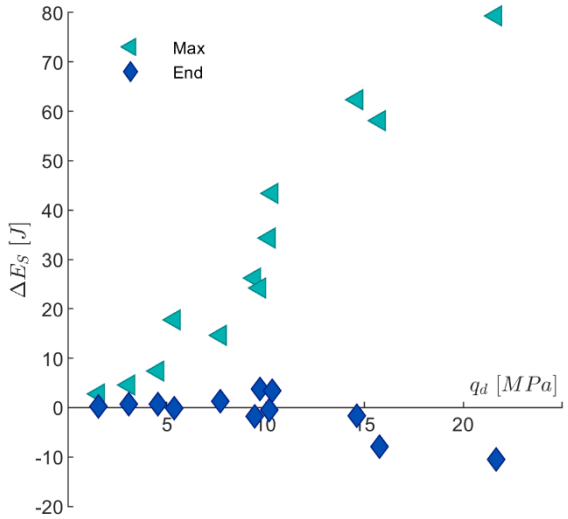

Figure 5-11 Maximum and end strain energy during dynamic probing vs average dynamic tip resistance

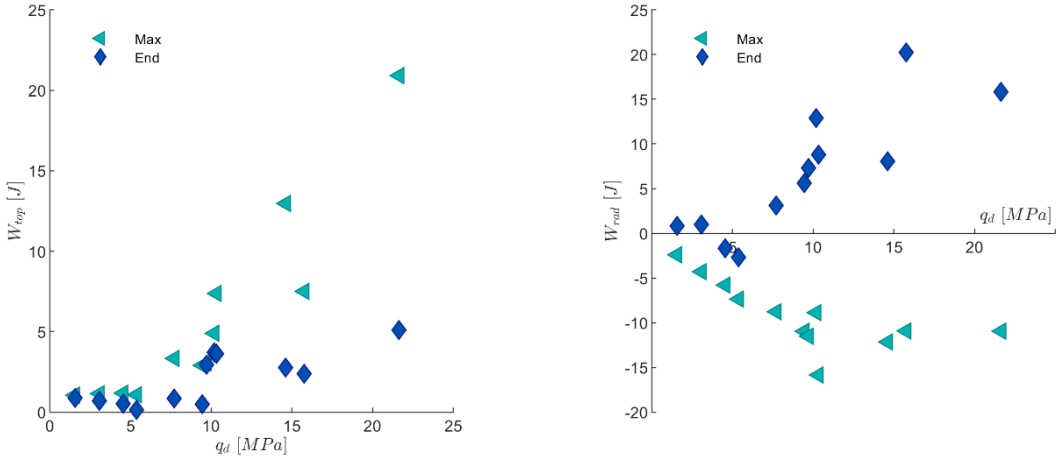

a) Top wall

b) Radial wall

Figure 5-12 Maximum and end work input: a) top wall; b) radial wall

The maximum and final values of work done by top walls and radial walls on the chamber are plotted also against penetration resistances in Figure 5-12. Generally, the top wall contributes positive work (downward movement) during the whole penetration process to the specimen. The magnitudes of maximum values for top walls approximately increase linearly with the penetration resistances. However, the radial walls move differently (outward movement) during the initial stages, contributing negative work. This is identical to that stated in Figure 5-9b. A linear relationship is also visible between the magnitudes of maximum radial work and the penetration resistances.

5.4.2 Energy-based interpretations of SPT test results

As presented in chapter 2, energy-based interpretation methods have been proposed for the SPT (Hettiarachchi & Brown, 2009; Schnaid et al., 2009; Schnaid et al., 2017). Schnaid et al., (2017) propsed an analytical method to estimate the mean dynamic equivalent penetration resistance q_{dE} as a function of the hammer height of fall h and the permanent penetration of the sampler $\Delta\rho$. The expression is

$$q_{dE} = \frac{\eta_3\eta_1(hm_hg) + \eta_3\eta_1(\Delta\rho m_hg) + \eta_3\eta_2(\Delta\rho m_rg)}{\Delta\rho a} \qquad \text{Eq. 5-22}$$

Where, m_h is the hammer mass, m_r is the rod mass, a is the cross-sectional area of the rod, g is the gravitational acceleration, η_1, η_2 and η_3 are the hammer, rod and system coefficients, respectively, used to account for energy losses (Odebrecht et al., 2005). This expression is relatively simple because it allows a direct calculation of dynamic resistance from the recorded penetration depth $\Delta\rho$ and no more empirical or adjustments factors are needed as in other calculation forms of dynamic resistance. However, since the coefficients should be calibrated, the expression is somewhat difficult to apply.

Expression Eq. 5-22 was used in dynamic penetration tests to make comparisons with static ones (Schnaid et al., 2017). It was found that the equivalent dynamic resistance computed using Eq. 5-22 was very similar to the static tip resistance. It is interesting to verify this finding via DEM simulations.

It is clear that the numerator in Eq. 5-22 expression is actually a formula calculating the delivered energy to the driven rod, which is a sum of energy delivered by the hammer impact W_H and by rod self-weight U_R. These two energy terms can be directly measured in DEM simulations. Therefore an applicable version of Eq. 5-22 for DEM calculations can be expressed as

$$q_{dE} = \frac{W_H + U_R}{\Delta\rho a} \qquad \text{Eq. 5-23}$$

As described in section 4.4, the reference static tip resistance q_e is obtained averaging the static tip resistance within the same depths as those measured during the 'deceleration' phase of dynamic probing. As illustrated in Figure 5-13, the equivalent dynamic penetration resistances thus computed are very close to the mean static tip resistances. For high density samples, the discrepancy observed in section 4.4 (figure 4-16) disappears. It is verified that the ratio of q_{dE} / q_e is independent of soil properties.

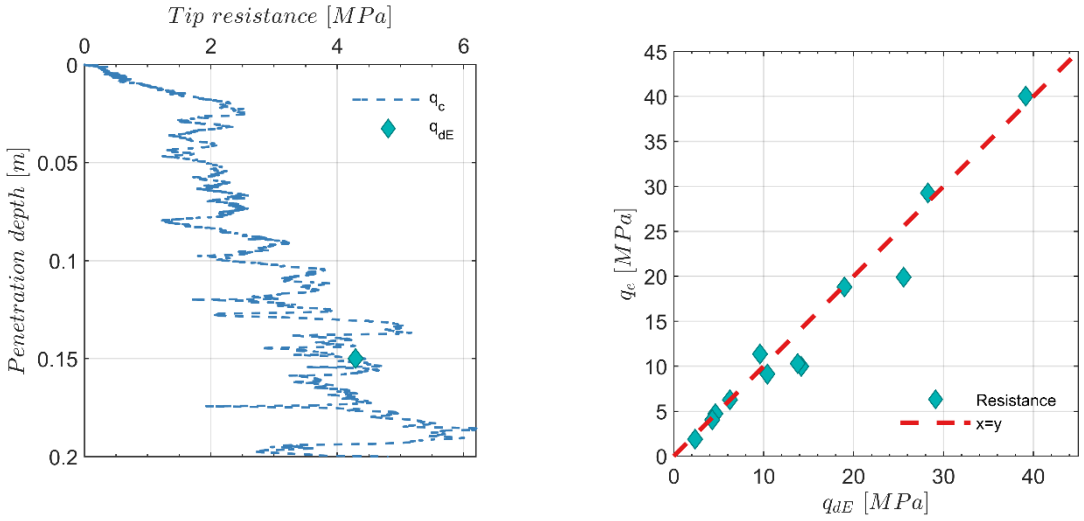

a) loose_200 b) all cases

Figure 5-13 Penetration resistance comparisons between static and dynamic tests: (a) a single case (Loose_200); (b) all cases

5.5 Microscale observations

One of the essential advantages of DEM-based models is that they can be examined at various scale levels (Butlanska et al., 2014). Macroscale results such as tip resistance examined in the previous section are system responses of direct engineering interest. The microscale level of resolution describes discrete variables that are directly derived from the basic components of the model (i.e., particles and contacts). Such variables include contact forces, coordination numbers, particle displacements, energy dissipation, particle radii, particle velocities, etc. Such raw data requires to be interpreted in post-processing to give useful information on the fundamental mechanisms (O'Sullivan, 2014).

5.5.1 Contact force evolution

The visualization of contact force evolution during dynamic rod probing facilitates a clear understanding of how tip resistance evolves with penetration depth. A procedure of residual force relaxation was conducted between the gap of the first 15 cm static penetration and subsequent dynamic

penetration. After the relaxation, it is viewed that the model has reached an appropriate state for launching dynamic penetration. The normal contact forces acting between particles form a homogeneous network (Figure 5-15a). It is interesting to observe contact force network developed in each stage of dynamic penetration. The evolution in time of contact force network is illustrated in Figure 5-15 for the representative sample (test Loose_200). In Figure 5-15, 3D contact force vectors are represented in planar projection along a vertical section containing the chamber axis.

Forces exceeding the whole ensemble average (μ) are plotted in dark grey if CF < μ +5σ while they are in black if CF > μ +5σ where σ is the standard deviation. The forces smaller than the average force are plotted in light grey. The lines join the centroids of contacting spheres and their thickness is proportional to the magnitude of the normal force. The selected time points include not only the characteristic time points t_0, t_1, t_2, t_3 and t_4 used for distinguishing the dynamic process, but also several time points between these characteristic points such as t_{0_1}, t_{1_1}, t_{1_2} and t_{2_1} (Figure 5-14). Clearer observation of contact force evolution with the rod advancing is thus achieved.

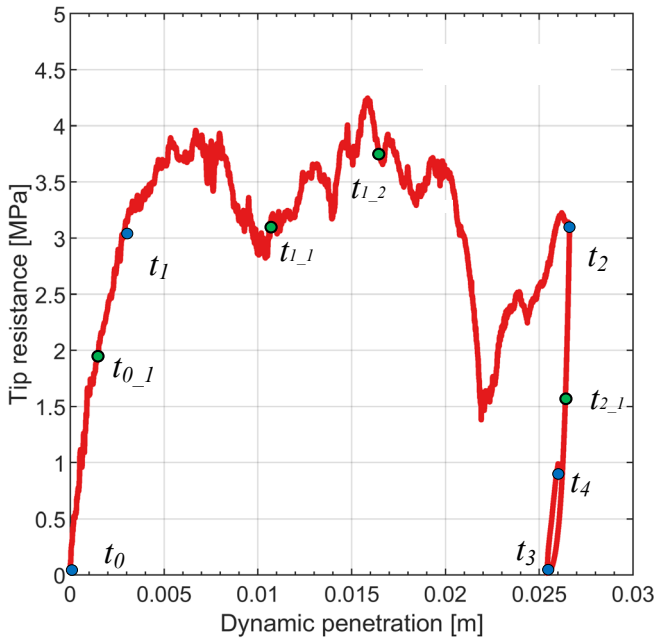

Figure 5-14 Example penetration curve marked with various time points during a blow (Loose_200)

During the whole penetration process, the magnitude of contact forces vary only within a small area below the rod tip. Firstly, the magnitudes of contact forces in this area increase sharply during the short impact period from time t_0 to t_1 (Figure 5-15a, b and c). Shortly after t_1, the contact forces maintain relatively constant magnitudes till t_2 while the penetration advances (Figure 5-15d, e and f). After t_2, the rod rebounds and the tip is progressively unloaded until the CF at the tip becomes almost 0 (Figure

5-15g and h). After t_3, small oscillations in the residual tip resistance continue until the final penetration depth, where the CFs are developed at the rod tip resisting the rod self-weight (Figure 5-15i).

The spatial distribution of contact forces is also interesting. The plots reveal two significant common features. The first one is that the strong force network clearly focuses on the rod tip and the other one is that the force network is sparser above the tip with relatively small forces appearing in the vicinity of the shaft. The phenomenon may be related to the restriction of particle rotation by which a small amount of particles around the tip are sufficient to transmit the force from the tip. The isotropic boundary condition does facilitate a relatively constant network at the areas away from the rod tip.

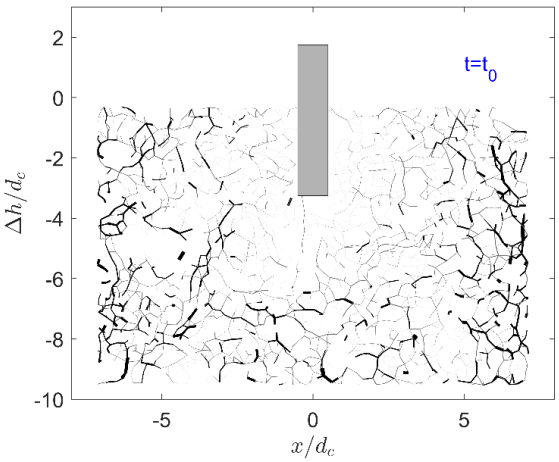

(a) $t=t_0$

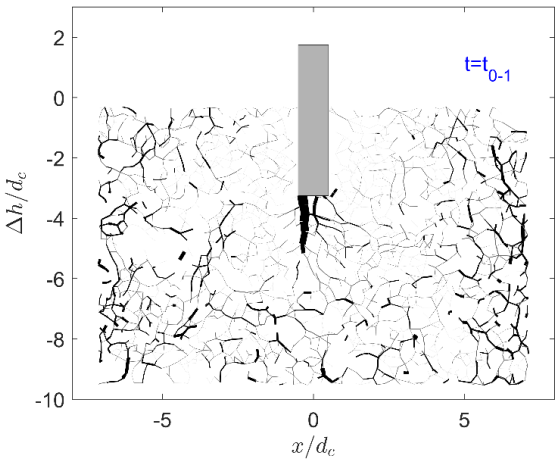

(b) $t=t_{0\_1}$

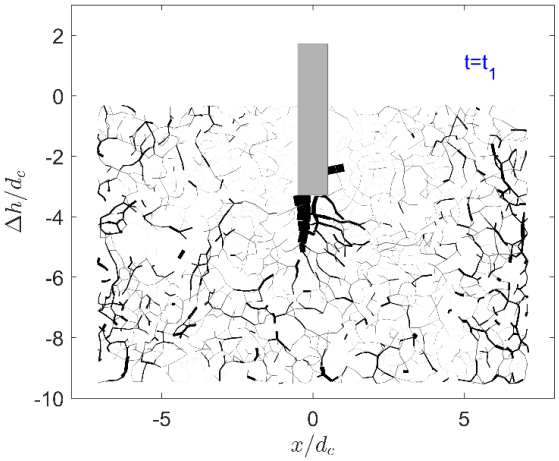

(c) $t=t_1$

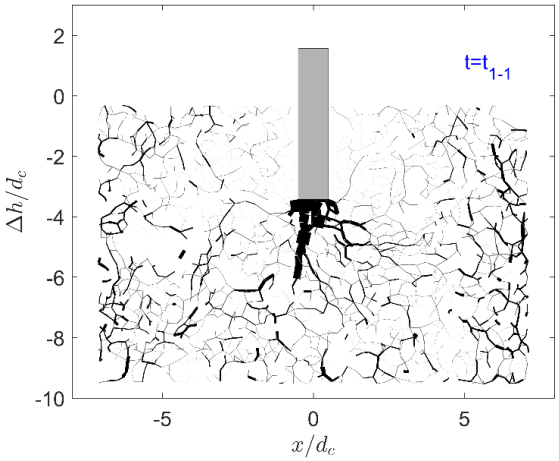

(d) $t=t_{1\_1}$

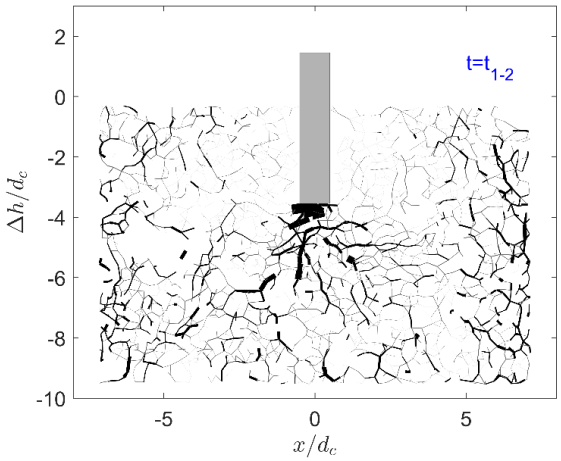

(e) $t=t_{1\_2}$

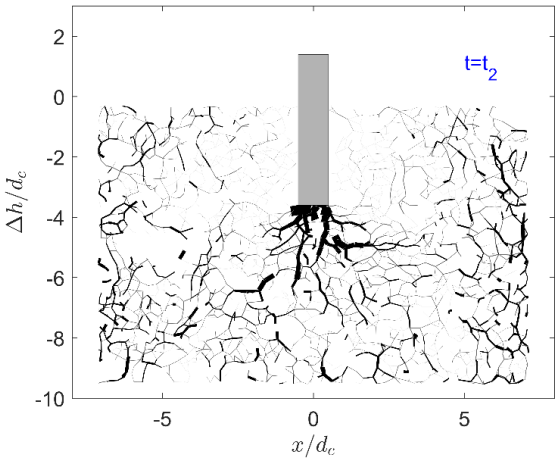

(f) $t=t_2$

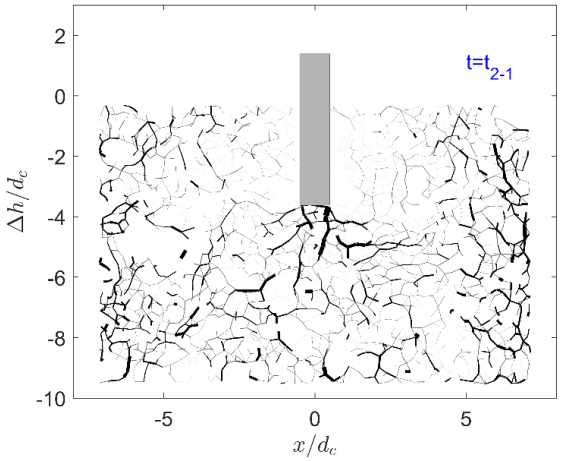

(g) $t=t_{2\_1}$

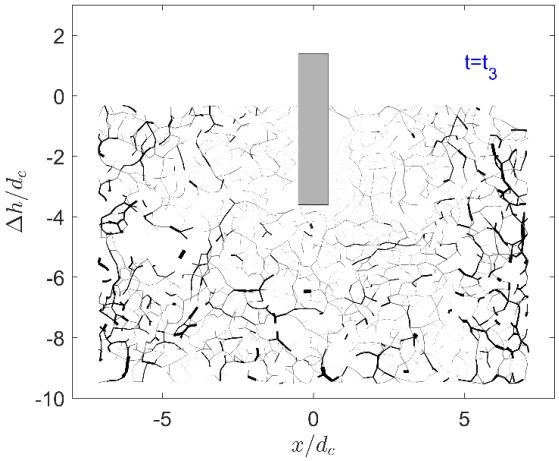

(h) $t=t_3$

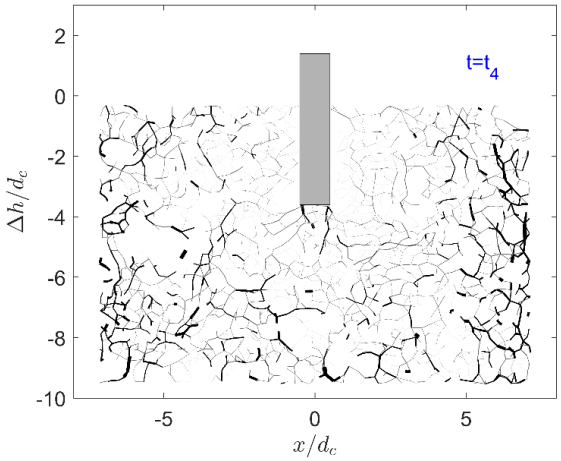

(i) $t=t_4$

Figure 5-15 Contact normal forces for particles lying within a vertical section of the chamber (test Loose_200). Forces exceeding average value +5 standard deviations are illustrated in black; large (above average but not extreme) are shown in dark gray; small (below average) marked in light gray.

5.5.2 Frictional dissipation

It has been noted how the hammer input energy is mostly dissipated by frictional sliding between contacts regardless of sample density and stress level. It is possible to visualize the spatial distribution of that dissipation at the microscale. Frictional dissipation takes place at contacts, but to facilitate visualization energy dissipated contributed by sliding contacts is allocated to particles. Therefore, energy dissipated by friction sliding at a given contact is equally divided between the two entities involved in each contact. Figure 5-16 shows dissipated energy distribution represented in a 4 cm thick cross-section along a vertical section containing the chamber axis. The evolution of frictional dissipation in time is illustrated by coloring balls with their accumulated frictional dissipation energy amount. It can be noticed that the area where the energy is mostly dissipated by friction is highly concentrated around the rod tip and reduces rapidly when moving further away from the rod tip. The maximum magnitude of dissipation is observed at the rod tip through the whole advance of the rod. Sliding occurs along the rod shaft but with smaller magnitudes.

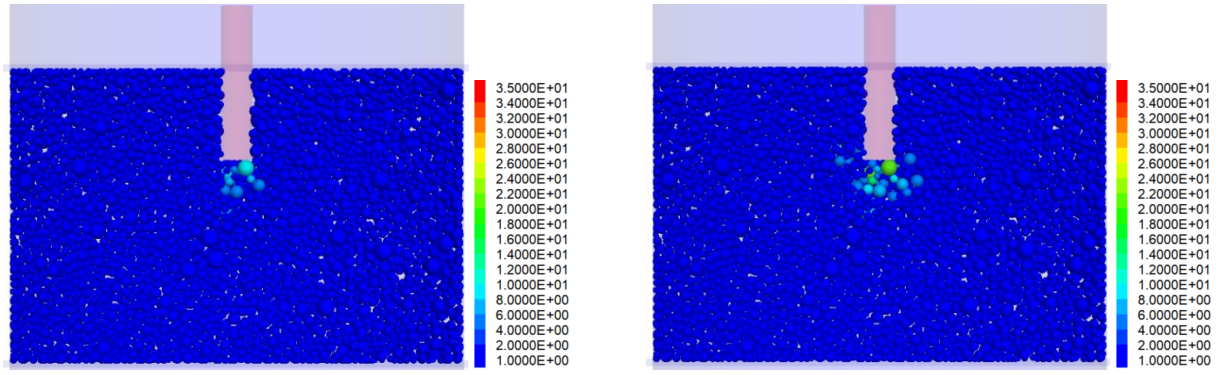

(a) $t=t_{0\_1}$ (b) $t=t_1$

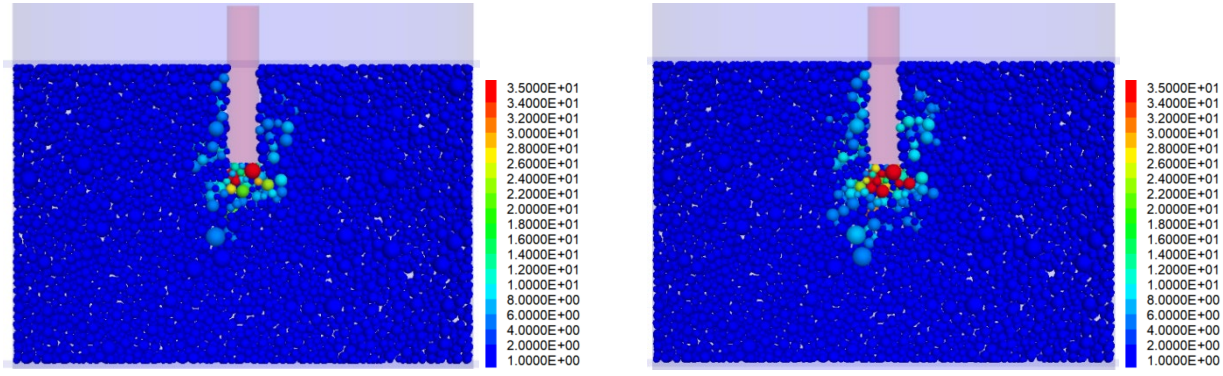

(c) $t=t_{1\_1}$ (d) $t=t_{1\_2}$

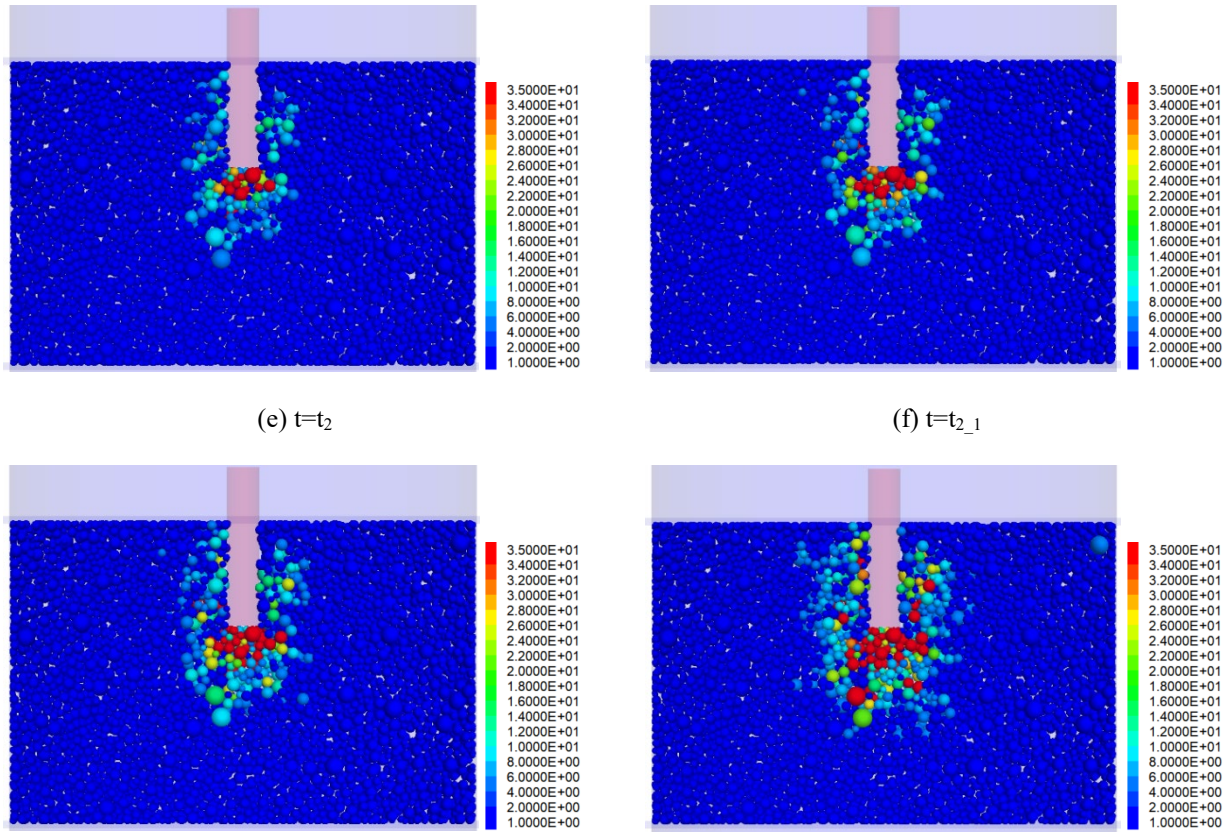

(e) $t=t_2$ (f) $t=t_{2\_1}$

(g) $t=t_3$ (h) $t=t_4$

Figure 5-16 Evolution of energy dissipated by frictional sliding under impact loading (balls colored by energy dissipation)

An alternative view of the same phenomenon is obtained using horizontal sections, 10 layers (5 cm each) are created by evenly cutting the specimen along z direction and are then translated downwards along z-axis (0.5 m between neighboring two layers) and rotated 30 degree along x-axis (Figure 5-17). The 10 layers are named by '***Layer***' + the number representing each layer from the top (1) to the bottom (10) and only layers involving energy dissipation are displayed in each plot. The same legend as that in Figure 5-16 is used. The energy distribution at each time point marked in Figure 5-14 expect for time

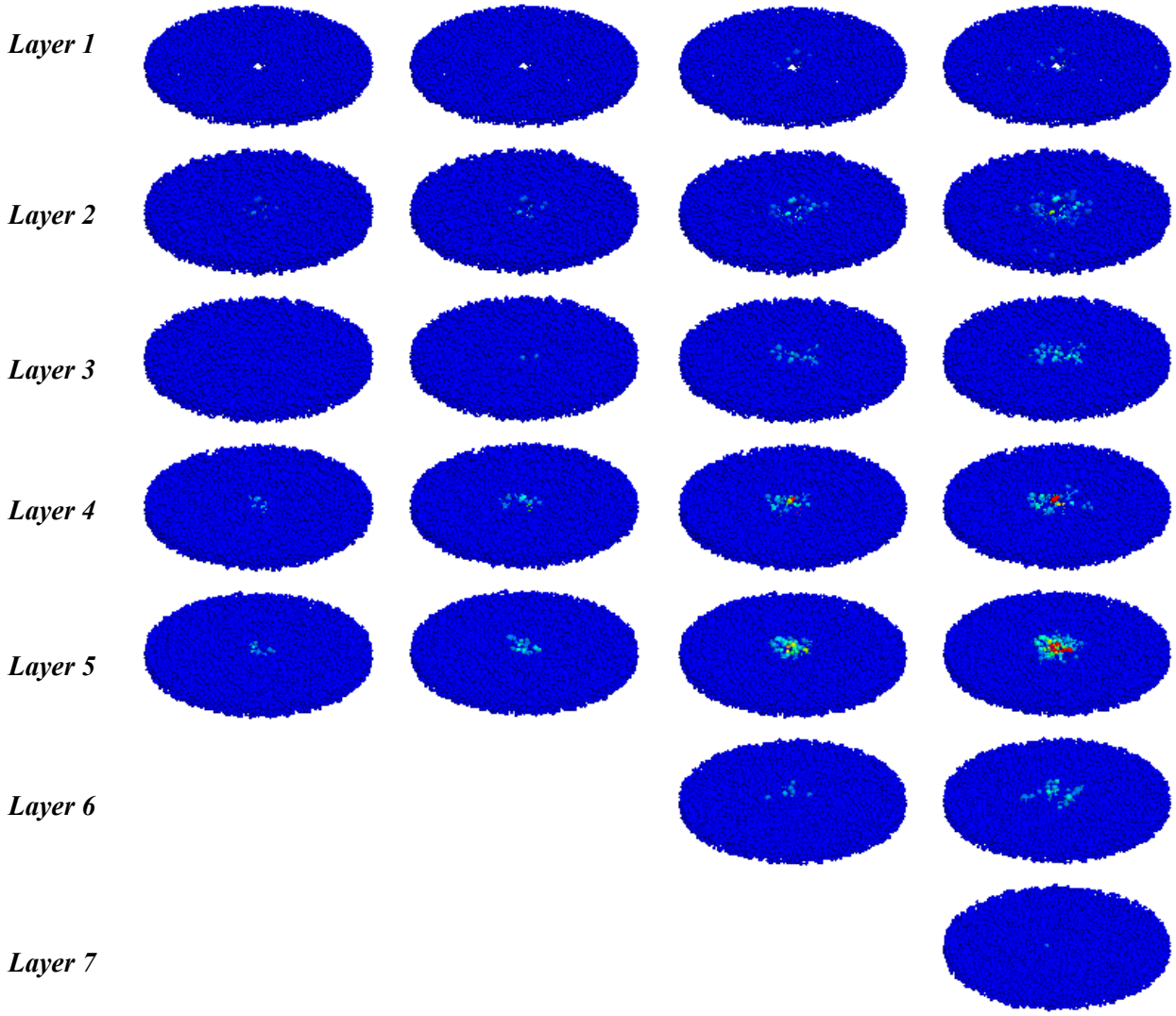

(a) $t=t_{0\_1}$ (b) $t=t_1$ (c) $t=t_{1\_1}$ (d) $t=t_{1\_2}$

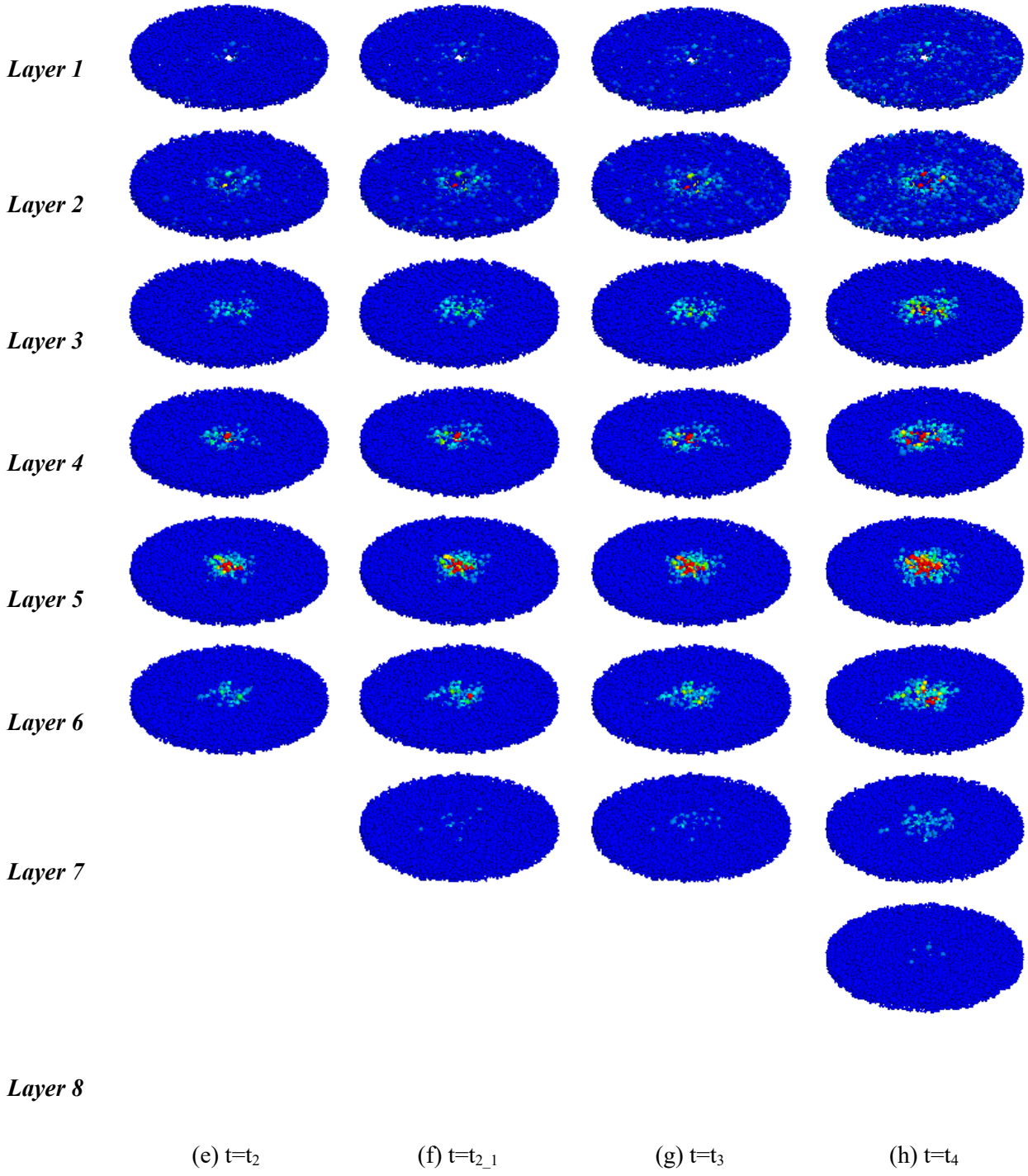

(e) $t=t_2$ (f) $t=t_{2\_1}$ (g) $t=t_3$ (h) $t=t_4$

Figure 5-17 Friction energy views by layers (5 cm each and with 30º of rotation along x-axis)

t_0 is plotted (Figure 5-17). At the initial state ($t= t_{0\_1}$), the dissipation emerges at the rod tip (Figure 5-17a). With the penetration going on, more layers are involved. Each involved layer keeps dissipating energy with the rod advances. At the final state, 8 of the 10 layers start playing roles in energy dissipation, even the final penetration of the rod stagnates at 17.5 cm depth from the top boundary

corresponding to the 4th layer. It indicates an impact excites the energy dissipation mechanism of particles further away from, especially below, the tip.

5.6 Summary

In this chapter, we carried out a comprehensive study over energy distributions excited by dynamic impacts in a 3D calibration chamber filled with discrete granular material. Energy balances were computed from both the rod and the chamber subsystems. This chapter mainly contributes the following conclusions:

- Energy balance has been observed on the driven rod and within the chamber system, indicating that the energy terms are properly considered. From the examined example, it is clear that the hammer energy input is mostly dissipated by frictional dissipation between contacts. The rod potential energy increment can not be neglected. Interesting phenomenon are seen when work done by chamber boundaries (W_{rad} and W_{top}) and strain energy ΔEs are plotted against penetration depth. The plots of these three energy terms are very similar to that of tip resistance. It is inferred that the increment of strain energy is concentrated at the rod tip surface. When the hammer impact starts, the radial wall moves outwards as a way of alleviating the fast energy input of the dropping hammer, while the top wall moves downwards compensating the energy loss caused by the rod.
- An average dynamic penetration resistance q_d was obtained and plotted with the energy terms. It is found the conclusion that energy input is mostly dissipated by friction is valid, but with limitations in the higher density specimens. The peak and end values of strain energy, top and radial work were plotted against the dynamic resistance. Linear relationship are observed between the peak values of the energy terms and resistance. A part of strain energy is released after rod unloading for the higher density specimens due to the limitations of DEM simulations for these specimens.
- The newly proposed energy-based interpretation method for representing dynamic penetration resistance (Schnaid et al. 2017) has been verified by DEM tools. The obtained dynamic resistance q_{dE} is found to have the same measurement as the average resistance of static penetration.
- The observations of contact force network and frictional energy distribution give particle-scale insights into dynamic penetration from a micromechanical scope. More related microscale observations such as particle displacement, coordination number, particle velocities and particle forces in the tests are expected to take place.

Chapter 6 A contact model for rough crushable particles

Based on a manuscript to be submitted.

6.1 Introduction

Surface roughness has been recognized as one of the material characteristics that directly affect mechanical behaviors of granular materials. This characteristic can be accurately characterized and quantified by advanced experiment imaging methods such as optical interferometry (Alshibli et al., 2015; Yao et al., 2018), scanning electron microscopy and atomic force microscopy for natural and artificial materials. From the assessment of roughness values, its effect on specific particle properties and thus on mechanical responses can be identified. Otsubo et al., (2015) showed that surface roughness can cause a significant reduction in stiffness, particularly at lower confining stresses. Nardelli & Coop (2018) demonstrated that particle roughness strongly affects the variability of inter-particle friction and the elastic behavior at low stress levels. These findings indicate that including particle surface roughness may be important for numerical analyses of granular materials, particularly if performed through discrete models. Modifying a contact model in DEM to include roughness effects may be thus an important step to achieve a more complete representation of soil behavior (Nadimi et al., 2019a).

Including roughness in the contact model may also help to solve another problem. According to Otsubo et al., (2015), to consider roughness effect in DEM simulations may serve as a solution to achieve a more realistic calibration of contact stiffness. The most common approach for calibration of contact stiffness has been to assign a value such that the grains are rigid enough to limit particle overlaps, (as excessive particle overlap quickly leads to unphysical results Masin, 2012), but not too rigid so as to excessively penalize the timestep (which decreases with increasing particle stiffness, Otsubo et al., 2017b). It is difficult to choose parameter values balancing those two contradictory requirements, and those that are chosen appear sometimes to have little physical basis. For instance, when a Hertz-Mindlin description of contact is used (see section 6.2.1) the normal stiffness is dependent on the shear modulus of the material, G. For quartz well accepted estimates of this property range from 27.9 GPa to 32.3 GPa (https://www.azom.com/properties.aspx?ArticleID=1114). However values used in DEM models of quartz sand are frequently smaller (see Table 6-1).

Table 6-1 *G*-values for quartz sand using Hertz-Mindlin contact model in DEM simulations

Examples	Poganski et al. (2017)	Zhang & Wang (2015)	Ciantia et al. (2019)	Huang et al. (2014)	Hanley et al. (2015)
G / GPa	0.3	1	9	29	29

This difficulty in selecting appropriate values of particle elastic stiffness is increased when particle breakage is also modeled, (Ciantia et al., 2014, 2015). Particle breakage plays a fundamental role in some geotechnical applications, e.g. driven piles (Zhang et al., 2013; Yang et al., 2014), cone penetration test (CPT) and standard penetration test (SPT). Generally speaking, a correct bulk reproduction of soil behavior in the crushing regime requires the correct representation of single particle breakage mechanisms (Ciantia et al., 2019b) which are known to be dominated by the characteristic strength of the particle that, in turn, it is size dependent (Weibull, 1939). Hence, most numerical research on this topic focusses on the limit strength of the particle only while little attention has been placed on the particle deformation required to reach this point. The effect was noted in a later study (Ciantia et al., 2019a) as shown in Figure 6-1, where a discrepancy in the unloading phase between experimental data and DEM simulations was observed. This may be a result of using unreasonable contact parameters.

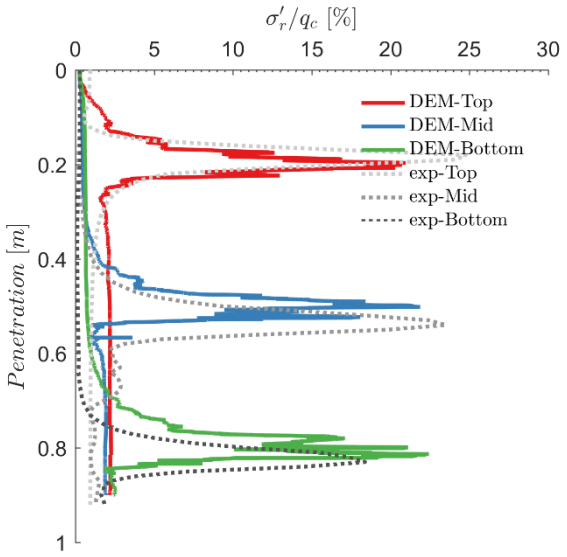

Figure 6-1 Discrepancy between experimental data and DEM simulation caused by using unreasonable contact parameters (Ciantia et al., 2019a)

A possible way out of these difficulties is explored here. By incorporating roughness in a contact model description the use of more realistic values of contact stiffness is possible, without losing the ability to obtain a good reproduction of high stress phenomena dominated by breakage.

In the following sections we first describe how a contact model including particle surface roughness for crushable particles is established. Contact model parameters are then recalibrated for a discrete analogue of a representative quartz sand and some simulations results obtained to validate the new model are presented and discussed.

6.2 Contact model for rough crushable particles

6.2.1 Model description

A rough contact model for crushable particles is introduced in detail in this section.

6.2.1.1 Implementation of surface roughness

For a standard Hertzian contact model, the normal force-displacement relationship for a smooth contact between two spheres is given as

$$F_n = \frac{4}{3} E' \sqrt{r'} \delta^{1.5} \qquad \text{Eq. 6-1}$$

where, F_n is the normal contact force, δ is the contact overlap and E' and r' are given by

$$E' = \left(\frac{1-\nu_1^2}{E_1} + \frac{1-\nu_2^2}{E_2} \right)^{-1} \qquad \text{Eq. 6-2}$$

$$r' = \left(\frac{1}{r_1} + \frac{1}{r_2} \right)^{-1} \qquad \text{Eq. 6-3}$$

The subscripts '1' and '2' refer to the two contacting particles. E_i, ν_i and r_i are the Young's modulus, the Poisson's ratio and the radius of particle i, respectively. The normal stiffness can be obtained by differentiating F_n with respect to δ from Eq. 6-1, hence

$$k_n = \left(6E'^2 r' F_n \right)^{1/3} \qquad \text{Eq. 6-4}$$

Inspired by Greenwood & Tripp (1967), Otsubo et al., (2017a) proposed a three-stage F_n-δ relationship for rough contact (Figure 6-2). Surface roughness S_q is used to reflect asperities on real particle surfaces.

It is defined as the root mean square of Z_i, which is the elevation of data point j relative to the reference surface

$$S_q = \sqrt{\frac{1}{n}\sum_{j=1}^{n}\left(Z_j^2\right)} \qquad \text{Eq. 6-5}$$

Where n is the number of measured data points.

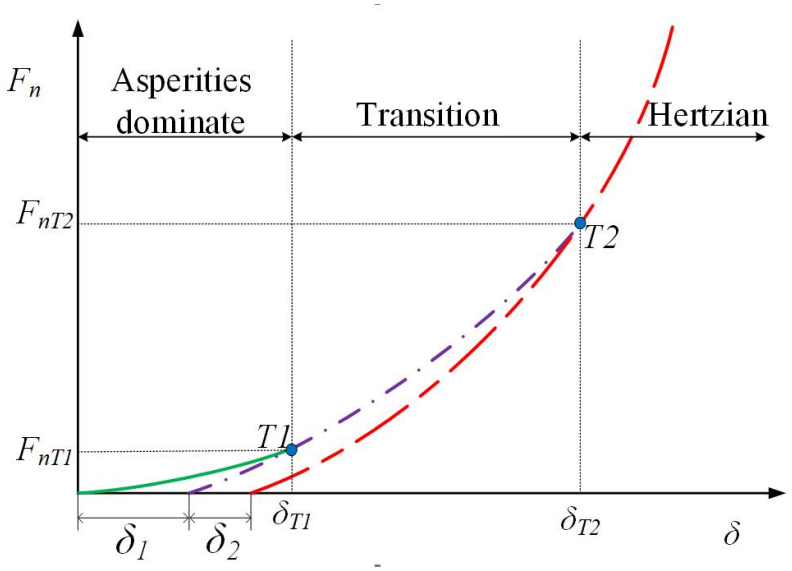

Figure 6-2 Schematic illustration of rough surface contact model

When

$$F_n < F_{nT1} = S_q E' \sqrt{2r' S_q} \qquad \text{Eq. 6-6}$$

asperities dominate the F_n-δ relationship and the contact is softer than when

$$F_n > F_{nT2} = 100 F_{nT1} \qquad \text{Eq. 6-7}$$

that is the threshold force above which the contact starts to behave in agreement with the standard Hertzian model. Thus, the F_n-δ relationship is thus described by three expressions, corresponding to three successive contact regimes: asperity-dominated, Eq. 6-8, transitional, Eq. 6-9 and Hertzian, Eq. 6-10.

$$F_n = F_{nT1}\left(\frac{\delta}{\delta_{T1}}\right)^c \qquad \delta \le \delta_{T1} \qquad \text{Eq. 6-8}$$

$$F_n = F_{nT2}\left(\frac{\delta-\delta_1}{\delta_{T2}-\delta_1}\right)^b \qquad \delta_{T1} < \delta < \delta_{T2} \qquad \text{Eq. 6-9}$$

$$F_n = \frac{4}{3}E'\sqrt{r'}\left(\delta-\delta_1-\delta_2\right)^{1.5} \qquad \delta_{T2} \le \delta \qquad \text{Eq. 6-10}$$

δ_{T1} and δ_{T2} are threshold contact displacements that correspond to contact forces equal to F_{nT1} and F_{nT2} respectively. b and c are constants that ensure slope continuity for the overall F_n-δ relation and depend only on two model parameters δ_1 and δ_2. The values of δ_1 and δ_2 are plastic residual contact displacements obtained if unloading from the transitional and Hertzian regime, respectively. They are both function of S_q and are expressed as:

$$\delta_1 = n_1 S_q \qquad \text{Eq. 6-11}$$

and

$$\delta_2 = n_2 S_q \qquad \text{Eq. 6-12}$$

Where n_1 and n_2 are model parameters. When S_q =0, the standard Hertzian theory is recovered.

The threshold displacements δ_{T1} and δ_{T2} are given by

$$\delta_{T2} = \left(\frac{3F_{nT2}}{4E'\sqrt{r'}}\right)^{2/3} + \delta_1 + \delta_2 \qquad \text{Eq. 6-13}$$

$$\delta_{T1} = \left(\frac{F_{nT1}}{F_{nT2}}\right)^{1/b}(\delta_{T2}-\delta_1) + \delta_1 \qquad \text{Eq. 6-14}$$

The constants b and c can be obtained

$$b = 1.5 * \left(1 + \frac{\delta_2}{\delta_{T2}-\delta_1-\delta_2}\right) \qquad \text{Eq. 6-15}$$

$$c = 100 b \delta_{T1} \frac{\left(\delta_{T1} - \delta_1\right)^{b-1}}{\left(\delta_{T2} - \delta_1\right)^{b}} \qquad \text{Eq. 6-16}$$

From Eq. 6-8, Eq. 6-9 and Eq. 6-10, the contact overlap at a given F_n can be obtained

$$\delta = \left(\frac{F_n}{F_{nT1}}\right)^{\frac{1}{c}} \delta_{T1} \qquad F_n < F_{nT1} \qquad \text{Eq. 6-17}$$

$$\delta = \left(\frac{F_n}{F_{nT2}}\right)^{\frac{1}{b}} (\delta_{T2} - \delta_1) + \delta_1 \qquad F_{nT1} \le F_n < F_{nT2} \qquad \text{Eq. 6-18}$$

$$\delta = \left(\frac{9F_n^2}{16E'^2 r'}\right)^{\frac{1}{3}} + \delta_1 + \delta_2 \qquad F_{nT2} \le F_n \qquad \text{Eq. 6-19}$$

Normal contact stiffness can be obtained by differentiating F_N with respect to δ

$$k_n = \frac{cF_{nT1}}{\delta_{T1}^{\ c}} \delta^{c-1} \qquad \delta < \delta_{T1} \qquad \text{Eq. 6-20}$$

$$k_n = \frac{F_{nT2} b \left(\delta - \delta_1\right)^{b-1}}{(\delta_{T2} - \delta_1)^{b}} \qquad \delta_{T1} \le \delta < \delta_{T2} \qquad \text{Eq. 6-21}$$

$$k_n = 2E' \sqrt{r'(\delta - \delta_1 - \delta_2)} \qquad \delta_{T2} \le \delta \qquad \text{Eq. 6-22}$$

The shear stiffness is taken as (Otsubo et al., 2015)

$$k_s = \frac{2(1-v)}{2-v} k_n \qquad \text{Eq. 6-23}$$

6.2.1.2 Crushing criterion

Particle crushing imposes a limit to the contact normal force acting on a particle. Following Ciantia et al., (2015), such limit can be expressed as:

$$F_n \le \sigma_{\lim} A_F \qquad \text{Eq. 6-24}$$

where σ_{lim} is the limit strength of the particle and A_F the contact area. Expressing the failure criteria in this way allows for a clear separation of the effects of particle strength (σ_{lim}) and, through contact area, (A_F) of particle stiffness.

- Particle strength, σ_{lim}:

  To incorporate the material strength natural variability into the model, the limit strength, σ_{lim}, for a given sphere diameter follows a normal distribution. The coefficient of variation of this distribution, '*var*', is a material parameter and is assumed particle-size independent. On the other hand, to take into account that smaller particles are stronger, size effects on particle strength are incorporated following McDowell & De Bono, (2013)

$$\sigma_{\lim} = \sigma_{\lim,0}\left(\frac{d}{d_0}\right)^{-3/m} \qquad \text{Eq. 6-25}$$

  where, m is a material parameter and $\sigma_{lim,0}$ is the mean limit strength at d_0 is the reference diameter (chosen as 2 mm).

- Contact area, A_F:

  The expression for contact area A_F is given by Otsubo et al., (2017a) as:

$$A_F = \pi r_H^2 = \pi r'\delta \qquad \text{Eq. 6-26}$$

  Where the contact overlap, δ, can be obtained from Eq. 6-8, Eq. 6-9, and Eq. 6-10. Stiffness will affect the way A_F evolves with F_n since, for a given contact force the contact area will be larger or smaller depending on the particle stiffness (slope of the F_n-δ curve).

It is possible to express the particle failure criteria using Eq. 6-24 as:

$$F_n \le \sigma_{\lim,0} f(\text{var})\left(\frac{d}{d_0}\right)^{-3/m} \pi r' \left(\frac{F_n}{S_q E'\sqrt{2r'S_q}}\right)^{\frac{1}{c}} \left\{\left(\frac{1}{100}\right)^{1/b}\left[\left(\frac{300 S_q E'\sqrt{2r'S_q}}{4E'\sqrt{r'}}\right)^{2/3} + n_2 S_q\right] + n_1 S_q\right\}$$

$$F_n < F_{nT1} \qquad \text{Eq. 6-27}$$

$$F_n \le \sigma_{\lim,0} f(\text{var})\left(\frac{d}{d_0}\right)^{-3/m} \pi r' \left\{\left(\frac{F_n}{100 S_q E'\sqrt{2r'S_q}}\right)^{\frac{1}{b}}\left[\left(\frac{300 S_q E'\sqrt{2r'S_q}}{4E'\sqrt{r'}}\right)^{2/3} + n_2 S_q\right] + n_1 S_q\right\}$$

$$F_{nT1} \le F_n < F_{nT2} \qquad \text{Eq. 6-28}$$

$$F_n \le \sigma_{\lim,0} f(\text{var}) \left(\frac{d}{d_0}\right)^{-3/m} \pi r' \left[\left(\frac{9F_n^2}{16E'^2 r'} \right)^{\frac{1}{3}} + n_1 S_q + n_2 S_q \right]$$

$$F_{nT2} \le F_n \qquad \text{Eq. 6-29}$$

Other aspects of the particle breakage model remain identical to those presented by Ciantia et al., (2015). Once a limit condition is reached, a particle splits into 14 smaller inscribed tangent spheres. The spawned fragments inherit the velocity and material parameters of the original particle apart from the intrinsic strength σ_{lim} that is randomly sampled from the distribution new size. A fraction of the broken particle volume is lost upon breakage, it is assumed that the material lost corresponds to fines that are accounted for in the determination of the material grading. As the number of fragments spawned in a breakage event increases, the amount of volume lost at each breakage reduces, but the computational cost increases. A numerically motivated comminution limit, d_c, is imposed to stop crushing of smaller particles. Grading state index I_G, introduced by Muir Wood (2007) to quantify grading by means of a scalar quantity Figure 6-3, is computed as the area ratio of the current grading to a limit grading. The limit grading is given by a fractal distribution with a fractal dimension α=2.6; this distribution can be expressed as (Einav, 2007)

$$\frac{M_{(L<d)}}{M_T} = \frac{d^{3-\alpha} - d_{\min}^{3-\alpha}}{d_{\max}^{3-\alpha} - d_{\min}^{3-\alpha}} \qquad \text{Eq. 6-30}$$

where, M_T is the total mass of the sample, $M_{(L<d)}$ is the mass of particles smaller than d, d_{max} and d_{min} are, respectively, the maximum and minimum particle sizes assumed for the limit distribution. The same limit distribution formula, but now with d_{max} given by the smallest particle created during the crushing event, is used during post-processing to assign a size distribution to the volume lost at each crushing event.

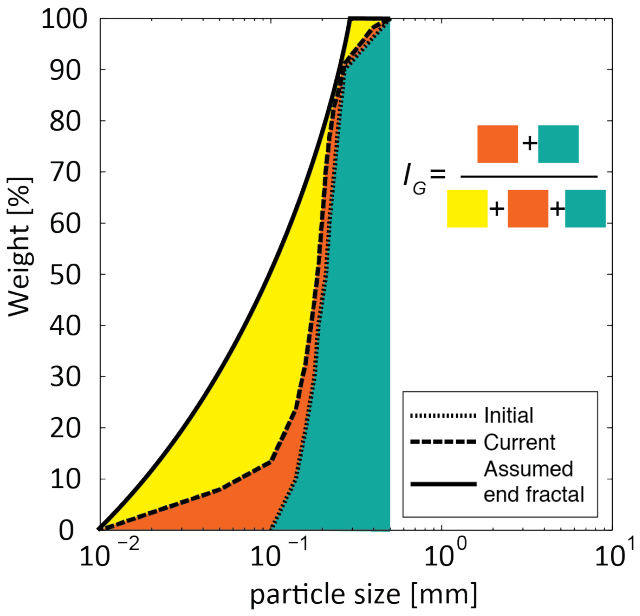

Figure 6-3 Grading index I_G definition

6.2.2 Numerical implementation

The newly proposed contact model for rough particles was implemented in PFC (Itasca, 2017) within a C++ coded user defined contact model (UDCM). Also, the failure criteria corresponding to the three contact regimes were compiled into the same UDCM, (instead of using FISH algorithms as done in previous work -Ciantia et al., 2015). The main difference between the FISH and UDCM crushing algorithms schemes is that a time-consuming loop through all the contacts is required in the FISH implementation, but not in the UDCM. In fact, in PFC5, during the execution of force-displacement law, there is a loop over all the contacts, regardless of the type of selected contact model. During one step, the UDCM collects the information of particles that meet the crushing criterion into a signal. The signal is then emitted to call another FISH function that performs the 14-ball replacement for these particles. Using the smooth contact model, Ciantia et al. (2017) presented the computational efficiency gains derived from using the UDCM to detect particle breakage (see detail in Appendix I).

6.2.3 Validation

To validate the correct implementation of the rough contact crushable model, the analytical expressions for ball-ball contact and ball-wall contact forces were independently evaluated in MATLAB for some elementary configurations (see detail in Appendix III) and the results compared with those obtained UDCM. The results obtained are illustrated in Figure 6-4 and the parameters adopted for this checks are listed in Table 6-2. Two tests are considered: the compression of two identical spheres and the

compression of a sphere between two rigid walls. In the figure F_1, F_2 and F_3 represent contact forces in asperity-dominated, transition and Hertzian regimes, respectively. A good agreement can be seen for the results of both model evaluations. The line labelled S_q=0, corresponding to a Hertzian smooth contact model with crushing inhibited, is included for reference. As expected, the representation of surface roughness in the contact model results in larger contact overlap than the smooth model. The difference increases with the value of F.

Table 6-2 Parameters for UDCM validation

Parameters	d / mm	G /GPa	v	φ	m	$\sigma_{lim,0}$ /GPa	S_q/μm	n_1	n_2
Values	2	32	0.2	0.275	7.5	3	1.0	1	2

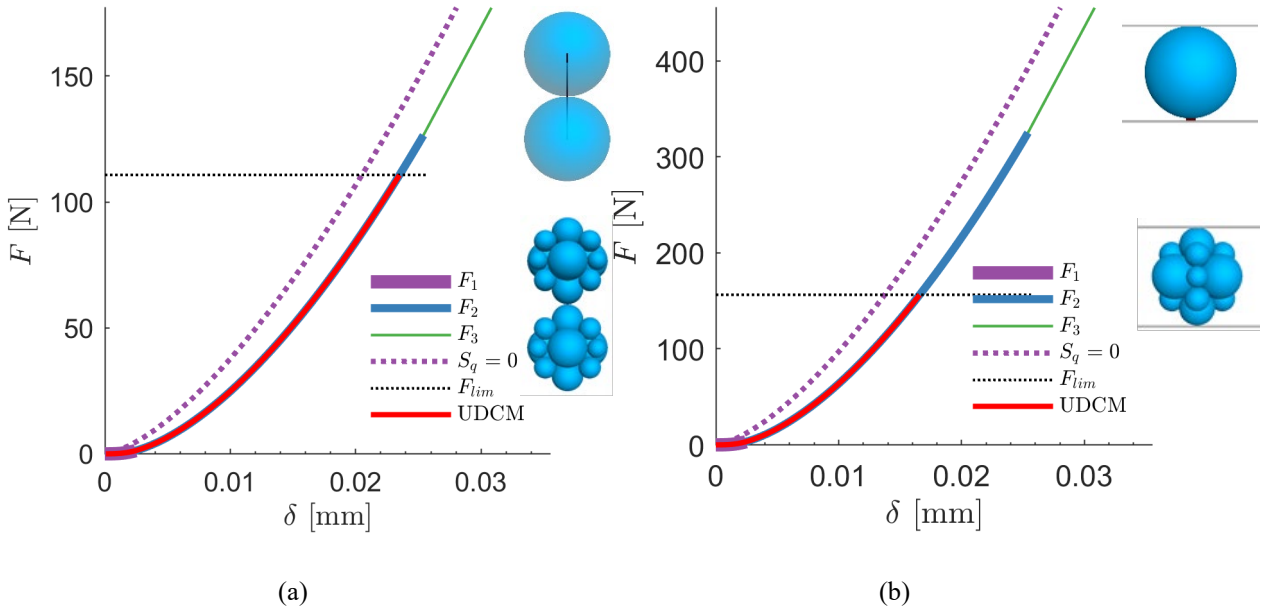

(a) (b)

Figure 6-4 Simple model testing: (a) ball-ball contact, (b) ball-wall contact.

6.3 Effect of contact roughness on single particle breakage

Introduction of roughness does not only result in a modified normal contact stiffness. Through their effect on contact area, the three new parameters (i.e. surface roughness S_q, and coefficients n_1 and n_2) will also modify the onset of particle breakage. A series of parametric analyses simulating single-particle crushing tests were performed to investigate this coupling. The simulation mimics particle crushing between steel plates, which is a classical experimental configuration for this kind of study. To

do so the moduli of steel ($G = 320$ GPa, $\nu = 0.2$) are used in Eq. 6-2 and, following Eq. 6-3, $r'=r_1$ in Eqs. 6-27, 6-28 and 6-29.

Table 6-3 Parameter variants for parametric study of single particle crushing test (Figure 6-5)

Tests	S_q /μm	n_1	n_2
Base	1.0	1.0	2.0
S_q_0.0	0.0	1.0	2.0
S_q_2.0	2.0	1.0	2.0
S_q_3.0	3.0	1.0	2.0
n_1_0.0	1.0	0.0	2.0
n_1_0.5	1.0	0.5	2.0
n_1_2.0	1.0	2.0	2.0
n_2_0.0	1.0	1.0	0.0
n_2_0.5	1.0	1.0	0.5
n_2_2.0	1.0	1.0	2.0

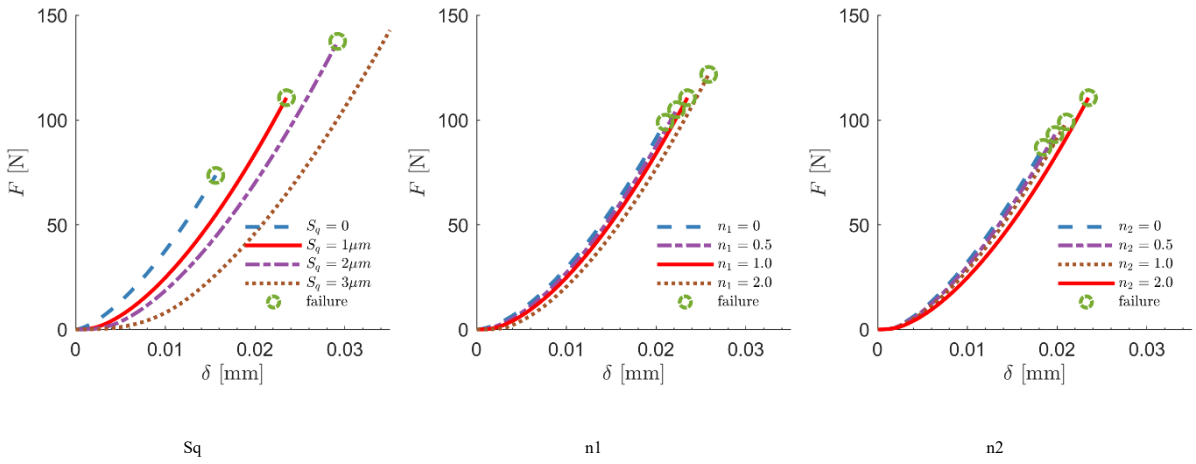

Figure 6-5 Parametric study over three new parameters (S_q, n_1, and n_2) in the crushing model

The reference parameter set used for this study is reported in Table 6-2, and the parameter variants considered in the analyses are reported in Table 6-3. The solid thick line illustrated in each subplot of Figure 6-5 represents the result of the reference parameter set. Increasing either roughness or the n_i ratios results in less stiff contact behaviour and increased pre-failure forces. Larger forces are required to crush rough particles, since, for given force, a more compliant contact results in larger particle overlaps and contact areas. The curves end when the particles fail, as the model does not intend to represent post-peak particle failure behaviour.

Resulting from a second parametric study (Figure 6-6) explore the effects of a larger range of S_q, n_1 and n_2 on the limiting crushing force F_{lim}. The study uses the analytical expression of the limiting force (Eqs. 6-27, 6-28 and 6-29) to obtain several relevant results for each parameter combination, namely

1. The values of forces F_{NT1} and F_{NT2} that mark the frontier between the asperity dominated, transitional and Hertzian contact regimes
2. Limiting forces evaluated according to each one of the three critical force expressions, Eqs. 6-27, 6-28 and 6-29, for the different contact regimes respectively named as F_{lim1}, F_{lim2} and F_{lim3}
3. The actual F_{lim} envelope, resulting from F_{lim1}, F_{lim2} and F_{lim3} for their corresponding contact regimes, respectively, on which the F_{lim} of the reference set is marked

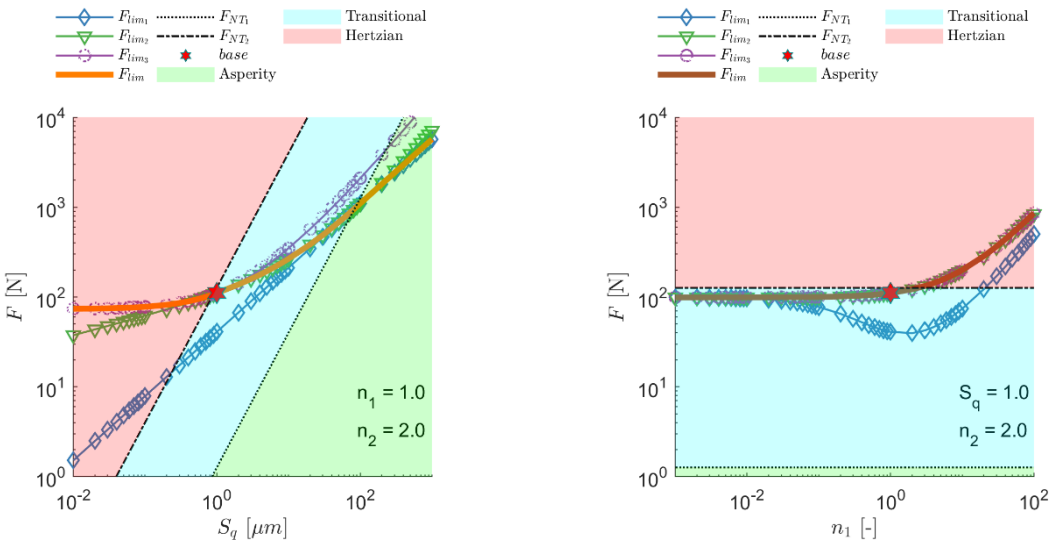

(a) (b)

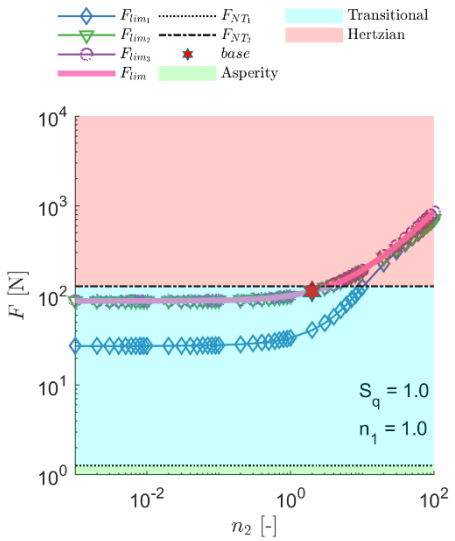

(c)

Figure 6-6 Parametric study over wide ranges of the new variables (S_q, n_1, and n_2). Other parameters as in the base parameter set in Table 6-3

The figures reflect how the frontiers between different particle crushing regimes depend only on roughness but not on parameters n_1 and n_2. Generally speaking, the effect of those two parameters is relatively modest, not affecting the ultimate force F_{lim} until they reach rather high values –i.e. values that would imply residual plastic normal displacements (δ_1, δ_2) much larger than roughness itself. The effect of roughness S_q is more significant. The results indicate that for relatively small roughness values, (say for $S_q < 0.1\ \mu m$), the crushing force F_{lim} is independent of roughness and failure takes place in the Hertzian regime. As roughness increases the crushing force F_{lim} increases significantly and failure takes place in the transition regime or even (for $S_q > 20\ \mu m$) in the asperity-dominated contact regime.

The previous study varied roughness while maintaining a constant particle diameter of 2 mm, -at the upper limit of what may be conventionally described as sand (ISO 14688-1, 2017). It is interesting to explore the effect of varying particle diameter while maintaining roughness constant. That is done in Figure 6-7 for a particle diameter range that goes from fine sands (0.1 mm) to medium gravels (10 mm). Roughness and other parameters have been kept constant, as listed in Table 6-2. For the particles without roughness ($S_q = 0$), failure takes place in the transition regime. With the increase of particle size, the limiting force increases and is approaching but not crossing the boundary between the transition and the Hertzian contact regimes (Figure 6-7a). The tendency of nominal tensile strength (limiting force of one particle divided by the cross sectional area of the particle) with particle size is identical to the common experimental observations that smaller particles are stronger than larger ones in particle strength (Figure 6-7b). Affected by the inclusion of roughness, the limiting force and strength increase, and that effect is nearly independent of particle size. Therefore, the curves with roughness ($S_q > 0$) are

simply an upward translation of the curves without roughness ($S_q = 0$). The failure of larger particles starts to take place above the Hertzian contact limit.

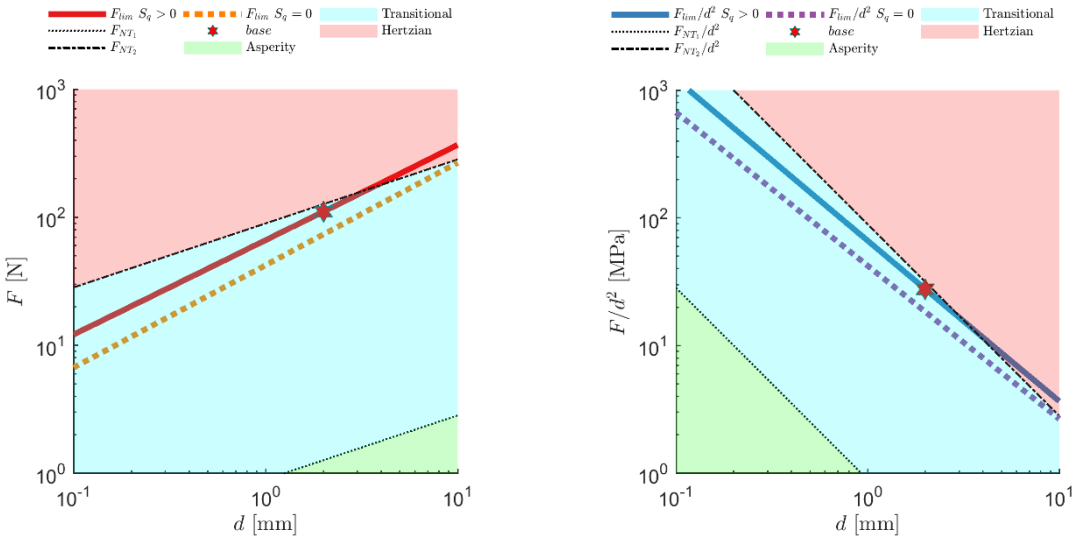

(a) (b)

Figure 6-7 Effect of contact roughness on size dependency of (a) particle breakage force (b) nominal tensile strength. Model evaluated for the base parameter set in Table 6-3

6.4 Recalibration of Fontainebleau sand

A recent study presented by Ciantia et al., (2019) describes the effect of grain crushing on the position of critical state line of a silica sand, e.g. Fontainebleau sand. The original Ciantia et al., (2015) crushing model was used in the study. The model parameters for the sand were calibrated through the efforts of reproducing a series of simple tests, including an oedometer test with a maximum applied vertical stress of 100 MPa. Three additional oedometer test with maximum stresses of 25 MPa, 50 MPa and 75 MPa were also performed. In DEM model, the oedometer tests were complemented in a 4 mm sided cube wade of frictionless rigid walls filling with 10,000 particles. The cube consisted of spherical particles with diameters ranging from 0.1 to 0.4 mm matching the PSD of Fontainebleau NE34 sand. The calibrated parameters are recalled in Table 6-4 as 'old' set. Using these parameters, the results of oedometer tests, e.g. loading-unloading response and corresponding I_G evolution were obtained (Figure 6-8a, b).

Although roughness was not considered in the study, the capacity of the DEM crushing model to successfully reproduce the loading response and I_G evolution were demonstrated. However, certain inaccuracies of the model responses should not be ignored, particularly the unloading curves, which

were indicated far too much elastic rebound. The incapability of reproducing the unloading response seems directly linked to the low G employed, as a value G=9 GPa was input. Of course this value has also the inconvenient of being very different from those expected from quartz.

In (Figure 6-8c, d) the same tests are simulated with the same model, but now using a higher –although realistic for quartz- G value (29 GPa). Now the loading-unloading curve match with the experimental data is clearly improved, however, a clear discrepancy is noticed in I_G tracking curve especially in the low-pressure regime. The increase of stiffness causes excessive and fast development of crushing events. This may be avoided if surface roughness is included in the model, according to the findings from the parametric study performed above.

Table 6-4 Calibrated parameters for Fontainebleau sand

Sets	G /GPa	ν	μ	m	$\sigma_{lim,0}$ /GPa	var	d_c/d_{50}	d_{max} /mm	d_{min} /mm	S_q /μm	n_1	n_2
Ciantia model-low G	9	0.2	0.275	10	1.9	0.36	0.55	0.27	0.01	-	-	-
Ciantia model-high G	29	0.2	0.275	10	6	0.36	0.55	0.27	0.01	-	-	-
Rough-crushable model	**32**	**0.19**	0.275	**12**	**3.75**	**0.38**	0.55	0.27	0.01	**0.6**	**0.05**	**5**

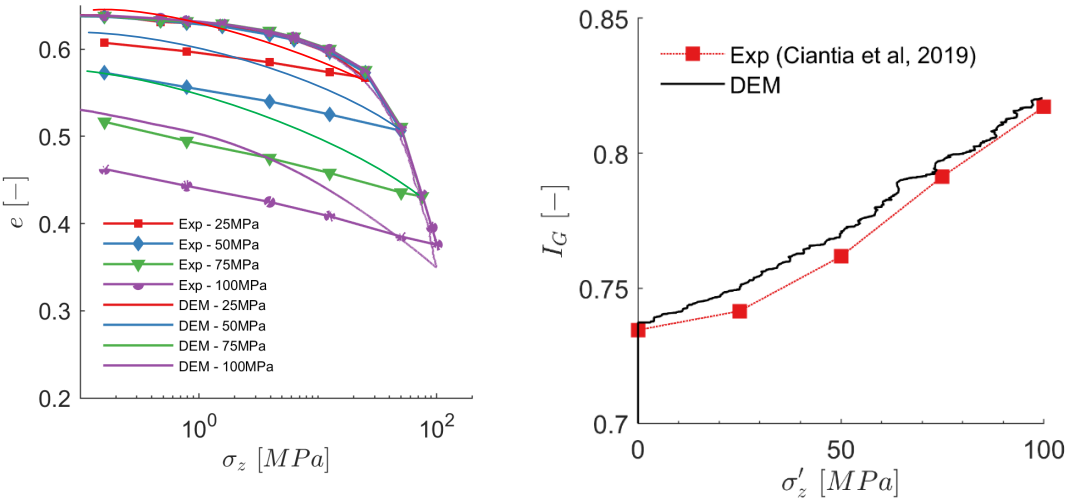

(a) (b)

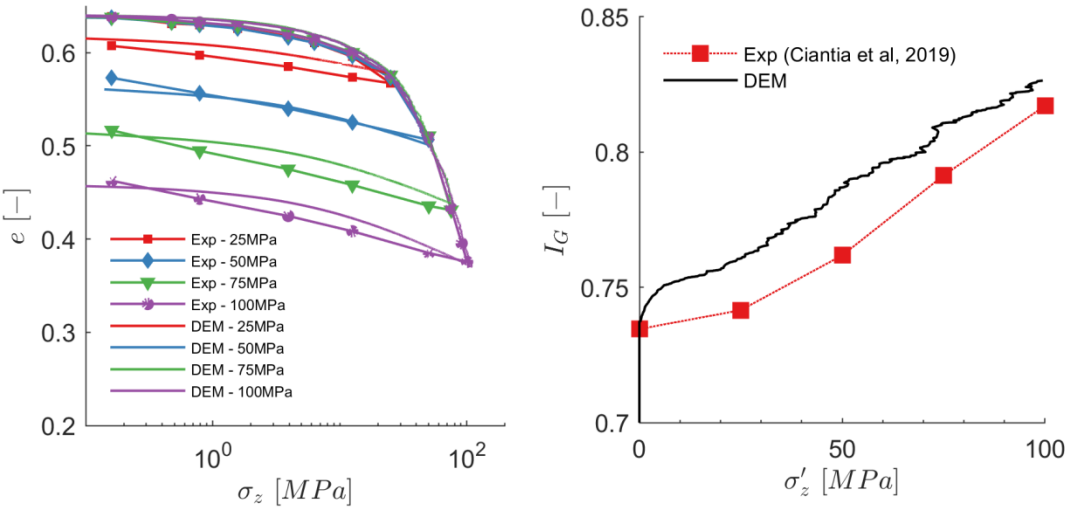

(c) (d)

Figure 6-8 Review of various parameter sets adopted in Fontainebleau sand oedometer test when roughness was not implemented: (a) and (b) for G=9 GPa, (c) and (d) for G=29 GPa

The use of the rough contact crushable model for Fontainebleau sand requires a recalibration of not only the 'old' model parameters (*G, v, μ, var*, *m* and $\sigma_{lim,0}$), but the three new parameters (S_q, n_1 and n_2). Generally, *G, v, μ,* S_q, n_1 and n_2 are contact parameters while *var*, *m* and $\sigma_{lim,0}$ define particle strength. Continuing the idea of using realistic values of *G*, a value of 32 GPa is selected from (https://www.azom.com/properties.aspx?ArticleID=1114) as SiO2 properties. By referring to the property values listed on that website, *v* is taken as 0.19. No more calibration is required for these two parameters. Note that these values would automatically give a good fit to the unload part of the oedometric curve (Figure 6-8c). Particle interface friction coefficient μ has the same value as that in the previous work (Ciantia et al., 2019c). The remaining parameters (S_q, n_1, n_2, $\sigma_{lim,0}$, *var* and *m*) are calibrated in a two phase procedure:

1. S_q is set as 0.6 μm , considered as a realistic roughness value for silica sand, as reported by Yao et al., (2018). As shown by the authors, surface roughness may vary depending on particle size, but the variations are relatively small. Hence, in this study, the S_q value is set as unique for all the particles. n_1 and n_2 are set as 0.05 and 5, respectively, after some tuning to better match the load displacement curve of a single particle test on a silica sand (Figure 6-9).

2. Experimental data on size dependency of flat-platen single particle crushing forces indicates the value of *m* (Figure 6-10a). The curve with the new parameters performs quite similar to the curve with the old parameters. Interestingly the Weibull modulus that best captures the experimental trends is 12. This indicates that scale effects are practically negligible (Figure

6-10b). This dataset also indicates a likely range for $\sigma_{lim,0}$. *var* is calibrated fitting a normal distribution to particle size strength variability as described in (Ciantia et al., 2019c).

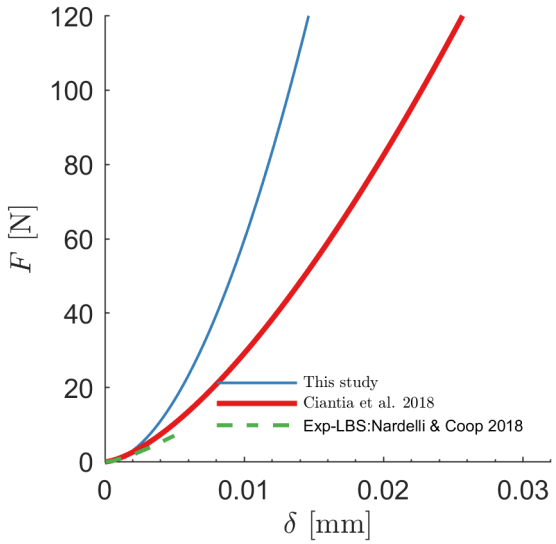

Figure 6-9 Microscale observation of the rough contact model employed

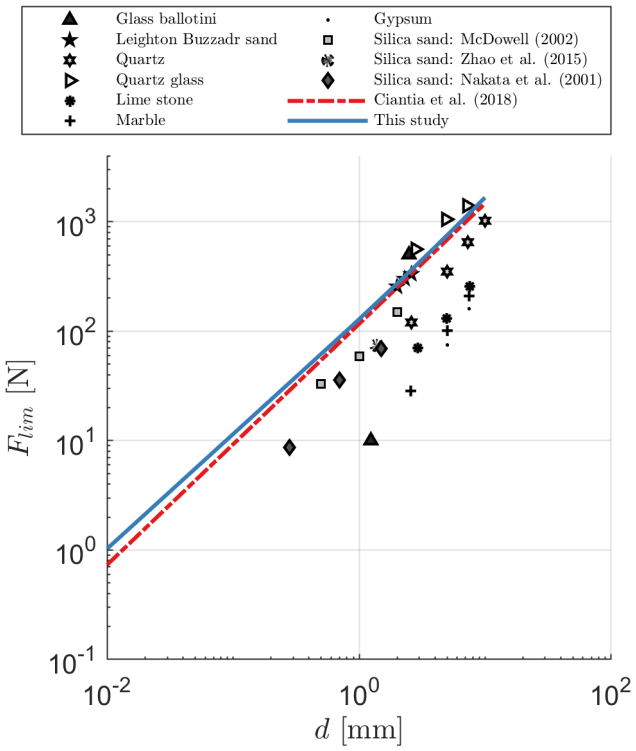

a)

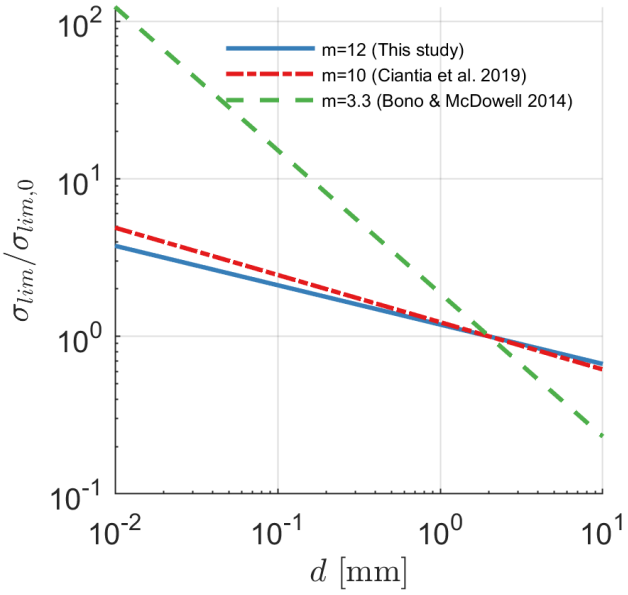

b)

Figure 6-10 a) Calibration of crushing-related parameters of the contact model using flat-platen single-particle crushing test data. b) effect of roughness on 'size effects'

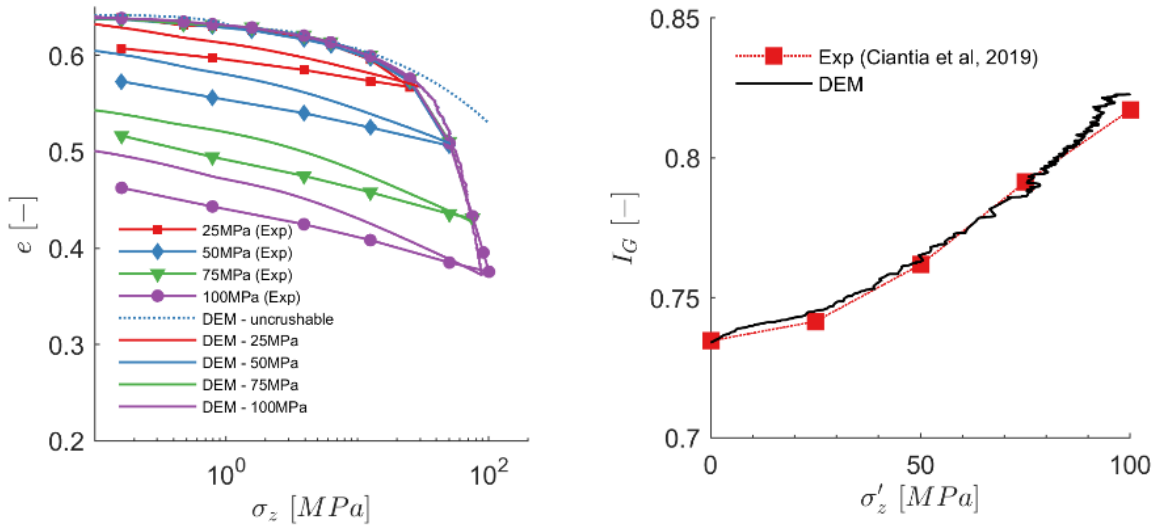

(a) (b)

Figure 6-11 Validation of crushing embedded in rough contact model via DEM simulation of high pressure oedometric compression tests in terms of a) effective vertical stress vs void ratio in loading-unloading and b) grading index evolution

With this estimation of parameters (Table 6-4), the DEM model for rough crushable particles is run to simulate the oedometric compression curve (both loading and unloading). The results are quite satisfactory (Figure 6-11). Clearly, the loading curve and grading evolution as good as those obtained

using the old model with a low G value (Figure 6-8a, b). The unloading curve is now captured almost as well as with the old model with the high G value (Figure 6-8c). The results reveal that the implementation of surface roughness is of great importance in successfully capturing experimental data from a more comprehensive perspective.

6.5 Further validation of the model

The rough crushable model for Fontainebleau sand has been successfully established after demonstrating the capacity of capturing experimental data. A further validation of the model was attempted. Luong & Touati, (1983) reported a series of high-pressure isotropic (σ_r=0.5, 6, 16 and 30 MPa) and triaxial compression tests on dense FS. These tests were also reproduced by Ciantia et al. (2019) using the 'low-G' parameter set with the smooth model.

Equivalent DEM simulations were performed to make comparisons with these tests in terms of mobilized strength and dilatancy with shear strain during these tests (Figure 6-12). In these simulations, the same parameters as in the oedometer test were used. Two sets of DEM simulations are presented: one with crushing prohibited, the other with crushing activated. During shearing, confining pressures were kept constant. Each test simulation continued to a deviatoric strain of 30% at which critical state conditions (i.e. a constant level of mobilized shear strength and void ratio) could be identified from the simulations. When crushing was prohibited, the simulations did not produce much difference for the tests at different confining pressures, leading to that experimental data could not be captured at high pressures. When crushing was activated, the mobilized strength and dilatancy with strain were captured as those in the experiments. The agreement between the simulated and experimental results reveals that the use of the new model is sound.

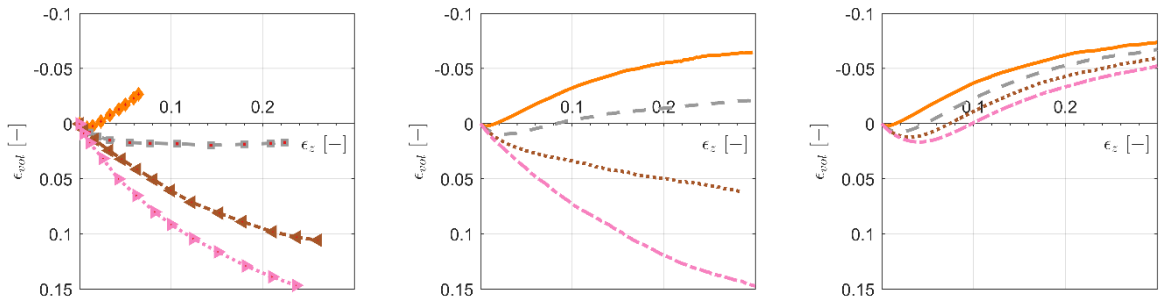

(a) (b) (c)

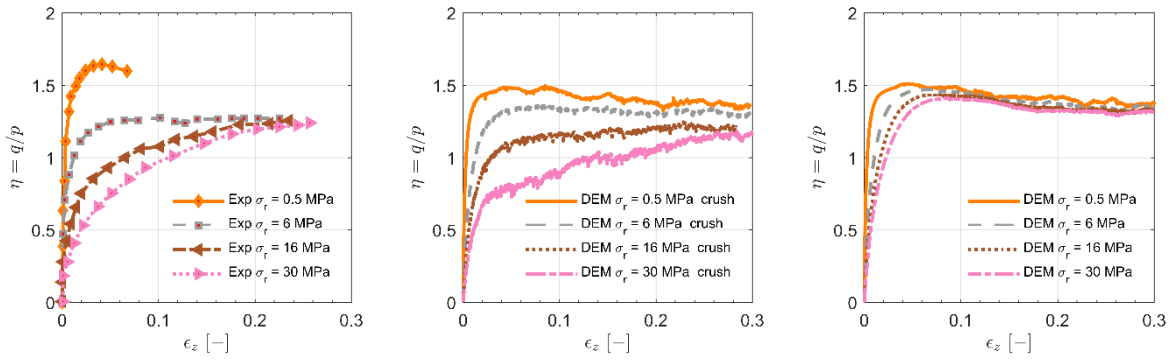

(d) (e) (f)

Figure 6-12 validation of new DEM rough crushing model: high-confinement-pressure drained triaxial compression tests by Luong & Touati, (1983) (a) experimental; (b) rough contact with crushing; (c) numerical without crushing volumetric response; (d) experimental; (e) numerical rough contact with crushing; (f) without crushing stress–strain response

6.6 Summary

This contribution documents the incorporation of particle surface roughness into DEM models for crushable sands. The effect of contact roughness on single particle breakage has been investigated via parametric studies. The model parameters for a discrete analogue of a representative quartz sand have been recalibrated. The main findings are listed as follows:

- The parametric study shows that increasing either roughness or the n_i ratios results in larger crushing forces and less stiff contact behaviour;
- The effect of roughness S_q is more significative than those of the n_i ratios. Generally, for relatively small roughness values, (S_q < 0.1 μm), the crushing force F_{lim} is independent of roughness, while with the increase of roughness (S_q > 0.1 μm) the crushing force F_{lim} increases significantly. The failure takes place in the transition regime or even (for S_q > 20 μm) in the asperity-dominated contact regime;
- The effect of contact roughness on limiting strength does not show much dependency on particle sizes;
- The recalibrated parameters for the rough crushable sand can better reproduce the oedometer test results, particularly in unloading parts. Realistic contact parameters are able to be used.

Chapter 7 Static & dynamic probing of rough breakable sands

7.1 Introduction

In geotechnical engineering, penetration tests have been widely applied to characterize soils, such as estimating soil strength and stiffness and to evaluate soil liquefaction potential. Considering different penetration principles, penetrometers can mainly be divided into two groups: static and dynamic. In static cone penetration test (CPT), a tip with a 60° apex angle is pushed into soil at a constant speed, meanwhile cone tip resistance q_c, sleeve friction resistance f_s and pore water pressure u are recorded. In contrast, dynamic penetration involves driving a device formed by rods or rigid tips into the soil by striking it with a weight. As explained in Chapter 2 there is a great variety of types and characteristics of the dynamic penetrometers including standard penetration test (SPT), Becker penetration test (BPT), dynamic cone penetration test (DCPT), etc.

As stated in section 2.3.4.2 via experimental evidence, grain strength or crushability considerably influences the responses of penetration tests. Typically, explanations of the response of penetration tests in experiments can be sought via various approaches such as analytical models and numerical models (e.g. discrete element method (DEM)). The accuracy of those models of penetration test response will be seriously hindered if particle crushability is ignored.

DEM has been widely used to model grain crushing and has gained wide acceptance partly due to the unique insight it provides in the micro-scale mechanics of granular materials (Zhou et al., 2019). In DEM, particle breakage can usually be considered with two different approaches. One solution is to treat each particle as an agglomerate represented by bonded smaller particles (Cheng et al., 2003; Wang et al., 2017). The other solution is to replace the particles with smaller particles once a predefined crushing criteria is attained (2D, Lobo-Guerrero & Vallejo, 2005; 3D, Ciantia et al., 2015). The second method is more computationally efficient, and therefore better adapted to field-scale applications. Lobo-Guerrero & Vallejo, (2005) considered pile installation (in 2D) into breakable grains. The shape effect of driven pile or penetrometer on penetration resistance and particle crushing was later studied by Lobo-Guerrero & Vallejo, (2007). Falagush et al., (2015) studied the effect of particle shape and crushing on CPT tip resistance. They showed that there was a considerable reduction in the tip resistance for

crushing model compared with an uncrushable model, and this reduction increased with confining stress. Ciantia et al., 2016b) built a three-dimensional DEM-based model to investigate the effect of grain crushing on the tip resistance of CPT. The granular material used in their study was pumice sand, a double-porosity crushable volcanic material. A good agreement with physical tests was obtained.

As shown previously (Chapter 6), surface roughness has an influence on particle crushability. Grain surface roughness is a physical property of granular materials which can be measured by some advanced experiment imaging methods such as optical interferometry, scanning electron microscopy and atomic force microscopy. Hence, it is interesting to investigate the mechanical response of penetration tests (static and dynamic) in crushable sands considering roughness.

The work in this chapter builds on related achievements presented in previous chapters/sections. In Chapter 4, the capabilities of DEM approach to model SPT in uncrushable sands have been demonstrated. To continue, energy balance analysis during the SPT has been carried out in Chapter 5. Later in Chapter 6, a contact model for rough crushable sand material has been proposed and validated. Therefore, further explorations are required for penetration tests in more complicated and realistic sand materials (rough, crushable).

In this chapter, the effect of particle crushability and roughness on both static and dynamic penetration test results are investigated. The chapter is organized as follows. First, the procedures of building virtual calibration chambers (VCCs) filled with either smooth or rough sand analogue of Fontainebleau sand are described. A series of static and dynamic tests are then carried out in the VCCs at low and high confining pressures. Particle crushability is considered as a variable in the tests. The effect of particle-scale properties on the relation between static and dynamic penetration are examined.

7.2 Model description

7.2.1 Model construction

Static and dynamic penetration tests were performed in 3-dimensional virtual calibration chamber (VCC) models. The construction of VCC models followed the same procedure and geometrical details described in Chapter 4 as shown in Figure 7-1. Discrete elements filling up the chamber represents an analogue of Fontainebleau sand particles.

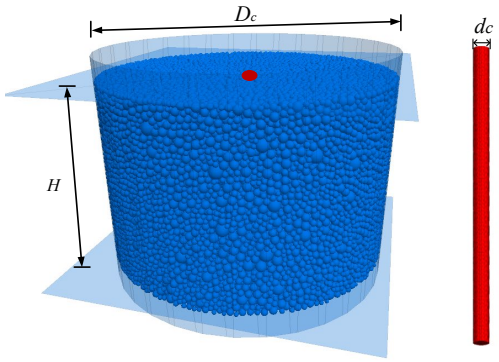

Variable (unit)	Symbol	DEM
Chamber diameter (mm)	D_c	760
Rod outside diameter (mm)	d_c	50.8
Chamber height (mm)	H	500
Scaling factor	-	79
mean element size (mm)	D_{50}	16.6
Chamber/rod diameter ratio	D_c / d_c=R_d	15
Rod/particle ratio	d_c / D_{50}=n_p	3.06

Figure 7-1 View and geometrical characteristics of virtual calibration chamber and rod

As stated in Chapter 6, the consideration of particle surface roughness in smooth contact model presents several advantages: (1) it is more realistic as particle surfaces are not smooth; (2) it facilitates a successful reproduction of both loading and unloading behavior of oedometer tests with FS and (3) more realistic values of model properties can be used.

Table 7-1 Calibrated model parameters for Fontainebleau sand: smooth and rough contact

Contact model	G /GPa	ν	μ	m	$\sigma_{lim,0}$ /GPa	var	d_c/d_{50}	d_{max}/ mm	d_{min}/ mm	S_q /μm	n_1	n_2
Smooth	9	0.2	0.275	10	1.9	0.36	0.55	0.27	0.01	0	0	0
Rough	**32**	**0.19**	0.275	**12**	**3.75**	**0.38**	0.55	0.27	0.01	**0.6**	**0.05**	**5**

Two sets of contact parameters representing a Hertzian (smooth) contact model and a rough contact model were employed for the discrete elements, respectively (Table 7-1). Note that the differences between the two models lie in shear modulus G, roughness S_q, particle intrinsic strength $\sigma_{lim,0}$, etc. The initial void ratio for all tests was 0.62, equivalent to a relative density of 74% for Fontainebleau sand. A total number of 82568 particles were generated to fill up the chamber. As explained in chapter 6 both sets of parameters are able to reproduce well the same oedometric loading curve as well as the triaxial shearing results, but the rough contact model improves the reproduction of the unloading branches.

7.2.2 Simulation program

Table 7-2 lists the specimens examined in this study by combining isotropic confining pressure P_0, contact model and crushability mechanism. In detail, relatively low (100 kPa) and high (400 kPa) isotropic confining pressures, respectively referred to in what follows by the shorthand '1.0' and '4.0',

were used to confine the specimens. Test are performed using both the smooth and the rough contact model; these are shorted as 'S' and 'R', respectively, in the names of specimens. Crushing was also enabled and disabled, respectively, in various specimens. In the sample ID name, 'nocru' indicates that crushing was disabled, whereas 'cru' means particles will break if the crushing criteria is met.

During the construction state, the pressures were maintained constant via servo control mechanism in all walls. During rod penetration, a slight change was made by fixing the bottom horizontal boundary. A specimen filled with particles using smooth contact parameters was initially built. The target void ratio was attained at 5 kPa isotropic compression after a certain number of cycles. Then another specimen with rough contacts was generated from the smooth specimen by simply replacing the smooth contact parameters with rough contact parameters. After the replacement, a number of cycles were applied to reach again an equilibrated state

Table 7-2 Simulation programs of DEM-based penetration tests

Sample ID	P_0 / 100 kPa	Contact model	Crushable
1.0_S_nocru	1.0	Smooth	No
1.0_S_cru	1.0	Smooth	Yes
1.0_R_nocru	1.0	Rough	No
1.0_R_cru	1.0	Rough	Yes
4.0_S_nocru	4.0	Smooth	No
4.0_S_cru	4.0	Smooth	Yes
4.0_R_nocru	4.0	Rough	No
4.0_R_cru	4.0	Rough	Yes

Both static and dynamic tests were scheduled to take place in each sample listed in Table 7-2. Geometrically, the CPT cone tip is different from the SPT split-spoon hollow sampler and so the penetration mechanics are necessarily distinct. Both static CPT and dynamic SPT are assumed to have the same close-ended flat tip for a more direct comparison. Static penetration was realized by pushing the rod at a constant rate of 40 cm/s. To avoid the distortions introduced by the fixed rigid bottom boundary, (i.e. the tip resistance becomes very high as approaching the bottom), the rod was pushed to a depth of 40 cm, instead of 50 cm which is the height of the chamber. On the other hand, dynamic penetration followed the same procedure described in Chapter 4, where a prescribed impact force was applied directly on the driven rod after this had been statically advanced to 15 cm depth.

7.3 Static penetration tests

7.3.1 Tip penetration resistances

The main result of interest in static penetration are the values of tip resistance. Raw penetrograms are obtained by plotting tip resistance against penetration depth, where different levels of noise can be observed. The noise is mainly affected by the ratio of cone to mean particle size n_p on the simulations (Arroyo et al., 2011). Generally, a low n_p value increases the noise of raw penetrograms, which become very jagged. The noise can be filtered out by fitting the raw penetration curves with the following equation:

$$q_e(h_p) = A\left[1 - \exp\left(-Bh_p\right)\right] \qquad \text{Eq. 7-1}$$

Where, q_e (MPa) is the static tip resistance, h_p is the penetration depth, A and B are fitting parameters. Parameter A (MPa) gives the value of rod resistance at steady state.

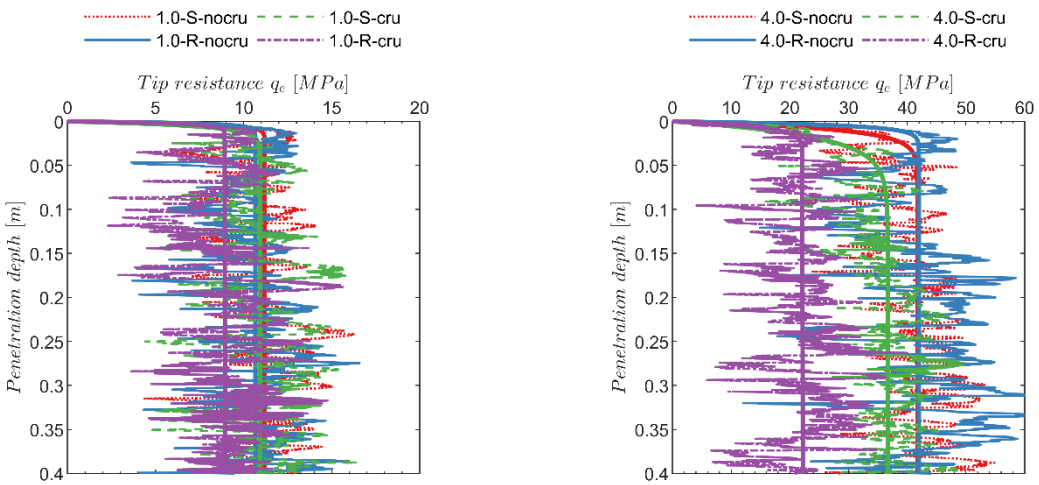

(a) (b)

Figure 7-2 Static penetration curves for test series confined at different stress levels: (a) 100 kPa; (b) 400 kPa

Figure 7-2 collects the raw static penetrograms for all the simulations as well as their fitted penetration curves. Table 7-3 summarizes the parameters of each adjusted penetration curve. For each case, the B value is relatively large, reflecting a quick increase of resistance in the initial stage of penetration. This phenomenon results from the use of flat-ended rod tip. It may be noted that from a depth of 0.05 m, the curves start oscillating around stable values, that is, the rising stage of resistance observed at the

beginning of penetration has surely been terminated at 0.05 m. Thus, from 0.05 m to 0.4 m depth, the probability distribution of tip resistance can be collected to examine the amplitude of these oscillations (Figure 7-3). Table 7-4 lists the mean value, μ, standard deviation, σ, and coefficient of variance, $C.V$ of tip resistance measured in associated tests. Although the R-squared value may appear too small, but very similar to those reported by Ciantia et al. (2016) for CPT in dense sand. Generally, a curve with more oscillations is characterized by a wider coverage of resistance values and smaller probability peak values.

Table 7-3 Parameters for adjusted penetration curves

Sample ID	A / MPa	B / -	R^2
1.0_S_nocru	11.2	364.2	0.16
1.0_S_cru	10.9	194.0	0.07
1.0_R_nocru	10.7	478.6	0.21
1.0_R_cru	8.9	444.3	0.06
4.0_S_nocru	41.7	112.0	0.30
4.0_S_cru	36.7	58.3	0.38
4.0_R_nocru	42.0	239.7	0.10
4.0_R_cru	22.2	167.3	0.10

The small rod diameter-to-mean particle ratio, n_p, (see table Table 7-1) results in jagged penetrograms with very strong oscillations, particularly when crushing is enabled or rough contact model is used (Figure 7-3). Even with different degree of oscillations, the fitted penetration curves in Figure 7-2 reveal clear estimation of resistance values of the tests. It may be observed that (1) when crushing is disabled, the tip resistance values are identical for both smooth and rough materials; (2) when crushing is allowed to occur, tip resistance decreases, and this effect is much increased in the rough contact material. The resistance in rough uncrushable sand almost doubles the resistance in rough crushable sand. It can be concluded that crushing is able to reduce tip resistance values and roughness enhances this effect.

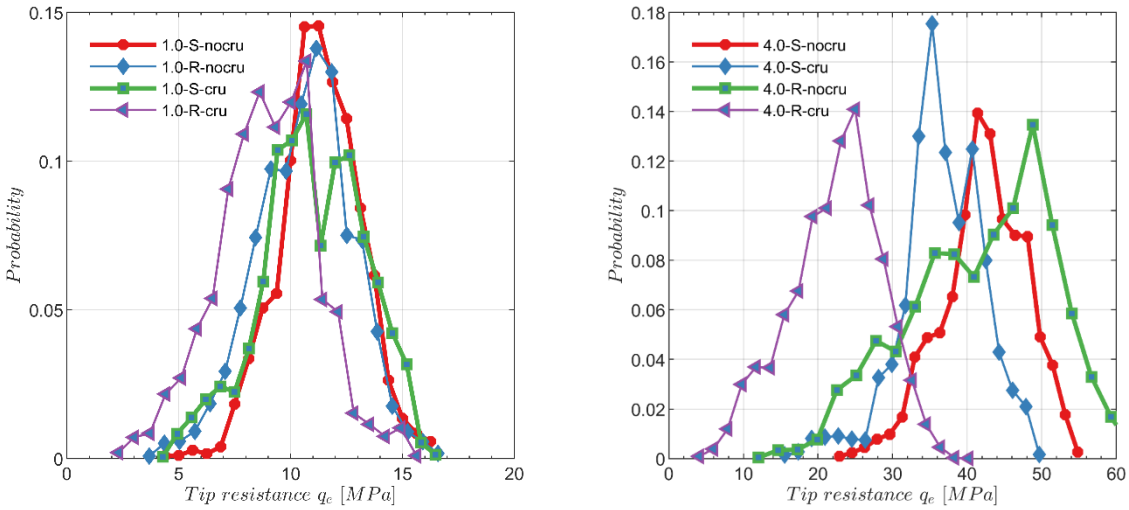

(a) (b)

Figure 7-3 Probability distribution of static tip resistance q_c: (a) 100 kPa; (b) 400 kPa

Table 7-4 Values of statistics theory associated with Figure 7-3

Tests	μ: MPa	σ: MPa	C.V
1.0_S_nocru	11.3	1.79	15.8%
1.0_S_cru	11.0	2.30	20.9%
1.0_R_nocru	10.6	2.11	19.9%
1.0_R_cru	8.9	2.23	24.9%
4.0_S_nocru	42.2	5.57	13.2%
4.0_S_cru	36.6	5.48	14.9%
4.0_R_nocru	41.9	9.62	23.0%
4.0_R_cru	22.3	6.11	27.4%

The steady state values of tip resistance (given by the A parameter of adjusted penetration curve) are plotted against vertical stress in Figure 7-4. Increasing the boundary confining stress does increase the tip resistance for both smooth and rough materials under crushable and uncrushable conditions. The increase rate does not depend on contact model type for non-crushable materials, while the rate decreases once the crushability is activated, particularly if surface roughness is present.

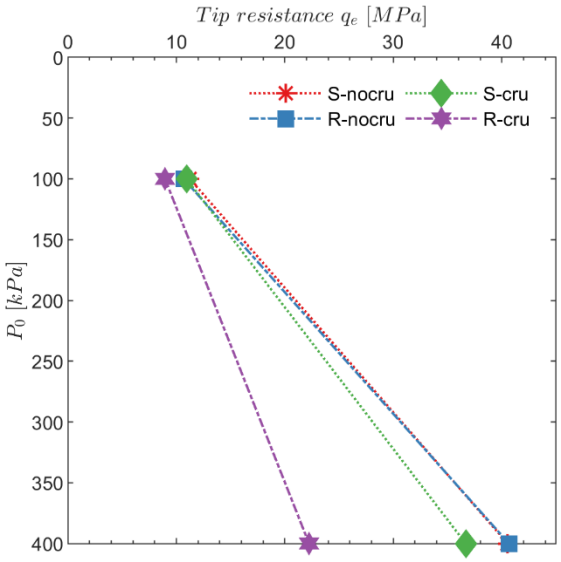

Figure 7-4 Fitted tip resistance vs sample initial confining pressure

7.3.2 Crushed particles

Figure 7-5 illustrates the evolution of crushing events divided by initial particle number with penetration depth. To have a better understanding of the response of crushable materials, the results are fitted by straight lines which are plotted together with the raw data. The parameters of the fitted lines are listed in Table 7-5. Crushing already takes place before static penetration phase (during initial chamber stress set-up), except for the test in '1.0-S-cru' sample. The ratios of the crushed particles to the initial particle number are relatively small. In addition as illustrated in Figure 7-6a, the crushed particles are evenly distributed in the specimen. With rod probing, more and more particles are compressed into breakage, with various rates in different crushable specimens. In general, crushing takes place at faster rates in rough materials than in smooth ones. At a given depth, more particles break at high confining pressure than at low confining pressure, particularly if particle surface is rough.

Table 7-5 Parameters for fitted lines of crushing events

Sample ID	Intercept	Slope	Fitted lines*	R^2
1.0_S_cru	0.05	0.6	y=0.05+0.6x	0.982
1.0_R_cru	0.14	1.3	y=0.14+1.3x	0.970
4.0_S_cru	0.51	0.7	y=0.51+0.7x	0.973
4.0_R_cru	0.83	1.7	y=0.83+1.7x	0.991

* x and y represent the variables on x-axis and y-axis in Figure 7-5, respectively.

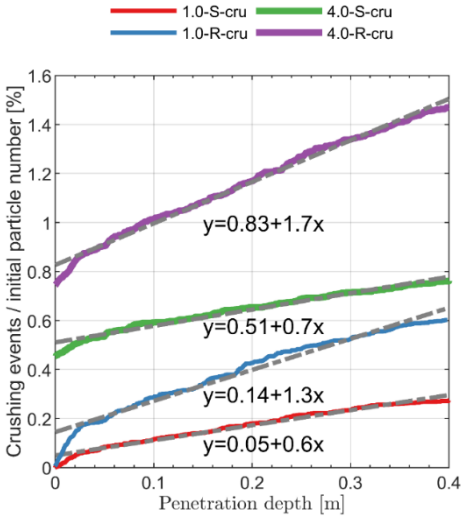

Figure 7-5 Curves expressing number of crushed particles divided by initial particle number against penetration depth and their fitted linear curves

As a consequence of the small number of crushing events the mass lost during the simulations is also relatively small. The ratios of crushing events to initial particle number during initial compression and static penetration are summarized in Table 7-6. It is apparent that, despite its large effect on the simulation outcomes, the percentage of crushing events taking place during the simulations is relatively small. The number of initial particles that is crushed during the simulations remains always below 1% of the initial number. Table 7-6 also compiles the mass lost ratio to the initial mass during the simulations. The mass loss is actually very small with values always below 0.5%.

Table 7-6 Crushing events during different simulation phases

Sample ID	Phase	Crushing events in phase / initial particle number (%)	Mass lost in phase / initial mass (%)
1.0_S_cru	Compression	0	0
1.0_S_cru	Penetration	0.27	0.18
1.0_R_cru	Compression	0.006	0.02
1.0_R_cru	Penetration	0.594	0.34
4.0_S_cru	Compression	0.45	0.28
4.0_S_cru	Penetration	0.31	0.15
4.0_R_cru	Compression	0.74	0.43
4.0_R_cru	Penetration	0.73	0.42

The percentage of crushing events during the penetration phase does seem sensible to contact model type, in which rough materials are more crushable. At small confining pressure, rod penetration is the dominating process leading to particle breakage, while at high confining pressure, more particles break during the initial stress installation phase than during the penetration phase.

It is interesting to visualize the spatial localization of the crushing events in different penetration depths. In Figure 7-6, the location of particles crushed within a vertical slice for the test in '4.0-R-cru' specimen is represented for three penetration phases: compression phase (previous to static penetration), 15 cm depth and 40 cm depth. It is obvious that before advancing the rod, crushing events are evenly distributed within the chamber. Adding now the particles crushed during the penetration phases for the same test a very different pattern appears. Most crushing events have concentrated within 2-3 radius from the rod. This is in agreement with the CPT work done in a more crushable sand (Ciantia et al., 2016b).

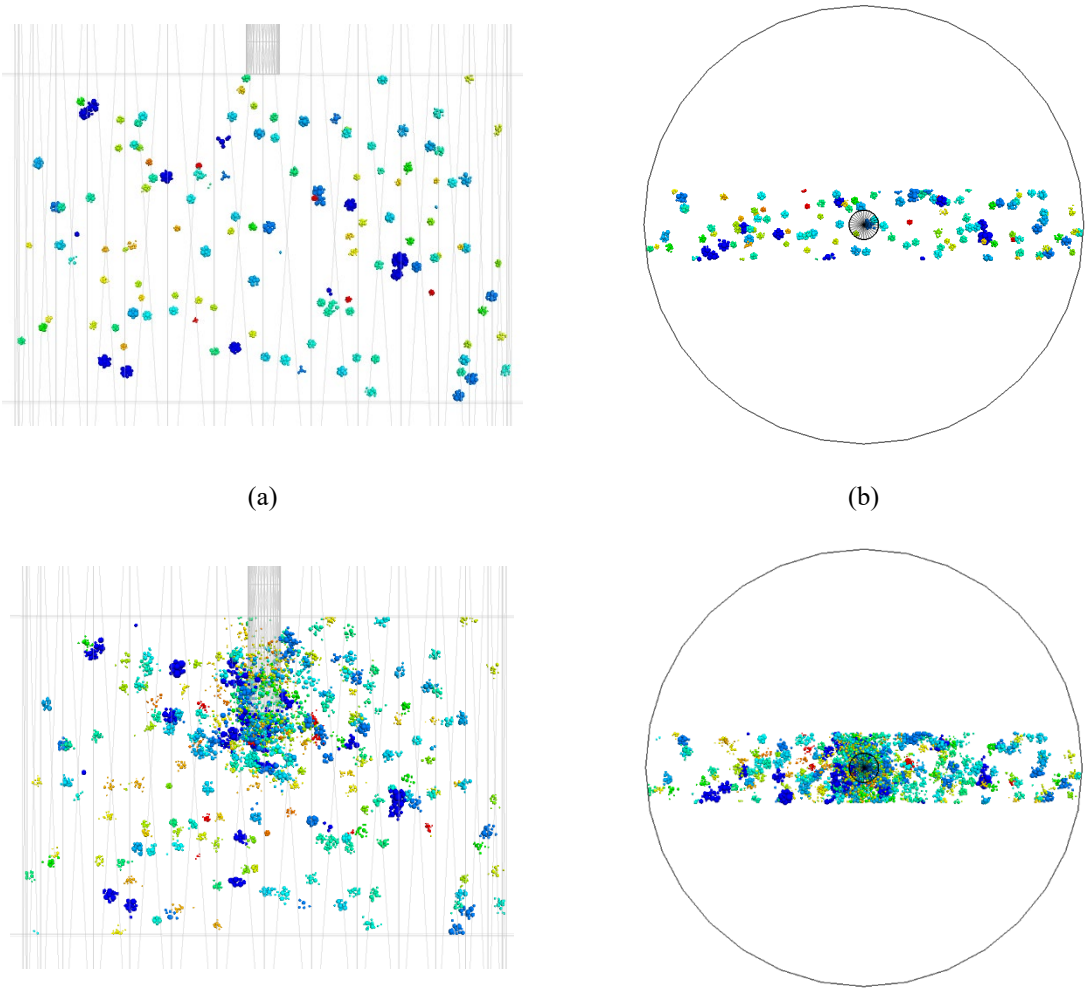

(a) (b)

(c) (d)

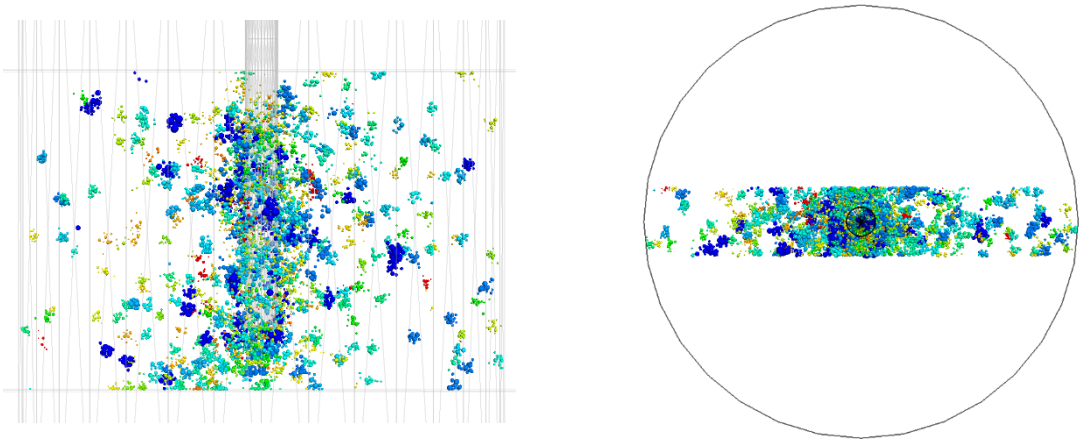

(e) (f)

Figure 7-6 Crushed particle locations within a vertical slice for the specimen with rough contact model: (a) horizontal projection of crushed particles before penetration, (b) vertical projection of crushed particles before penetration, (c) horizontal projection of crushed particles at 15 cm depth, (d) vertical projection of crushed particles at 15 cm depth, (e) horizontal projection of crushed particles at 40 cm depth, and (f) vertical projection of crushed particles at 40 cm depth.

7.3.3 Energy distribution

In Chapter 5, an energy analysis of penetration test in a VCC was presented for uncrushable DEM. In this section, such analysis is extended to the crushable case. We focus in the 4.0 test series as this is the one in which more crushing took place and the associated phenomena are more visible.

7.3.3.1 Effect of particle breakage on particulate systems

Energy dissipation in crushable granular assemblies has attracted interests of many researchers (Bolton, Nakata, & Cheng, 2008; Russell & Einav, 2013; Wang & Yan, 2012; Wang & Arson, 2018). Not surprisingly, DEM models serve as a very powerful tool in this type of analysis. Generally speaking, a particle crushing event in DEM simulations causes a sudden loss of stored strain energy in this particle. This localized loss of energy is also accompanied by broader changes at the network scale, e.g. dissipation induced inter-granular friction as forces are redistributed around the network after particle crushing. Therefore, besides common energy terms, one more energy term expressing localized energy loss at particle breakage events should be tracked.

This idea has been explored before, in simulations where particles were represented by bonded agglomerates (Bolton et al., 2008). It appeared that localized breakage energy was a negligible fraction of total energy input and that the major effect of particle breakage was indirect, in the changes induced on network-wide inter-particle friction dissipation (Bolton et al., 2008; Wang & Yan, 2012).

In this study an alternative particle crushing approach is used, which is a multigenerational approach where single elements break and are replaced by newly generated smaller grains. The daughter grains inherit the velocity and material parameters of the mother particle, expect for the intrinsic strength ($\sigma_{lim,0}$) that is randomly assigned according to the particle strength criteria. This approach is advantageous in computational efficiency at a sample scale, but clearly is not able to conserve particle mass and, therefore, also unable to conserve the kinetic energy of particles in the granular system. Note that the underlying assumption is that the mass lost is formed by finer particles that may have a small influence on the macroscopic mechanical response. However, some doubts remained about the energetic impact of breakage using this model and it was decided to explore them in a simplified element-test setting, before addressing the more complex case of VCC simulations.

To start, a simple uniaxial compression test in a small cell containing enough particles is selected. Therefore, the oedometer test settings used in the 'rough contact model' study (Chapter 6) is recalled here for energy analysis. The newly calibrated Fontainebleau sand properties including roughness values are adopted. Particle crushability regime is activated and prohibited, respectively, in two parallel oedometer tests. Several energy components are tracked. These energy components are boundary work W, energy dissipated by frictional sliding D_F and by damping D_D, changes in elastic strain energy stored at contacts E_S and in kinetic energy E_K.

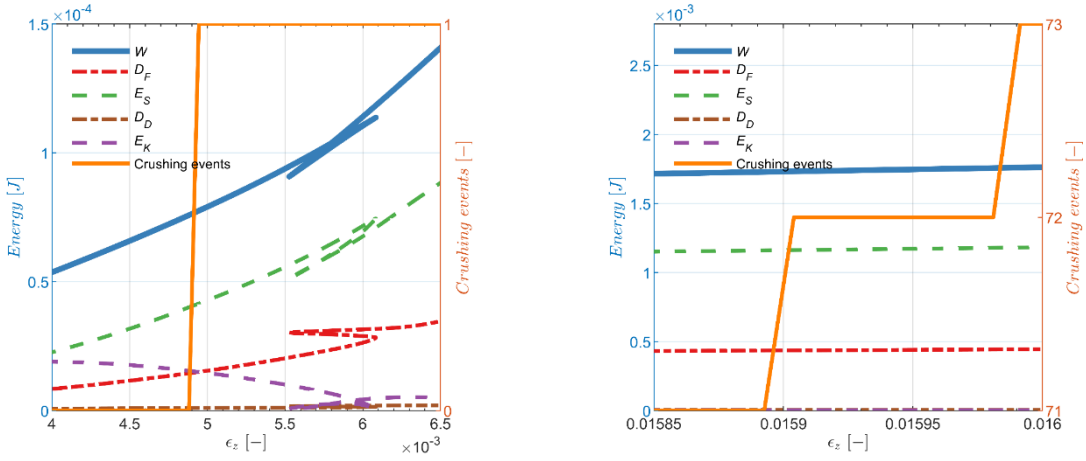

(a) (b)

Figure 7-7 Change in energy distribution after one crushing event: (a) 1st crushing; (b) 72nd crushing

It is interesting to look into detail how a single particle crushing event is reflected on the energy terms. This is done in Figure 7-7 where energy distribution in the system after a first crushing event and another crushing event (72nd) is presented. The first crushing event is encountered in the particulate system at the initial stage of compression where energy components are quite small. Clearly, the crushing induces

a slight drop in the strain energy and the kinetic energy of the system, while a slight rise in slip energy. However, when the 72nd crushing occurs, no obvious changes are visible in the energy distribution of the system, even they have small values as well. It indicates that the effect of a single particle crushing event on energy distribution in a particulate system could be ignored during compression tests. The mass lost have a very small influence on the energy distribution response.

Figure 7-8 illustrates the evolution of axial stress-strain relationship and the related energy components with axial strain in the two tests. Breakage energy is not defined on the basis of previously mentioned findings of other researchers. In Figure 7-8, several meaningful findings are revealed:

(1) When particles are not allowed to break, strain energy E_S keeps increasing with boundary work input W (Figure 7-8a). A considerable percent of the work input is stored as elastic strain energy at contact points. Relatively small amount of the work input is lost in friction. Kinetic energy and damping work are negligible.

(2) Figure 7-8b illustrates energy components in crushable sands, as well as crushing events. When particle crushing regime is activated, it is clear that the boundary work input W is reduced to a considerable degree, compared with the boundary input in uncrushable sands (Figure 7-8a). The different capacity of both materials to absorb boundary work appears mostly due to strain energy stored at the contacts. Particle crushing strongly limits the ability of the granular material to store energy at the contacts, as it imposes an upper limit in the contact forces that a given contact will withstand.

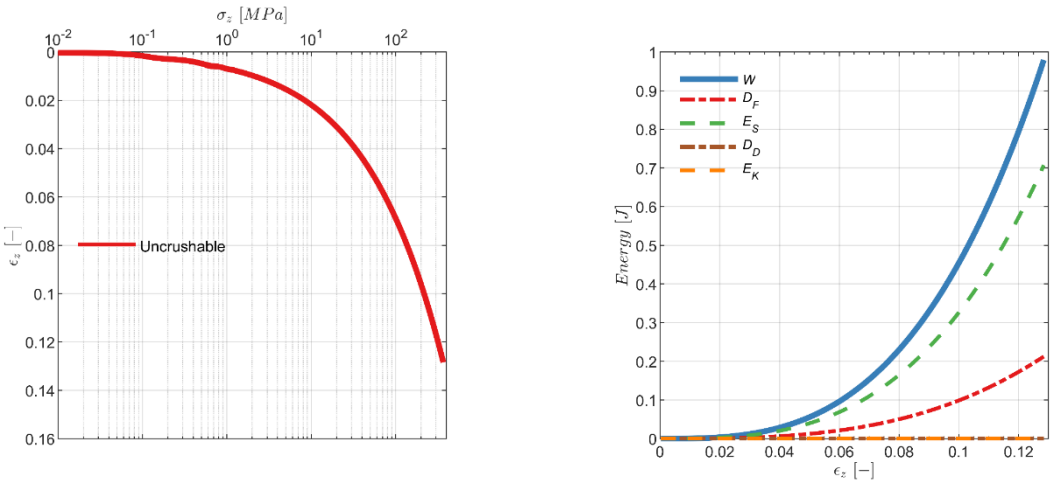

(a)

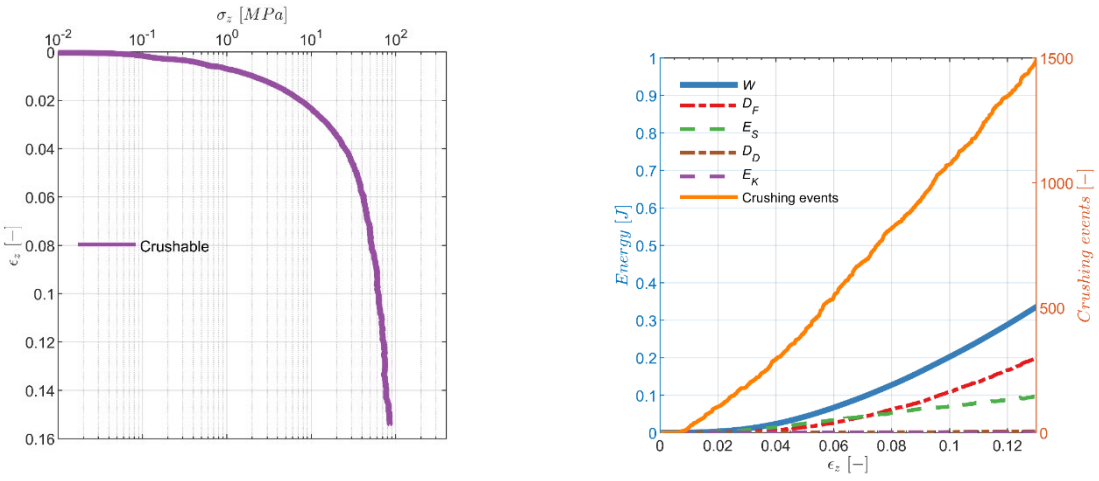

(b)

Figure 7-8 Stress-strain evolution and energy distribution in two oedometer tests: (a) uncrushable, (b) crushable (with recorded crushing events)

7.3.3.2 Energy dissipation in granular assemblies

In the previous section we showed that, in agreement with previous research, for the crushing models employed here the indirect effect of particle crushing on the energy balance –(i.e that due to network-mediated effects of crushing) was far more important that the negligible direct effect (i.e. the localized loss due to particle substitution). Bearing that in mind we address now the effect of crushing on energy terms during penetration in the VCC.

Table 7-7 Energy components in static penetration tests (0.4m penetration depth)

Sample ID	D_F	D_D	E_K	E_S	W	D_F / W
Units	kJ	kJ	kJ	kJ	kJ	-
4.0_S_nocru	39.4	0.032	1.9e-4	0.31	40.3	0.978
4.0_S_cru	33.2	0.052	3.6e-4	0.30	33.9	0.980
4.0_R_nocru	38.6	0.024	8.7e-5	0.16	39.3	0.982
4.0_R_cru	20.9	0.053	6.3e-5	0.099	21.1	0.991

Table 7-7 summarizes the value of each energy component tracked in the 4.0 test series (Table 7-2) at a penetration depth of 0.4m. Energy data view at this depth is representative as the rod probing advances with a constant rate. It is clear that damping work and kinetic energy of particles are negligible as they have relatively small values. It is valid that for the static tests, frictional energy D_F between contacts is

almost equal to rod work input W, indicating that particle frictional sliding contributes mostly to the energy dissipation. Differences appear in comparisons of frictional energy between the tests, clearly showing that contact model and particle crushability matter in energy dissipation mechanisms.

Further studies are required to visualize the effect of contact model and particle crushability on energy dissipation. The evolution of the frictional energy against penetration depth to 0.4 m is illustrated (Figure 7-9). The frictional energy curves all increase linearly with the penetration depth. No clear discrepancies are observed on the curves for uncrushable sands. However, it is obvious that at a given depth, tests in crushable sands are dissipating less energy than that in uncrushable sands, particularly if the particle surface is rough. In other words, less work input from the rod is needed to reach a certain depth if particles are allowed to crush, particularly if they are not smooth. Interestingly, the effects of particle crushing on resistance values and frictional energy (Table 7-8) at a given depth are very similar for both smooth and rough materials.

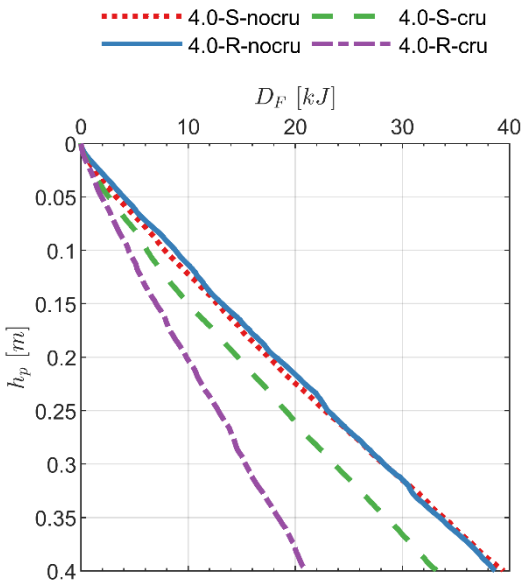

Figure 7-9 Frictional energy vs penetration depth for 4.0 test series

Table 7-8 Effect of particle crushability on resistance and frictional energy

Contact type	$q_{c,hard}/q_{c,crushable}$	$D_{F,hard}/D_{F,crushable}$
Smooth	1.13	1.18
Rough	1.91	1.85

Despite strain energy having little influence on energy dissipation during penetration, its evolution with penetration depth remains interesting. It is done in Figure 7-10 with the rod advancing to a depth of 0.4

m for the 4.0 test series. The strain energy curves present large oscillations similar to those observed in penetration resistance curves (Figure 7-2) and their magnitudes become relatively constant after a shallow depth of 0.05m,. It is clear that at a given depth (after 0.05 m) the magnitudes of strain energy vary depending on particle contact model and crushability. The test in the smooth uncrushable sands (test 4.0-S-nocru) has a maximum strain energy, followed in sequence by those in the smooth crushable sands (test 4.0-S-cru), rough uncrushable sands (test 4.0-R-nocru) and rough crushable sands (test 4.0-R-cru).

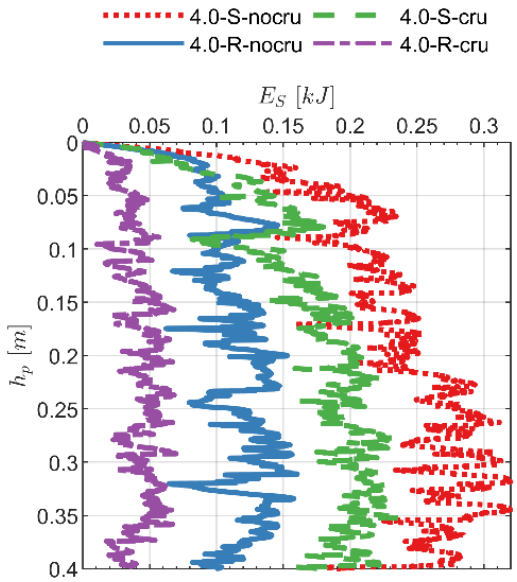

Figure 7-10 Strain energy vs penetration depth for 4.0 test series

7.4 Dynamic penetration tests

The results of DEM-based dynamic probing tests were collected in Table 7-9, where v_{peak} is the rod peak velocity, q_d is the dynamic tip resistance, $\Delta\rho$ is the penetration depth per blow, N is the SPT blow counts, E_{blow} is the energy delivered by hammer to driven rod, ER is the energy input ratio and N_{60} is the normalized blow counts. The number of crushing events is also counted. It might be appropriate to analyze the tests under low (100 kPa) and high (400 kPa) confining pressure separately.

Table 7-9 Results of DEM-based dynamic probing tests

Sample ID	v_{peak} : *m/s*	q_d : *MPa*	$\Delta\rho$: *cm*	*N*	E_{blow} : *J*	*ER: %*	N_{60}	*N of crushing events*
1.0_S_nocru	1.34	10.2	0.78	38	194	41.0	26	-
1.0_S_cru	1.31	9.5	0.82	37	194	41.0	25	4
1.0_R_nocru	1.30	9.8	0.78	38	182.7	38.7	24	-
1.0_R_cru	1.30	9.1	0.8	37	182.3	38.9	23	27
4.0_S_nocru	1.21	20.6	0.18	167	165	35.0	97	-
4.0_S_cru	1.17	19.6	0.18	167	151	32.2	89	0
4.0_R_nocru	1.19	25.4	0.24	125	162	34.5	71	-
4.0_R_cru	1.40	16.8	0.54	55	184	39.0	36	9

7.4.1 Tests at low confining pressure

For the tests at low confining pressure (1.0 test series), several interesting findings related to the effect of particle surface roughness and particle breakage on the mechanical responses of dynamic probing can be discovered. Including the two particle scale characteristics is unquestionably adding the complexity of the sand particles. In the simplest sand material (test 1.0_S_nocru in Table 7-9), the rod is driven to a permanent penetration of 0.78 cm with a peak velocity of 1.34 m/s. The blow number *N* and energy efficiency *ER* are recorded as 38 and 41%, respectively, contributing to a normalized value of blow count as 26.

Derived from Table 7-9, Table 7-10 collects all the SPT related results for 1.0 test series normalized by the results obtained from 1.0_S_nocru test. It is clear that very few discrepancies appear for these SPT related results, for the tests at low confining pressure.

Table 7-10 Selected results of 1.0 test series normalized by the results obtained from 1.0_S_nocru in Table 7-9

Sample ID	v_{peak} :	$\Delta\rho$: *cm*	*N*	*ER: %*	N_{60}
1.0_S_nocru	1	1	1	1	1
1.0_S_cru	0.98	1.05	1.03	1	0.96
1.0_R_nocru	0.98	1	1	1.05	0.92
1.0_R_cru	0.98	1.03	1.03	1.05	0.90

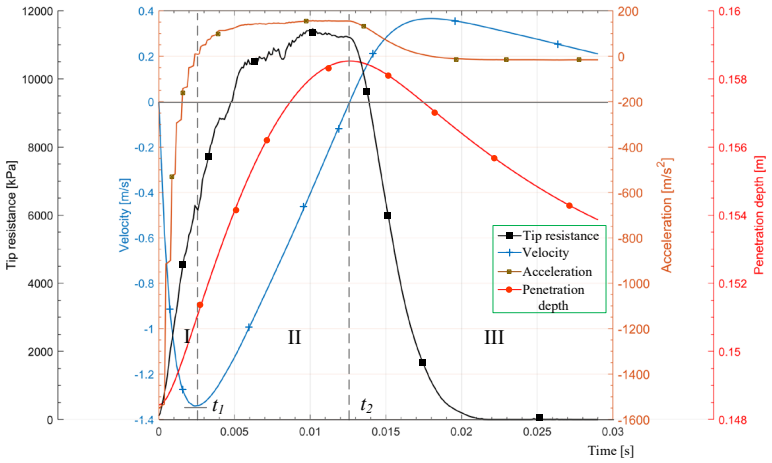

Figure 7-11 Evolution of tip resistance, rod velocity, rod acceleration and penetration depth during one impact with time for 1.0_S_nocru test, zoon-in view till 0.03 s

Similar to Figure 4-6, the evolution in time of tip resistance, rod velocity, rod acceleration and penetration depth during one impact for the 1.0_S_nocru test is illustrated in Figure 7-11 as a representative example. The record was interrupted after 0.03 s, as by then the first three continuous phases (I, II and III) had terminated and been clearly displayed. Time points t_1 and t_2 are identified as characteristic points distinguishing the 3 phases. The phase I, II, and II corresponds to a quasi-linear rise (*acceleration*), steady oscillations (*deceleration*) and a fast reduction (*unloading*) in tip resistance, respectively.

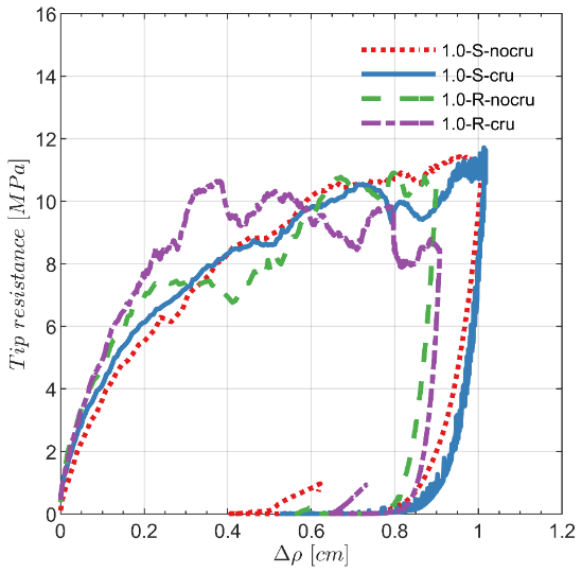

Figure 7-12 Penetration curves for dynamic probing tests in samples confined at 100 kPa

Of particular interest is the dynamic penetration curve of samples tested under low confinement (1.0 test series) illustrated (Figure 7-12), by plotting tip resistance with dynamic penetration distance $\Delta\rho$. As previously presented, the values of tip resistances and final penetration distances are almost identical. However, very clear effects of particle roughness and crushability on the tracks of the penetration curves recorded for tests at low confining pressures is observed, particularly in the phase of quasi-linear rise and reduction. More detailed discussions are presented below, with separate investigation on the effect of surface roughness and crushability.

Figure 7-13 illustrates the penetration curves for dynamic probing tests in both smooth and rough sand materials. The characteristic time points t_1 and t_2 are also marked in the plots. Several common observations facilitated by crushable sands are summarized as follows:

(1) A sharper rise in resistance is encountered across phase *I*, which terminates after t_1,;
(2) The resistance values are more stable in phase *II* (from t_1 to t_2), particularly for rough material; this may result from the fact that there are more particles crushed in rough material (Table 7-9)
(3) Slightly shorter penetration depth is reached in phase *III*;
(4) More oscillations occur in resistance through the whole penetration process.

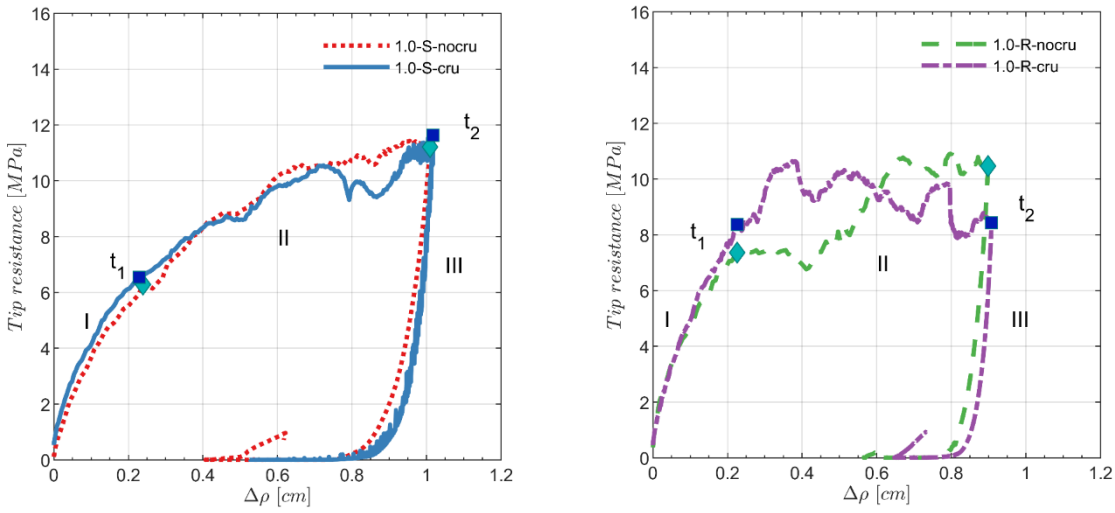

(a) (b)

Figure 7-13 Influence of particle breakage on penetrograms recorded during dynamic probing test in: (a) smooth material and (b) rough material

Figure 7-14 illustrates the influence of surface roughness on penetration curves recorded in both uncrushable and crushable materials. It is clear that the effects of surface roughness on penetration resistance are very similar to those described above of particle crushability, except for that in unloading.

The rods driven in both uncrushable and crushable materials arrives at the same distance, but with a sharper reduction slope if particles are rough. Moreover, the rod rebounds less in rough material.

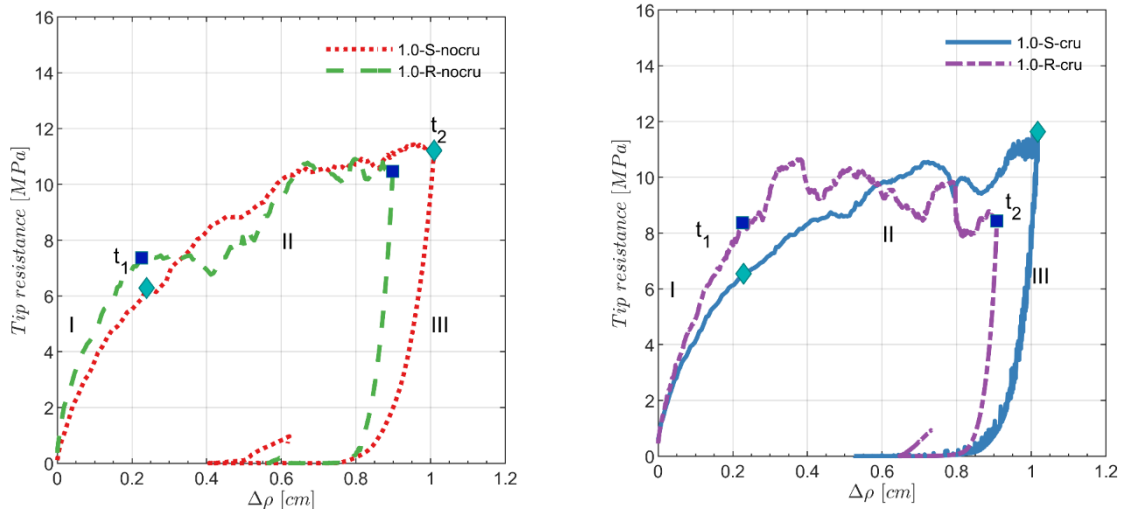

(a) (b)

Figure 7-14 Influence of surface roughness on penetrograms recorded during dynamic probing test in: (a) uncrushable and (b) crushable sands

7.4.2 Test at high confining pressure

The penetration depth during a single blow $\Delta\rho$ is relatively small corresponding to blow numbers above the limit of acceptance for field tests ($N = 100$), for all the tests in highly confined samples except for the 4.0_R_cru one (Table 7-9 and Table 7-11). However, the rod peak velocity and energy efficiency does not vary very much between all the tests.

Table 7-11 Selected results of 4.0 test series normalized by the results obtained from 4.0_S_nocru in Table 7-9

Sample ID	v_{peak} : *m/s*	$\Delta\rho$: *cm*	*N*	*ER: %*	N_{60}
4.0_S_nocru	1	1	1	1	1
4.0_S_cru	0.97	1	1	0.92	0.91
4.0_R_nocru	0.98	1.3	0.75	0.99	0.73
4.0_R_cru	1.15	3	0.33	1.11	0.37

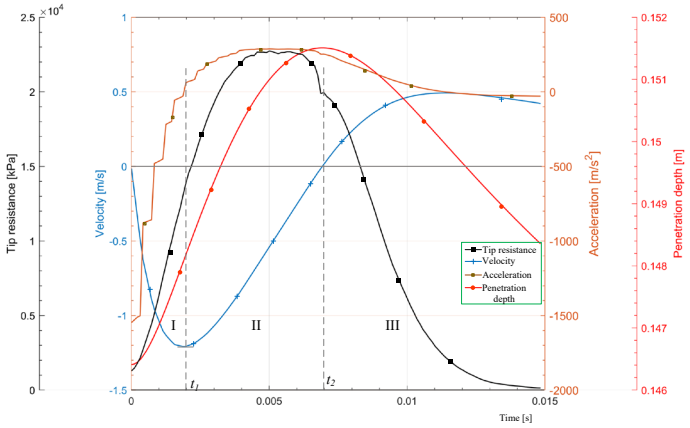

(a) 4.0_S_nocru

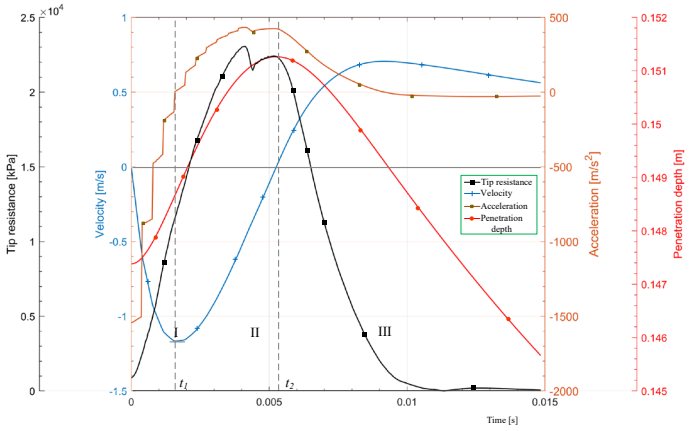

(b) 4.0_S_cru

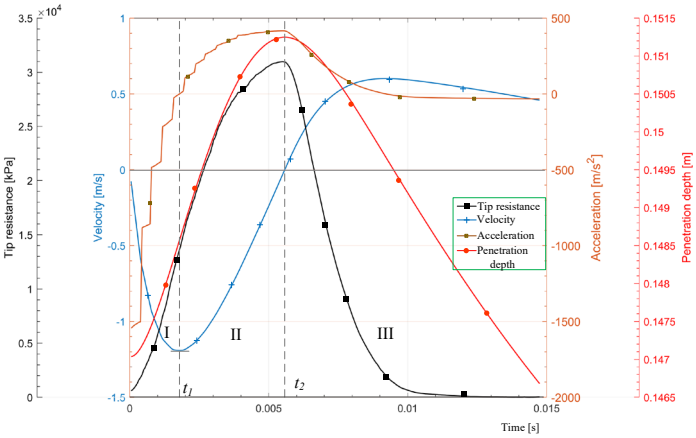

(c) 4.0_R_nocru

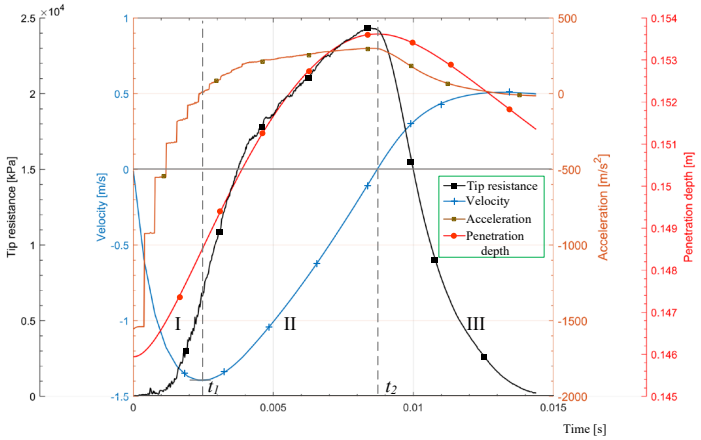

(d) 4.0_R_cru

Figure 7-15 Evolution of tip resistance, rod velocity, rod acceleration and penetration depth during one impact with time for 4.0 test series

Figure 7-15 illustrates the evolution in time of rod velocity, rod acceleration, rod tip position and tip resistance for the 4.0 test series till the time of 0.015 s. These impact dynamics present considerable differences from those seen in Figure 7-11:

(1) The rise of resistance in phase *I* is relatively slower, resulting in a relatively smaller value of resistance after t_1;
(2) The resistance in phase II is not oscillating around a relatively constant value;
(3) The velocity in phase III reaches a high value.

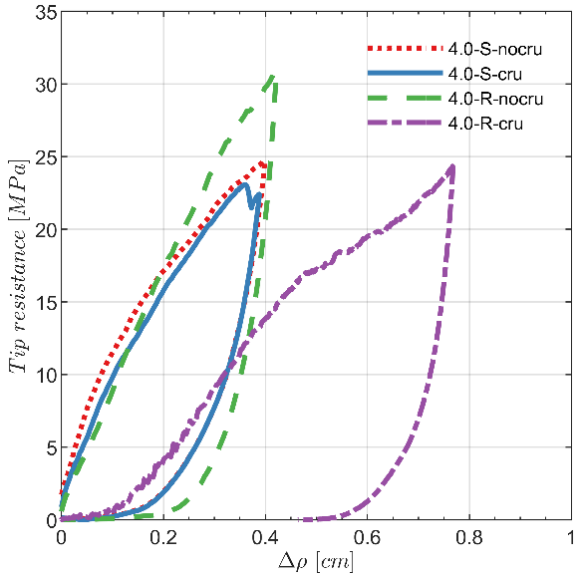

Figure 7-16 Penetration curves of dynamic probing test results in samples confined by 400 kPa

Figure 7-16 illustrates the dynamic penetration curves recorded from tests conducted in highly confined samples. For tests in smooth material, the penetration curves for crushable and uncrushable sand materials are almost identical as no particles are impacted to crush in crushable sand (Table 7-9). A slightly higher peak value of resistance appears for the test in rough uncrushable material. It is interesting to note a quite distinct track of the penetration curve for 4.0_R_cru, where the rise stage is flatter and the rod is driven to a deeper distance. This phenomenon can be related with two aspects:

(1) Crushable materials are less capable in resisting the rod than uncrushable ones;
(2) Crushed particles lead to an increase of cone/particle size ratio (Figure 7-6).

7.5 Correlations between dynamic and static test results

In chapter 4 and chapter 5, attempts have been made to relate the static and dynamic penetration resistances for tests in uncrushable smooth sand materials. Two types of dynamic resistance were measured: average dynamic resistance q_d and energy-based dynamic resistance q_{dE}. In this section, the applicability of previously proposed correlations are examined for tests in more complicated sands, e.g. rough and/or crushable sand.

7.5.1 Average dynamic resistance q_d

The dynamic resistance q_d is computed averaging the tip resistance measured during the '*deceleration*' phase (phase *II* in Figure 7-11), following the same procedure described in Chapter 4. The fitted parameter *A*, describing the rod resistance at steady state (collected in Table 7-3), is selected for comparisons with equivalent dynamic resistance value. As shown in chapter 4, static and dynamic tip resistances measured in uncrushable smooth materials are very close to each other if they are below 10 MPa. Above this value, the dynamic resistance is smaller than the static one. This discrepancy may result from the fact that the energy delivered by hammer impact in the dynamic test is insufficient to mobilize the available penetration resistance. In addition, ignoring some natural features of particles in numerical simulations such as crushability may also attribute to the discrepancy.

As illustrated in Figure 7-17a, similarities in resistances between the static and dynamic tests in samples confined by low pressures are clear, regardless of particle roughness and crushability. However, if one or two of the two particle characteristics are not included, the similarities disappear in highly confined samples, with a good match observed only from the test in rough crushable material.

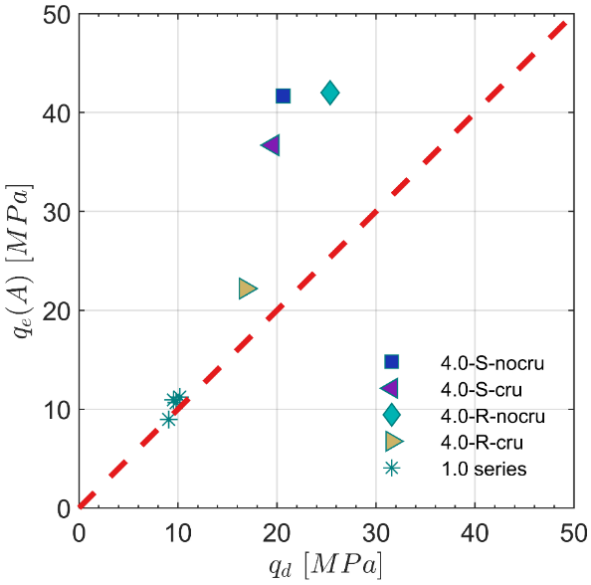

Figure 7-17 $q_e\,(A)$ vs q_d

7.5.2 Energy-based dynamic resistance q_{dE}

Inspired by Schnaid et al. (2017), the energy-based dynamic penetration q_{dE} is estimated from the ratio of the sum of energy delivered to the sampler and work done by rod self-weight to rod penetration displacement $\Delta\rho$ recorded after a single blow (Eq. 5-23). q_{dE} has been validated to be equal to the static penetration resistance q_e for test in uncrushable smooth materials, independent of ground conditions. Figure 7-18 shows that this finding is still valid for tests in more complicated models (i.e. rough, crushable).

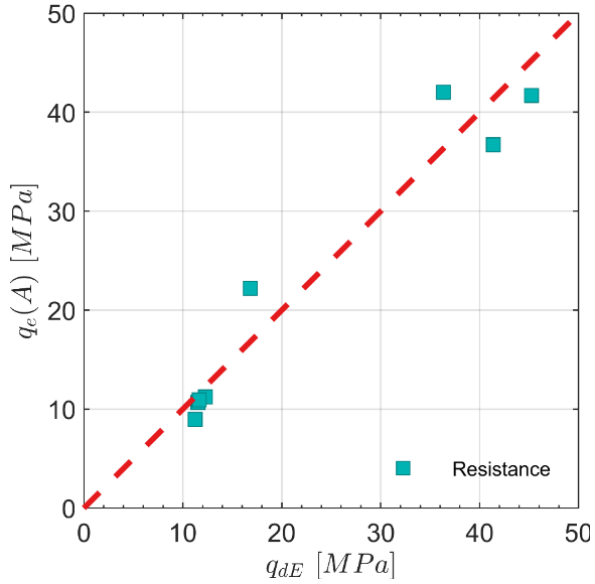

Figure 7-18 $q_e\,(A)$ vs q_{dE}

7.5.3 Comments

Numerous correlations relating the ratios of q_c/N_{60} with the mean grain size D_{50}, fines content FC%, and, relative density have been empirically proposed from geotechnical engineering practice (Ahmed et al., 2014; Tarawneh, 2014; Robertson et al., 1983; Tarawneh, 2017). The correlations are crucial in saving considerable costs of site investigation by facilitating the common practice that only one of the two tests is needed to carry out. However, representing the dynamic penetration mechanism relying on a single blow count number while disregarding other interdependent variables (i.e. hammer falling height h, $\Delta\rho$, hammer mass m_h) may not be appropriate. Due to that reason, this type of approach introduces inevitable errors (Schnaid et al., 2009). In addition, many SPT-CPT correlations become less reliable for crushable sands (Ahmed et al., 2014).

In recent years, the use of energy-based dynamic resistance has been proposed to relate the static penetration resistance, opening new ways in interpreting soil properties (Hettiarachchi & Brown, 2009; Schnaid et al., 2009). Compared with the use of a simple N-value, the use of dynamic resistance allows for a more comprehensive consideration of equipment (hammer, rod and sampler) variables in describing dynamic penetration mechanism. Schnaid et al. (2017) recommended that the use of N-value without further specifications should be discontinued and replaced by q_{dE} when representing dynamic penetration resistance. The work in this thesis, to an extent, provides a validation for that recommendation from a numerical perspective.

7.6 Summary

This chapter has presented an extensive work assembling the achievements obtained in previous chapters, in relation with dynamic probing approach, rough crushable contact model, energy analysis, efficient UDCM technique, etc. A series of tests have been conducted to investigate the influence of particle crushability and contact types (smooth and rough) on the mechanical responses of penetration tests under static and dynamic probing conditions. The major conclusions are summarized as follows:

- Particle crushing is able to reduce tip resistance recorded in static penetration tests, and roughness enhances this effect.
- In static tests, at a given confinement, the number of crushed particles are relatively small particularly if the material is smooth. Most crushing events are localized within 2-3 radius from the rod.
- Particle crushing strongly limits the ability of granular material to store energy at the contacts, as it imposes an upper limit in the contact forces that a given contact will withstand.

- The effect of a single particle crushing event on energy distribution in a particulate system could be ignored during compression tests. The mass lost have a very small influence on the energy distribution response.
- For static tests, particle frictional sliding at contacts dissipates mostly the energy input from outer boundaries. Contact model and particle crushability matter in energy dissipation mechanisms.
- For dynamic tests at low confining pressure, roughness and crushability mainly influence the track of dynamic penetrometer. Less rebound has been observed in rough materials.
- Finally, the effect of the particle-scale properties on the relation between static and dynamic penetration has been examined.

Chapter 8 Conclusions and future work recommendations

8.1 Summary

The objective of this thesis was to use DEM simulations to advance the interpretation of dynamic probing test in granular materials, taking realistic particle scale characteristics into consideration.

The main contributions and conclusions of this work are summarized as follows:

SPT in a virtual calibration chamber (*Chapter 4*). The DEM-based virtual calibration chamber technique was applied to study the standard penetration test in granular materials. A macro-element approach has been used to model the driving rod with a realistic specification of the dynamic driving force. The chamber was filled with a discrete analogue of a representative quartz sand, whose contact properties have been calibrated reproducing laboratory test results.

Input energy normalization has been shown to be as effective an approach as in field testing to eliminate result variability derived by driving system characteristics. Results exploring the effects of relative density and confinement have shown a good agreement with well-known experimentally-based expressions. Tip resistance measured under impact dynamic penetration conditions is close to that measured under static penetration conditions, in line with recent experimental work by Schnaid et al. (2017).

Energy balance analysis during the SPT (*Chapter 5*). To go beyond the consideration of variable energy inputs, a more comprehensive study of energetic balances in the virtual calibration chamber dynamic experiments has been carried out. Energy balance has been observed both on the driven rod and within the chamber system, indicating a correct consideration of the proposed energy components. The evolution and distribution of each energy component with penetration depth has been characterized. Hammer input energy is mostly dissipated by frictional sliding between particle contacts. The energy-based interpretation approach for SPT dynamic resistance promoted by Schnaid et al. (2017) has been validated. Microscale investigation of the energy terms during the dynamic experiments gave particle scale insights on energy dissipation mechanisms.

Development of contact model for rough crushable particles (*Chapter 6*). A novel model describing the contact behavior of rough crushable particles has been proposed. The model was implemented in PFC within a C++ coded user defined contact model (UDCM), whose computational efficiency has been validated in comparison with equivalent FISH codes. Parametric studies have been presented to investigate the effect of contact roughness on single particle breakage. The contact parameters for the discrete analogue of the quartz sand have been recalibrated taking the particle scale features (roughness and crushability) into account. The newly calibrated parameters have enabled the use of realistic values and thereafter can reproduce better uniaxial test results, particularly in unloading parts.

Static & dynamic probing of rough breakable sands (*Chapter 7*). The newly developed contact model for rough breakable particles has been used for simulations of both static and dynamic penetration tests. A study of the effect of particle surface roughness and particle crushability on mechanical responses of penetration tests has been carried out. An energy-related study has also been conducted for the crushable materials. It has shown that, particle crushing reduces tip resistance, which is enhanced if roughness is present. The effect of the particle-scale properties on the static and dynamic relationship has also been examined.

8.2 Recommendations for future work

This section describes several aspects that have not been addressed or fully developed in this doctoral thesis. This may encourage future researchers to improve or complete the current work.

8.2.1 Dynamic penetration test

Regarding the dynamic penetration tests performed in this doctoral thesis, the following lines of further research are envisaged:

- The rod of standard penetration test has been driven into the soils with a particular specification of dynamic driving force that corresponds to SPT. It is therefore interesting to examine the applicability of this approach in DEM simulations of other types of widely used dynamic probing tests.
- The rod tip was assumed to be close-ended representing a plugged sampler, which is a common assumption in existing energy-based SPT interpretation methods but may introduce certain simplicities. Therefore, an examination of the conditions leading to plugging remains interesting, although requires applying significantly smaller scaling factors to particle sizes.

- In this work dynamic probing was conducted in samples representing quartz sands, although particles were allowed to crush, the percentage of crushing events was generally relatively small and hence had slight influence on penetration resistance. Dynamic probing may be carried out in low-strength sands such as volcanic pumice sand, and the SPT interpretation methods already validated for uncrushable sands can also be examined for highly crushable sands.
- In the early time, the energy transferred to the sampler through a short rod was assumed to be a reduced amount. However, with the recent improvement of energy measurement precision, researchers have shown that the importance of short rod effects may have been overestimated. Therefor it is also interesting to explore rod length effect on SPT results in further DEM VCC tests.

8.2.2 Particle characteristics

Spherical particles were used to fill the testing samples, with the rotation prohibited in order to roughly mimic the effect of non-spherical particles. Although the results obtained are always satisfactory in comparison with related experimental results or empirical expressions, this approach seems unnecessarily reductive and remains to be improved by means of, for instance, rolling resistance contact. A good choice could be the one recently proposed by Rorato (2019), which has proved to be able to represent the rotational restrictions of a wide range of sand types with various angularities.

Appendix I Enhancing efficiency of DEM modeling of particle breakage

Based on the published manuscript of the following conference paper:

Ciantia, M., Zhang, N., & Arroyo, M. (2017). Enhancing Efficiency of DEM Modeling of Particle Breakage. In *25th UKACM Conference on Computational Mechanics*. Birmingham, http://ukacm2017.ukacm.org/wp-content/uploads/2017/04/Proceedings-UKACM2017-compressed.pdf.

Abstract

In geotechnical practice, the discrete element method (DEM) is gaining wide acceptance as a powerful modelling tool. One field for which DEM is well adapted is that of crushable soils. Grain crushing has been modelled in DEM employing two alternative approaches: the multigenerational approach, in which single particles break and are replaced by new, smaller fragments; or by using agglomerates. The latter, despite being very helpful for the understanding of the micromechanics occurring in a single particle, becomes impractical when applied for modelling large scale problems. This work focuses on the enhancement of model efficiency from code-specific issues, as indicated in a series of simulation of high pressure isotropic compression of crushable sands. A recently developed model for crushable soils using multigenerational approach is adopted. It is shown that the advantageous code implementation adopted allows a considerable savings in computational cost with little influence on the accuracy in terms of grain size distribution evolution and mechanical behaviour.

I-a. Introduction

The mechanical effects of grain crushing are important for several geotechnical problems, such as side friction on driven piles (Yang et al., 2010) railway ballast durability (Sun et al., 2014) and slaking induced irreversible deformations (Kikumoto et al., 2016). These, and other applications, have motivated efforts to experimentally investigate the mechanical consequences of particle breakage (Coop et al., 2004) to incorporate grain crushing into constitutive models for soils (Muir Wood, 2007) and to model soil crushing using DEM (Cheng et al., 2004). To model particle fragmentation using DEM two

alternative approaches may be used: replacing the breaking grains with new, smaller fragments; or by using bonded agglomerates. The latter, despite being very helpful for the understanding of the micromechanics occurring to a single grain (Bolton et al., 2008), becomes an unpractical tool if larger scale problems are intended to be modelled. On the other hand, the former is more practical and has been adopted intensively for large scale 2D problems (Lobo-Guerrero & Vallejo, 2005) and recently in a 3D case (Ciantia et al., 2015). Computing efficiency becomes more fundamental when model size increases. As indicated by Ciantia et al. (2015), in the case of crushing model, non-conservative particle spawning and upscaling particle sizes are both promising techniques to reduce computational cost. This work focuses on different technique such as code-specific issues. The crushing model used to simulate cone penetration tests using the commercial PFC3D code (Itasca Consulting Group, 2016) in crushable soil gave very good results (Ciantia et al., 2016b). However, the failure criterion was coded by means of FISH (short for FLACish, a PFC built-in programming language) functions. FISH functions result in communication overheads that might be avoided if the contact model source code is directly modified. In this work the efficiency of using a user defined contact model (UDCM) instead of FISH functions for the modelling of grain crushing is tested. In particular, the numerical investigation concentrates on a series of simulation of high pressure isotropic compression of crushable particles.

I-b. Crushing Model description

The numerical models applied here are built using the PFC3D code (Itasca Consulting Group, 2016). This code implements the DEM in a similar form to that originally described by Cundall & Strack, (1979). For completeness an overview of the DEM model for crushable soil proposed by Ciantia et al. (2015) is given here. Coulomb friction and the simplified Hertz-Mindlin contact model were used. The failure criterion is based on the work of Russell and Muir Wood (Russell et al., 2009); a two-parameter material strength criterion is used along with consideration of the elastic stresses induced by point loads on a sphere. A particle subject to a set of external point forces reaches failure when the maximum applied force reaches the following limit condition:

$$F \le \sigma_{\lim} A_F \;\Rightarrow\; F \le \left\{ \sigma_{\lim 0} f(\mathrm{var}) \left(\frac{d}{N d_0} \right)^{-3/m} \pi \left[\frac{3}{4} \frac{\left(\frac{1-\nu_1^2}{E_1} + \frac{1-\nu_2^2}{E_2} \right)}{\left(\frac{1}{r_1} + \frac{1}{r_2} \right)} \right]^{2/3} \right\}^3 \qquad \text{Eq. I-1}$$

Where σ_{lim} is the limit strength of the material and A_F is the contact area. *f(var)* is a function used to incorporate the natural material variability into the model. The limit strength, σ_{lim}, is assumed to be normally distributed for a given sphere size. The coefficient of variation of the distribution, *var*, is taken

to be a material parameter. The mean strength value (σ_{lim0}) depends on the particle diameter (d) where m is a material constant, d_0 is the reference diameter (2 mm) and N is the scaling factor. The latter is used to model large scale problems and particle size scaling is required (Ciantia et al., 2016) in order to reduce the number of particles of the model. A_F depends on the contact force and the particle's elastic properties. r_1 and r_2 are the radii of the contacting spheres and E_i, ν_i are the Young's Moduli and Poisson's ratio respectively. Once the limit condition is reached, the spherical particle will split into smaller inscribed tangent spheres. The crushed fragments assume the velocity and material parameters of the original particle. Ciantia et al., (2016a) concluded that a 14-ball crushed configuration can adequately represent macroscopic behaviour.

I-c. DEM Model numerical implementation

Particle crushing can be implemented in PFC by using either FISH algorithms or within a C++ coded user defined contact model (UDCM). The main difference between the FISH and UDCM crushing algorithms schemes is that the FISH implementation requires a time-consuming loop through all the contacts that the UDCM does not need. In fact, in PFC5, there is a loop over all the contacts during the force-displacement law, no matter which contact model is used. The contact model force-displacement method is executed for each contact, and in the case of this UDCM it emits a signal if the crushing criterion is met. The UDCM then uses another FISH function that performs the 14-ball substitution by listening to this signal, and is therefore automatically triggered anytime the criterion has been met in a contact. Therefore, differently from the FISH crushing formulation, there is no need for an extra loop over the contacts using FISH functions

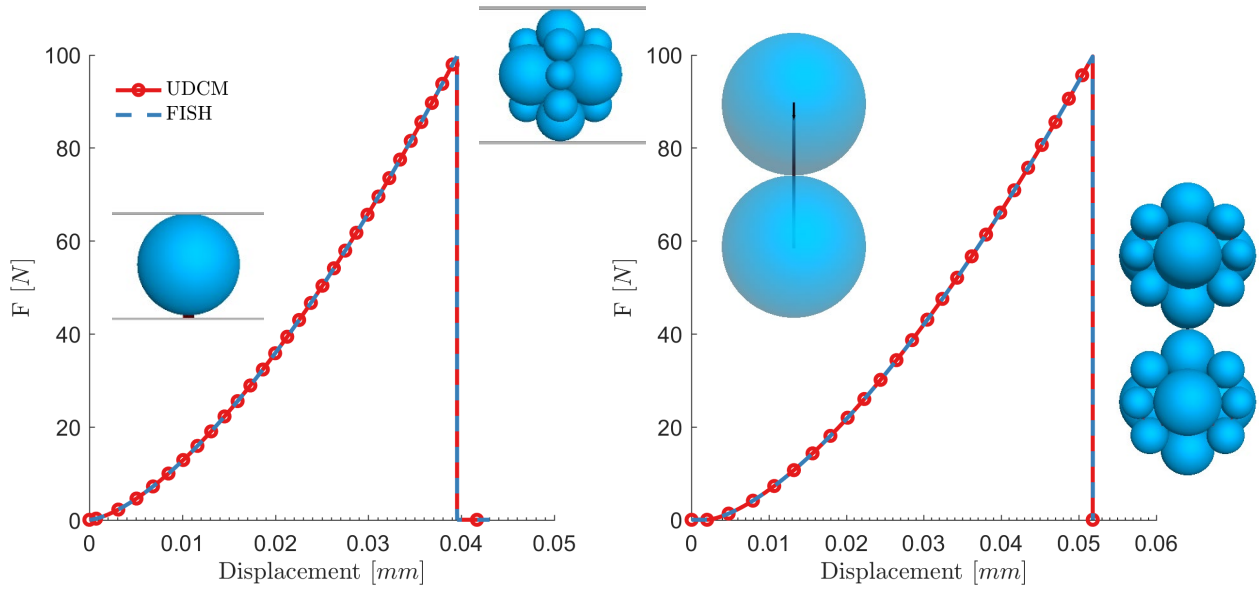

a) b)

Figure I-1 a) Initial uncrushed particle, b) Particle splitting configuration

In the FISH implementation, the failure criterion is evaluated every n_{crush} mechanical time-steps. Figure I-1 shows preliminary simulation results used to validate the correct implementation of the UDCM. To test ball-wall contacts the compression of a sphere between two rigid walls is simulated. On the other hand, to test ball-ball contacts, the compression of two spheres is modelled.

I-d. High pressure isotropic compression and computational efficiency

Now that the UDCM is already validated, an isotropic compression test on 10,000 crushable spheres is performed. The DEM specimen was created by filling a 4-cm sided cube with spheres having a particle size distribution (PSD) with particle diameters ranging from 1.44 to 2.16 mm (Figure I-2a). Gravity was set to zero and the specimen boundaries were defined using "wall" elements. Target stress values were attained by using a servo-control to adjust the wall positions. Following Ciantia et al. (2015) a stress control isotropic compression test was run. A logarithmic control of the load increment was used

$$p'_{i+1} = p'_i + L_R \left[p'_{ref} + \log\left(\frac{p'_i}{p'_{ref}} \right) \right] \qquad \text{Eq. I-2}$$

where L_R is a load increase coefficient, i indicates the step of the calculation and p'_{ref} is a reference stress of 1 kPa. The model parameters and some model characteristics are summarized in Table I-1. In Figure I-2 comparisons between the UDCM and the FISH crushing implementation are reported in terms of PSD and porosity evolution. It is interesting to observe the influence n_{crush} may have on the mechanical response. In particular, choosing a high value of n_{crush} may lead to a non-realistic response. In this work and for the L_R used, it is clear that a n_{crush} value of 100 is too high to capture all the expected crushing events, while the FISH-10 model has an n_{crush} value (n_{crush} =10) that is small enough to give the same response of the n_{crush} =1 (FISH-1) model. This means that for this set of analyses the highest n_{crush} that can be used to obtain the correct mechanical response is 10. The UDCM isotropic compression response is very similar to the one of the FISH-10 and FISH-1 models and, as detailed in Table 1, it results to be more efficient. In particular, the UDCM simulation results 2.14 and 11 times faster than FISH-10 and FISH-1 models respectively.

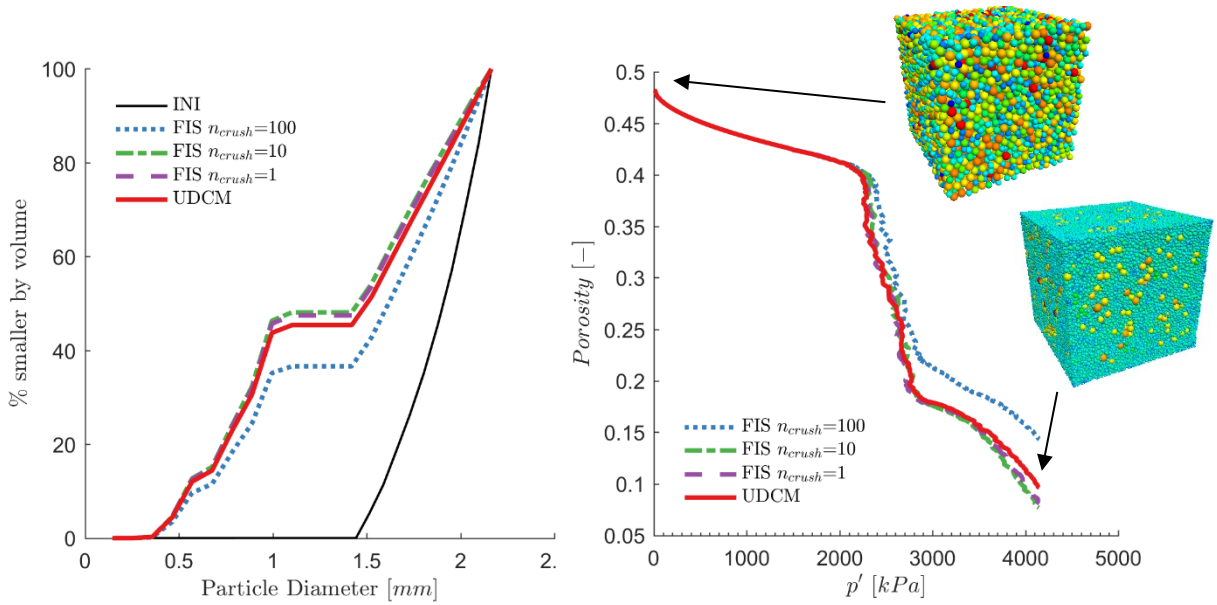

a) b)

Figure I-2 Comparison of (a) Initial and final PSDs and (b) porosity evolution with mean effective stress (p') for the 4 DEM models.

Table I-1 Discrete-element method input parameters and results

Test-ID	μ_w [-]	E_w [MPa]	μ_b [-]	E_b [MPa]	ν	$\sigma_{lim,0}$ [MPa]	m	variance	ncrush	LR	Np,0	Np,end	Time* [h]
FISH-100	0.4	866	0.4	866	0.3	116	5	0.0	100	0.01	10k	72,101	3:15
FISH-10	0.4	866	0.4	866	0.3	116	5	0.0	10	0.01	10k	86,388	8:04
FISH-1	0.4	866	0.4	866	0.3	116	5	0.0	1	0.01	10k	85,868	17:39
UDCM	0.4	866	0.4	866	0.3	116	5	0.0	-	0.01	10k	83,905	3:46

* performed using the same hardware (Intel® Xeon® CPU E5-2637 v3 at 3.50 GHz with 64.00 GB of Ram)

I-e. Conclusions

In this paper, the computational efficiency of using an inbuilt C++ crushing contact law using the commercial PFC3D code (Itasca Consulting Group, 2016) is tested. The correct implementation of the failure criterion is first tested on simple ball-wall or ball-ball models. The computational efficiency of using a user defined contact model (UDCM) is then evaluated by simulating a high pressure isotropic compression of a 4-cm sided cube containing 10,000 crushable spheres. The UDCM results to be at

least 2 times faster than the failure criterion coded by means of FISH (short for FLACish, a PFC built-in programming language) functions. The efficiency of using a UDCM is expected to increase with increasing number of contact in the DEM model as the FISH implementation requires a time-consuming loop through all the contacts that the UDCM does not need. It is also shown that the FISH coded crushing model is highly sensitive to n_{crush} the parameter that regulates the number of mechanical time steps after which the failure criterion is evaluated.

Appendix II Scripts A

Scripts in this appendix are compiled in MATLAB and deal with the analytical expression for ball-ball contact force. Ball-wall contact force can be easily addressed by changing ball properties to wall properties in these scripts. Matteo Ciantia is greatly acknowledged for his help.

```
%% INPUT parameters
clc
clear
close all

stampare=1;

G=32e9;  %Pa
nu=0.2;
Sq=1e-6;  %m
Sq2=1e-5;
n1=1;  % -
n2=2; % -
slim=3e9;  %Pa
d0= 2e-3; % m
d=1e-3 * 2;
G_wall=32e9; %Pa
%G_wall=G
d_wall=d/2;
nu_wall=0.2; %
m=7.5;

force_base=110.7;
%% DERIVED DATA
E_wall=2*G_wall/(1+nu_wall);
E=2*G/(1+nu);
Sq=Sq;
delta_1=Sq*n1;
delta_2=Sq*n2;
E_p=E_pr(G,nu,G_wall,nu_wall);
G_p=E_p*(1+nu)/2;
rp=r_pr(d/2,d/2);

%% for a single radius
Fnt1 = Sq*E_p*sqrt(2*rp*Sq);
Fnt2 = 100*Fnt1;

if Sq==0
    d_t2=0;
    bb=1;
    b=1;
    d_t1=0;
    c=1;
```

```
    dd1=0;
    dd2=d_t1;
    dd3=[d_t2:(d0/2-d_t2)/100:d0/2];

    N1=0;
    N2=0;
    N3=4/3*E_p*sqrt(rp).*(dd3-delta_1-delta_2).^(3/2);

    fcn3 = @(xx3) (slim*(d/d0)^(3/m))*pi*rp*((3*xx3/(4*E_p*sqrt(rp)))^(2/3)
+ Sq*n1 + Sq*n2) - xx3;
    [Fn_lim3,fval] = fsolve(fcn3,1);
        Fn_lim1=0;
        Fn_lim2=0;
        Fnt1=0;
        Fnt2=0;
else
    d_t2=((3*Fnt2/(4*E_p*sqrt(rp)))^(2/3) + delta_1 + delta_2);
    bb=(1/(50*sqrt(2)*(Sq)^(3/2)))*(d_t2-delta_1)*((d_t2-delta_1-
delta_2)^(1/2));
    b=(3/2)*(1+delta_2/(d_t2-delta_1-delta_2));
    d_t1=((1/100)^(1/b))*(d_t2-delta_1)+delta_1;
    c=100*b*d_t1*((d_t1-n1*Sq)^(b-1))/(d_t2-n1*Sq)^(b);

    dd1=[0:d_t1/100:d_t1];
    dd2=[d_t1:(d_t2-d_t1)/100:d_t2];
    dd3=[d_t2:(d0/2-d_t2)/100:d0/2];

    N1=Fnt1.*(dd1./d_t1).^c;
    N2=Fnt2.*((dd2-delta_1)./(d_t2-delta_1)).^b;
    N3=4/3*E_p*sqrt(rp).*(dd3-delta_1-delta_2).^(3/2);

    Fn_lim1_an=((slim*(d/d0)^(3/m))*pi*rp*((1/Fnt1)^(1/c))*d_t1)^(c/(c-1));

    fcn1 = @(xx1) ((slim*(d/d0)^(3/m))*pi*rp*((xx1/Fnt1)^(1/c))*d_t1) -
xx1;
    [Fn_lim1,fval] = fsolve(fcn1,Fnt1);

    fcn2 = @(xx2) (slim*(d/d0)^(3/m))*pi*rp*(((xx2/Fnt2)^(1/b))*(d_t2-
Sq*n1)+Sq*n1) - xx2;
    [Fn_lim2,fval] = fsolve(fcn2,Fnt2);

    fcn3 = @(xx3) (slim*(d/d0)^(3/m))*pi*rp*((3*xx3/(4*E_p*sqrt(rp)))^(2/3)
+ Sq*n1 + Sq*n2) - xx3;
    [Fn_lim3,fval] = fsolve(fcn3,Fnt2*1000);
end

delta=[0:(d0/2)/100:d0/2];


Fn_lim1
Fn_lim2
Fn_lim3

Fnt1
Fnt2

 [F_lim,Fn_lim1,Fn_lim2,Fn_lim3,fnt1,fnt2,caso] =
Flimit(slim,d0,m,Sq,n1,n2,d,d,G,nu,G,nu);
 [F_lim,Fn_lim1,Fn_lim2,Fn_lim3,fnt1,fnt2,caso] =
Flimit(slim,d0,m,Sq,n1,n2,d,d_wall,G,nu,G_wall,nu_wall);
```

Appendix III Scripts B

Scripts in this appendix deal with the implementation of user-defined rough crushable contact model. Matteo Ciantia and Sacha Emam are strongly acknowledged for their help.

C++ scripts:

```
#pragma once
// contactmodelCRHertzLNK2019.h

#include "contactmodel/src/contactmodelmechanical.h"

#ifdef CRHertz_LIB
#  define CRHertz_EXPORT EXPORT_TAG
#elif defined(NO_MODEL_IMPORT)
#  define CRHertz_EXPORT
#else
#  define CRHertz_EXPORT IMPORT_TAG
#endif

namespace cmodelsxd {
    using namespace itasca;

    class ContactModelCRHertz : public ContactModelMechanical {
    public:
        enum PropertyKeys { kwHzShear=1
                          , kwHzPoiss
                          , kwHzRadius
                          , kwFric
                          , kwRoughness
                          , kwD1
                          , kwD2
                          , kwDT1
                          , kwDT2
                          , kwNT1
                          , kwNT2
                          , kwStrength
                          , kwHzS
                          , kwHzF
                          , kwDpNRatio
                          , kwDpSRatio
                          , kwDpMode
                          , kwDpF
                          , kwDpAlpha
                          , kwRGap
                          };

        CRHertz_EXPORT ContactModelCRHertz();
        CRHertz_EXPORT virtual ~ContactModelCRHertz();
        virtual void               copy(const ContactModel *c);
        virtual void               archive(ArchiveStream &);
```

```
        virtual QString  getName() const { return "crhertz"; }
        virtual void     setIndex(int i) { index_=i;}
        virtual int      getIndex() const {return index_;}

        virtual QString  getProperties() const {
            return "hz_shear"
                   ",hz_poiss"
                   ",hz_radius"
                   ",fric"
                   ",roughness"
                   ",d1"
                   ",d2"
                   ",dt1"
                   ",dt2"
                   ",nt1"
                   ",nt2"
                   ",strength"
                   ",hz_slip"
                   ",hz_force"
                   ",dp_nratio"
                   ",dp_sratio"
                   ",dp_mode"
                   ",dp_force"
                   ",dp_alpha"
                   ",rgap"
            ;
        }

        enum EnergyKeys { kwEStrain=1,kwESlip,kwEDashpot};
        virtual QString  getEnergies() const { return "estrain,eslip,edashpot";}
        virtual double   getEnergy(uint i) const;  // Base 1
        virtual bool     getEnergyAccumulate(uint i) const; // Base 1
        virtual void     setEnergy(uint i,const double &d); // Base 1
        virtual void     activateEnergy() { if (energies_) return; energies_ =
NEWC(Energies());}
        virtual bool     getEnergyActivated() const {return (energies_ !=0);}

        enum FishCallEvents { fActivated=0, fSlipChange, fBroken};
        virtual QString  getFishCallEvents() const { return
"contact_activated,slip_change,broken_ball"; }
        virtual QVariant getProperty(uint i,const IContact *) const;
        virtual bool     getPropertyGlobal(uint i) const;
        virtual bool     setProperty(uint i,const QVariant &v,IContact *);
        virtual bool     getPropertyReadOnly(uint i) const;

        virtual bool     supportsInheritance(uint i) const;
        virtual bool     getInheritance(uint i) const { assert(i<32); quint32 mask =
to<quint32>(1 << i);  return (inheritanceField_ & mask) ? true : false; }
        virtual void     setInheritance(uint i,bool b) { assert(i<32); quint32 mask =
to<quint32>(1 << i);  if (b) inheritanceField_ |= mask;  else inheritanceField_ &=
~mask; }

        virtual uint     getMinorVersion() const;

        virtual bool    validate(ContactModelMechanicalState *state,const double
&timestep);
        virtual bool    endPropertyUpdated(const QString &name,const
IContactMechanical *c);
        virtual bool    forceDisplacementLaw(ContactModelMechanicalState *state,const
double &timestep);
```

```
        virtual DVect2  getEffectiveTranslationalStiffness() const { return
effectiveTranslationalStiffness_;}
        virtual DAVect  getEffectiveRotationalStiffness() const { return DAVect(0.0);}

        virtual ContactModelCRHertz *clone() const { return
NEWC(ContactModelCRHertz()); }
        virtual double              getActivityDistance() const {return rgap_;}
        virtual bool                isOKToDelete() const { return !isBonded(); }
        virtual void                resetForcesAndMoments() { hz_F(DVect(0.0));
dp_F(DVect(0.0)); if (energies_) energies_->estrain_ = 0.0; }

        virtual bool     checkActivity(const double &gap) { return gap <= rgap_; }

        virtual bool     isSliding() const { return hz_slip_; }
        virtual bool     isBonded() const { return false; }
        virtual void     propagateStateInformation(IContactModelMechanical*
oldCm,const CAxes &oldSystem=CAxes(),const CAxes &newSystem=CAxes());
        virtual void     setNonForcePropsFrom(IContactModel *oldCM);

        const double & hz_shear() const {return hz_shear_;}
        void           hz_shear(const double &d) {hz_shear_=d;}
        const double & hz_poiss() const {return hz_poiss_;}
        void           hz_poiss(const double &d) {hz_poiss_=d;}
        const double & fric() const {return fric_;}
        void           fric(const double &d) {fric_=d;}
        const double & roughness() const {return roughness_;}
        void           roughness(const double &d) {roughness_=d;}
        const double & d1() const {return d1_;}
        void           d1(const double &d) {d1_=d;}
        const double & d2() const {return d2_;}
        void           d2(const double &d) {d2_=d;}
        const double & dt1() const {return dt1_;}
        void           dt1(const double &d) {dt1_=d;}
        const double & dt2() const {return dt2_;}
        void           dt2(const double &d) {dt2_=d;}
        const double & nt1() const {return nt1_;}
        void           nt1(const double &d) {nt1_=d;}
        const double & nt2() const {return nt2_;}
        void           nt2(const double &d) {nt2_=d;}
        const DVect &  hz_F() const {return hz_F_;}
        void           hz_F(const DVect &f) { hz_F_=f;}
        bool           hz_S() const {return hz_slip_;}
        void           hz_S(bool b) { hz_slip_=b;}
        const double & hn() const {return hn_;}
        void           hn(const double &d) {hn_=d;}
        const double & hs() const {return hs_;}
        void           hs(const double &d) {hs_=d;}
        const double & rgap() const {return rgap_;}
        void           rgap(const double &d) {rgap_=d;}
        const double & hz_radius() const {return hz_radius_;}
        void           hz_radius(const double &d) {hz_radius_=d;}
        const double & st1() const {return st1_;}
        void           st1(const double &d) {st1_=d;}
        const double & st2() const {return st2_;}
        void           st2(const double &d) {st2_=d;}

        bool     hasDamping() const {return dpProps_ ? true : false;}
        double   dp_nratio() const {return (hasDamping() ? (dpProps_->dp_nratio_) :
0.0);}
        void     dp_nratio(const double &d) { if(!hasDamping()) return;
dpProps_->dp_nratio_=d;}
        double   dp_sratio() const {return hasDamping() ? dpProps_->dp_sratio_: 0.0;}
```

```
        void     dp_sratio(const double &d) { if(!hasDamping()) return;
dpProps_->dp_sratio_=d;}
        int      dp_mode() const {return hasDamping() ? dpProps_->dp_mode_: -1;}
        void     dp_mode(int i) { if(!hasDamping()) return; dpProps_->dp_mode_=i;}
        DVect    dp_F() const {return hasDamping() ? dpProps_->dp_F_: DVect(0.0);}
        void     dp_F(const DVect &f) { if(!hasDamping()) return; dpProps_->dp_F_=f;}
        double   dp_alpha() const {return hasDamping() ? dpProps_->dp_alpha_: 0.0;}
        void     dp_alpha(const double &d) { if(!hasDamping()) return;
dpProps_->dp_alpha_=d;}

        bool    hasEnergies() const {return energies_ ? true:false;}
        double  estrain() const {return hasEnergies() ? energies_->estrain_: 0.0;}
        void    estrain(const double &d) { if(!hasEnergies()) return;
energies_->estrain_=d;}
        double  eslip() const {return hasEnergies() ? energies_->eslip_: 0.0;}
        void    eslip(const double &d) { if(!hasEnergies()) return;
energies_->eslip_=d;}
        double  edashpot() const {return hasEnergies() ? energies_->edashpot_: 0.0;}
        void    edashpot(const double &d) { if(!hasEnergies()) return;
energies_->edashpot_=d;}

        uint inheritanceField() const {return inheritanceField_;}
        void inheritanceField(uint i) {inheritanceField_ = i;}

        const DVect2 & effectiveTranslationalStiffness()  const          {return
effectiveTranslationalStiffness_;}
        void           effectiveTranslationalStiffness(const DVect2 &v )
{effectiveTranslationalStiffness_=v;}

    private:
        static int index_;

        bool   updateStiffCoef(const IContactMechanical *con);
        bool   updateEndStiffCoef(const IContactMechanical *con);
        bool   updateEndFric(const IContactMechanical *con);
        bool   updateEndRoughness(const IContactMechanical *con);
        bool   updateEndStrength(const IContactMechanical *con);
        void   updateEffectiveStiffness(ContactModelMechanicalState *state);
        void   updateDT();
        // inheritance fields
        quint32 inheritanceField_;

        // hertz model
        double      hz_shear_;  // Shear modulus
        double      hz_poiss_;  // Poisson ratio
        double      fric_;      // Coulomb friction coefficient
        bool        hz_slip_;      // the current sliding state
        DVect       hz_F_;      // Force carried in the hertz model
        double      rgap_;      // Reference gap
        double      hz_radius_;  // Shear modulus

        // Roughness
        double      roughness_;  // roughness Sq for double-stiffness model
        double      d1_;         // roughness constant d1 for double-stiffness model
        double      d2_;         // roughness constant d2 for double-stiffness model
        double      dt1_;        // roughness transition overlap dt1 for double-
stiffness model
        double      dt2_;        // roughness transition overlap dt2 for double-
stiffness model
        double      nt1_;        // roughness transition force nt1 for double-
stiffness model
```

```
        double      nt2_;        // roughness transition force nt2 for double-
stiffness model

        // crushing
        double st1_;             // crushing strength end1
        double st2_;             // crushing strength end2

        //viscous model
        struct dpProps {
            dpProps() : dp_nratio_(0.0), dp_sratio_(0.0), dp_mode_(0),
dp_F_(DVect(0.0)),dp_alpha_(0.0) {}
            double dp_nratio_;     // normal viscous critical damping ratio
            double dp_sratio_;     // shear  viscous critical damping ratio
            int    dp_mode_;       // for viscous mode (0-4) 0 = dashpots, 1 = tensile
limit, 2 = shear limit, 3 = limit both
            DVect  dp_F_;          // Force in the dashpots
            double dp_alpha_;      // exponent
        };
        dpProps *   dpProps_;

        // energies
        struct Energies {
            Energies() : estrain_(0.0), eslip_(0.0),edashpot_(0.0) {}
            double estrain_;  // elastic energy stored in contact
            double eslip_;    // work dissipated by friction
            double edashpot_;    // work dissipated by dashpots
        };
        Energies *   energies_;


        double      hn_;                            // normal stiffness coefficient
        double      hs_;                            // shear stiffness coefficient
        DVect2  effectiveTranslationalStiffness_;  // effective stiffness
    };
} // namespace cmodelsxd
// EoF
```

//

To continue with cpp file,

//

```
// contactmodelCRHertz.cpp
#include "contactmodelCRHertz.h"

#include "module/interface/icontactmechanical.h"
#include "module/interface/icontact.h"
#include "module/interface/ipiecemechanical.h"
#include "module/interface/ipiece.h"
#include "module/interface/ifishcalllist.h"

#include "version.txt"

#include "utility/src/tptr.h"
#include "base/src/mathutil.h"
```

```
#include "kernel/interface/iprogram.h"
#include "module/interface/icontactthermal.h"
#include "contactmodel/src/contactmodelthermal.h"

#ifdef CRHertz_LIB
    int __stdcall DllMain(void *,unsigned, void *) {
        return 1;
    }

    extern "C" EXPORT_TAG const char *getName() {
#if DIM==3
        return "contactmodelmechanical3dCRHertz";
#else
        return "contactmodelmechanical2dCRHertz";
#endif
    }

    extern "C" EXPORT_TAG unsigned getMajorVersion() {
        return MAJOR_VERSION;
    }

    extern "C" EXPORT_TAG unsigned getMinorVersion() {
        return MINOR_VERSION;
    }

    extern "C" EXPORT_TAG void *createInstance() {
        cmodelsxd::ContactModelCRHertz *m = new cmodelsxd::ContactModelCRHertz();
        return (void *)m;
    }
#endif

namespace cmodelsxd {
    static const quint32 shearMask     = 0x00002;
    static const quint32 poissMask     = 0x00004;
    static const quint32 fricMask      = 0x00008;
    static const quint32 roughnessMask = 0x00010;
    static const quint32 strengthMask  = 0x00010;

    using namespace itasca;

    int ContactModelCRHertz::index_ = -1;
    UInt ContactModelCRHertz::getMinorVersion() const { return MINOR_VERSION;}

    ContactModelCRHertz::ContactModelCRHertz() :
inheritanceField_(shearMask|poissMask|fricMask|roughnessMask|strengthMask)
                                            , hz_shear_(0.0)
                                            , hz_poiss_(0.0)
                                            , hz_radius_(0.0)
                                            , fric_(0.0)
                                            , roughness_(0.0)
                                            , d1_(0.0)
                                            , d2_(0.0)
                                            , dt1_(0.0)
                                            , dt2_(0.0)
                                            , nt1_(0.0)
                                            , nt2_(0.0)
                                            , st1_(0.0)
                                            , st2_(0.0)
                                            , hz_slip_(false)
                                            , hz_F_(DVect(0.0))
                                            , rgap_(0.0)
```

```
                                          , dpProps_(0)
                                          , energies_(0)
                                          , hn_(0.0)
                                          , hs_(0.0)
                                          ,
effectiveTranslationalStiffness_(DVect2(0.0)) {
    }

    ContactModelCRHertz::~ContactModelCRHertz() {
        if (dpProps_)
          delete dpProps_;
        if (energies_)
          delete energies_;
    }

    void ContactModelCRHertz::archive(ArchiveStream &stream) {
        stream & hz_shear_;
        stream & hz_poiss_;
        stream & hz_radius_;
        stream & fric_;
        stream & roughness_;
        stream & d1_;
        stream & d2_;
        stream & dt1_;
        stream & dt2_;
        stream & nt1_;
        stream & nt2_;
        stream & st1_;
        stream & st2_;
        stream & hz_slip_;
        stream & hz_F_;
        stream & hn_;
        stream & hs_;
        stream & rgap_;

        if (stream.getArchiveState()==ArchiveStream::Save) {
            bool b = false;
            if (dpProps_) {
                b = true;
                stream & b;
                stream & dpProps_->dp_nratio_;
                stream & dpProps_->dp_sratio_;
                stream & dpProps_->dp_mode_;
                stream & dpProps_->dp_F_;
                stream & dpProps_->dp_alpha_;
            } else
                stream & b;

            b = false;
            if (energies_) {
                b = true;
                stream & b;
                stream & energies_->estrain_;
                stream & energies_->eslip_;
                stream & energies_->edashpot_;
            } else
                stream & b;
        } else {
            bool b(false);
            stream & b;
            if (b) {
                if (!dpProps_)
```

```
                dpProps_ = NEWC(dpProps());
            stream & dpProps_->dp_nratio_;
            stream & dpProps_->dp_sratio_;
            stream & dpProps_->dp_mode_;
            stream & dpProps_->dp_F_;
            if (stream.getRestoreVersion() >= 2)
                stream & dpProps_->dp_alpha_;
        }
        stream & b;
        if (b) {
            if (!energies_)
                energies_ = NEWC(Energies());
            stream & energies_->estrain_;
            stream & energies_->eslip_;
            stream & energies_->edashpot_;
        }
    }

    stream & inheritanceField_;
    stream & effectiveTranslationalStiffness_;
}

void ContactModelCRHertz::copy(const ContactModel *cm) {
    ContactModelMechanical::copy(cm);
    const ContactModelCRHertz *in = dynamic_cast<const ContactModelCRHertz*>(cm);
    if (!in) throw std::runtime_error("Internal error: contact model dynamic cast
failed.");

    hz_shear(in->hz_shear());
    hz_poiss(in->hz_poiss());
    hz_radius(in->hz_radius());
    fric(in->fric());
    d1(in->d1());
    d2(in->d2());
    dt1(in->dt1());
    dt2(in->dt2());
    nt1(in->nt1());
    nt2(in->nt2());
    st1(in->st1());
    st2(in->st2());
    roughness(in->roughness());
    hz_S(in->hz_S());
    hz_F(in->hz_F());
    hn(in->hn());
    hs(in->hs());
    rgap(in->rgap());
    if (in->hasDamping()) {
        if (!dpProps_)
            dpProps_ = NEWC(dpProps());
        dp_nratio(in->dp_nratio());
        dp_sratio(in->dp_sratio());
        dp_mode(in->dp_mode());
        dp_F(in->dp_F());
        dp_alpha(in->dp_alpha());
    }
    if (in->hasEnergies()) {
        if (!energies_)
            energies_ = NEWC(Energies());
        estrain(in->estrain());
        eslip(in->eslip());
        edashpot(in->edashpot());
    }
```

```
    inheritanceField(in->inheritanceField());
    effectiveTranslationalStiffness(in->effectiveTranslationalStiffness());
}

QVariant ContactModelCRHertz::getProperty(uint i,const IContact *) const {
  QVariant var;
  switch (i) {
      case kwHzShear:   return hz_shear_;
      case kwHzPoiss:   return hz_poiss_;
      case kwHzRadius:  return hz_radius_;
      case kwFric:      return fric_;
      case kwRoughness: return roughness_;
      case kwD1:        return d1_;
      case kwD2:        return d2_;
      case kwDT1:       return dt1_;
      case kwDT2:       return dt2_;
      case kwNT1:       return nt1_;
      case kwNT2:       return nt2_;
      case kwStrength:  {    // SE: return a DVect3 with x=st1 and y=st2 ?
                            DVect ret(0.0);
                            ret.rx() = st1_;
                            ret.rx() = st2_;
                            var.setValue(ret);
                            return var;
                        }
      case kwHzS:       return hz_slip_;
      case kwHzF:       var.setValue(hz_F_); return var;
      case kwRGap:      return rgap_;
      case kwDpNRatio:  return dpProps_ ? dpProps_->dp_nratio_ : 0.0;
      case kwDpSRatio:  return dpProps_ ? dpProps_->dp_sratio_ : 0.0;
      case kwDpMode:    return dpProps_ ? dpProps_->dp_mode_   : 0;
      case kwDpAlpha:   return dpProps_ ? dpProps_->dp_alpha_  : 0.0;
      case kwDpF:{
          dpProps_ ? var.setValue(dpProps_->dp_F_) : var.setValue(DVect(0.0));
          return var;
        }
  }
  assert(0);
  return QVariant();
}

bool ContactModelCRHertz::getPropertyGlobal(uint i) const {
    switch (i) {
        case kwHzF: // fall through
        case kwDpF: return false;
    }
    return true;
}

bool ContactModelCRHertz::setProperty(uint i,const QVariant &v,IContact *) {
    dpProps dp;
    switch (i) {
        case kwHzShear: {
            if (!v.canConvert<double>())
                throw Exception("hz_shear must be a double.");
            double val(v.toDouble());
            if (val<0.0)
                throw Exception("Negative shear modulus (hz_shear) not allowed.");
            hz_shear_ = val;
            return true;
        }
```

```
            case kwHzPoiss: {
                if (!v.canConvert<double>())
                    throw Exception("hz_poiss must be a double.");
                double val(v.toDouble());
                if (val<=-1.0 || val>0.5)
                   throw Exception("Poisson ratio (hz_poiss) must be in range (-
1.0,0.5].");
                hz_poiss_ = val;
                return true;
            }
            case kwFric: {
                if (!v.canConvert<double>())
                    throw Exception("fric must be a double.");
                double val(v.toDouble());
                if (val<0.0)
                    throw Exception("Negative fric not allowed.");
                fric_ = val;
                return false;
            }
            case kwRoughness: {
                if (!v.canConvert<double>())
                    throw Exception("roughness must be a double.");
                double val(v.toDouble());
                if (val<0.0)
                    throw Exception("Negative roughness not allowed.");
                roughness_ = val;
                return true;
            }
            case kwD1: {
                if (!v.canConvert<double>())
                    throw Exception("d1 must be a double.");
                double val(v.toDouble());
                if (val<0.0)
                    throw Exception("Negative d1 not allowed.");
                d1_ = val;
                updateDT();
                return true;
            }
            case kwD2: {
                if (!v.canConvert<double>())
                    throw Exception("d2 must be a double.");
                double val(v.toDouble());
                if (val<0.0)
                    throw Exception("Negative d2 not allowed.");
                d2_ = val;
                updateDT();
                return true;
            }
            case kwStrength: {
                if (!v.canConvert<double>())
                    throw Exception("strength must be a double.");
                double val(v.toDouble());
                if (val<0.0)
                    throw Exception("Negative strength not allowed.");
                st1_ = val;
                st2_ = val;
                return false;
            }
            case kwRGap: {
                if (!v.canConvert<double>())
                    throw Exception("Reference gap must be a double.");
                double val(v.toDouble());
```

```
            rgap_ = val;
            return false;
        }
        case kwDpNRatio: {
            if (!v.canConvert<double>())
                throw Exception("dp_nratio must be a double.");
            double val(v.toDouble());
            if (val<0.0)
                throw Exception("Negative dp_nratio not allowed.");
            if (val == 0.0 && !dpProps_)
                return false;
            if (!dpProps_)
                dpProps_ = NEWC(dpProps());
            dpProps_->dp_nratio_ = val;
            return true;
        }
        case kwDpSRatio: {
            if (!v.canConvert<double>())
                throw Exception("dp_sratio must be a double.");
            double val(v.toDouble());
            if (val<0.0)
                throw Exception("Negative dp_sratio not allowed.");
            if (val == 0.0 && !dpProps_)
                return false;
            if (!dpProps_)
                dpProps_ = NEWC(dpProps());
            dpProps_->dp_sratio_ = val;
            return true;
        }
        case kwDpMode: {
            if (!v.canConvert<int>())
               throw Exception("The viscous mode dp_mode must be 0, 1, 2, or 3.");
            int val(v.toInt());
            if (val == 0 && !dpProps_)
                return false;
            if (val < 0 || val > 3)
               throw Exception("The viscous mode dp_mode must be 0, 1, 2, or 3.");
            if (!dpProps_)
                dpProps_ = NEWC(dpProps());
            dpProps_->dp_mode_ = val;
            return false;
        }
        case kwDpAlpha: {
            if (!v.canConvert<double>())
                throw Exception("dp_alpha must be a double.");
            double val(v.toDouble());
            if (val<0.0)
                throw Exception("Negative dp_alpha not allowed.");
            if (val == 0.0 && !dpProps_)
                return false;
            if (!dpProps_)
                dpProps_ = NEWC(dpProps());
            dpProps_->dp_alpha_ = val;
            return true;
        }
    }
    return false;
}

bool ContactModelCRHertz::getPropertyReadOnly(uint i) const {
    switch (i) {
        case kwHzF:
```

```
        case kwDpF:
        case kwHzS:
        case kwHzRadius:
        case kwDT1:
        case kwDT2:
        case kwNT1:
        case kwNT2:
            return true;
        default:
            break;
    }
    return false;
}

bool ContactModelCRHertz::supportsInheritance(uint i) const {
    switch (i) {
        case kwHzShear:
        case kwHzPoiss:
        case kwFric:
        case kwRoughness:
        case kwStrength:
            return true;
        default:
            break;
    }
    return false;
}

double ContactModelCRHertz::getEnergy(uint i) const {
    double ret(0.0);
    if (!energies_)
        return ret;
    switch (i) {
        case kwEStrain:  return energies_->estrain_;
        case kwESlip:    return energies_->eslip_;
        case kwEDashpot: return energies_->edashpot_;
    }
    assert(0);
    return ret;
}

bool ContactModelCRHertz::getEnergyAccumulate(uint i) const {
    switch (i) {
        case kwEStrain:  return false;
        case kwESlip:    return true;
        case kwEDashpot: return true;
    }
    assert(0);
    return false;
}

void ContactModelCRHertz::setEnergy(uint i,const double &d) {
    if (!energies_) return;
    switch (i) {
        case kwEStrain:  energies_->estrain_ = d; return;
        case kwESlip:    energies_->eslip_   = d; return;
        case kwEDashpot: energies_->edashpot_= d; return;
    }
    assert(0);
    return;
}
```

```
    bool ContactModelCRHertz::validate(ContactModelMechanicalState *state,const double
&) {
        assert(state);
        const IContactMechanical *c = state->getMechanicalContact();
        assert(c);

        if (state->trackEnergy_)
            activateEnergy();

        updateStiffCoef(c);
        if ((inheritanceField_ & shearMask) || (inheritanceField_ & poissMask))
            updateEndStiffCoef(c);

        if (inheritanceField_ & fricMask)
            updateEndFric(c);

        if (inheritanceField_ & roughnessMask)
            updateEndRoughness(c);

        if (inheritanceField_ & strengthMask)
            updateEndStrength(c);

        updateEffectiveStiffness(state);
        return checkActivity(state->gap_);
    }

    bool ContactModelCRHertz::updateStiffCoef(const IContactMechanical *con) {
        double hnold = hn_;
        double hsold = hs_;
        double c12 = con->getEnd1Curvature().y();
        double c22 = con->getEnd2Curvature().y();
        double reff = c12+c22;
        if (reff == 0.0)
            throw Exception("CRHertz contact model undefined for 2 non-curved
surfaces");
        hz_radius_ = 1.0 /reff;
        hn_ = 4.0/3.0 * (hz_shear_/(1 -hz_poiss_)) * sqrt(hz_radius_);
        hs_ = (2.0*(1-hz_poiss_)/(2.0- hz_poiss_))*(3.0/2.0)*pow(hn_,(2.0/3.0));
        nt1_ = roughness_*(hz_shear_/(1 -hz_poiss_))*sqrt(2.0*hz_radius_*roughness_);
        nt2_ = 100.0*nt1_;
        updateDT();
        return ( (hn_ != hnold) || (hs_ != hsold) );
    }

    void ContactModelCRHertz::updateDT() {
        dt2_ = pow(3.0*nt2_*(1.0-hz_poiss_)/(4.0*hz_shear_*sqrt(hz_radius_)),2.0/3.0)
+ (d1_ + d2_)*roughness_;
        double b = 1.5*(1.0 + d2_*roughness_ / (dt2_ - (d1_ + d2_)*roughness_));
        dt1_ = pow(1.0/100.0,1.0/b) *(dt2_ - d1_*roughness_) + d1_*roughness_;
    }

    static const QString gstr("hz_shear");
    static const QString nustr("hz_poiss");
    bool ContactModelCRHertz::updateEndStiffCoef(const IContactMechanical *con) {
        assert(con);
        double g1 = hz_shear_;
        double g2 = hz_shear_;
        double nu1 = hz_poiss_;
        double nu2 = hz_poiss_;
        QVariant vg1 = con->getEnd1()->getProperty(gstr);
        QVariant vg2 = con->getEnd2()->getProperty(gstr);
        QVariant vnu1 = con->getEnd1()->getProperty(nustr);
```

```
        QVariant vnu2 = con->getEnd2()->getProperty(nustr);
        if (vg1.isValid() && vg2.isValid()) {
            g1 = vg1.toDouble();
            g2 = vg2.toDouble();
            if (g1 < 0.0 || g2 < 0.0)
                throw Exception("Negative shear modulus not allowed in CRHertz contact
model");
        }
        if (vnu1.isValid() && vnu2.isValid()) {
            nu1 = vnu1.toDouble();
            nu2 = vnu2.toDouble();
            if (nu1 <= -1.0 || nu1 > 0.5 || nu2 <= -1.0 || nu2 > 0.5)
                throw Exception("Poisson ratio should be in range (-1.0,0.5] in
CRHertz contact model");
        }
        if (g1*g2 == 0.0) return false;
        double es = 1.0 / ((1.0-nu1) / (2.0*g1) + (1.0-nu2) / (2.0*g2));
        double gs = 1.0 / ((2.0-nu1) / g1 + (2.0-nu2) /g2);
        hz_poiss_ = (4.0*gs-es)/(2.0*gs-es);
        hz_shear_ = 2.0*gs*(2-hz_poiss_);
        if (hz_shear_ < 0.0)
            throw Exception("Negative shear modulus not allowed in CRHertz contact
model");
        if (hz_poiss_ <= -1.0 || hz_poiss_ > 0.5)
            throw Exception("Poisson ratio should be in range (-1.0,0.5] in CRHertz
contact model");
        return updateStiffCoef(con);
    }

    static const QString fricstr("fric");
    bool ContactModelCRHertz::updateEndFric(const IContactMechanical *con) {
        assert(con);
        QVariant v1 = con->getEnd1()->getProperty(fricstr);
        QVariant v2 = con->getEnd2()->getProperty(fricstr);
        if (!v1.isValid() || !v2.isValid())
            return false;
        double fric1 = std::max(0.0,v1.toDouble());
        double fric2 = std::max(0.0,v2.toDouble());
        double val = fric_;
        fric_ = std::min(fric1,fric2);
        return ( (fric_ != val) );
    }

    static const QString roughnessstr("roughness");
    bool ContactModelCRHertz::updateEndRoughness(const IContactMechanical *con) {
        assert(con);
        QVariant v1 = con->getEnd1()->getProperty(roughnessstr);
        QVariant v2 = con->getEnd2()->getProperty(roughnessstr);
        if (!v1.isValid() || !v2.isValid())
            return false;
        double r1 = std::max(0.0,v1.toDouble());
        double r2 = std::max(0.0,v2.toDouble());
        double val = roughness_;
        roughness_ = sqrt(r1*r1+r2*r2);
        return updateStiffCoef(con);
    }

    static const QString strengthstr("strength");
    bool ContactModelCRHertz::updateEndStrength(const IContactMechanical *con) {
        assert(con);
        QVariant v1 = con->getEnd1()->getProperty(strengthstr);
        QVariant v2 = con->getEnd2()->getProperty(strengthstr);
```

```
        if (v1.isValid())
            st1_ = std::max(0.0,v1.toDouble());
        if (v2.isValid())
            st2_ = std::max(0.0,v2.toDouble());
        return false;
    }

    bool ContactModelCRHertz::endPropertyUpdated(const QString &name,const
IContactMechanical *c) {
        assert(c);
        QStringList availableProperties = getProperties().simplified().replace("
","").split(",",QString::SkipEmptyParts);
        QRegExp rx(name,Qt::CaseInsensitive);
        int idx = availableProperties.indexOf(rx)+1;
        bool ret=false;

        if (idx<=0)
            return ret;

        switch(idx) {
            case kwHzShear: {
                if (inheritanceField_ & shearMask)
                    ret = updateEndStiffCoef(c);
                break;
            }
            case kwHzPoiss: {
                if (inheritanceField_ & poissMask)
                    ret = updateEndStiffCoef(c);
                break;
            }
            case kwFric: {
                if (inheritanceField_ & fricMask)
                    ret = updateEndFric(c);
                break;
            }
            case kwRoughness: {
                if (inheritanceField_ & roughnessMask)
                    ret = updateEndRoughness(c);
                break;
            }
            case kwStrength: {
                if (inheritanceField_ & strengthMask)
                    ret = updateEndStrength(c);
                break;
            }
        }
        return ret;
    }

    void ContactModelCRHertz::updateEffectiveStiffness(ContactModelMechanicalState
*state) {
        effectiveTranslationalStiffness_ = DVect2(hn_,hs_);
        double overlap = rgap_ - state->gap_;
        if (overlap <= 0.0) return;
              double alpha=3.0/2.0;
        double kn = alpha*hn_*pow(overlap,alpha-1.0);
        double ks = hs_ * pow(hz_F_.x(),(alpha-1.0)/alpha);
        DVect2 ret(kn,ks);
        // correction if viscous damping active
        if (dpProps_) {
            DVect2 correct(1.0);
            if (dpProps_->dp_nratio_)
```

```
                correct.rx() = sqrt(1.0+dpProps_->dp_nratio_*dpProps_->dp_nratio_) -
dpProps_->dp_nratio_;
            if (dpProps_->dp_sratio_)
                correct.ry() = sqrt(1.0+dpProps_->dp_sratio_*dpProps_->dp_sratio_) -
dpProps_->dp_sratio_;
            ret /= (correct*correct);
        }
        effectiveTranslationalStiffness_ = ret;
    }

    bool ContactModelCRHertz::forceDisplacementLaw(ContactModelMechanicalState
*state,const double &timestep) {
        assert(state);
        if (dt2_ < dt1_)
            throw Exception("Incompatible condition (dt2 < dt1) in CRHertz contact
model");

        if (state->activated()) {
            if (cmEvents_[fActivated] >= 0) {
                FArray<QVariant,2> arg;
                QVariant v;
                IContact * c = const_cast<IContact*>(state->getContact());
                TPtr<IThing> t(c->getIThing());
                v.setValue(t);
                arg.push_back(v);
                IFishCallList *fi =
const_cast<IFishCallList*>(state->getProgram()->findInterface<IFishCallList>());
                fi->setCMFishCallArguments(c,arg,cmEvents_[fActivated]);
            }
        }

        double overlap = rgap_ - state->gap_;
        DVect trans = state->relativeTranslationalIncrement_;
#ifdef THREED
        DVect norm(trans.x(),0.0,0.0);
#else
        DVect norm(trans.x(),0.0);
#endif
        DAVect ang  = state->relativeAngularIncrement_;
        // normal force in CRHertz part
        double b = 1.5*(1.0 + d2_*roughness_ / (dt2_ - (d1_ + d2_)*roughness_));
        double c = 100.0*b*dt1_*pow(dt1_-d1_*roughness_,b-1.0)/pow(dt2_-
d1_*roughness_,b);
        double fn = 0.0;
        double kn = 0.0;
        if (overlap < dt1_) {
            fn = nt1_*pow(overlap/dt1_,c);
            kn = c*nt1_/pow(dt1_,c)*pow(overlap,c-1.0);
        } else if (dt2_ <= overlap) {
            fn = (4.0/3.0)*hz_shear_/(1.0-hz_poiss_)*sqrt(hz_radius_)*pow(overlap -
(d1_ + d2_)*roughness_,1.5);
            kn = 2.0*hz_shear_/(1.0-hz_poiss_)*sqrt(hz_radius_)*sqrt(overlap - (d1_ +
d2_)*roughness_);
        } else {
            fn = nt2_ * pow((overlap - d1_*roughness_)/(dt2_ - d1_*roughness_),b);
            kn = nt2_*b*pow((overlap - d1_*roughness_)/(dt2_ - d1_*roughness_),b-
1.0)/(dt2_ - d1_*roughness_);
        }

        // initial tangent shear stiffness
        double ks = 2.0*(1.0-hz_poiss_)/(2.0-hz_poiss_)*kn;
```

```
        DVect fs_old = hz_F_;
        fs_old.rx() = 0.0;

        DVect u_s = trans;
        u_s.rx() = 0.0;
        DVect vec = u_s * ks;

        DVect fs = fs_old - vec;

        if (state->canFail_) {
            // resolve sliding
            double crit = fn * fric_;
            double sfmag = fs.mag();
            if (sfmag > crit) {
                double rat = crit / sfmag;
                fs *= rat;
                if (!hz_slip_ && cmEvents_[fSlipChange] >= 0) {
                    FArray<QVariant,3> arg;
                    QVariant p1;
                    IContact * c = const_cast<IContact*>(state->getContact());
                    TPtr<IThing> t(c->getIThing());
                    p1.setValue(t);
                    arg.push_back(p1);
                    p1.setValue(0);
                    arg.push_back(p1);
                    IFishCallList *fi =
const_cast<IFishCallList*>(state->getProgram()->findInterface<IFishCallList>());
                    fi->setCMFishCallArguments(c,arg,cmEvents_[fSlipChange]);
                }
                hz_slip_ = true;
            } else {
                if (hz_slip_) {
                    if (cmEvents_[fSlipChange] >= 0) {
                        FArray<QVariant,3> arg;
                        QVariant p1;
                        IContact * c = const_cast<IContact*>(state->getContact());
                        TPtr<IThing> t(c->getIThing());
                        p1.setValue(t);
                        arg.push_back(p1);
                        p1.setValue(1);
                        arg.push_back(p1);
                        IFishCallList *fi =
const_cast<IFishCallList*>(state->getProgram()->findInterface<IFishCallList>());
                        fi->setCMFishCallArguments(c,arg,cmEvents_[fSlipChange]);
                    }
                    hz_slip_ = false;
                }
            }
        }

        hz_F_ = fs ;          // total force in hertz part
        hz_F_.rx() += fn;
        state->force_  = hz_F_;
        effectiveTranslationalStiffness_ = DVect2(kn,ks);
        // 3) Account for dashpot forces
        if (dpProps_) {
            dpProps_->dp_F_.fill(0.0);
            double vcn = dpProps_->dp_nratio_ * 2.0 * sqrt(state->inertialMass_*kn);
            double vcs = dpProps_->dp_sratio_ * 2.0 * sqrt(state->inertialMass_*ks);
            double fac = 1.0;
            if (dpProps_->dp_alpha_ > 0.0) fac = pow(overlap,dpProps_->dp_alpha_);
            // First damp all components
```

```
            dpProps_->dp_F_  = u_s * (-1.0* vcs*fac) / timestep; // shear component
            dpProps_->dp_F_ -= norm * vcn*fac / timestep;       // normal component
            // Need to change behavior based on the dp_mode
            if ((dpProps_->dp_mode_ == 1 || dpProps_->dp_mode_ == 3)) {
                // limit the tensile if not bonded
                if (dpProps_->dp_F_.x() + hz_F_.x() < 0)
                    dpProps_->dp_F_.rx() = - hz_F_.rx();
            }
            if (hz_slip_ && dpProps_->dp_mode_ > 1) {
                // limit the shear if not sliding
                double dfn = dpProps_->dp_F_.rx();
                dpProps_->dp_F_.fill(0.0);
                dpProps_->dp_F_.rx() = dfn;
            }
            state->force_ += dpProps_->dp_F_;
            // Correct effective translational stiffness
            DVect2 correct(1.0);
            if (dpProps_->dp_nratio_)
                correct.rx() = sqrt(1.0+dpProps_->dp_nratio_*dpProps_->dp_nratio_) -
dpProps_->dp_nratio_;
            if (dpProps_->dp_sratio_)
                correct.ry() = sqrt(1.0+dpProps_->dp_sratio_*dpProps_->dp_sratio_) -
dpProps_->dp_sratio_;
            effectiveTranslationalStiffness_ /= (correct*correct);
        }

        // 5) Compute energies
        if (state->trackEnergy_) {
            assert(energies_);
            energies_->estrain_ =  0.0;
            if (kn)
              energies_->estrain_ =(3.0/2.0)*hz_F_.x()*hz_F_.x()/(((3.0/2.0)+1.0)*kn);
            if (ks) {
                double smag2 = fs.mag2();
                energies_->estrain_ += 0.5*smag2 / ks;

                if (hz_slip_) {
                    DVect avg_F_s = (fs + fs_old)*0.5;
                    DVect u_s_el =  (fs - fs_old) / ks;
                    energies_->eslip_ -= std::min(0.0,(avg_F_s | (u_s + u_s_el)));
                }
            }
            if (dpProps_) {
                energies_->edashpot_ -= dpProps_->dp_F_ | trans;
            }
        }

        // Crushing
        double carea = dPi*hz_radius_*overlap;
        bool broke1(false);
        bool broke2(false);
        if (st1_ > 0.0 && fn > st1_*carea) broke1 = true;
        if (st2_ > 0.0 && state->end2Curvature_.y() > 0.0 && fn > st2_*carea) broke2 =
true;

        // emit fishcall event
        if (cmEvents_[fBroken] >= 0 && (broke1 || broke2)) {
            QVariant v;
            FArray<QVariant,4> arg;
            IContact * c = const_cast<IContact*>(state->getContact());

            TPtr<IThing> t(c->getIThing());
```

```
            v.setValue(t);
            arg.push_back(v);
            if (broke1) {
                v.setValue(c->getEnd1()->getIThing()->getID());
                arg.push_back(v);
            }
            if (broke2) {
                v.setValue(c->getEnd2()->getIThing()->getID());
                arg.push_back(v);
            }
            IFishCallList *fi =
const_cast<IFishCallList*>(state->getProgram()->findInterface<IFishCallList>());
            fi->setCMFishCallArguments(c,arg,cmEvents_[fBroken]);
        }

        state->momentOn1_.fill(0.0);
        state->momentOn2_.fill(0.0);
        // The state force has been updated - update the state with the resulting
torques

state->getMechanicalContact()->updateResultingTorquesLocal(state->force_,&state->momen
tOn1_,&state->momentOn2_);
        return true;
    }

    void ContactModelCRHertz::propagateStateInformation(IContactModelMechanical*
old,const CAxes &oldSystem,const CAxes &newSystem) {
        // Only do something if the contact model is of the same type
        if (old->getContactModel()->getName().compare("crhertz",Qt::CaseInsensitive)
== 0) {
            ContactModelCRHertz *oldCm = (ContactModelCRHertz *)old;
#ifdef THREED
            // Need to rotate just the shear component from oldSystem to newSystem

            // Step 1 - rotate oldSystem so that the normal is the same as the normal
of newSystem
            DVect axis = oldSystem.e1() & newSystem.e1();
            double c, ang, s;
            DVect re2;
            if (!checktol(axis.abs().maxComp(),0.0,1.0,1000)) {
                axis = axis.unit();
                c = oldSystem.e1()|newSystem.e1();
                if (c > 0)
                  c = std::min(c,1.0);
                else
                  c = std::max(c,-1.0);
                ang = acos(c);
                s = sin(ang);
                double t = 1. - c;
                DMatrix<3,3> rm;
                rm.get(0,0) = t*axis.x()*axis.x() + c;
                rm.get(0,1) = t*axis.x()*axis.y() - axis.z()*s;
                rm.get(0,2) = t*axis.x()*axis.z() + axis.y()*s;
                rm.get(1,0) = t*axis.x()*axis.y() + axis.z()*s;
                rm.get(1,1) = t*axis.y()*axis.y() + c;
                rm.get(1,2) = t*axis.y()*axis.z() - axis.x()*s;
                rm.get(2,0) = t*axis.x()*axis.z() - axis.y()*s;
                rm.get(2,1) = t*axis.y()*axis.z() + axis.x()*s;
                rm.get(2,2) = t*axis.z()*axis.z() + c;
                re2 = rm*oldSystem.e2();
            } else
                re2 = oldSystem.e2();
```

```
            // Step 2 - get the angle between the oldSystem rotated shear and
newSystem shear
            axis = re2 & newSystem.e2();
            DVect2 tpf;
            DMatrix<2,2> m;
            if (!checktol(axis.abs().maxComp(),0.0,1.0,1000)) {
                axis = axis.unit();
                c = re2|newSystem.e2();
                if (c > 0)
                    c = std::min(c,1.0);
                else
                    c = std::max(c,-1.0);
                ang = acos(c);
                if (!checktol(axis.x(),newSystem.e1().x(),1.0,100))
                    ang *= -1;
                s = sin(ang);
                m.get(0,0) = c;
                m.get(1,0) = s;
                m.get(0,1) = -m.get(1,0);
                m.get(1,1) = m.get(0,0);
                tpf = m*DVect2(oldCm->hz_F_.y(),oldCm->hz_F_.z());
            } else {
                m.get(0,0) = 1.;
                m.get(0,1) = 0.;
                m.get(1,0) = 0.;
                m.get(1,1) = 1.;
                tpf = DVect2(oldCm->hz_F_.y(),oldCm->hz_F_.z());
            }
            DVect pforce = DVect(0,tpf.x(),tpf.y());
#else
            oldSystem;
            newSystem;
            DVect pforce = DVect(0,oldCm->hz_F_.y());
#endif
            for (int i=1; i<dim; ++i)
                hz_F_.rdof(i) += pforce.dof(i);
            oldCm->hz_F_ = DVect(0.0);
            if (dpProps_ && oldCm->dpProps_) {
#ifdef THREED
                tpf = m*DVect2(oldCm->dpProps_->dp_F_.y(),oldCm->dpProps_->dp_F_.z());
                pforce = DVect(oldCm->dpProps_->dp_F_.x(),tpf.x(),tpf.y());
#else
                pforce = oldCm->dpProps_->dp_F_;
#endif
                dpProps_->dp_F_ += pforce;
                oldCm->dpProps_->dp_F_ = DVect(0.0);
            }

            if(oldCm->getEnergyActivated()) {
                activateEnergy();
                energies_->estrain_ = oldCm->energies_->estrain_;
                energies_->eslip_ = oldCm->energies_->eslip_;
                energies_->edashpot_ = oldCm->energies_->edashpot_;
                oldCm->energies_->estrain_ = 0.0;
                oldCm->energies_->eslip_ = 0.0;
                oldCm->energies_->edashpot_ = 0.0;
            }
            rgap_ = oldCm->rgap_;
        }
    }
```

```
    void ContactModelCRHertz::setNonForcePropsFrom(IContactModel *old) {
        // Only do something if the contact model is of the same type
        if (old->getName().compare("crhertz",Qt::CaseInsensitive) == 0 && !isBonded())
{
            ContactModelCRHertz *oldCm = (ContactModelCRHertz *)old;
            hn_ = oldCm->hn_;
            hs_ = oldCm->hs_;
            fric_ = oldCm->fric_;
            rgap_ = oldCm->rgap_;

            if (oldCm->dpProps_) {
                if (!dpProps_)
                    dpProps_ = NEWC(dpProps());
                dpProps_->dp_nratio_ = oldCm->dpProps_->dp_nratio_;
                dpProps_->dp_sratio_ = oldCm->dpProps_->dp_sratio_;
                dpProps_->dp_mode_ = oldCm->dpProps_->dp_mode_;
            }
        }
    }

} // namespace cmodelsxd
// EoF
```

References

Abou Matar, H., & Goble, G. (1997). SPT Dynamics Analysis and Measurements. *Geotechnical and Geoenvironmental Engineering*, *123*(10), 921–928.

Ahmed, S. M., Agaiby, S. W., & Abdel-Rahman, A. H. (2014). A unified CPT-SPT correlation for non-crushable and crushable cohesionless soils. *Ain Shams Engineering Journal*, *5*(1), 63–73. https://doi.org/10.1016/j.asej.2013.09.009

Alshibli, K. A., Druckrey, A. M., Al-Raoush, R. I., Weiskittel, T., & Lavrik, N. V. (2015). Quantifying morphology of sands using 3D imaging. *Journal of Materials in Civil Engineering*, *27*(10), 1–10. https://doi.org/10.1061/(ASCE)MT.1943-5533.0001246

Aoki, N., & Cintra, J. C. A. (2000). The application of energy conservation Hamilton's principle to the determination of energy efficiency in SPT test. In *Proc., 6th Int. Conf. on the Application of Stress-Wave Theory to Piles* (pp. 457–460).

Arroyo, M., Butlanska, J., Gens, A., Calvetti, F., & Jamiolkowski, M. (2011). Cone penetration tests in a virtual calibration chamber. *Géotechnique*, *61*(6), 525–531. https://doi.org/10.1680/geot.9.P.067

ASTM D1586 -11. (2011). Standard Test Method for Standard Penetration Test (SPT) and Split-Barrel Sampling of Soils. In *Annual Book of ASTM Standards*. Philadelphia. https://doi.org/10.1520/D1586-11.2

ASTM D6951. (2003). Standard Test Method for Use of the Dynamic Cone Penetrometer in Shallow Pavement Applications. In *ASTM International, West Conshohocken, PA*. (pp. 1–7).

B. Tarawneh. (2014). Correlation of standard and cone penetration tests for sandy and silty sand to sandy silt soil. *Electronic Journal of Geotechnical Engineering*, *19*(September), 6717–6727. https://doi.org/10.13140/2.1.3552.5124

Benz Navarrete, M. A. (2009). *Mesures dynamiques lors du battage du pénétromètre Panda 2*. Retrieved from http://scholar.google.com/scholar?hl=en&btnG=Search&q=intitle:Mesures+Dynamiques+Lors+du+Battage+du+Penetrometre+Panda+2#0

Bolton, M. D., Nakata, Y., & Cheng, Y. P. (2008). Micro- and macro-mechanical behaviour of DEM crushable materials. *Géotechnique*, *58*(6), 471–480. https://doi.org/10.1680/geot.2008.58.6.471

Butlanska, J., Arroyo, M., Amoroso, S., & Gens, A. (2018). Marchetti Flat Dilatometer Tests in a Virtual Calibration Chamber. *Geotechnical Testing Journal*, *41*(5), 930–945.

Butlanska, Joanna, Arroyo, M., Gens, A., & Sullivan, C. O. (2014). Multi-scale analysis of cone penetration test (CPT) in a virtual calibration chamber. *Canadian Geotechnical Journal*, *51*(1), 51–66. https://doi.org/dx.doi.org/10.1139/cgj-2012-0476

Calvetti, F., Prisco, C., & Nova, R. (2015). Experimental and Numerical Analysis of Soil – Pipe Interaction Experimental and Numerical Analysis of Soil – Pipe Interaction, *0241*(October). https://doi.org/10.1061/(ASCE)1090-0241(2004)130

Cao, Z., Youd, T. L., & Yuan, X. (2013). Chinese dynamic penetration test for liquefaction evaluation in gravelly soils. *Journal of Geotechnical and Geoenvironmental Engineering*, *139*(8), 1320–1333. https://doi.org/10.1061/(ASCE)GT.1943-5606.0000857

Cavarretta, I., Coop, M., & O'Sullivan, C. (2010). The influence of particle characteristics on the behaviour of coarse grained soils. *Géotechnique*, *60*(6), 413–423. https://doi.org/10.1680/geot.2010.60.6.413

Cheng, Y. P., Bolton, M. D., & Nakata, Y. (2004). Crushing and plastic deformation of soils simulated using DEM. *Géotechnique*, *54*(2), 131–141. https://doi.org/10.1680/geot.2004.54.2.131

Cheng, Y. P., Nakata, Y., & Bolton, M. D. (2003). Discrete element simulation of crushable soil. *Géotechnique*, *53*(7), 633–641. https://doi.org/10.1680/geot.2003.53.7.633

Ciantia, M. O., Arroyo, M., Calvetti, F., & Gens, A. (2015). An approach to enhance efficiency of DEM modelling of soils with crushable grains. *Geótechnique*, *65*(2), 91–110. https://doi.org/[http://dx.doi.org/10.1680/geot.13.P.218

Ciantia, M. O., Boschi, K., Shire, T., & Emam, S. (2018). Numerical techniques for fast DEM large-scale model generation. *Engineering and Computational Mechanics*, (under review). https://doi.org/10.1680/jencm.18.00025

Ciantia, M. O., O'Sullivan, C., & Jardine, R. J. (2019a). Pile penetration in crushable soils : Insights from micromechanical modelling. In *Proceedings of the XVII ECSMGE-2019* (pp. 298–317). https://doi.org/10.32075/17ECSMGE-2019-1111

Ciantia, M., Zhang, N., & Arroyo, M. (2017). Enhancing Efficiency of DEM Modeling of Particle Breakage. In *25th UKACM Conference on Computational Mechanics*. Birmingham,.

Ciantia, M.O., Arroyo, M., Calvetti, F., & Gens, A. (2016a). A numerical investigation of the incremental behavior of crushable granular soils. *International Journal for Numerical and Analytical Methods in Geomechanics*, *40*(13), 1773–1798. https://doi.org/10.1002/nag

Ciantia, M O, Arroyo, M., Butlanska, J., & Gens, A. (2016b). DEM modelling of cone penetration tests in a double-porosity crushable granular material. *Computers and Geotechnics*, *73*, 109–127. https://doi.org/10.1016/j.compgeo.2015.12.001

Ciantia, M O, Arroyo, M., & Gens, A. (2014). Particle failure in DEM models of crushable soil response. *Numerical Methods in Geotechnical Engineering*, (September), 345–350. https://doi.org/10.13140/2.1.1866.1762

Ciantia, M O, Arroyo, M., O'Sullivan, C., & Gens, A. (2019b). Micromechanical Inspection of Incremental Behaviour of Crushable Soils. *Acta Geotechnica*.

Ciantia, M O, Arroyo, M., O'Sullivan, C., Gens, A., & Liu, T. (2019c). Grading evolution and critical state in a discrete numerical model of Fontainebleau sand. *Géotechnique*, 1–15. https://doi.org/10.1680/jgeot.17.P.023

Ciantia, Matteo Oryem, Boschi, K., Shire, T., & Emam, S. (2018). Numerical techniques for fast DEM large-scale model generation. *Proceedings of the Institution of Civil Engineers - Engineering and Computational Mechanics*. https://doi.org/10.1680/jencm.18.00025

Cil, M. B., & Alshibli, K. A. (2012). 3D assessment of fracture of sand particles using discrete element method. *Géotechnique Letters*, *2*(3), 161–166. https://doi.org/10.1680/geolett.12.00024

Cil, M. B., & Alshibli, K. A. (2014). 3D evolution of sand fracture under 1D compression. *Géotechnique*, *64*(5), 351–364. https://doi.org/10.1680/geot.13.P.119

Climent, N., Arroyo, M., O'Sullivan, C., & Gens, A. (2014). Sand production simulation coupling DEM with CFD. *European Journal of Environmental and Civil Engineering*, *18*(9), 983–1008. https://doi.org/10.1080/19648189.2014.920280

Coop, M. R., Sorensen, K. K., Freitas, T. B., & Georgoutsos, G. (2004). Particle breakage during shearing of a carbonate sand. *Geotechnique*, (3), 157–163.

Crandall. (1970). The role of damping in vibration theory. *Journal of Sound and Vibration*, *11*(1), 3–18.

Cundall, P. A. (1987). Distinct element models of rock and soil structure. In *Analytical and computational methods in engineering rock mechanics (ed. E. T. Brown)* (pp. 129–163). London, UK: Allen and Unwin.

Cundall, P. A., & Strack, O. D. L. (1979). A discrete numerical model for granular assemblies. *Géotechnique*, *29*(1), 47–65.

Daniel, C. R., & Howie, J. A. (2005). Effect of hammer shape on energy transfer measurement in the Standard Penetration Test. *Soils and Foundations*, *45*(5), 121–126.

Daniel, C. R., Howie, J. A., Jackson, R. S., & Walker, B. (2005). Review of Standard Penetration Test Short Rod Corrections. *Journal of Geotechnical and Geoenvironmental Engineering*, *131*(4), 489–497.

Daniel, C. R., Jackson, R. S., Howie, J. A., & Walker, B. (2003). Development of a Spreadsheet for Modeling SPT Stress Wave Data. *Geotechnical Testing Journal*, *26*(3), 320–327. Retrieved from papers3://publication/uuid/867B7687-E650-4FAD-93E0-3544656AC861

Décourt, L., & Quaresma Filho, A. R. (1994). Practical applications of the standard penetration test complemented by torque measurements, SPT-T: Present stage and future trends. In *Proceedings XIII ICSMFE* (Vol. 1, pp. 143–148). New Delhi.

Deger, T. T. (2014). *Overburden Stress Normalization and Rod Length Corrections for the Standard Penetration Test (SPT)*. University of California, Berkeley.

Dejong, J. T., Ghafghazi, M., Sturm, A. P., Wilson, D. W., Dulk, J. Den, Armstrong, R. J., … Davis, C. A. (2017). Instrumented Becker Penetration Test . I : Equipment , Operation , and Performance. *Journal of Geotechnical and Geoenvironmental Engineering*, *143*(9), 1–12. https://doi.org/10.1061/(ASCE)GT.1943-5606.0001717.

Edil, T. B., & Benson, C. H. (2005). *Investigation of the DCP and SSG as Alternative Methods to Determine Subgrade Stability*.

Einav, I. (2007). Breakage mechanics-Part I: Theory. *Journal of the Mechanics and Physics of Solids*, *55*(6), 1274–1297. https://doi.org/10.1016/j.jmps.2006.11.003

EN ISO 22476-2. (2002). Geotechnical engineering - Field testing-Dynamic probing. In *ISO standards*.

Escobar, E., Benz, M., Gourvès, R., & Breul, P. (2013). Dynamic cone penetration tests in granular media: Determination of the tip's dynamic load-penetration curve. *AIP Conference Proceedings*, *1542*, 389–392. https://doi.org/10.1063/1.4811949

Escobar, E, Navarrete, M. A. B., Gourvès, R., Breul, P., & Chevalier, B. (2016a). In-situ determination of soil deformation modulus and the wave velocity parameters using the Panda 3 ®. In *ISC5 Geotechnical and Geophysical Site Characterisation 5 – Lehane, Acosta-Martínez and Kelly (Eds)* (pp. 279–284). Sydney, Australia.

Escobar, Esteban, Benz, M., Gourvès, R., Breul, P., & CHEVALIER, B. (2016b). LE GRIZZLY 3 ® A ÉNERGIE VARIABLE : NOUVEAUX DÉVELOPPEMENTS DE L ' ESSAI DE PÉNÉTRATION DYNAMIQUE. In *Journées Nationales de Géotechnique et de Géologie de l'Ingénieur*.

Fairhurst, C. (1961). Wave mechanics of percussive drilling. *Mine and Quarry Engineering*, *27*(3), 122–130.

Falagush, O., Mcdowell, G. R., & Yu, H. (2015). Discrete element modeling of Cone Penetration Tests incorporating particle shape and crushing. *International Journal of Geomechanics*, *15*(6), 04015003. https://doi.org/10.1061/(ASCE)GM.1943-5622.0000463.

Feng, Y. T., Zhao, T., Kato, J., & Zhou, W. (2017). Towards stochastic discrete element modelling of spherical particles with surface roughness: A normal interaction law. *Computer Methods in Applied Mechanics and Engineering*, *315*(November), 247–272. https://doi.org/10.1016/j.cma.2016.10.031

Gibbs, H., & Holtz, W. (1957). Research on Determining the Density of Sands by Spoon Penetration Testing. In *Proc., 4th International Conference on Soil Mechanics and Foundation Engineering* (pp. 35–39). London. Retrieved from https://scholar.google.it/scholar?hl=it&as_sdt=0%2C5&q=research+and+determining+the+density+of+sands+by+spoon+penetration+tests&btnG=

Gourves, R., & Barjot, R. (1995). The Panda ultralight dynamic penetrometer. In *Proceeding of ECSMFE* (pp. 83–88). Copenhagen, Denmark.

Greenwood, J. A., & Tripp, J. H. (1967). The Elastic Contact of Rough Spheres. *Journal of Applied Mechanics*, 153–159.

Guo, Y., & Yu, X. (Bill). (2015). Soil Plugging Mechanism on Large Diameter Pipe Piles : Insight from Discrete Element. In *IFCEE 2015* (pp. 1075–1086).

Hanley, K. J., Huang, X., & O'Sullivan, C. (2017). Energy dissipation in soil samples during drained triaxial shearing. *Géotechnique*, (2011), 1–13. https://doi.org/10.1680/jgeot.16.P.317

Hanley, Kevin J, Sullivan, C. O., & Huang, X. (2015). Particle-scale mechanics of sand crushing in compression and shearing using DEM. *Soils and Foundations*, *55*(5), 1100–1112. https://doi.org/10.1016/j.sandf.2015.09.011

Hatanaka, M., & Feng, L. (2006). Estimating relative density of sandy soils. *Soils and Foundations*, *46*(3), 299–313.

Hatanaka, Munenori, & Uchida, A. (1996). Empirical Correlation between Penetration Resistance and Internal Friction Angle of Sandy Soils. *Soils and Foundations*, *36*(4), 1–9. https://doi.org/10.3208/sandf.36.4_1

Hettiarachchi, H., & Brown, T. (2009). Use of SPT Blow Counts to Estimate Shear Strength Properties of Soils: Energy Balance Approach. *Journal of Geotechnical and Geoenvironmental Engineering*, *135*(6), 830–834. https://doi.org/10.1061/(ASCE)GT.1943-5606.0000016

Holmen, J. K., Olovsson, L., & Børvik, T. (2017). Discrete modeling of low-velocity penetration in sand. *Computers and Geotechnics*, *86*, 21–32.

https://doi.org/10.1016/j.compgeo.2016.12.021

Howie, J. A., Daniel, C. R., Jackson, R. S., & Walker, B. (2003). *Comparison of energy measurement methods in the Standard Penetration Test*.

Huang, A. B., & Ma, M. Y. (1994). An analytical study of cone penetration test in granular material. *Can. Geotech*, *31*(1), 91–103.

Huang, X., Hanley, K. J., O'Sullivan, C., & Kwok, F. C. Y. (2014). Effect of sample size on the response of DEM samples with a realistic grading. *Particuology*, *15*, 107–115. https://doi.org/10.1016/j.partic.2013.07.006

Idriss, I. M., & Boulanger, R. W. (2008). *Soil liquefaction during earthquakes* (Vol. 264). https://doi.org/10.1126/science.287.5454.803e

Ishikawa, K., Ito, A., Ogura, H., & Shimohira, Y. (2013). Estimation of sand N -value using pressurized sand tank and verification of vertical loading test of model pile. *AIJ J. Technol. Des*, *19*(41), 107–112. https://doi.org/10.3130/aijt.19.107

ISO 14688-1. (2017). Geotechnical investigation and testing, Identification and classification of soil, Part 1: Identification and description.

Itasca, C. G. I. (2017). PFC — Particle Flow Code, Ver. 5.0. Minneapolis.

Itasca Consulting Group. (2016). PFC3D: Itasca Consulting Group, Inc. (2014) PFC — Particle Flow Code, Ver. 5.0 Minneapolis, USA.

Itasca Consulting Group, I. (2008). PFC3D – Particle Flow Code in 3 Dimensions, Ver. 4.0 User's Manual. Minneapolis.

Jardine, R. J., Yang, Z. X., Foray, P., & Zhu, B. (2013). Interpretation of stress measurements made around closed-ended displacement piles in sand. *Géotechnique*, *63*(8), 613–627. https://doi.org/10.1680/geot.9.P.138

Jiang, M. J., Konrad, J. M., & Leroueil, S. (2003). An efficient technique for generating homogeneous specimens for DEM studies. *Computers and Geotechnics*, *30*(7), 579–597. https://doi.org/10.1016/S0266-352X(03)00064-8

Jiang, M. J., Yu, H., & Harris, D. (2006). Discrete element modelling of deep penetration in granular soils. *Int. J. Numer. Anal. Meth. Geomech.*, *30*(4), 335–361. https://doi.org/10.1002/nag.473

Kikumoto, M., Putra, A. D., & Fukuda, T. (2016). Slaking and deformation behaviour, *66*(9), 771–785.

Kovacs, W. D., & Salomone, L. A. (1982). SPT hammer energy measurement. *Journal of*

Geotechnical Engineering Division, *108*.

Ladd, R. (1978). Preparing Test Specimens Using Undercompaction. *Geotechnical Testing Journal*, *1*(1), 16–23. https://doi.org/https://doi.org/10.1520/GTJ10364J

Lee, C., Lee, J.-S., An, S., & Lee, W. (2010). Effect of Secondary Impacts on SPT Rod Energy and Sampler Penetration. *Journal of Geotechnical and Geoenvironmental Engineering*, *136*(3), 522–526.

Leung, C. F., Lee, F. H., & Yet, N. S. (1996). The role of particle breakage in pile creep in sand. *Canadian Geotechnical Journal*, *33*(6), 888–898.

Liao, S. S. C., & Whitman, R. V. (1986). Overburden correction factors for SPT in sand. *Journal of Geotechnical Engineering*, *112*(3), 373–377.

Lobo-Guerrero, S., & Vallejo, L. E. (2005). DEM analysis of crushing around driven piles in granular materials. *Géotechnique*, *55*(8), 617–623. https://doi.org/10.1680/geot.2005.55.8.617

Lobo-Guerrero, Sebastian, & Vallejo, L. E. (2007). Influence of pile shape and pile interaction on the crushable behavior of granular materials around driven piles: DEM analyses. *Granular Matter*, *9*(3–4), 241–250. https://doi.org/10.1007/s10035-007-0037-3

Lukiantchuki, J. A., Bernardes, G. P., & Esquivel, E. R. (2017). Energy ratio (ER) for the standard penetration test based on measured field tests. *Soils and Rocks*, *40*(2), 77–91. https://doi.org/10.28927/SR.402077

Luong, M. P., & Touati, A. (1983). Sols Grenus Sous Fortes Contraintes. *Rev Fr Geotech*, (24), 51–63.

Ma, G., Chen, Y., Yao, F., Zhou, W., & Wang, Q. (2019). Evolution of particle size and shape towards a steady state: Insights from FDEM simulations of crushable granular materials. *Computers and Geotechnics*, *112*(April), 147–158. https://doi.org/10.1016/j.compgeo.2019.04.022

Marcuson, W. F., & Bieganousky, W. A. (1977). Laboratory standard penetration tests on fine sands. *Journal of Geotechnical Engineering Division*, *103*(GT-6), 565–588.

Masin, D. (2012). Asymptotic behaviour of granular materials. *Granular Matter*, *14*(6), 759–774.

McDowell, G. R., & De Bono, J. P. (2013). On the micro mechanics of one-dimensional normal compression. *Géotechnique*, *63*(11), 895–908. https://doi.org/10.1680/geot.12.P.041

Meyerhof, G. G. (1957). Discussion on Research on Determining the Density of Sands by Spoon Penetration Testing. In *Proc. 4th International Conference on Soil Mechanics and*

Foundation Engineering (Vol. 3, p. 110). London.

Mohammadi, S. D., Nikoudel, M. R., Rahimi, H., & Khamehchiyan, M. (2008). Application of the Dynamic Cone Penetrometer (DCP) for determination of the engineering parameters of sandy soils. *Engineering Geology Journal*, *101*, 195–203. https://doi.org/10.1016/j.enggeo.2008.05.006

Monforte, L., Arroyo, M., Maria, J., & Gens, A. (2018). Coupled effective stress analysis of insertion problems in geotechnics with the Particle Finite Element Method. *Computers and Geotechnics*, *101*(May), 114–129. https://doi.org/10.1016/j.compgeo.2018.04.002

Moug, D. M., Boulanger, R. W., DeJong, J. T., & Jaeger, R. A. (2019). Axisymmetric Simulations of Cone Penetration in Saturated Clay. *Journal of Geotechnical and Geoenvironmental Engineering*, *145*(4). https://doi.org/10.1061/(ASCE)GT.1943-5606.0002024.

Muir Wood, D. (2007). The magic of sands. *Canadian Geotechnical Journal*, (44), 1329–1350. https://doi.org/10.1139/T07-060

Nadimi, S., & Fonseca, J. (2018). A micro finite-element model for soil behaviour: Numerical validation. *Geotechnique*, *68*(4), 364–369. https://doi.org/10.1680/jgeot.16.P.163

Nadimi, Sadegh, Fonseca, J., Andò, E., & Viggiani, G. (2019a). A micro finite-element model for soil behaviour: experimental evaluation for sand under triaxial compression. *Géotechnique*, 1–6. https://doi.org/10.1680/jgeot.18.t.030

Nadimi, Sadegh, Ghanbarzadeh, A., Neville, A., & Ghadiri, M. (2019b). Effect of particle roughness on the bulk deformation using coupled boundary element and discrete element methods. *Computational Particle Mechanics*, (0123456789). https://doi.org/10.1007/s40571-019-00288-3

Nardelli, V., & Coop, M. R. (2018). The experimental contact behaviour of natural sands : normal and tangential loading. *Geótechnique*. https://doi.org/https://doi.org/10.1680/jgeot.17.P.167

O'Donovan, J., O'Sullivan, C., Marketos, G., & Muir Wood, D. (2015). Analysis of bender element test interpretation using the discrete element method. *Granular Matter*, *17*(2), 197–216. https://doi.org/10.1007/s10035-015-0552-6

O'Sullivan, C. (2011). Particulate discrete element modelling: a geomechanics perspective. *Taylor & Francis*, *11*(December), 574. https://doi.org/10.1061/(ASCE)GM.1943-5622.0000024.

O'Sullivan, C. (2014). Advancing geomechanics using DEM. In *The International Symposium on Geomechanics from Micro to Macro (IS-Cambridge 2014)* (pp. 21–32). https://doi.org/10.1201/b17395-4

Odebrecht, E., Schnaid, F., Rocha, M. M., & de Paula Bernardes, G. (2005). Energy Efficiency for Standard Penetration Tests. *Journal of Geotechnical and Geoenvironmental Engineering*, *131*(10), 1252–1263. https://doi.org/10.1061/(ASCE)1090-0241(2005)131:10(1252)

Otsubo, M., O'Sullivan, C., Hanley, K. J., & Sim, W. W. (2017a). The influence of particle surface roughness on elastic stiffness and dynamic response. *Géotechnique*, *67*(5), 452–459. https://doi.org/10.1680/jgeot.16.P.050

Otsubo, M., O'sullivan, C., & Shire, T. (2017b). Empirical assessment of the critical time increment in explicit particulate discrete element method simulations. *Computers and Geotechnics*, *86*, 67–79. https://doi.org/10.1016/J.COMPGEO.2016.12.022

Otsubo, M., O'sullivan, C., Sim, W. W., & Ibraim, E. (2015). Quantitative assessment of the influence of surface roughness on soil stiffness. *Géotechnique*, *65*(8), 694–700. https://doi.org/10.1680/geot.14.T.028

Pender, M. J., Wesley, L. D., Larkin, T. J., & Pranjoto, S. (2006). Geotechnical properties of a pumice sand. *Soils and Foundations*, *46*(1), 69–81.

Plumelle, C., & Schlosser, F. (1991). Three Full-Scale Experiments of French Project on Soil Nailing: CLOUTERRE. *Transportation Research Record*, *1330*, 80–86.

Poganski, J., Schweiger, H. F., Kargl, G., & Kömle, N. I. (2017). DEM Modelling of a Dynamic Penetration Process on Mars as a Part of the NASA InSight Mission. *Procedia Engineering*, *175*, 43–50. https://doi.org/10.1016/j.proeng.2017.01.013

Quezada, J. C., Breul, P., Saussine, G., & C, F. R. (2014). Penetration test in coarse granular material using Contact Dynamics Method. *Computers and Geotechnics Journal*, *55*, 248–253. https://doi.org/10.1016/j.compgeo.2013.09.006

Robertson, P. K., Campanella, R. G., & Wightman, A. (1983). SPT-CPT Correlations. *Journal of Geotechnical Engineering*, *109*(11), 1449–1459. https://doi.org/https://doi.org/10.1061/(ASCE)0733-9410(1983)109:11(1449)

Rorato, R, Arroyo, M., Andò, E., & Gens, A. (2019a). Sphericity measures of sand grains. *Engineering Geology*, *254*, 43–53. https://doi.org/10.1016/j.enggeo.2019.04.006

Rorato, Riccardo. (2019b). *Imaging and discrete modelling of sand shape*.

Russell, A. R., & Einav, I. (2013). Energy dissipation from particulate systems undergoing a single particle crushing event. *Granular Matter*, *15*(3), 299–314. https://doi.org/10.1007/s10035-013-0408-x

Russell, A. R., Muir Wood, D., & Kikumoto, M. (2009). Crushing of particles in idealised granular assemblies. *Journal of the Mechanics and Physics of Solids*, *57*(8), 1293–1313.

https://doi.org/10.1016/j.jmps.2009.04.009

Scala, A. . (1956). Simple method offlexible pavement design using cone penetrometers. In *Proceedings of 2nd Australian—New Zealand Conference on Soil Mechanics and Foundation Engineering*. New Zealand.

Schmertmann, J. H. (1979). Statics of SPT. *Journal of the Geotechnical Engineering Division*, *105*(5), 655–670.

Schmertmann, J. H., & Palacios, A. (1979). Energy dynamics of SPT. *Journal of the Geotechnical Engineering Division*, *105*(GT8), 909–926.

Schnaid, F., Lourenço, D., & Odebrecht, E. (2017). Interpretation of static and dynamic penetration tests in coarse-grained soils. *Géotechnique Letters*, *7*(2), 113–118. https://doi.org/10.1680/jgele.16.00170

Schnaid, Fernando, Odebrecht, E., Rocha, M. M., & Bernardes, G. D. P. (2009). Prediction of Soil Properties from the Concepts of Energy Transfer in Dynamic Penetration Tests. *Journal of Geotechnical and Geoenvironmental Engineering*, *135*(May 2012), 1092–1100. https://doi.org/10.1061/(ASCE)GT.1943-5606.0000059

Seed, H. B., Tokimatsu, K., Harder, L. F., & Chung, R. M. (1985). Influence of SPT Procedures in Soil Liquefaction Resistance Evaluations. *Journal of Geotechnical Engineering*, *111*(12), 1425–1445. https://doi.org/10.1061/(ASCE)0733-9410(1985)111:12(1425)

Seif El Dine, B., Dupla, J. C., Frank, R., Canou, J., & Kazan, Y. (2010). Mechanical characterization of matrix coarse-grained soils with a large-sized triaxial device. *Canadian Geotechnical Journal*, *47*(4), 425–438. https://doi.org/10.1139/T09-113

Sharif, Y., Brown, M. J., Ciantia, M. O., Knappett, J., Davidson, C., Cerfontaine, B., … Ball, J. (2019). Numerically modelling the installation and loading of screw piles using DEM. In *Proceedings of the 1st International Screw Pile Symposium on Screw Piles for Energy Applications* (pp. 101–108).

Shen, C., Liu, S., Wang, L., & Wang, Y. (2018). Micromechanical modeling of particle breakage of granular materials in the framework of thermomechanics. *Acta Geotechnica*, *0123456789*. https://doi.org/10.1007/s11440-018-0692-z

Skempton, A. W. (1986). Standard penetration test procedures and the effects in sands of overburden pressure, relative density, particle size, ageing and overconsolidation. *Géotechnique*, *36*(3), 425–447.

Sun, Q. D., Indraratna, B., & Nimbalkar, S. (2014). Effect of cyclic loading frequency on the permanent deformation and degradation of railway ballast, *64*(9), 746–751.

Sun, Z., Tang, H., Espinoza, D. N., Balhoff, M. T., & Killough, J. E. (2018). Discrete element

modeling of grain crushing and implications on reservoir compaction. *Journal of Petroleum Science and Engineering*, *171*(July), 431–439. https://doi.org/10.1016/j.petrol.2018.07.046

Sy, a., & Campanella, R. G. (1991). An alternative method of measurement SPT Energy. In *Proceedings of the 2nd International conference on recent advances in Geotechnical Engineering and soils dynamics* (pp. 499–505).

Sy, A., & Campanella, R. G. (Dick). (1993). Dynamic performance of the Becker hammer drill and penetration test. *Canadian Geotechnical Journal*, *30*(4), 607–619. https://doi.org/10.1139/t93-053

Tapias, M., Alonso, E. E., & Gili, J. a. (2015). A particle model for rockfill behaviour. *Géotechnique*, (12), 975–994. https://doi.org/10.1680/geot.14.P.170

Tarawneh, B. (2017). Predicting standard penetration test N-value from cone penetration test data using artificial neural networks. *Geoscience Frontiers*, *8*(1), 199–204. https://doi.org/10.1016/j.gsf.2016.02.003

Thongmunee, S., Matsumoto, T., Kobayashi, S., Kitiyodom, P., & Kurosawa, K. (2011). Experimental and numerical studies on push-up load tests for sand plugs in a steel pipe pile. *Soils and Foundations*, *51*(5), 959–974.

Ting, J. M., Corkum, B. T., Kauffman, C. R., & Greco, C. (1989). Discrete numerical model for soil mechanics. *Journal of Geotechnical Engineering*, *115*(3), 769–787. https://doi.org/10.1061/(ASCE)0733-9410(1989)115

Tran, Q. A. (2015). *Modélisation numérique du comportement des milieux granulaires à partir de signaux pénétrométriques - approche micromécanique par la méthode des éléments discrets*. *Sciences-New York*. UNIVERSITE BLAISE PASCAL – CLERMONT II.

Tran, Q. A., Chevalier, B., Benz, M., Breul, P., & Gourvès, R. (2017). Modeling of light dynamic cone penetration test – Panda 3 ® in granular material by using 3D Discrete element method. In *Powders & Grains 2017*. https://doi.org/10.1051/epjconf/201714016003

Tran, Q. A., Chevalier, B., & Breul, P. (2016). Discrete modeling of penetration tests in constant velocity and impact conditions. *Computers and Geotechnics*, *71*, 12–18. https://doi.org/10.1016/j.compgeo.2015.08.010

UNE-EN ISO 22476-3. (2005). Investigación y ensayos geotécnicos - Ensayos de campo - Parte 3: Ensayo de penetración estándar.

Wang, B., Martin, U., & Rapp, S. (2017). Discrete element modeling of the single-particle crushing test for ballast stones. *Computers and Geotechnics*, *88*, 61–73.

Wang, J., & Yan, H. (2012). DEM analysis of energy dissipation in crushable soils. *Soils and Foundations*, *52*(4), 644–657. https://doi.org/10.1016/j.sandf.2012.07.006

Wang, P., & Arson, C. (2018). Energy distribution during the quasi-static confined comminution of granular materials. *Acta Geotechnica*, *13*(1). https://doi.org/10.1007/s11440-017-0622-5

Weibull, W. (1939). A statistical theory of strength of materials. *IVB-Handl.*

Wesley, L. (2007). Geotechnical characteristics of a pumice sand. *Characterisation and Engineering Properties of Natural Soils*, 2449–2473. Retrieved from http://scholar.google.com/scholar?hl=en&btnG=Search&q=intitle:Geotechnical+characteristics+of+a+pumice+sand#5

Wilson, R., Dini, D., & Van Wachem, B. (2017). The influence of surface roughness and adhesion on particle rolling. *Powder Technology*, *312*, 321–333. https://doi.org/10.1016/j.powtec.2017.01.080

Yang, Z. X., Jardine, R. J., Zhu, B. T., Foray, P., & Tsuha, C. H. C. (2010). Sand grain crushing and interface shearing during displacement pile installation in sand. *Géotechnique*, *60*(6), 469–482. https://doi.org/10.1680/geot.2010.60.6.469

Yang, Z. X., Jardine, R. J., Zhu, B. T., & Rimoy, S. (2014). Stresses Developed around Displacement Piles Penetration in Sand. *Journal of Geotechnical and Geoenvironmental Engineering*, *140*(3), 04013027. https://doi.org/10.1061/(ASCE)GT.1943-5606.0001022

Yao, T., Baudet, B. A., & Lourenço, S. D. N. (2018). Quantification of the surface roughness of quartz sand using optical interferometry. *Meccanica*, 1–8. https://doi.org/10.1007/s11012-018-0879-2

Yimsiri, S., & Soga, K. (2000). Micromechanics-based stress–strain behaviour of soils at small strains. *Géotechnique*, *50*(5), 559–571. https://doi.org/10.1680/geot.2000.50.5.559

Youd, B. T. L., Idriss, I. M., Andrus, R. D., Arango, I., Castro, G., Christian, J. T., … Ii, K. H. S. (2001). Liquefaction resistance of soils: Summary report from the 1996 and 1998 NCEER Workshops on Evaluation of Liquefaction Resistance of Soils. *Journal of Geotechnical and Geoenvironmental Engineering*, *127*(10), 817–833.

Zhang, F., Damjanac, B., & Huang, H. (2013). Coupled discrete element modeling of fluid injection into dense granular media. *Journal of Geophysical Research: Solid Earth*, *118*(6), 2703–2722. https://doi.org/10.1002/jgrb.50204

Zhang, N, Arroyo, M., Gens, A., & Ciantia, M. (2018a). DEM modelling of dynamic penetration in granular material. In *9th European Conference on Numerical Methods in Geotechnical Engineering*. Porto.

Zhang, N, & Evans, T. M. (2019). Discrete numerical simulations of torpedo anchor installation in granular soils. *Computers and Geotechnics*, *108*, 40–52. https://doi.org/10.1016/j.compgeo.2018.12.013

Zhang, Ningning, Arroyo, M., Ciantia, M., & Gens, A. (2018b). DEM investigation of particle crushing effects on static and dynamic penetration tests. In *Proceedings of China-Europe Conference on Geotechnical Engineering (Wu W and Yu HS (eds))* (pp. 274–278).

Zhang, Z., & Wang, Y. (2015). Three-dimensional DEM simulations of monotonic jacking in sand. *Granular Matter*, *17*(3), 359–376. https://doi.org/10.1007/s10035-015-0562-4

Zhou, W., Xu, K., Ma, G., & Chang, X. (2019). On the breakage function for constructing the fragment replacement modes. *Particuology*, (January). https://doi.org/10.1016/j.partic.2018.08.006

Zhu, F., & Zhao, J. (2019). A peridynamic investigation on crushing of sand particles. *Geotechnique*, *69*(6), 526–540. https://doi.org/10.1680/jgeot.17.P.274

Zhu, H. P., Zhou, Z. Y., Yang, R. Y., & Yu, A. B. (2007). Discrete particle simulation of particulate systems: Theoretical developments. *Chemical Engineering Science*, *62*(13), 3378–3396. https://doi.org/10.1016/j.ces.2006.12.089